# Evaluating the Effect of a Strong Metal-Support Interaction on the Activity of Molybdenum Carbide Supported Platinum Water-Gas Shift Catalysts

by

Neil Michael Schweitzer

A dissertation submitted in partial fulfillment
of the requirements for the degree of
Doctor of Philosophy
(Chemical Engineering)
in the University of Michigan
2010

Doctoral Committee:

Associate Professor Suljo Linic, Co-Chair
Professor Levi T. Thompson Jr., Co-Chair
Professor James E. Penner-Hahn
Professor Phillip E. Savage
Principal Scientist Susanne M. Opalka, United Technologies Research Center

*To Nonnie and Granny,*
*your unwavering love and support still resonate in my heart*

**Acknowledgments**

I'd like to first thank my advisors, Professor Suljo Linic and Professor Levi Thompson. I was granted the unique opportunity to learn a wide range of experimental and theoretical tools, to travel to many conferences to hear talks from experts from around the world, and to work with and learn from a wide range of scientists with expertise in many different aspects of catalysis research. Over the past five years, I have grown substantially as a scientist, a professional, and a person. I owe most of that growth not only to the guidance and support provided Prof. Linic and Prof. Thompson, but also to the challenge of upholding the lofty standards established in their groups and the creative freedom provided by them to meet these expectations. They have dedicated countless hours and late nights toward my development and success, to which I am eternally grateful.

My Ph.D committee has been exceedingly helpful during the writing process of this thesis work. Prof. Phil Savage has offered advice pertaining to the content of the chapters and the statistical analysis of the data. Prof. James Penner-Hahn has provided expert guidance related to the analysis and presentation of the x-ray absorption spectroscopy data presented throughout this work. Dr. Susanne Opalka has worked with me collaboratively on the density functional theory calculations, particularly the calculations involving platinum structures. Their input has raised the quality of this work, and the time they have dedicated to this project is very appreciated.

During the past five years, I had the benefit of working closely with some extraordinary students. When I was a young grad student, I was able to learn the basics of catalysis research and the usage of equipment from several particularly helpful students: Dr. Chang Hwan Kim, Dr. Easwar Ranganathan, Dr. Timothy King, Dr. Worajit Setthapun, Prof. Andre Taylor, Dr. Randolph McGee, and Dr.

William Johnson from the Thompson group, as well as Dr. Eranda Nikolla, Dr. Siris Laursen and Dr. Joydeep Mukherjee from the Linic group. Additionally, in recent years, I have learned, struggled, and succeeded alongside many students with very bright futures: Dr. Peter Aurora, Richard Ezike, Adam Lausche, Leon Webster, Josh Grilly, Kanako Okada, Binay Prasad, Aaron Shinkle, and Priyanka Pande of the Thompson group, and Phillip Christopher, David Ingram, Adam Holewinski, Matthew Morabito, Marimuthu Andiappan, Michelle Przybylek, and Thomas Yeh of the Linic Group. Additionally, I have had the pleasure of mentoring two undergraduate students: Annie Su and Chris Hilger.

There are two colleagues I would like to thank in particular. I have collaborated directly with Hongliang Xin of the Linic group on projects requiring extensive theoretical calculations. Hongliang is an expert in theoretical calculations, and I have learned a great deal from comprehensive conversations with him. I also collaborated with Josh Schaidle of the Thompson group. Josh and I have spent a number of sleepless nights at Argonne National Laboratory performing x-ray adsorption spectroscopy experiments. Additionally, we have spent countless hours talking about catalysis in general, and he has been a great friend.

Much of my research was conducted using the facilities, resources, and experience of the Materials Research Collaborative Access Team (MRCAT) of the Advanced Photon Source Division (APS) of Argonne National Laboratory. I am particularly grateful to APS for granting us time to use the synchrotron radiation sources, and the MRCAT beamline scientists Soma Chattopadhyay and Tomohiro Shibata for teaching me how to use the synchrotron equipment, and even, at times, sacrificing time with their families to ensure the success of our experiments. I’d like to thank Dr. Neng Guo and Dr. Rodrigo Lobo for their assistance using the facilities at APS. Finally, I’d like to particularly thank Dr. Jeff Miller who selflessly spent countless hours teaching me the fundamentals of X-ray adsorption spectroscopy and discussing the applications of this technique to catalytic systems with me. The results obtained from these experiments proved

paramount in this work and would have been impossible to obtain without his help.

I'd like to thank Dr. John Mansfield, Dr. Kai Sun, Dr. Haiping Sun, and Dr. Ying Qi of the Electron Microbeam Analysis Laboratory (EMAL) at the University of Michigan. EMAL is an indispensable resource for graduate students at the University of Michigan, and the accessibility and quality of the instruments are indicative of the passion and expertise exhibited by those mentioned above.

Funding of my projects was made possible by The National Science Foundation (CBET 0933239, CTS-CAREER 0543067 and NSF CBET 0756255), the International Molybdenum Association, US Department of Energy DOE-BES, Division of Chemical Sciences, and the Office of Naval Research (N000140810122).

Since I was in high school, I have always benefited from having a distinct group of friends at different stages of my life in which I could confide in and lean on when I was in need; my time in Ann Arbor has been no exception. I have been blessed to befriend a number of people in graduate school, particularly Dr. Joe and Megan Mayne, Peter Burgardt, Dr. Michael Senra, Liz Ranney, Bean Getsoian, Michael Hoepfner, Dr. Dan and Erin McNerny, Dr. Ashish Agarwal, Dr. Meghan Cuddihy, Tom Westrich, Dr. Kevin and Dr. Georgina Critchley, Dr. Jim and Dr. Amy Bucher, Dr. Daniel and Dr. Michelle Lilly, Dr. Ben Gould, Sean Langlier, Ramsey Zeitoun, Elizabeth Stewart, Lindsay Lack, Nicki Ingram, Joy Racowski, and Dr. Obiefune Ezekoye. Additionally, I have made numerous friends through the incredible ultimate Frisbee community in Ann Arbor.

Last but not least, I must thank my family. The road leading toward the completion of this work has been a tumultuous journey, and it was only by the love and support of my family that I have completed this voyage. This includes my parents, Michael and Marta Schweitzer, my sister Jeni Schweitzer, the Wood family: T.J., Julie, Thomas, and Benjamin, the Hammer family: Andrew, Natalie,

Joshua, and Noelle, and the Hickman family: Carl, Cheryl, and Carla. Finally, I want to specifically acknowledge Amanda Hickman, whose love and passion drives me to be a better man, and whose support and strength enables me to do so.

## Table of Contents

## List of Figures

**Figure**

## List of Tables

**Table**

# Chapter 1

# Introduction

## 1. A historical perspective of heterogeneous catalysis

Catalysts are used in a variety of processes including the production of food, the refining of petroleum, the production of plastics, the reduction of pollutants, and many others [1,2]. Some of the most important technological advances involving heterogeneous catalysis, most of which have occurred during the last century, have helped shape history and have contributed to a significant increase in the standard of living for most of the population. A sustained standard of living for future generations will require comparable advancements.

One of the earliest advances in catalysis was the development of the Haber-Bosch process. In 1908, Fritz Haber, a German chemist, developed an Fe based catalyst, capable of producing liquid ammonia from ambient nitrogen [1,4] using hydrogen in the following reaction:

$$N_2 + 3H_2 \rightleftharpoons 2NH_3 \qquad \text{Eq. 1.1}$$

Carl Bosch, an employee of BASF, directed the development of an industrial process using Haber's catalyst. The first ammonia synthesis plant was constructed in Oppau, Germany in 1911 using an improved Fe catalyst that is still very similar to the catalyst used today [1,4]. The ammonia produced from the Haber-Bosch process has two primary uses: fertilizer and explosives. Figure 1.1 shows how "Haber-Bosch ammonia" has effected the world's population over time. In 2009, almost 50% of the world population was fed from food grown using "Haber-Bosch ammonia" [5]. During World War I, the Haber-Bosch process was

the single source for ammonia used in the production of explosives. Without this additional resource, Germany may have surrendered to the Allies much sooner [5]. The development of Haber-Bosch process is considered one of the most important developments of the twentieth century (for a detailed analysis of the effect of this process on the history of the twentieth century and beyond, the reader is referred to Erisman et al. [5]).

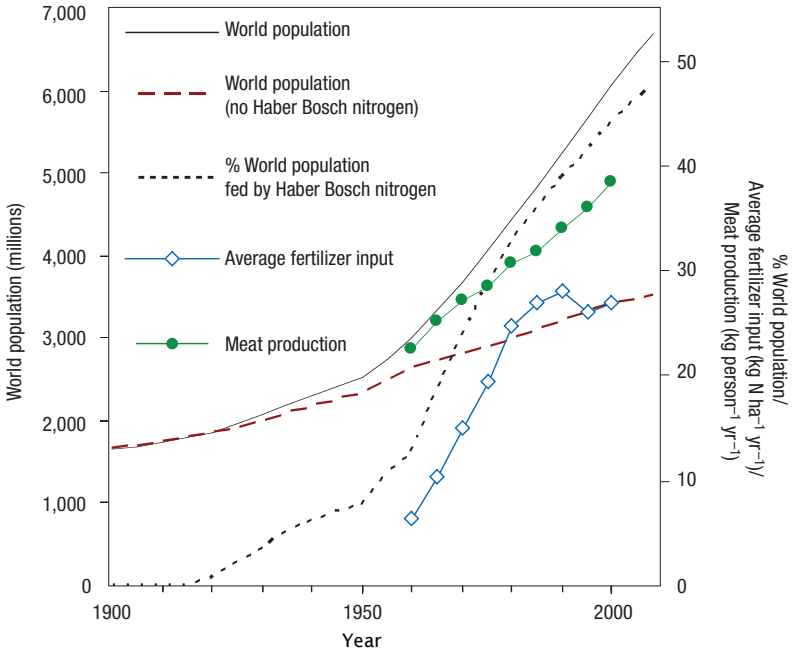


**Figure 1.1: Trends in world population and fertilizer use over time. Taken from Erisman et al. [5]**

Another major development in heterogeneous catalysis which has affected human history was the Fisher-Tropsch synthesis (FTS) process: the production of hydrocarbon fuels from CO and $H_2$. FTS is generally characterized by the following reaction:

$$nCO + (2n+1)H_2 \rightleftharpoons C_nH_{2n+2} + nH_2O \qquad \text{Eq. 1.2}$$

This reaction was initially discovered by scientists Paul Sabatier and J.B. Senderens in 1902 when they showed that methane could be produced from CO and $H_2$ using a Co, Fe, or Ni catalyst [1]. In 1925, Franz Fischer and Hans Tropsch produced liquid hydrocarbons and solid paraffins on a Co-Fe catalyst [1].

Further process development took place in the 1930s, and the first FTS plant went into production in Germany by 1936 [1,3]. These plants used coal gasification technology as a source for CO and $H_2$, and by 1940 produced one million tons of product yearly [6]. Since Germany had no domestic source of fuel, these plants were the primary source (over 90% of the fuel consumed at that time was attained from FTS plants [6]) of diesel fuel for Nazi Germany during World War II (WWII). After WWII, the German plants were discontinued. The only operating plant in the world was in Sasolburg, South Africa [1,3]. However, research and process development of the FTS process has again attracted interest from oil companies [1].

One of the most important advances in catalysis in recent history was the development of automotive catalytic converters. In the 1950s, scientists were beginning to understand the effects of automotive exhaust on air pollution and smog formation [4]. This sparked research in automotive emission controls in the 1960s [1], and in 1970, the United States passed the Clean Air Act which required an immediate 90% reduction in CO, hydrocarbons (HC's), and NO emissions from car exhaust [1,4]. The biggest difficulties in developing catalysts for this system are the wide range of conditions under which they must perform (i.e. varying concentrations and flow rates of reactants, varying temperature regimes, and the presence of potential poisons such as sulfur molecules) and the complex chemistry associated with an exhaust stream containing a large variety of components [1,4]. From 1972 to 1979, three-way catalysts containing Pt, Pd, and Rh were developed which successfully met the standards of the time. However, standards are perpetually growing more stringent, and it is assured that emission controls will remain a very active branch of catalytic research in the future [1].

## 2. Hydrogen production technology

Catalysis also plays an essential role in fossil fuel refining and hydrogen production [1,7]. Additionally, emerging technologies which will one day supplant

fossil fuel based technologies (such as the production of biofuels, synthetic fuel technologies, photo-catalytic and electro-catalytic water splitting, and fuel cells) will also require highly efficient and selective catalysts [7]. An important commodity chemical that is used now for fossil fuel refining and will be used in the immediate future in alternative energy processes is hydrogen.

Industrially, hydrogen is produced either from hydrocarbon steam reforming, coal gasification, or biomass gasification. Hydrocarbon steam reforming is the most common method (essentially the reverse reaction of FTS (eq. 1.2), but $CO_2$ is also a major byproduct) [1]. A process flow diagram for an example system is given in figure 1.2. Initially, the hydrocarbon fuel is fed to a high temperature reactor with steam, where it is reformed into syn gas (a mixture of $H_2$, CO, $CO_2$, and unreacted fuel). The concentration of CO is typically around 10%. Since CO is a poison to many catalysts (such as fuel cell catalysts and

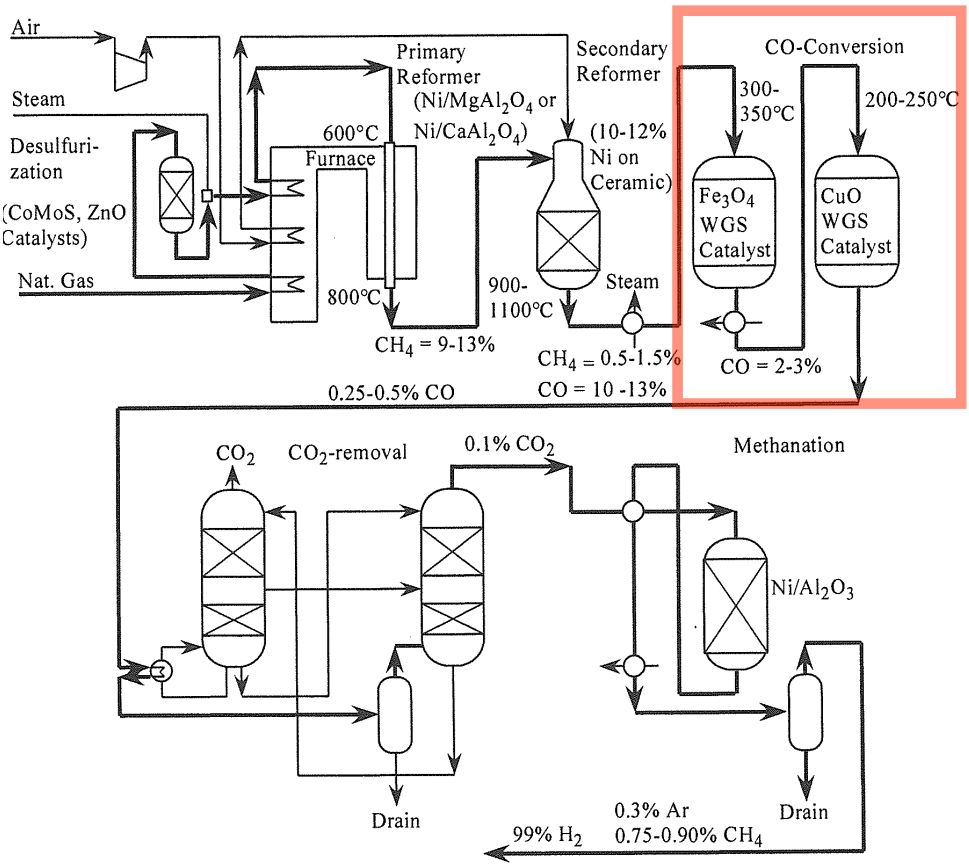


**Figure 1.2: An example process flow diagram for a natural gas steam reforming process. The water-gas shift units are outlined in a red box. Taken from *Fundamentals of Industrial Catalytic Process, Second Edition* [1].**

ammonia synthesis catalysts [1,8]), it is necessary to reduce the CO concentration in the hydrogen product to below 5 ppm (parts per million) [1]. The rest of the process is dedicated to removing CO and $CO_2$ from the hydrogen.

The water-gas shift reaction (WGS) is used in the first stages of hydrogen purification:

$$CO + H_2O \rightleftharpoons CO_2 + H_2 \qquad \text{Eq. 1.3}$$

The benefit of using WGS is that in the process of removing CO, additional hydrogen is produced. However, the main disadvantage of WGS is that it is slightly exothermic and equilibrium limited. For this reason, the reaction is performed in two stages, a high temperature reactor and a low temperature reactor. Figure 1.3 shows the equilibrium concentration of CO as a function of temperature for typical inlet streams to high temperature and low temperature WGS reactors. The high temperature WGS reactor typically operates around 300°C and uses an iron based catalyst to achieve CO concentrations of approximately 2-3%. The low temperature reactor operates in the range of 200° C-250°C using a $Cu/Zn/Al_2O_3$ catalyst and approaches concentrations of CO below 0.5%.

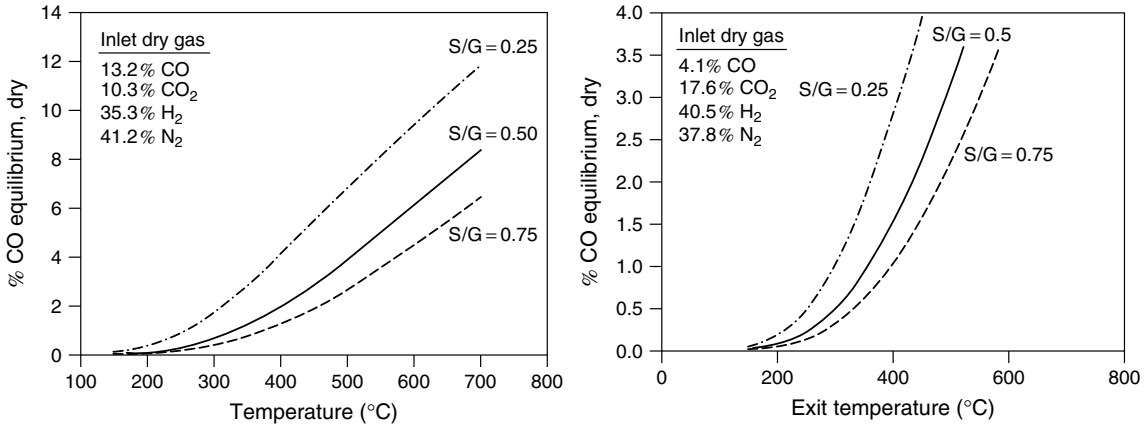


**Figure 1.3: CO equilibrium concentrations as a function of temperature for the WGS reaction for a typical high temperature WGS inlet (left) and low temperature WGS inlet (right). S/G refers to various steam to dry gas ratios. Taken from Ladebeck et al. [8]**

In an industrial process, post-WGS CO concentrations are further reduced to ppm levels by employing either methanation or selective oxidation processes [1,8]. Final purification can also employ $CO_2$ sequestration technology [1].

The hydrogen production process could benefit from the development of catalyst more active than the low temperature $Cu/Zn/Al_2O_3$ catalyst. If a catalyst was developed which exhibited rates higher than the copper catalyst, it is possible that the dual stage WGS strategy described above could be replaced with a single stage [8]. The focus of this work is to study alternative materials for low temperature WGS. These materials will encompass alternative catalytic metals such as platinum as well as alternative support materials — transition metal carbides. The reasons for identifying these specific materials will be discussed in more detail below, but first, if one is to study and discover new materials for catalytic systems, it is necessary to understand important, fundamental aspects of heterogeneous catalysis.

## 3. Understanding catalysis fundamentals

Two goals of studying heterogeneous catalysis are: 1) understanding properties of materials that contribute to observed reaction rates and selectivities, and 2) designing and discovering new materials that exhibit high reaction rates or selectivities. The fundamental mechanisms which control reaction rates on catalytic surfaces arise from a subtle balance of thermodynamics and chemical kinetics. In this section, we will review the concepts which lead to an understanding of the catalytic systems and observed catalytic rates.

### *3.1. Reaction rates and rate constants*

There are numerous textbooks devoted to discussing chemical kinetics in great detail, but for this discussion, it is sufficient to establish that for a given homogeneous reaction, the forward reaction rate is proportional to the product of the reactant concentrations (raised to some power) by a proportionality constant *k*, called the reaction rate constant. For example, consider the elementary,

equilibrium reaction presented in eq. 1.4. The overall rate expression and forward rate expression are then presented by eq. 1.5 and 1.6 respectively:

$$AB + C \rightleftharpoons A + BC \quad \text{Eq. 1.4}$$

$$r = k^{+}([AB][C] - [A][BC]/K_{eq}) \quad \text{Eq. 1.5}$$

$$r^{+} = k^{+}[AB][C] \quad \text{Eq. 1.6}$$

where *r* is the rate, *k* is the rate constant, and $K_{eq}$ is the equilibrium constant. In these equations, the superscript '+' represents quantities of the forward reaction while the superscript '-' represents the reverse reaction. The equilibrium constant is related to concentrations and rate constants by eq. 1.7, therefore eq. 1.5 is simply the sum of the forward rate (the first term) and the reverse rate (the second term).

$$K_{eq} = \frac{[A][BC]}{[AB][C]} = \frac{k^{-}}{k^{+}} \quad \text{Eq. 1.7}$$

The reaction rate constant is a function of temperature, described by the Arrhenius equation:

$$k = A_{app} \cdot e^{(-\Delta E_{a,app}/RT)} \quad \text{Eq. 1.8}$$

where $A_{app}$ is the apparent pre-exponential constant, $E_{a,app}$ is the apparent activation energy, *R* is the ideal gas constant, and *T* is the reaction temperature. If a catalyst is used in the reaction, the reaction rate increases because the catalyst has either lowered the apparent activation barrier, increased the apparent pre-exponential factor, or both. The distinction of "apparent" is used here to emphasize that these values are calculated from observed, overall reaction rates. If the overall mechanism is one single reaction, the apparent activation energy and apparent pre-exponential factor would be the same as the activation energy and pre-exponential factor of the reaction (assuming there are

no mass transfer limitations). However, reactions occurring over catalytic surfaces are the net results of several elementary steps which occur on the surface.

For example, a common proposed mechanism for the water-gas shift reaction (Eq. 1.3) is the red-ox mechanism [9,10,11], illustrated in R.1-R.8:

$$CO + {}^* \rightleftharpoons CO^* \quad \text{R.1}$$

$$H_2O + {}^* \rightleftharpoons H_2O^* \quad \text{R.2}$$

$$H_2O^* + {}^* \rightleftharpoons OH^* + H^* \quad \text{R.3}$$

$$OH^* + {}^* \rightleftharpoons O^* + H^* \quad \text{R.4}$$

$$CO^* + O^* \rightleftharpoons CO_2^* + {}^* \quad \text{R.5}$$

$$H^* + H^* \rightleftharpoons H_2^* + {}^* \quad \text{R.6}$$

$$CO_2^* \rightleftharpoons CO_2 + {}^* \quad \text{R.7}$$

$$H_2^* \rightleftharpoons H_2 + {}^* \quad \text{R.8}$$

In this mechanism, * represents an adsorption site on the surface and X* represents an adsorbed species, X, on the surface. The apparent activation energy and apparent pre-exponential factors of the overall, observed rate contain contributions from each of the elementary steps considered rate limiting steps (contributions from the other steps to these quantities are insignificant). The red-ox mechanism illustrates three general types of elementary reactions which occur in every heterogeneous catalytic mechanism: R.1 and R.2 are reactant adsorption steps, R.3-R.6 are surface reactions, and R.7 and R.8 are product desorption steps. For a detailed description of how to derive microkinetic models of reaction mechanism on catalyst surfaces and their affect on apparent activation energies and apparent pre-exponential factors, refer to Lynggaard et al. [12]

It is relatively simple to see how thermodynamics might play a role in adsorption and desorption of species on a surface. If a molecule binds strongly to

a surface, it should be easy to adsorb the molecule but difficult to desorb the molecule. The opposite would be true if the molecule adsorbed weakly to a surface. However, it is less obvious how thermodynamics may affect surface reactions and observable kinetics. However, through the study of transition state theory, this link can be established.

### *3.2. Transition state theory*

Figure 1.4 shows the potential energy diagram for the elementary reaction in eq. 1.4. The x-axis of figure 1.4 is the reaction coordinate. The y-axis is the free energy of the system. For this reaction, the reaction coordinate is related to the relative distance of atom B from atom A and atom C. For example, initially the distance A-B is at some equilibrium bond distance and the distance B-C is very large (relative to a typical bond distance). As the reaction continues, the distance A-B will grow and the distance B-C will decrease until the distance B-C reaches some equilibrium bond distance and the distance A-B is very large. At this point, the reaction products have formed.

As the reaction coordinate moves forward from the reactants, the free energy of the system begins to rise until it reaches a maximum. This state is

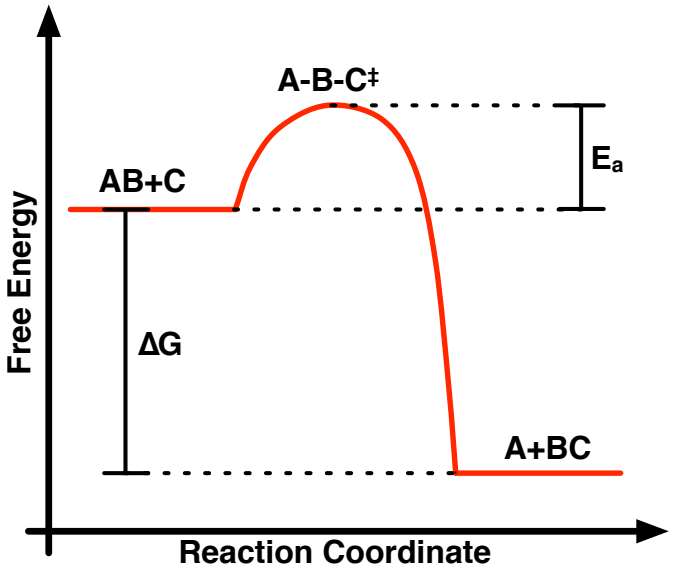


**Figure 1.4: Potential energy diagram for the arbitrary reaction AB+C ⇌ A+BC**

defined as the transition state. The energy required to achieve this state is the activation barrier of the reaction, and is labeled $E_a$ in figure 1.4. The difference between the energy of the products and the reactants is the change in free energy of the reaction (for reactions on surfaces, changes in entropy are negligible compared to changes in enthalpy, so this value is approximately the same as the change in enthalpy).

As indicated in the previous section, the magnitude of the activation barrier and pre-exponential factor of the rate constant dictates the rate of the reaction. Transition state theory (TST) allows us to derive these kinetic parameters from a thermodynamic standpoint. TST was first derived in 1935 by Henry Eyring and by M.G. Evans and M. Polanyi almost simultaneously [13]. The derivation that follows is oversimplified but is suitable for this discussion. For a more detailed derivation, refer to the following references [13,14,15].

The derivation starts by rewriting the reaction equation as a series of reactions including the transition state:

$$AB + C \rightleftharpoons [A - B - C]^{\ddagger} \rightarrow A + BC \qquad \text{Eq. 1.9}$$

A key assumption of TST is that the reactants and transition state are in quasi-equilibrium. One of the consequences of this assumption is that the forward reaction rate is directly proportional to the rate by which the transition state complex decomposes into the products. This rate is written in eq. 1.10. Additionally, the equilibrium constant for eq. 1.9 is also given in eq. 1.11 and 1.12:

$$r^{+} = \nu \, [A - B - C]^{\ddagger} \qquad \text{Eq. 1.10}$$

$$K_{eq}^{\ddagger} = \frac{[A - B - C]^{\ddagger}}{[AB][C]} \qquad \text{Eq. 1.11}$$

$$\ln K_{eq}^{\ddagger} = -\Delta G^{\circ\ddagger}/RT = -(\Delta H^{\circ\ddagger} - T\Delta S^{\circ\ddagger})/RT \qquad \text{Eq. 1.12}$$

In eq. 1.10, *v* is the frequency that a transition state complex forms the products. By combining Eq 1.10 with 1.11 and 1.12, the forward reaction rate constant of the overall reaction (eq. 1.6) can be derived as eq 1.13. Further, using statistical mechanics, it can be shown that *v* can be defined as eq. 1.14.

$$k^{+} = \nu e^{\left(\Delta S^{\circ\ddagger}/R\right)} e^{\left(-\Delta H^{\circ\ddagger}/RT\right)} \qquad \text{Eq. 1.13}$$

$$\nu = \frac{\mathbf{k}T}{h} \qquad \text{Eq. 1.14}$$

In eq 1.14, **k** is the Boltzmann constant and *h* is the Planck constant. By comparing eq. 1.13 and 1.8, it can be observed that:

$$A \approxeq \frac{\mathbf{k}T}{h} e^{\left(\Delta S^{\circ\ddagger}/R\right)} \qquad \text{Eq. 1.15}$$

$$E_a \approxeq \Delta H^{\circ\ddagger} \qquad \text{Eq. 1.16}$$

It should be noted that eq. 1.15 and 1.16 are only approximations, and one should only expect to get orders of magnitude approximations to the true values (see reference 13 for a complete derivation of *A* and $E_a$).

The significant conclusion to draw from this analysis is that the kinetics of the reactions can be estimated directly from thermodynamic properties for the reaction step. Consider reaction R.3 from the red-ox mechanism for water-gas shift described above. If we assume that for any given catalytic surface, the reaction path is the same (i.e. the adsorbed water molecule and dissociation products are on the same sites in a similar geometry and the dissociation dynamics are similar), then the pre-exponential factor for the rate constant of the dissociation step should be similar for different surfaces because $\Delta S^{\circ\ddagger}$ should not change significantly. Therefore, the difference in reaction rates on different surfaces will only stem from differences in the activation barrier of the reaction step, which is directly related to the change in enthalpy of transition state. In the next section, we will discuss these consequences in more detail.

### *3.3. Brønsted-Evans-Polanyi (BEP) relationships and the Sabatier principle*

In surface science, it has been shown that, for classes of reactions, there is a linear relationship between the reaction enthalpy of a reaction step and the activation barrier of the step [16,17,18]. This relationship is referred to as a Brønsted-Evans-Polanyi (BEP) relationship. For example, figure 1.5 illustrates a BEP relationship for the dissociation of diatomic molecules on terrace and step sites for a number of different metal surfaces. The illustration on the right depicts this relationship with a potential energy diagram. Essentially, as the heat of reaction for a particular step increases, so does the activation barrier. Therefore, endothermic and slightly exothermic reaction steps will have relatively large reaction barriers while highly exothermic steps will have very small reaction barriers.

In 1920, a French chemist, Paul Sabatier, proposed a principle which helps explain the effect of BEP relationships on catalysis. Sabatier proposed that

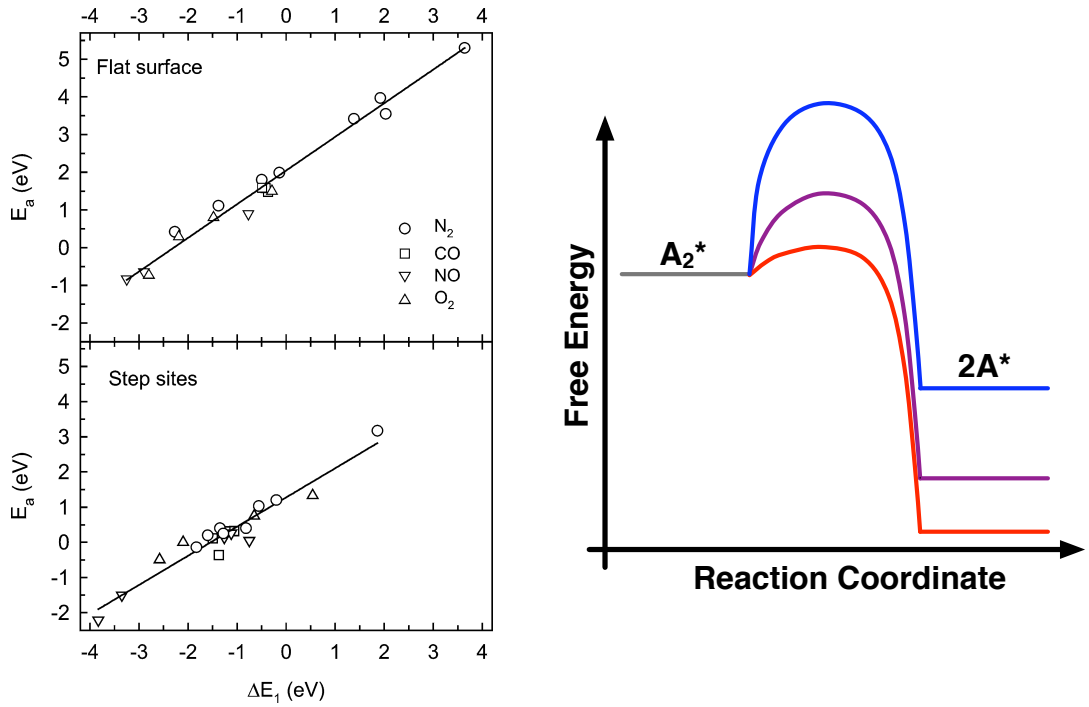


**Figure 1.5: LEFT- Brønsted-Evans-Polanyi (BEP) relationships for the dissociation of diatomic molecules on terrace and step sites of several different metals. $\Delta E_1$ refers to the dissociation enthalpy and $E_a$ refers to the activation energy of dissociation. Taken from *Bligaard et al.* [17]. RIGHT- illustration of the BEP relationship with a potential energy diagram.**

if the heat of reaction for a catalytic step was small, the reaction would be slow because the activation barrier would be significant. On the other hand, if a reaction step was very exothermic, then the products of the step would be too stable on the surface; they would be unable to participate in further reaction steps and essentially poison the surface. Therefore, the optimal catalyst would bind adsorbates strongly enough to reduce the activation barrier to an acceptable amount, but weakly enough that the surface would not be poisoned by the intermediates. This idea is the foundation of a common phenomenon found in catalysis referred to as volcano curves. Figure 1.6 shows a volcano curve for the WGS reaction [19]. For this reaction, when metals are supported on an inert support (i.e. A support which is not chemically active), the catalytic activity of the catalyst tracks very well with the atomic oxygen binding energy of the metal (this energy is used as a descriptor of the water dissociation energy of the metal). The metals with the highest activity (most notably, Cu) exhibit an intermediate oxygen binding energy. Metals to the left of Cu bind oxygen too strongly, such that the metals are essentially oxidized. The metals to the right bind oxygen so weakly, the activation barrier for water dissociation (eq. R.3) is very high.

For many relatively simple reactions, probable reaction mechanisms have been determined through experiment, typically through a combination of

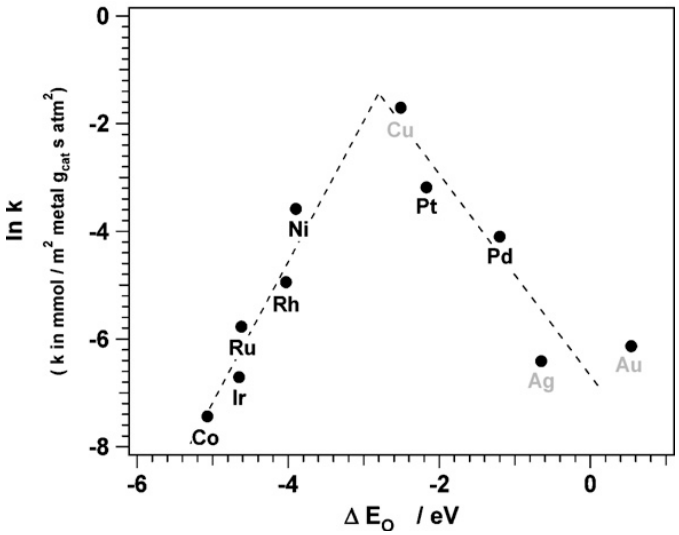


**Figure 1.6: WGS activity for metals supported on an inert supports as a function of atomic oxygen binding energy. The plot makes a familiar "volcano curve." Taken from *Boisen et al.* [19]**

spectroscopic, kinetic, and isotopic labeling experiments. Using microkinetic modeling and density functional theory (DFT) calculations, it is then relatively simple to develop volcano curves for particular reactions. Upon examination of a series of volcano curves for a variety of reactions (i.e. over a wide range of catalysts descriptors, such as oxygen binding energy, carbon binding energy, hydrogen binding energy, etc.), one will notice that some metals (typically Fe, Co, Ru, Rh, among others) typically lie on the left side of the volcano while other metals (Au, Ag, Pt, Pd) typically lie on the right side. In other words, in terms of chemical activity, metals near the middle of the periodic table seem to always be more active than metals near the right side of the periodic table. In the next section, we will review the mechanism by which metals form bonds with adsorbates, and try to understand this trend.

One point of emphasis that arises from the discussion above is the subtle difference between describing a reactive surface as chemically active (the strength by which a surface binds adsorbates) versus catalytically active (exhibiting high catalytic rates). As implied above, surfaces which are not chemically active may not be catalytically active either. However, surfaces which have a high chemical activity will also not necessarily be catalytically active. The surface with the highest catalytic activity will be the one with an intermediate chemical activity.

### *3.4. Chemical bonding and metal electronic structure*

Understanding of the bonding mechanism between metals and adsorbates first requires an understanding of the bonding mechanism between simple atoms. Figure 1.7a shows the bonding mechanism which occurs between two hydrogen atoms. Initially, when the hydrogen atoms are far apart, each 1s orbital is occupied by a single electron, and the states are at the same energy. As the atoms approach each other, the energy of the s-states increases due to Pauli repulsion. However, once the atoms pass a critical threshold, the s-states hybridize with one another forming bonding and anti-bonding states, constraining

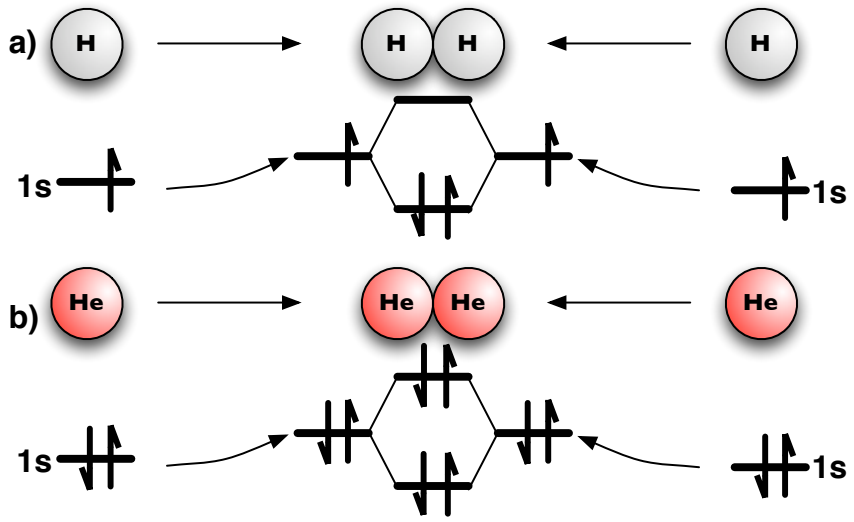


**Figure 1.7: Illustrations of the binding mechanism of diatomic molecules with a single s orbital.**

the hydrogen atoms to an equilibrium bond distance. The bonding states are fully occupied and the anti-bonding states remain empty, therefore the energy of the bound molecule is less than the energy of the separate atoms, and the molecule is stable. Figure 1.7b illustrates the same mechanism for helium atoms. However, in this case, when the chemical bond is formed, both the bonding and anti-bonding states are occupied. For this reason, the energy of the molecule is greater than the energy of the separate atoms, so the molecule decomposes into its atomic parts.

For the simple molecules in figure 1.7, it is very easy to understand molecular binding through the formation of discrete bonding and anti-bonding states. However, as the size of the molecule grows, representing the large number of states involved becomes more difficult. Figure 1.8 illustrates how the number of bonding and anti-bonding states increases when super hydrogen molecules are formed (i.e. molecules made up of more than two hydrogen atoms). In each molecule, the bottom state represents a fully bonding state while the top state represents a fully anti-bonding state. States in the middle of these represent states of varying degrees of bonding and anti-bonding.

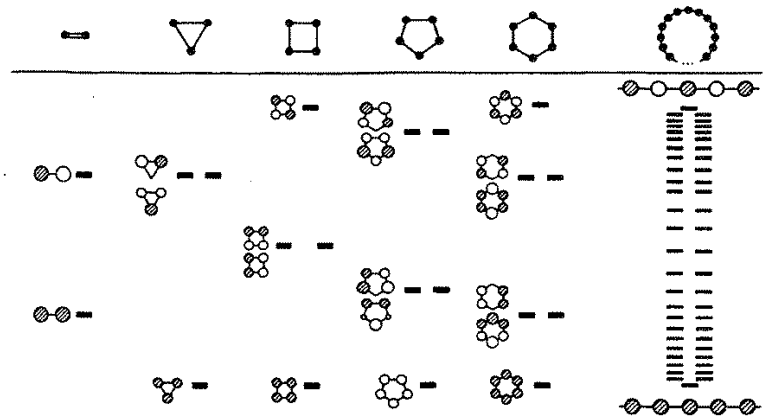

**Figure 1.8: Illustration of the bonding and anti-bonding states involved in the formation of hydrogen super-molecules. Taken from *Solids and Surfaces: A Chemist's View of Bonding in Extended Structures* [20]**

Figure 1.8 illustrates that as the size of the molecule grows, the number of discrete states created from the bonding and anti-bonding interactions approaches a continuum (this continuum would be approached even faster if one considered atoms other than hydrogen which have a larger number of atomic orbitals). For this reason, the electronic structure of metal surfaces are typically represented as bands of densities of states. Figure 1.9 shows the density of states spectra for Mo and Pt surfaces. In these figures, the y-axis is energy referenced to the Fermi level, and the x-axis is the density of states. The contributions to the total density of states by the individual states are represented by simpler, elliptical functions. The black curve represents the sp-band (in metals,

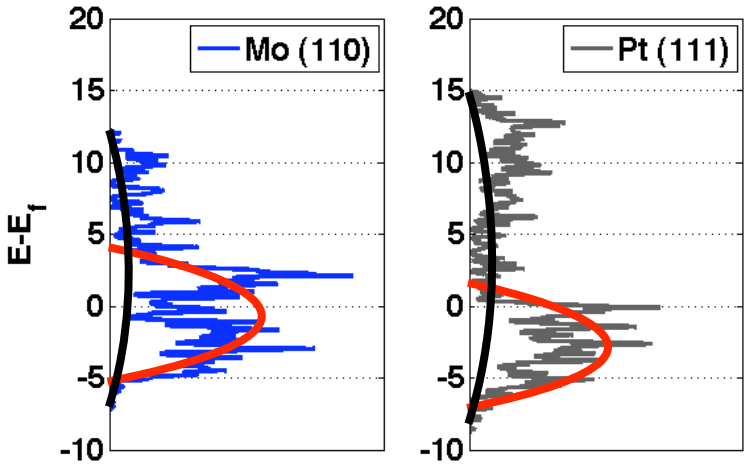


**Figure 1.9: Calculated density of states spectra of an Mo(110) and Pt(111) surface. s- and p-states are indicated by the black curves while d-states are represented by red curves.**

the s and p states are typically represented as one band) of the metal while the red curve distinguishes the d-band. States that are above the Fermi level ($E-E_f>0$) are unoccupied states while states below the Fermi level are occupied states. Since molybdenum has five d-electrons, we expect the Fermi level to cut through half the d-states while the Fermi level cuts through the top of the Pt d-band because Pt has nine d-electrons.

In the 1990s, Bjork Hammer and Jens Nørskov published a series of papers establishing a model for determining trends in the chemical activity for transition metals that later became known as the “d-band model” [21-25]. The model treats the interactions of adsorbate states with the sp-band and the d-band of the metal surface separately, but the larger impact of the model was the realization that since all transition metals have one valance s-electron (hybridization between the s and d states of the metals results in charge transfer between the s and d states yielding these results) and no p-electrons, the interaction of the sp-states of any metal with the adsorbate can be considered essentially the same. The only difference between different transition metals is the occupation of the d-states. Furthermore, the interaction of the surface d-states with adsorbates can be characterized by a single descriptor, the d-band center. This model is illustrated in figure 1.10, using the binding of $H_2$ as an example.

The bonding and anti-bonding orbitals discussed at the beginning of this section are displayed on the right side of figure 1.10. Initially, these orbitals hybridize with the sp-states (not shown) of the metal forming the new, hybridized bonding (solid line) and anti-bonding (dotted line) states displayed in the right-center of figure 1.10. As mentioned above, these interactions are essentially the same for all the transition metals because the electronic structure of the sp-states of all the transition metals are very similar. The d-band for two different metals are displayed on the left of figure 1.10. These metals are characterized by their d-band centers, which are represented by dashed lines. The blue d-band is populated by more electrons than the red d-band because the d-band center is

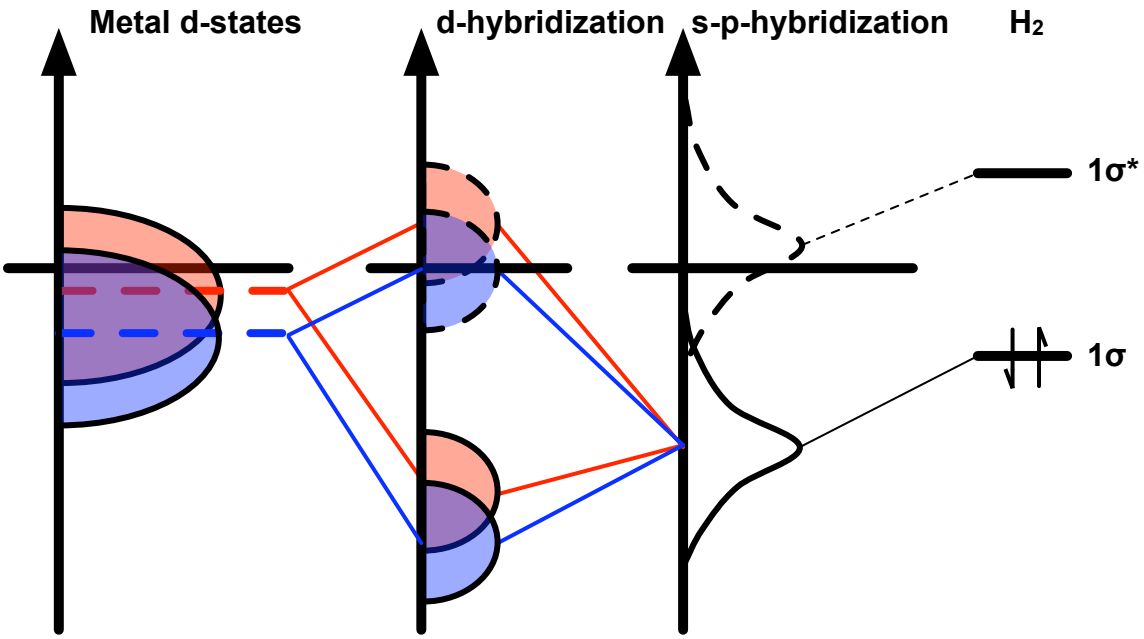


**Figure 1.10: Illustration of the interaction of a hybridized adsorbate binding state with the d-band of two different metals. The red d-band has a higher d-band center than the blue band. Therefore, when the adsorbate state hybridizes with the red d-band, the anti-bonding states are higher in energy than the states of the blue d-band, relative to the Fermi level. Consequently, the blue anti-bonding states are occupied by more electrons than the red anti-bonding states, so the red states form a stronger bond. Adapted from *Hammer et al.* [23]**

lower (i.e. a lower energy than the red d-band relative to the Fermi level). The newly hybridized bonding state of the adsorbate interacts further with the d-band of the metals and forms additional bonding and anti-bonding states, displayed in the left-center of figure 1.10. Since the blue d-band had a lower d-band center then the red d-band, the new bonding and anti-bonding states of the blue d-band emerge at a lower energy than bonding and anti-bonding orbitals of the red d-band. In both cases, the bonding orbitals are fully occupied. However, the anti-bonding states in both cases are only partially occupied. Since the blue d-band started at a lower energy and the anti-bonding states formed at a lower energy than the same states for the red d-band, the anti-bonding orbitals of the blue d-band have a higher occupancy than the anti-binding states of the red d-band. Consequently, the red d-band will form a stronger bond with $H_2$ than the blue d-band, which is weakened by the higher occupancy of the anti-bonding orbitals.

In short, the d-band model says that metals in which the d-band center is closer to the Fermi level will bind adsorbates more strongly than metals in which the d-band center is further from the Fermi level. Figure 1.11 shows the correlation of d-band center with oxygen binding energy over several different transition metal surfaces.

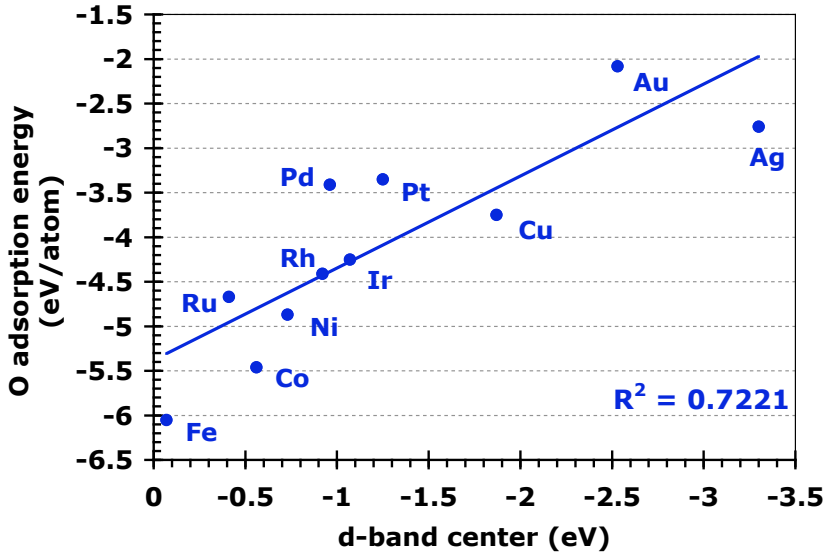


**Figure 1.11: Correlation of atomic oxygen binding energy with the d-band center of various transition metal (111) surfaces. Data taken from *Greeley et al.* [26]**

Although the model results in only a general correlation, its significance is that it provides an intuitive basis for which to predict the relative activity of metals. For example, the Fisher-Tropsch reaction requires CO dissociation while the CO oxidation reaction ($CO+0.5O_2 \rightarrow CO_2$) merely requires CO adsorption and oxidation. Therefore, it is not surprising that Fe and Co make good FTS catalysts since the d-band center of these metals is high in energy (i.e. close to the Fermi level). They bind CO strong enough to dissociate it. On the other hand, Pt has a low d-band center, and therefore makes a good CO oxidation catalyst. It binds CO strongly, but not so strong that CO dissociates.

Now that we can understand how adsorbate binding occurs on surfaces, we can explore strategies that can be employed to tune the chemical activity of metals, and more importantly, optimize catalytic rates.

### *3.5. Optimizing catalytic activity*

There are two methods by which one can increase the activity of a catalyst: increase the catalytic activity of the active sites and/or increase the number of active sites per gram of catalyst.

It was implied in the preceding sections that the catalytic activity of active sites can be optimized by “fine tuning” the chemical activity of the sites. Changing the chemical activity of an active site can be accomplished by forming an alloy, using promoters, synthesizing metal particles with low-index surfaces, changing the size of the metal particles, or taking advantage of what is referred to as a “support effect.” Optimizing the number of active sites per gram of catalyst is typically achieved by manipulating the dispersion of the metal phase. This can be accomplished by adapting the catalysts synthesis procedure or by using a support effect.

A support effect can be defined as follows: “an interaction of the support or carrier with the active catalytic phase, which causes a measurable change in turnover frequency” [1]. Boudart classified support effects into six different categories [1]:

1. Strong interaction of unreduced metal-oxides with alumina, silica, or zeolite supports
2. Support-induced size and morphology
3. Contamination of the metal by support materials either during preparation or during reduction of the catalyst
4. Bifunctional catalysts (i.e. reactions on both metal and support)
5. Spillover of species from the metal to the support and vice-versa
6. A change in the electronic properties of small crystallites due to intimate contact with the support

One class of catalysts which have been shown to exhibit a support effect is WGS catalysts. In studying catalysts which exhibit a support effect, it is convenient to describe them using Boudart's classifications. It is likely that observed changes in catalytic activity that result when different supports are used benefit from many of the characteristics classified by Boudart. However, these classifications can be used as foundation for a systematic approach to study these catalysts. In the next section, we will examine WGS catalysts in this context.

## 4. Water-Gas shift catalysts

As mentioned above, the current industrial catalysts for low temperature WGS have the nominal formulation of $Cu/Zn/Al_2O_3$. One disadvantage of this type of catalyst is that it is pyrophoric (violently oxides in air, releasing copious amounts of heat), which makes handling of the catalyst more difficult. Furthermore, oxidation of the catalyst can drastically alter its characteristics [8]. For this reason, there has been a growing interest in developing a catalyst which is more durable under oxidizing conditions [27,28]. Consequently, there have recently been a number of studies examining oxide supported noble metals WGS

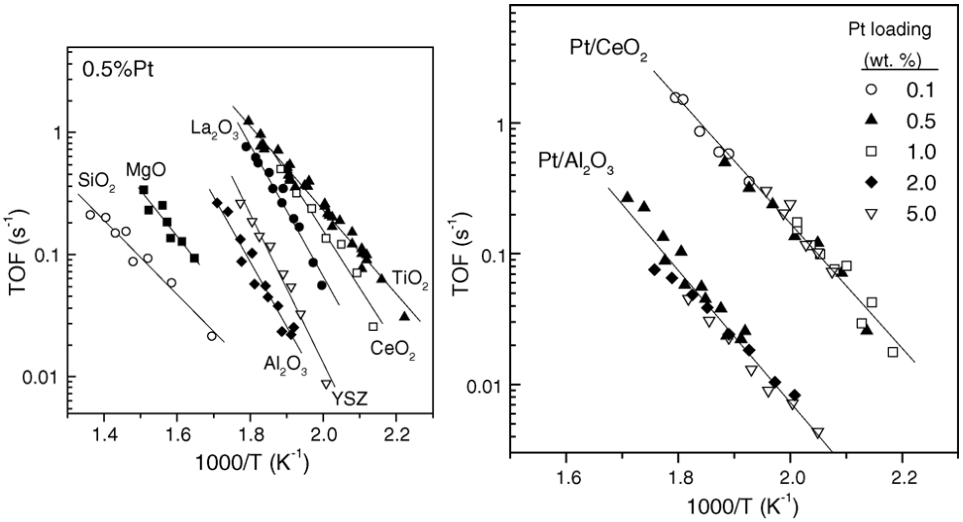


**Figure 1.12: Arrehnius plots of the WGS activity of different Pt WGS catalysts as a function of temperature. Left - Pt WGS catalysts with similar weight loadings but different supports, Right - catalysts with the same support ($CeO_2$ or $Al_2O_3$) but various weight loadings. The weight loadings had a direct effect on the size and dispersion of the metal phase. Taken from Panagiotopoulou et al. [30]**

catalysts. In a series of papers, Panagiotopoulou et al. [29-31] reported activities for a wide range of noble metal WGS catalysts using various oxide supports and reported that the catalyst turnover frequencies (TOF, i.e. the rate normalized to the number of active sites, as determined from chemisorption experiments) was dependent on the nature of the oxide support. Figure 1.12 demonstrates a support effect for Pt WGS catalysts. Generally, reducible supports yielded catalysts with higher TOF's than catalysts using irreducible supports. Similar results were observed Ru, Rh, and Pd catalysts as well [30]. Additionally, the TOF's were independent of metal loading or particle size. The most active Pt catalysts they found were $Pt/TiO_2$ and $Pt/CeO_2$. These have been reported as highly active catalysts elsewhere as well [28,32-34].

One commonly accepted reason these catalysts exhibit a support effect is because they are bifunctional in nature; the Pt particles provide binding sites for CO while either the support or the metal-support interface provides active sites for $H_2O$ activation [32,35,36]. Many studies have even proposed that the nature of the support changes the mechanism of WGS. Some supports enable the red-ox mechanism (described in section 3) while others facilitate mechanisms that go through a reactive intermediate (i.e. carbonate, formate, or carboxyl. See figure 1.13).

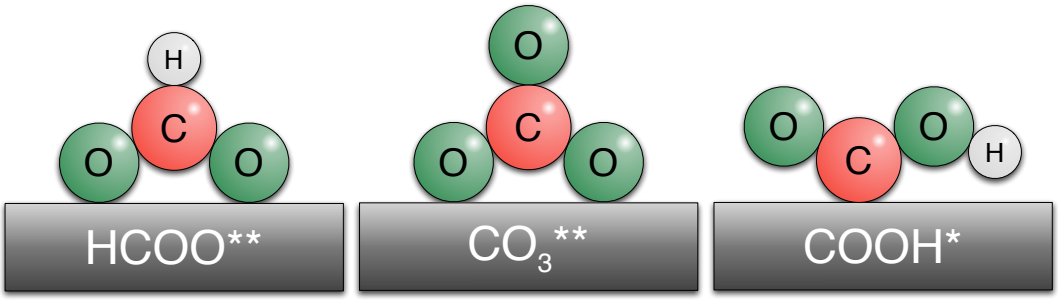


**Figure 1.13: Common proposed reaction intermediates for WGS mechanisms: HCOO** (formate), $CO_3$** (carbonate), and COOH* (carboxyl).**

Azzam et al. [35] used a combination of diffuse reflectance fourier transform spectroscopy (DRIFTS) and pulse chemisorption experiments to suggest that $Pt/TiO_2$, $Pt/CeO_2$, and $Pt/ZrO_2$ all facilitate different WGS

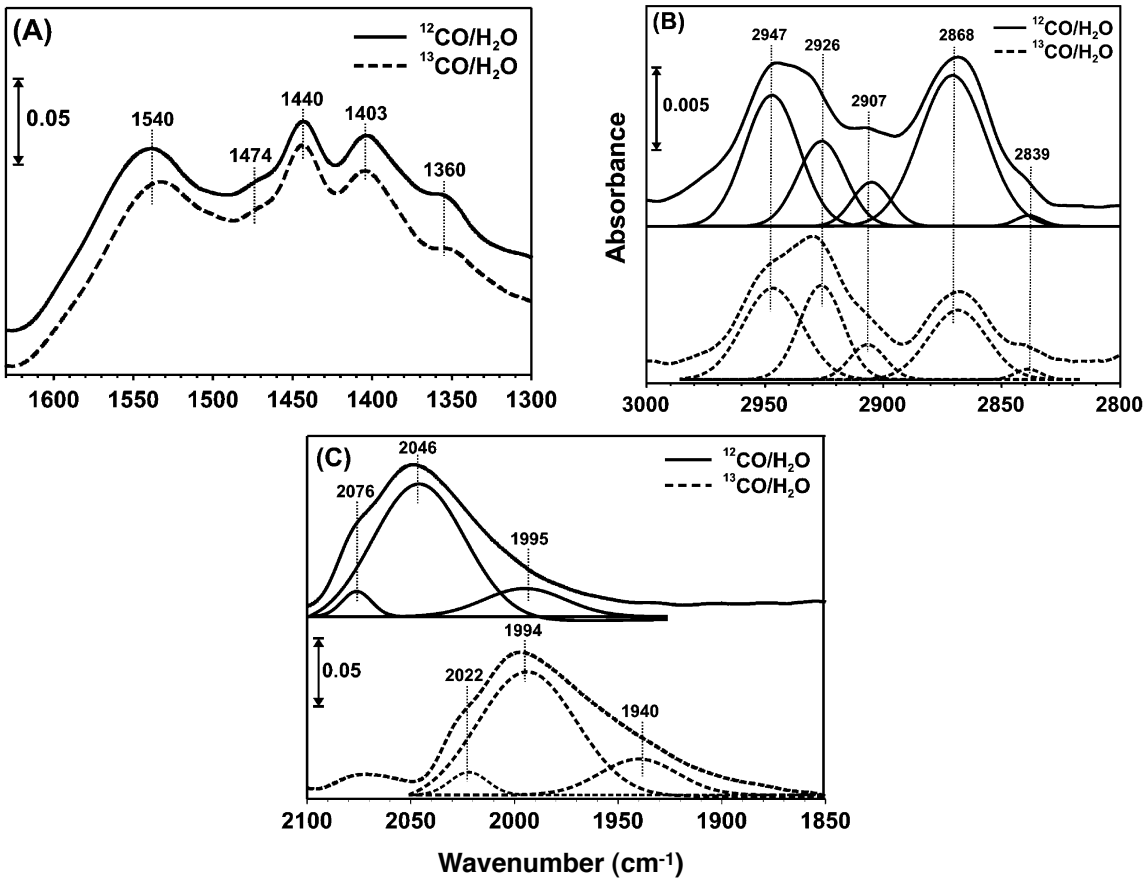


**Figure 1.14: SSITKA-DRIFTS experiments as reported from Kalamaras et al. [37]. (A) IR region containing O-C-O stretches (carbonate, formate, and carboxlyate), (B) vCH, δCH, and $vOCO_a$ stretches, and (C) linear bound CO**

mechanisms. Specifically, the $Pt/TiO_2$ catalyst facilitates a red-ox type mechanism while the $Pt/CeO_2$ and $Pt/ZrO_2$ catalysts exhibit a mechanism which involves formate intermediates. Kalamaras et al. [37] also proposed that the red-ox mechanism is the predominant mechanism on $Pt/TiO_2$ using *in-operando* SSITKA-DRIFTS (steady-state isotopic transient kinetic analysis — diffuse reflectance fourier transform spectroscopy) analysis. Their key results are presented in figure 1.14. First, the authors exposed $Pt/TiO_2$ to WGS conditions using $^{12}CO$ and allowed the system to reach steady state. Once steady state was reached, the $^{12}CO$ was replaced with $^{13}CO$. Throughout the duration of the experiments, the IR spectra for carbonate, formate, carboxylate, and linear CO were monitored. As shown in figure 1.14, under steady state conditions using $^{12}CO$, all the suspected reaction intermediates were present on the surface.

However, when $^{12}CO$ was switched to $^{13}CO$, the only species which experienced a red shift was linearly bound CO (since the carbon in these species was replaced with a heavier carbon isotope, the vibrational modes “slow down” and experience a shift to a lower wavenumber/frequency). These results suggest that although common intermediate species are formed under WGS conditions, they were merely spectator species (i.e. they are not involved in the reaction). The only carbon species involved in the WGS mechanism was the linearly bound CO species, thus the mechanism must involve a red-ox type mechanism for $Pt/TiO_2$ catalysts.

In contrast, $Pt/CeO_2$ is proposed to facilitate an associative mechanism, which would have the following elementary steps:

$$CO + {}^* \rightleftharpoons CO^* \quad \text{A.1}$$

$$H_2O + {}^* \rightleftharpoons H_2O^* \quad \text{A.2}$$

$$H_2O^* + {}^* \rightleftharpoons OH^* + H^* \quad \text{A.3}$$

$$CO^* + OH^* \rightleftharpoons HCOO^{**} \quad \text{A.4}$$

$$HCOO^{**} + H_2O \rightleftharpoons H_2 + CO_2^* + OH^* \quad \text{A.5}$$

$$CO_2^* \rightleftharpoons CO_2 + {}^* \quad \text{A.6}$$

A key feature of this mechanism is that CO reacts with surface hydroxyl groups to form a formate intermediate. This intermediate then decomposes to form both products. This mechanism has been supported by a series of papers by Jacobs and Davis [36,38] using a wide variety of experimental tools. It was also proposed by Azzam et al. [35] that the associative mechanism is the predominant mechanism for $Pt/CeO_2$ catalysts.

Grabow et al. [10] studied the WGS mechanism on the Pt(111) surface using DFT calculations and proposed another mechanism, the carboxyl mechanism:

$$CO + * \rightleftharpoons CO^* \quad \text{C.1}$$

$$H_2O + * \rightleftharpoons H_2O^* \quad \text{C.2}$$

$$H_2O^* + * \rightleftharpoons OH^* + H^* \quad \text{C.3}$$

$$CO^* + OH^* \rightleftharpoons COOH^* \quad \text{C.4}$$

$$COOH^* + OH^* \rightleftharpoons CO_2 + H_2O^* \quad \text{C.5}$$

$$H_2O^* \rightleftharpoons OH^* + H^* \quad \text{C.6}$$

$$2H^* \rightleftharpoons H_2 + 2^* \quad \text{C.7}$$

The carboxyl intermediate has, to the author's knowledge, never been detected using spectroscopy methods. However, Grabow et al. argued that it should be very difficult to detect the presence of a true intermediate because the lifetime of the species should be very short. They also predicted experimental rates using a microkinetic model derived from their new mechanism, and showed that the predicted values followed very closely with measured rates for a $Pt/Al_2O_3$ catalyst.

Due to the distinct support effect of Pt WGS catalysts discussed above, this system is ideal for studying the changes induced on active metal catalysts by new support materials. Using the knowledge attained in literature discussed above, we can determine factors that are attributed to the new support. The new support materials we will study are transition metal carbides.

## 5. Transition Metal Carbides

Although many groups have investigated the use of transition metal carbides as catalysts, few have studied the use of these materials as catalyst supports. Levy and Boudart [39] were among the first to report carbides as being catalytically active. They demonstrated that tungsten carbide showed activity towards hydrogen and oxygen adsorption that was significantly different from tungsten metal, and reflected characteristics usually associated with noble metals. Since their work, a significant number of contributions have reported

carbides and nitrides to be active for a wide range of reactions [40-44 and references therein].

Moon et al. [45] was among the first to study molybdenum carbide, $Mo_2C$, as a low temperature WGS catalysts, and showed that, depending on the pretreatment procedure used, the activity rivaled that of a $Cu/Zn/Al_2O_3$ catalyst. Since then, there have only been a few studies [11,46] on the WGS mechanism for $Mo_2C$, which will be discussed in more detail in chapter 4.

This discussion will focus on $Mo_2C$, as this is the support material used in this dissertation work. We will first describe the geometric and electronic structure of molybdenum carbides and discuss how the structure differs from that of molybdenum. We will also review previous work which has been conducted on the use of these materials as catalyst supports.

### *5.1. The structure of molybdenum carbide*

The crystal structure of molybdenum carbide can take different forms depending on synthesis conditions [47]. α-$MoC_{1-x}$ (where x can range from 0 to 0.5) has an fcc crystal structure, depicted in figure 1.15. β-$Mo_2C$ was originally thought to have an hcp unit cell. In 1963, Parthé et al. [48] published a paper refuting this claim reporting that the structure was orthorhombic, but closely resembled an hcp structure, with a slight distortion (space group: $D_{2h}^{14} - Pbcn$ a = 4.724Å, b = 6.004Å, c = 5.199Å, see figure 1.15).

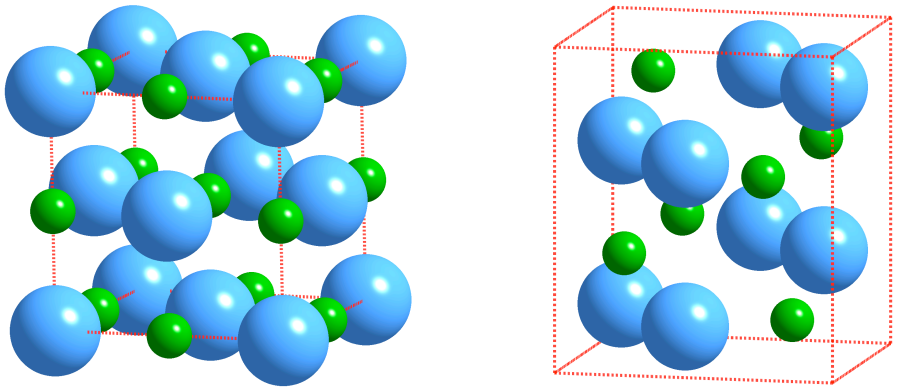

**α-$MoC_{1-x}$ - fcc** **β-$Mo_2C$ - orthorhombic**

**Figure 1.15: Crystal structure of LEFT - α-MoC1-x and RIGHT - β-Mo2C**

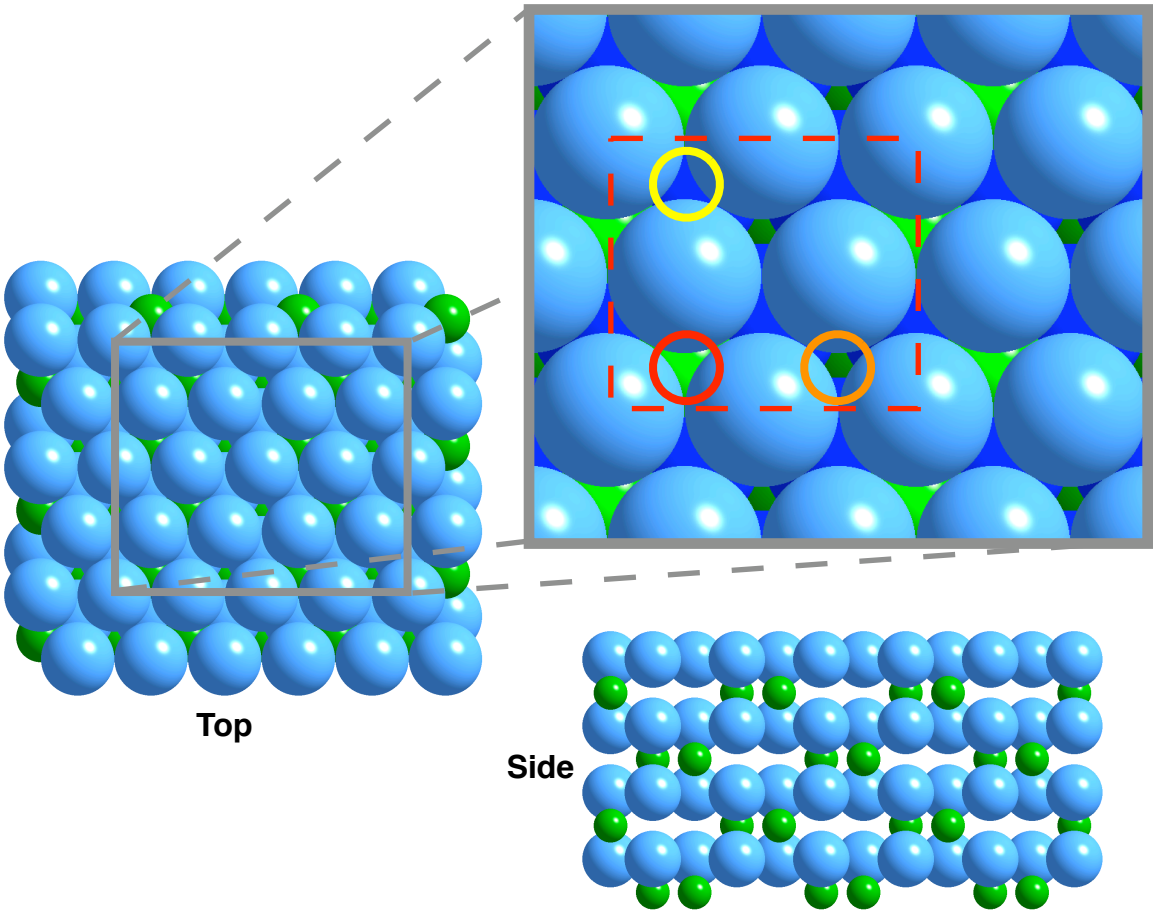


**Figure 1.16: The Mo-terminated β-$Mo_2C$ (100) surface. In the zoomed image, the top layer Mo atoms are light blue, the second layer C atoms are bright green, the third layer Mo atoms are royal blue, and the fourth layer C atoms are dark green. The surface unit cell is outlined by a red-dashed box, and carbon, hcp, and fcc hollow sites are labeled with red, yellow, and orange circles, receptively.**

Figure 1.16 shows the Mo-terminated (100) surface for β-$Mo_2C$. This surface represents the closest-packed molybdenum surface. The surface is constructed from four atomic layers of alternating Mo-C-Mo-C sheets which repeat into the bulk. In the expanded image in figure 1.16, the top layer molybdenum atoms are light blue, the second layer carbon atoms are bright green, the third layer molybdenum atoms are dark blue, and the fourth layer carbon atoms are dark green. The surface unit cell is outlined by a red box. The carbons atoms run in a “zigzag” pattern under the top layer of molybdenum. However, the carbons are spaced such that there are lattice vacancies between rows of carbon, as seen in the side view of the surface. In the following carbon layer, the carbon rows are shifted such that the vacancies of the fourth row are

situated below the rows from the second layer. This unusual filling exhibited by the carbon atoms generates three unique adsorption hollow sites on the surface (along with the top sites provided by the molybdenum atoms themselves). The first is referred to as a 'carbon' site since it has a second layer carbon immediately below it. This is generally the least chemically active of the hollow sites [52]. The second is referred to as an 'hcp' site and has a third layer molybdenum atom below. The third is called an 'fcc' site and is the most chemically active of the sites [52]. According to the bulk structure, the (100) surface can also be carbon terminated. If this is the case, then carbon atoms would occupy all the fcc sites on the surface. Additionally, the surface may have mixed terminations depending on the external conditions (temperature, pressure, and composition of gas phase) of the catalytic environment. In this project, we are primarily interested in the surface as it would exist under WGS conditions. Thus, determining the proper surface termination will require structural characterization. This will be discussed in further detail in chapter 4.

Figure 1.17 compares the electronic structure of Mo(110) and $Mo_2C$(100). As a result of the interactions between the d-band of molybdenum and the s- and p-states of carbon, the Mo d-band is broadened. Generally, the new d-band can

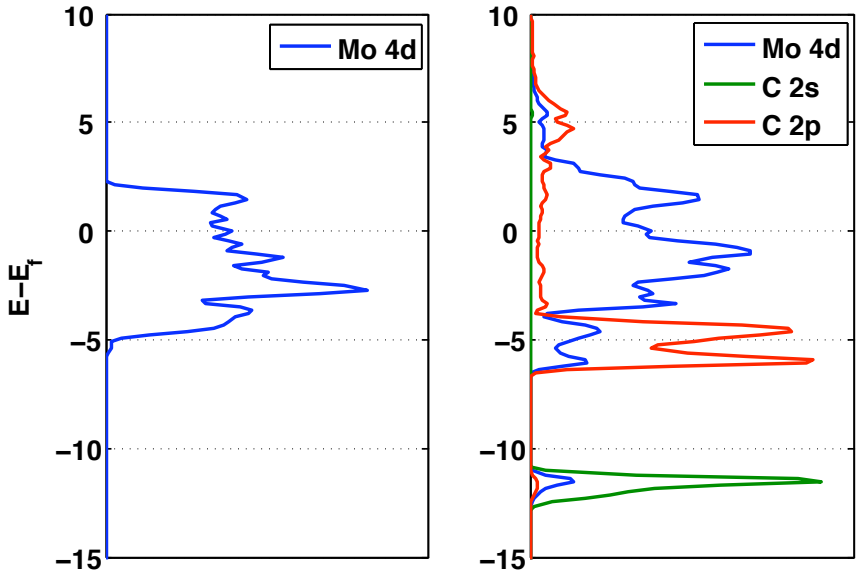


**Figure 1.17: Calculated d-bands for Mo(110) and Mo-terminated β-$Mo_2C$(100). Included with the $Mo_2C$ d-band are the carbon s (red) and p (green) bands.**

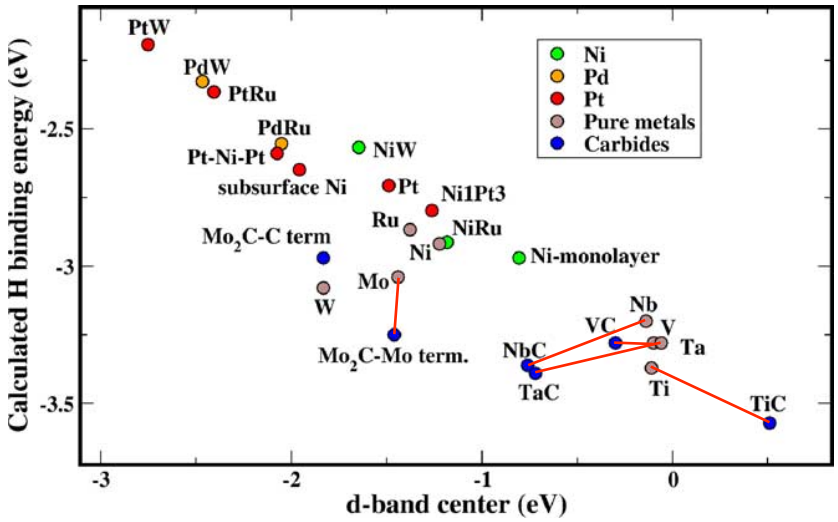


**Figure 1.18: Correlation between the d-band center and hydrogen binding energy for several metals and carbides. Lines are drawn connecting carbides to their parent metals. Taken from Kitchin et al. [52]**

be divided into three regions: bonding interactions with the C s- and p-states occur below -4 eV, noninteracting d-states are localized around the Fermi level, and anti-bonding states occur above 3.5 eV. This general structure is typical for transition metal carbides and nitrides [49-52]. One can calculate the change in the d-band center caused by the hybridization of the Mo d-states with the carbon states, but it has been shown that this shift does not tract well with adsorption energies, as the d-band model would suggest [52]. Figure 1.18 presents a correlation between the d-band center of several different metal and carbide surfaces with the hydrogen binding energies of the surface. As can be seen, the change in d-band center on going from a metal to its respective carbide does not track well with the chemical activity of these sites. Developing a modified d-band model has been the focus of continuing, recent work. [50-51] Nonetheless, transition metal carbides exhibit chemical activities that are very different from the parent metals.

### *5.2. Transition metal carbides as catalyst supports*

There have only been only a few studies using high surface area carbides and nitrides catalyst supports [53,54]. These catalysts have shown a range of activities and selectivities. Additionally, these supports exhibit a support effect for

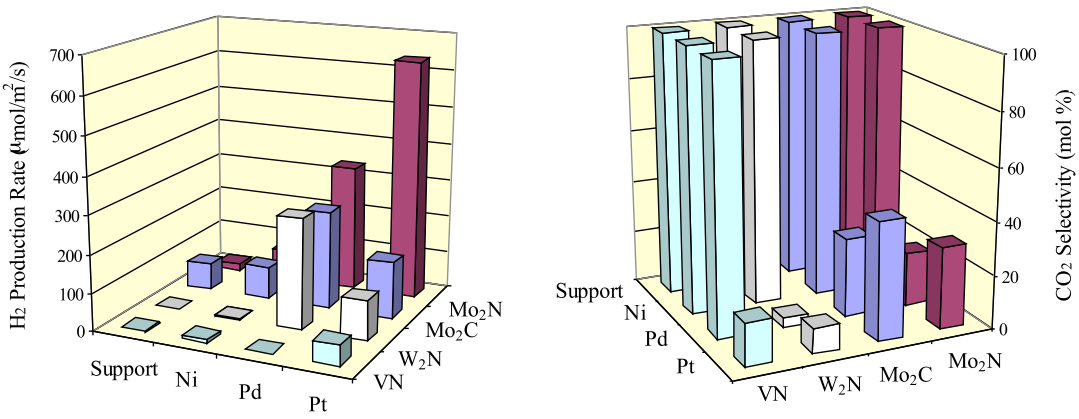


**Figure 1.19: $H_2$ production rates (left) and $CO_2$ selectivity (right) for methanol steam reforming on various metals supported on various carbide and nitride supports. Taken from the dissertation of Worajit Setthapun. [53]**

WGS and methanol steam reforming, as the performance of a particular metal is affected by the nature of the support. Figure 1.19 shows results for methanol steam reforming on various catalyst; figure 1.20 shows the same for WGS. It is noted that among the WGS catalysts, $Pt/Mo_2C$ performed the best.

The previous investigations of carbide and nitride supported catalysts have mainly used combinatorial synthesis and high-through put methodologies to identify highly active catalysts (and highly selective catalysts in the case of methanol steam reforming). However, the identification of the underlying catalytic mechanisms that contribute to the observed support effect has proven difficult.

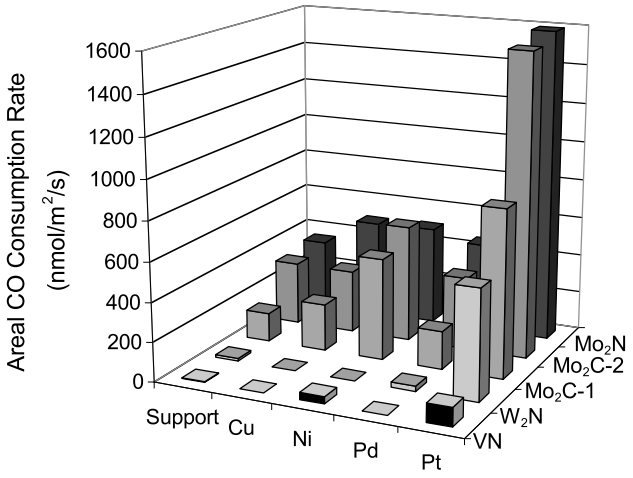


**Figure 1.20: WGS rates for various metals supported on various carbide and nitride supports. Taken from the dissertation of Timothy King. [54]**

Preliminary analyses of the active mechanisms have relied heavily on reactor kinetic studies, yielding kinetic rate constants and reaction orders. These studies have drawn the following conclusions for the Pt/$Mo_2C$ WGS catalyst [53]:

- The $Mo_2C$ support alone is an active WGS catalyst. Results from kinetic studies agree best with a proposed red-ox mechanism.
- The addition of Pt significantly enhances the WGS rate. By comparing rate data with many different rate models, it was determined that the kinetics most closely followed a Langmuir-Hinshelwood rate law.
- To this point, thorough characterization of the Pt particles has been unsuccessful. The contrast between Mo and Pt is not high enough to observe the particles using conventional TEM. Additionally, dispersion calculations are difficult because chemical probes bind to both the support and metal.

This work represents efforts to fundamentally understand the mechanisms by which the support effect is manifest in carbide-supported WGS catalysts. One very important aspect of this endeavor is to characterize the supported metal particles. Along with results from techniques used previously, this research used X-ray absorption spectroscopy (XAS). A description of this technique is provided in section 6.

## 6. X-ray absorption spectroscopy

X-ray absorption spectroscopy has been used as a material characterization technique since the 1970s [57]. This technique is useful because it provides information about the geometric and electronic structure of the sample and can also provide in-situ results for some systems. Additionally, this information is element specific. A sample spectra for a Pt reference foil is presented in figure 1.21. The x-axis is the energy of the x-ray, and the y-axis is a normalized absorption coefficient. This data represents the Pt L3 edge and

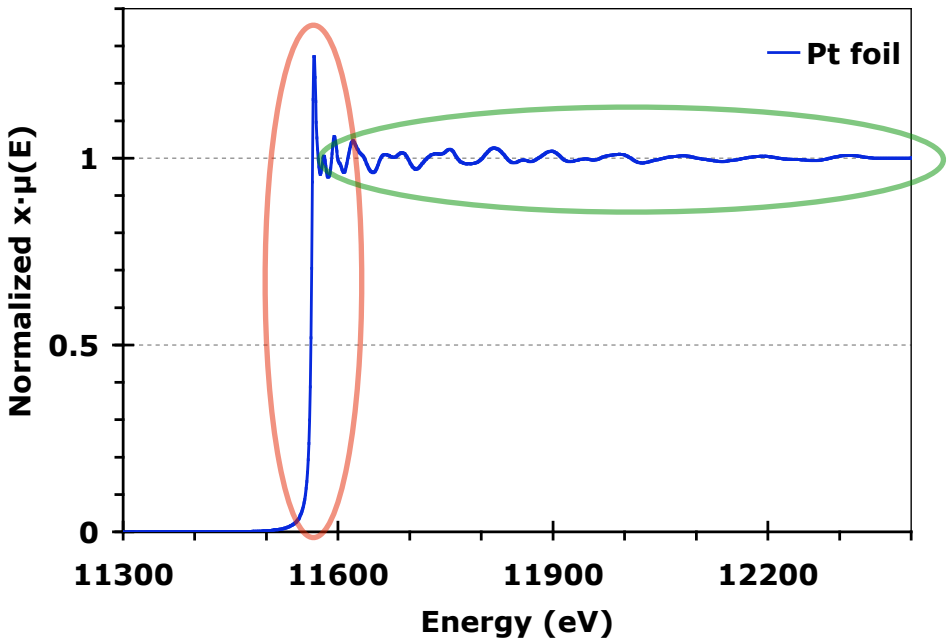


**Figure 1.21: XAS Pt L3 spectra for a Pt reference foil. The XANES region is indicated by a red oval, and the EXAFS region is indicated by a green oval.**

shows features which are typical for all XAS spectra. The large step in the absorption coefficient (around 11564 eV for the Pt L3 edge) is called the x-ray absorption near-edge structure (XANES) and provides information about the electronic structure of the absorbing atom. In the region at energies above the XANES region, the absorption coefficient oscillates around a single value. These oscillations are referred to as the extended x-ray absorption fine structure (EXAFS) and provide geometric information about the atoms surrounding the absorbing atom. Analysis of this data is discussed in detail below, however, several reviews are also available on the subject [55-58].

### *6.1. General experimental setup*

Figure 1.22 illustrates a typical set up for XAS experiments. The x-ray source for these experiments is synchrotron radiation. The reason synchrotron radiation is used is because the energy of the x-ray can be easily adjusted. In figure 1.22, the grey boxes represent ion chambers, which are simply used to measure the intensity of the x-ray beam. In a typical experiment, the energy of the x-rays starts at a relatively low energy and is ramped to some higher value.

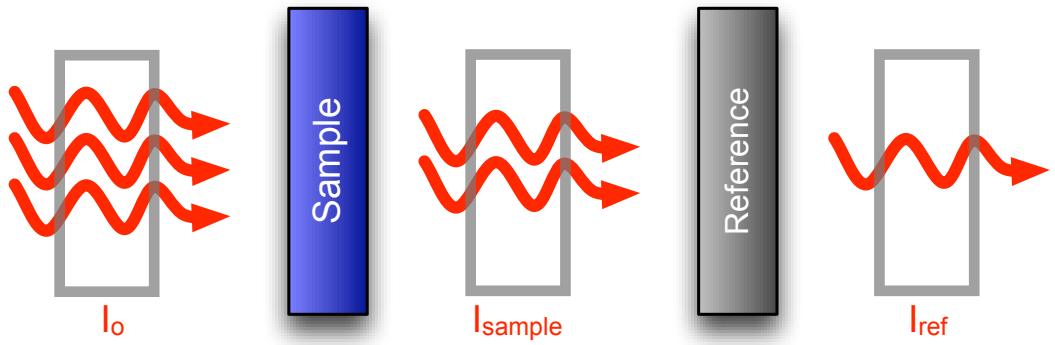


**Figure 1.22: Illustration of a typical XAS experimental set-up. The grey boxes represent ion chambers which record the intensity of the x-rays. The intensity is measured three times: the initial intensity from the synchrotron source is measured ($I_o$), the intensity after the x-rays pass through the sample ($I_{sample}$), and the intensity after the x-rays pass through the reference ($I_{ref}$).**

Throughout the duration of this process, intensity of the x-ray is measured as a function of x-ray energy. The intensity of the x-ray beam is measured at three different points within the experimental setup: the initial intensity from the synchrotron source ($I_o$), the intensity after the x-rays pass through the sample ($I_{sample}$), and the intensity after the x-rays pass through the reference ($I_{ref}$). The reference sample is included to calibrate the sample spectrum, discussed further below. As the energy of the x-rays increase, the sample will absorb some of the x-rays at some characteristic energy and the values of $I_{sample}$ and $I_{ref}$ will drop. The recorded intensities are then converted into the spectra similar to that presented in figure 1.20 by calculating the absorption coefficient of the material as a function of energy using the Beer-Lambert law:

$$x \cdot \mu(E) = \ln\left(\frac{I}{I_o}\right) \qquad \text{Eq. 1.17}$$

where $x$ is the thickness of the sample, $\mu(E)$ is the absorption coefficient as a function of x-ray energy, $I$ is the intensity of the x-ray exiting the sample, and $I_o$ is the energy of the x-ray entering the sample.

Alternatively, the experiment can also be performed by detecting the amount of fluorescence or electrons produced when the x-ray is absorbed by the

sample as a function of energy. In this case, the absorption coefficient is directly proportional to the magnitude of fluorescence or electrons emitted.

Figure 1.23 shows the results of an XAS experiments performed over a very wide energy range. Ignoring the absorption peaks, one can observe in figure 1.23 that as the x-ray energy increases, the overall value of the absorption coefficient decreases. Therefore, to obtain a spectra like the one in figure 1.21, data processing is required. These steps include the following:

1. The data set is calibrated using the reference data:

    1.1. Typically, a metal foil is used as a reference material. The XAS spectra for this material is collected simultaneously to the sample data, as depicted in figure 1.19.

    1.2. The derivative of the reference data is plotted as a function of energy. The maximum value of this plot is defined as $E_o$, the experimentally measured value of the absorption edge

    1.3. The value of $E_o$ for the reference spectra is shifted to the theoretical value. The sample spectra is then calibrated by shifting the spectra by the same amount

2. The general background of the sample is removed by fitting the pre-edge data to a line.

3. The data is normalized by fitting the post-edge data to a cubic and extrapolating the value to $E_o$. The value at $E_o$ is then used as the normalization constant.

4. The background of the post edge data is subtracted out by fitting the post-edge data to a cubic spline.

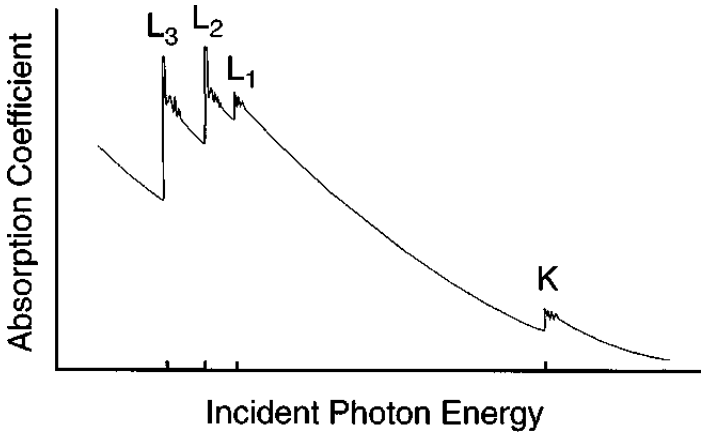


**Figure 1.23: Schematic of XAS results for a single material recorded over a very large energy range. Taken from Rehr et al. [55]**

### *6.2. X-ray absorption near-edge structure (XANES)*

Figure 1.24 illustrates the underlying, atomistic mechanism involved with the XANES phenomenon. Also provided is an illustration defining the different absorption edges. Essentially, when the energy of the x-ray is the same as the energy difference between a core electron state and the valance states of an atom, an electron in the core state is promoted to the valence state. If the energy of the x-ray is too small, this excitation cannot occur. As the energy of the x-rays

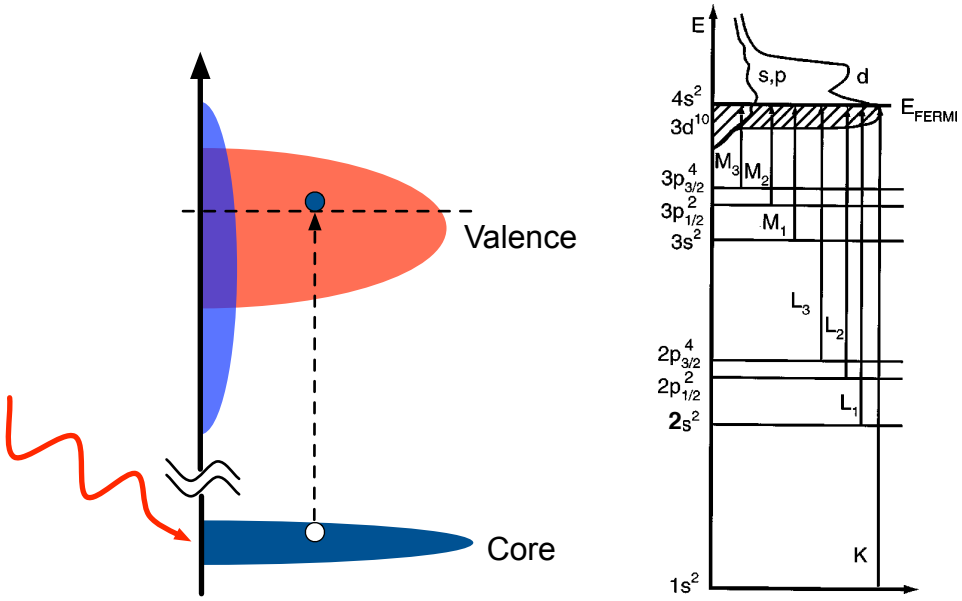


**Figure 1.24: Illustration of the XANES mechanism (left) and identification of different XANES edges (right, taken from Rehr et al. [54]).**

**Table 1.1: Allowed electron transitions for the K and L edges in XAS. *n* refers to the quantum number of the valence states of the absorbing atom**

| Edge | Allowed transitions |
|---|---|
| K | $1s \rightarrow np$ |
| L1 | $2s \rightarrow np$ |
| L2 | $2p_{1/2} \rightarrow ns$ |
| | $2p_{1/2} \rightarrow nd_{3/2}$ |
| L3 | $2p_{3/2} \rightarrow ns$ |
| | $2p_{3/2} \rightarrow nd_{3/2}$ |
| | $2p_{3/2} \rightarrow nd_{5/2}$ |

continues to increase beyond this point, this process results in the ejection of electrons from the atoms (i.e. the photoelectron effect). The different absorption edges in figure 1.23 originate from the different core states from which the electron is promoted. The K edge corresponds to transitions from the 1s orbital and is the highest energy edge. L edges correspond to transitions emanating from orbitals of the second quantum number, but they are further distinguished by the l quantum number in which the electron originates. For example, the L1 edge stems from the 2s orbital, the L2 edge from the $2p_{1/2}$ orbital and the L3 from the $2p_{3/2}$ orbital. M edges represent transitions from the third shell and are labeled the same as the L edges with the $3d_{3/2}$ edge named M4 and the $3d_{5/2}$ named M5.

According to Fermi's golden rule, electron transitions from core states to valence states have the following selection rules: $\Delta l = \pm 1$ and $\Delta j = 0, \pm 1$ [67]. The consequence of this is that excited core electrons can only access certain valance states depending on the core state they originate from. Table 1.1 shows the allowed electron transitions from each edge.

The origin on the XANES spectra has been known for sometime, and it was suggested early on that the intensity of the XANES peak was related to the

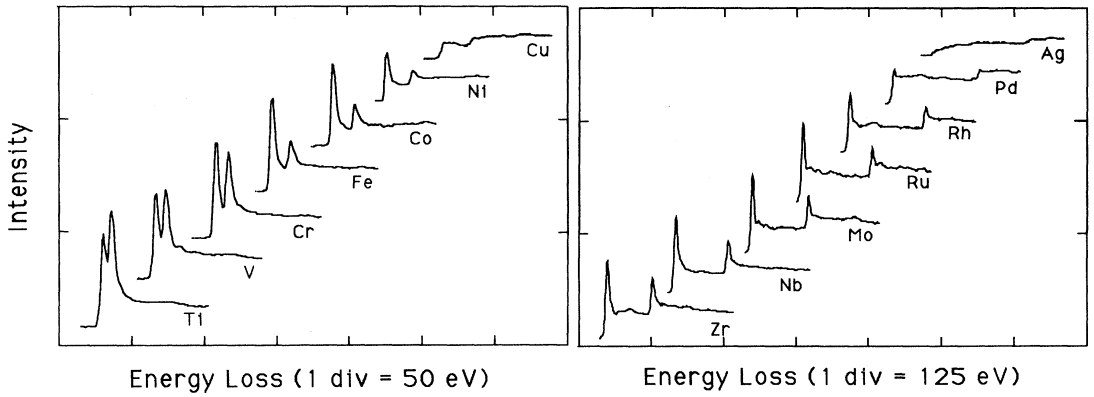


**Figure 1.25: XANES spectra for selected metals of the 3d (left) and 4d (right) transition metals. Taken from Pearson et al. [60]**

filling of the valence orbitals. For example, figure 1.25 displays the L2 and L3 edge for a series of metals in the 3d and 4d transition metals. Metals near the left side of the transition metal block (i.e. metals with few d-electrons, Ti, V, Zr, Nb) exhibit large XANES peaks (also refereed to in literature as “white lines”). As the number of d-electrons in the metals increase, the L2 edge first begins to decrease and the L3 edge follows. Atoms with full d-shells (Cu and Ag) exhibit no white line. This properties is useful because it allows XANES to be used to “map out” the density of states of the d-states above the fermi level. Ankudinov et al. [58] set forth a procedure that could be used to transform XANES into local density of states for the absorbing atom. This is useful to understand the effect of bonding (either of adsorbates or bonding in alloys) on the electronic structure of metal sites and understand possible mechanisms that affect the structure such as charge transfer or hybridization mechanisms.

### *6.3. Extended X-ray absorption fine structure (EXAFS)*

Figure 1.26 illustrates the EXAFS mechanism. A thorough discussion of the theory behind EXAFS mechanism can be found in Rehr et al. [55] The nuclei of the atoms in the material rest in a potential field created by the orbiting electrons. Initially, this system is at an equilibrium state close to the ground state of the material. When the materials is exposed to x-rays and absorption takes place above the absorption edge, an electron is ejected from the potential field surrounding the absorbing atom. The ejected electron emanates from the

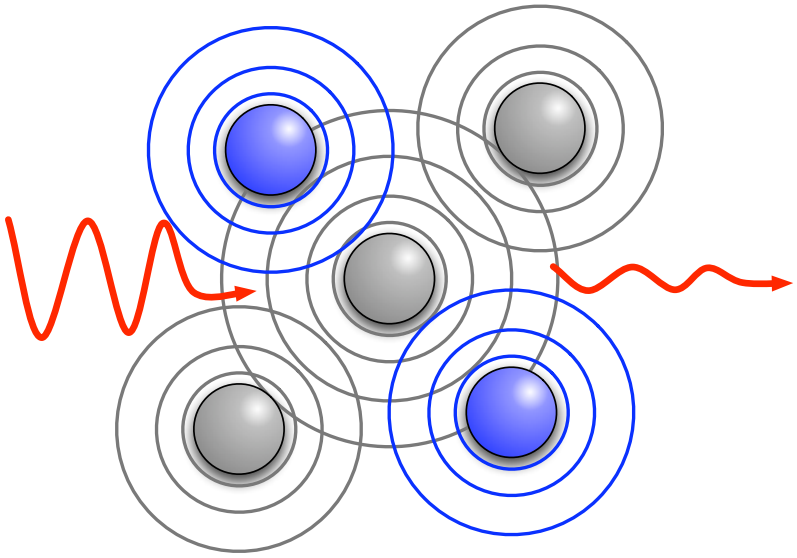

**Figure 1.26: Illustration of the underlying mechanism producing the EXAFS features in XAS experiments. Adapted from Rehr et al. [55]**

absorbing atom as a wave, much like throwing a stone into a pond creates a ripple on the surface of the water. When the water ripple encounters larger stones resting in the water, the ripple is reflected off the stones back to the original source. This is analogous to the mechanism that occurs in EXAFS. As the photoelectron in the potential field emanates away from the absorbing atom, it is reflected back by the surrounding atoms. The resulting wave patterns interfere constructively and deconstructively resulting in perturbations in the measured absorption coefficient.

It was not until the 1970s that a modern theory for interpreting EXAFS data and obtaining geometric information about the atoms surrounding the absorbing atom was developed [61-64], but since then there has been a tremendous amount of work developing the theory necessary for EXAFS interpretation. Equation 1.18 is referred to as the EXAFS equation, and describes the EXAFS phenomenon using geometric properties of the absorbing atom and it's environment.

$$\chi(k) = S_0^2 \sum_j \frac{N_j e^{-2k^2\sigma_j^2} e^{-2R_j/\lambda(k)} f_j(k)}{kR_j^2} \sin\left[2kR_j + \delta_j(k)\right] \quad \text{Eq. 1.18}$$

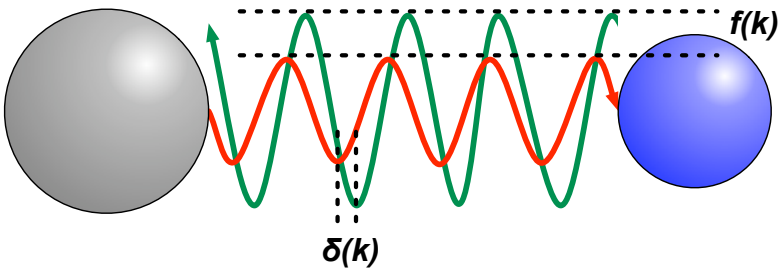


**Figure 1.27: Illustration of the scattering amplitude [f(k)] and phase shift [δ(k)] functions. The outgoing photoelectron wave (red) scatters off the neighboring scattering atoms. The phase and amplitude of the scattered photoelectron wave (green) is uniquely shifted depending on the nature of the scattering atom.**

The equation is typically used in k-space, and is summed over all scattering paths. It has three functions which are a function of k: $f_j(k)$ is the scattering amplitude function and accounts for a change in the amplitude of the scattering wave as it reflects off the scattering atom, $\delta_j(k)$ is the phase shift function and accounts for the shift in the phase of the scattering wave as it reflects off the scattering atom, and $\lambda(k)$ is the photoelectron mean free path function. The scattering amplitude function and phase shift function are illustrated in figure 1.27. These are both functions of the nature of the scattering atom and the bond distance.

Equation 1.18 also has several independent variables: $N_j$ is the average coordination number of the scattering atom, $R_j$ is the bond distance to the scattering atom, $\sigma_j$ is the root mean square deviation in the bond length which helps account for the temperature dependent atomic oscillation of the scattering atom around its equilibrium lattice position, and $S_o^2$ which is the amplitude reduction factor which accounts for a relaxation of the system caused by the creation of a core-hole [55].

Equation 1.18 is typically used to fit experimental data to theoretical fits. The results of these fits can give values for the independent variables listed above. First, the experimental EXAFS data (typically the data greater than 10eV above $E_o$) is converted to k-space and then into r-space using a Fourier-transform (see figure 1.28). Next, scattering amplitude and phase shift functions can either be generated using theoretical software or derived using experimental

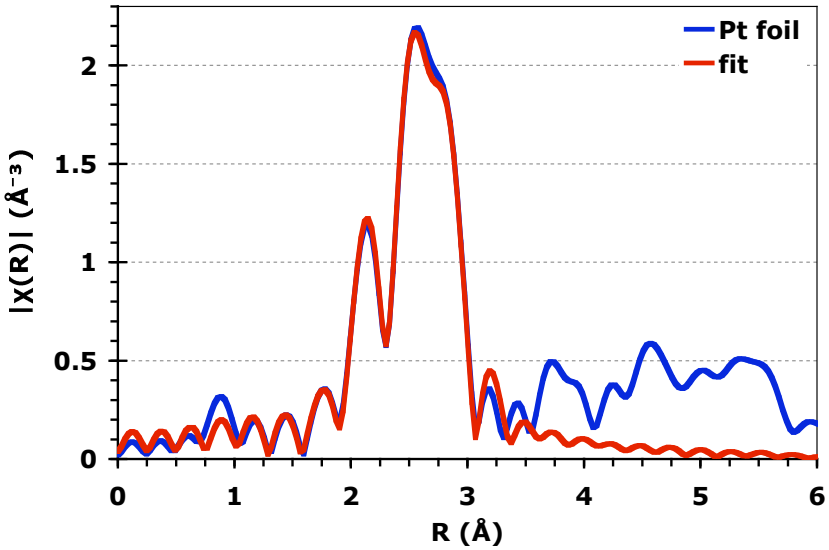


**Figure 1.28: EXAFS spectra and theoretical fit for $Pt/Al_2O_3$ displayed in R-space**

reference materials. One popular software package used extensively in this work is FEFF. A detailed account of the theory used by FEFF can be found in literature [65,66]. Finally, the experimental data is fit using a least squares analysis and equation 1.18, generating values for the independent variables. Details of the fitting procedure are also available in literature [58,63-64]. Figure 1.28 shows an example of an EXAFS spectra for a Pt reference foil and a best fit. It's worth noting that the largest peaks are between 2Å and 3Å. These typically correspond to first nearest neighbor, metal scattering coordination shells. Large peaks below 2Å are typically attributed to scattering of p-block elements (i.e. C, O, Cl, etc.), although the peaks below 2Å in figure 1.28 are relatively small and are probably due to noise. Peaks above three are due to second, third, and fourth coordination shell scattering as well as multi-body scattering. In this work, fittings will be performed on first neighbor scattering paths only.

## 7. Structure of the Thesis

This thesis is composed of 6 chapters. Chapter 2 will focus on the synthesis mechanism for the catalysts, specifically the loading mechanism of the metal onto the carbide support. Several different metals will be examined, and the results will offer insight into the interaction between the metal and the support

which will prove useful when characterizing the particles. This project will extensively use XAS.

Chapter 3 will focus on characterizing the Pt particles. In additional to extensive analysis from XAS results, this chapter will also include results from WGS reaction kinetics, X-ray diffraction (XRD), scanning electron microscopy (SEM), and DFT calculations.

In chapter 4, we will thoroughly examine the WGS mechanism on $Mo_2C$ and $Pt/Mo_2C$ catalyst surface and understand how Pt and $Mo_2C$ work in tandem for this mechanism. We will employ pulse chemisorption experiments and *in-situ* x-ray photoelectron spectroscopy (XPS) to study the dynamics of the mechanism and characterize the surface under reaction conditions. Then, we will use DFT calculations with microkinetic modeling results to fully describe the mechanism on the surface.

In chapter 5, we will compare the activity of $Pt/Mo_2C$ to several other oxide supported Pt catalysts. We use DFT to understand what characteristics of the carbide support distinguish it from the other catalysts; specifically how does its role in the mechanism differ from the oxides and how well does it perform this role relative to similar oxides.

Finally, chapter 6, will present general conclusions and suggestions for immediate future work as well as possible, related projects based on the conclusions of this work.

## 8. References


1. Bartholomew, C.H. and R.J. Farrauto, *Fundamentals of Industrial Catalytic Processes, Second Edition*. John Wiley and Sons, Inc. 2006
2. Leach, B.E., *Applied Industrial Catalysis, Volume 1*, Academic Press, Inc. 1983
3. Leach, B.E., *Applied Industrial Catalysis, Volume 2*, Academic Press, Inc. 1983
4. Leach, B.E., *Applied Industrial Catalysis, Volume 3*, Academic Press, Inc. 1983
5. Erisman, J.W., M.A. Sutton, J. Galloway, Z. Kilmont, and W. Winiwarter, *How a Century of Ammonia Synthesis Changed the World*. Nature Geoscience, 2008. 1: p. 636-639
6. Leckel, D., *Diesel Production from Fisher-Tropsch: the Past, the Present, and New Concepts*. Energy & Fuels, 2009. 23: p. 2342-2358
7. Armor, J.N., *Catalysis and the Hydrogen Economy*. Catalysis Letters, 2005. 101(3-4): p. 131-135
8. Ladebeck, J.R. and J.P. Wagner, *Catalyst Development for Water-Gas Shift*. Handbook of Fuel Cells - Fundamentals, Technology, and Applications. John Wiley and Sons, Inc. 2003. Vol 3, part 2, p. 190-201
9. Ovesen, C.V., P. Stoltze, J.K. Nørskov, and C.T. Campbell, *A Kinetic Model of the Water Gas Shift Reaction.* Journal of Catalysis, 1992. 134: p. 445-468
10. Grabow, L.C., A.A. Gokhale, S.T. Evans, J.A. Dumesic, and M. Mavrikakis, *Mechanism of the Water Gas Shift Reaction on Pt: First Principles, Experiments, and Microkinetic Modeling*. Journal of Physical Chemistry C, 2008. 112: p.4608-4617
11. Liu, P. and J.A. Rodriguez, *Water-Gas Shift Reaction on Molybdenum Carbide Surfaces: Essential Role of the Oxycarbide.* Journal of Physical Chemistry B, 2006. 110: p. 19418-19425
12. Lynggaard, H., A. Andreasen, C. Stegelmann, and P. Stoltze, *Analysis of Simple Kinetic Models in Heterogeneous Catalysis.* Progress in Surface Science, 2004. 77: p. 71–137
13. Laidler, K.J., *Chemical Kinetics*. Harper & Row. 1987
14. Boudart, M., *Kinetics of Chemical Processes*. Prentice-Hall, Inc. 1968

15. McQuarrie, D.A. and J.D. Simon, *Physical Chemistry: a Molecular Approach*. University Science Books, 1997

16. Nørskov, J.K., T. Bligaard, A. Logadottir, S. Bahn, L.B. Hansen, M. Bollinger, H. Bengaard, B. Hammer, Z. Sljivancanin, M. Mavrikakis, Y. Xu, S. Dahl, and C. J. H. Jacobsen, *Universality in Heterogeneous Catalysis.* Journal of Catalysis, 2002. 209: p. 275–278

17. Bligaard, T., J.K. Nørskov, S. Dahl, J. Matthiesen, C.H. Christensen, and J. Sehested, *The Brønsted–Evans–Polanyi relation and the volcano curve in heterogeneous catalysis.* Journal of Catalysis, 2004. 224: p. 206–217

18. Schumacher, N., A. Boisen, S. Dahl, A.A. Gokhale, S. Kandoi, L.C. Grabow, J.A. Dumesic, M. Mavrikakis, and I. Chorkendorff, *Trends in low-temperature water–gas shift reactivity on transition metals.* Journal of Catalysis, 2005. 229: p. 265–275

19. Boisen, A., T.V.W. Janssens, N. Schumacher, I. Chorkendorff, and S. Dahl, *Support effects and catalytic trends for water gas shift activity of transition metals.* Journal of Molecular Catalysis A: Chemical, 2010. 315: p. 163–170

20. Hoffmann, R., *Solids and Surfaces: A Chemist's View of Bonding in Extended Structures.* Wiley-VCH, Inc. 1988

21. Nørskov, J.K., *Effective medium potentials for molecule-surface interactions: $H_2$ on Cu and Ni surfaces.* Journal of Chemical Physics, 1989. 90: p. 7461-7471

22. Hammer, B., and J.K. Nørskov, Why Gold is the noblest of all the metals. Nature, 1995. 376: p. 238-240

23. Hammer, B and J.K. Nørskov, *Electronic factors determining the reactivity of metal surfaces.* Surface Science, 1995. 343: 211-220

24. Hammer, B., Y. Morikawa, and J.K. Nørskov. *CO Chemisorption at Metal Surfaces and Overlayers.* Physical Review Letters, 1996. 76: p. 2141-2144

25. Hammer, B., *Special Sites at Noble and Late Transition Metal Catalysts*. Topics in Catalysis, 2006. 37: p. 3-16

26. Greeley, J. and J.K. Nørskov, *A general scheme for the estimation of oxygen binding energies on binary transition metal surface alloys.* Surface Science, 2005. 592: p. 104–111

27. Iida, H., and A. Igarashi, *Characterization of a Pt/TiO2 (Rutile) Catalyst for Water-Gas Shift Reaction at Low-Temperature*. Applied Catalysis A: General, 2006. 298: p. 152–160

28. Phatak, A.A., N. Koryabkina, S. Rai, J.L. Ratts, W. Ruettinger, R.J. Farrauto, G.E. Blau, W.N. Delgass, and F.H. Ribeiro, *Kinetics of the Water–Gas Shift Reaction on Pt Catalysts Supported on Alumina and Ceria.* Catalysis Today, 2007. 123: p. 224–234

29. Panagiotopoulou P. and D.I. Kondarides, *Effect of Morphological Characteristics of $TiO_2$ - Supported Noble Metal Catalysts on Their Activity for the Water–Gas Shift Reaction.* Journal of Catalysis, 2004. 225: p. 327–336

30. Panagiotopoulou P. and D.I. Kondarides, *Effect of the Nature of the Support on the Catalytic Performance of Noble Metal Catalysts for the Water–Gas Shift Reaction.* Catalysis Today, 2006. 112: p. 49–52

31. Panagiotopoulou P. and D.I. Kondarides, *A Comparative Study of the Water-Gas Shift Activity of Pt Catalysts Supported on Single ($MO_x$) and Composite ($MO_x/Al_2O_3$, $MO_x/TiO_2$) Metal Oxide Carriers.* Catalysis Today, 2007. 127: p. 319–329

32. K.G. Azzam, I.V. Babich, K. Seshan, L. Lefferts, *Bifunctional Catalyst for the Single-Stage Water–Gas Shift Reaction in Fuel Cell Applications. Part 2. Roles of the Support and Promoter on Catalyst Activity and Stability.* Journal of Catalysis, 2007. 251: p. 163–171

33. González, I.D., R.M. Navarro, M.C. Álvarez-Galván, F. Rosa, and J.L.G. Fierro, *Performance Enhancement in the Water–Gas Shift Reaction of Platinum Deposited Over a Cerium-Modified $TiO_2$ Support.* Catalysis Communications, 2008. 9: p. 1759–1765

34. Thinon, O., K. Rachedi, F. Diehl, P. Avenier, and Y. Schuurman, *Kinetics and Mechanism of the Water–Gas Shift Reaction Over Platinum Supported Catalysts* Topics in Catalysis, 2009. 52: p. 1940–1945

35. K.G. Azzam, I.V. Babich, K. Seshan, L. Lefferts, *Bifunctional Catalyst for the Single-Stage Water–Gas Shift Reaction in Fuel Cell Applications. Part 1. Effect of the Support on the Reaction Sequence.* Journal of Catalysis, 2007. 251: p. 153–162

36. Jacobs, G., A.C. Crawford, and B.H. Davis, *Water-gas Shift: Steady State Isotope Switching Study of the Water-Gas Shift Reaction Over Pt/ceria Using in-situ DRIFTS.* Catalysis Letters, 2005. 100(3–4): p. 147-152

37. Kalamaras, C.M., P. Panagiotopoulou, D.I. Kondarides, and A.M. Efstathiou, *Kinetic and Mechanistic Studies of the Water–Gas Shift Reaction on $Pt/TiO_2$ Catalyst.* Journal of Catalysis, 2009. 264(2): p. 117-129

38. Jacobs, G., S. Ricote, and B.H. Davis, *Low Temperature Water-Gas Shift: Type and Loading of Metal Impacts Decomposition and Hydrogen Exchange Rates of Pseudo-stabilized Formate Over Metal/ceria Catalysts.* Applied Catalysis A: General, 2006. 302: p. 14–21

39. Levy, R.B. and M. Boudart, *Platinum-Like Behavior of Tungsten Carbide in Surface Catalysis.* Science, 1973. 181(4099): p. 547-549

40. Chen, J.G. *Carbide and Nitride Overlayers on Early Transition Metal Surfaces: Preparation, Characterization, and Reactivities.* Chemical Reviews, 1996. 96: p. 1477−1498

41. Furimsky, E. *Metal Carbides and Nitrides as Potential Catalysts for Hydroprocessing.* Applied Catalysis A: General, 2003. 240: p. 1–28

42. Diaz, B., S.J. Sawhill, D.H. Bale, R. Main, D.C. Phillips, S. Korlann, R. Self, and M.E. Bussell, *Hydrodesulfurization Over Supported Monometallic, Bimetallic and Promoted Carbide and Nitride Catalysts.* Catalysis Today, 2003. 86: p. 191–209

43. Ledoux, M.J., C. Pham-Huu, and R.R. Chianelli, *Catalysis with Carbides.* Current Opinion in Solid State & Materials Science, 1996. 1: p. 96-100

44. Oyama, S.T., *Preparation and Catalytic Properties of Transition Metal Carbides and Nitrides.* Catalysis Today, 1992. 15: p. 179-200

45. Moon, D.J. and J.W. Ryu, *Molybdenum Carbide Water–Gas Shift Catalyst for Fuel Cell-Powered Vehicles Applications.* Catalysis Letters, 2004. 92(1–2): p. 17-24

46. Tominaga H. and M. Nagai, *Density Functional Theory of Water-Gas Shift Reaction on Molybdenum Carbide*. Journal of Physical Chemistry B, 2005. 109: p. 20415-20423

47. Hanif, A., T. Xiao, A.P.E. York, J. Sloan, and M.L.H. Green, *Study on the Structure and Formation Mechanism of Molybdenum Carbides*. Chemistry of Material, 2002. 14: p. 1009-1015

48. Parthé, E. and V. Sadagopan, *The Structure of Dimolybdenum Carbide by Neutron Diffraction Technique.* Acta Crystallographica, 1963. 16: p. 202-205

49. Gelatt, C.D., A.R. Williams, and V.L. Moruzzi, *Theory of bonding of Transition Metals to nontransition Metals.* Physical Review B, 1983. 27(4): p. 2005-2013

50. Ruberto, C., A. Vojvodic, and B.I. Lundqvist, *Nature of Chemisorption on Tit*anium *Carbide and Nitride*. Surface Science, 2006. 600: p. 1612–1618

51. Vojvodic, A., A. Hellman, C. Ruberto, and B.I. Lundqvist, *From Electronic Structure to Catalytic Activity: A Single Descriptor for Adsorption and Reactivity on Transition-Metal Carbides.* Physical Review Letters, 2009. 103:146103

52. Kitchin, J.R., J.K. Nørskov, M.A. Barteau, J.G. Chen, *Trends in the Chemical Properties of Early Transition Metal Carbide Surfaces: A Density Functional Study.* Catalysis Today, 2005. 105: p. 66–73

53. Setthapun, W., *Carbide and Nitride Supported Methanol Steam Reforming Catalysts.* 2007, The University of Michigan

54. King, T., *Carbide and Nitride Supported Water-Gas Shift Catalysts.* 2007, The University of Michigan

55. Rehr, J.J. and R.C. Albers, *Theoretical approaches to x-ray absorption fine structure*. Reviews of Modern Physics, 2000. 72(3): p. 621-654

56. Russell, A.E. and A. Rose, *X-ray Absorption Spectroscopy of Low Temperature Fuel Cell Catalysts.* Chemical Reviews, 2004. 104: p. 4613 −4635

57. Chen, J., *NEXAFS Investigations of Transition Metal Oxides, Nitrides, Carbides, Sulfides and Other Interstitial Compounds.* Surface Science Reports, 1997. 30: p. 1-152

58. Newville, M., *Fundamentals of XAFS.* Consortium for Advanced Radiation Sources, University of Chicago, Chicago, IL. Revisions 2004.

59. Ankudinov, A.L., A.I. Nesvizhskii, and J.J. Rehr, *Hole Counts from X-ray Absorption Spectra,* Journal of Synchrotron Radiation, 2001. 8: p. 92-95

60. Pearson, D.H., C.C. Ahn, and B. Fultz., *White Lines and d-electron occupancies for the 3d and 4d Transition Metals*. Physical Review B, 1993. 47(14): p. 8471-8478

61. Sayer, D.E. And E.A. Stern, *New Technique for Investigating Noncrystalline Structures: Fourier Analysis of the Extended X-Ray - Absorption Fine Structure*. Physical Review Letters, 1971. 27:18 p. 1204-1207

62. Stern, E.A. *Theory of the Extended X-Ray-Absorption Fine Structure*. Physical Review B, 1974. 10:8 p. 3027-3037

63. Lytle, F.W., D.E. Sayers, and E.A. Stern, *Extended X-Ray-Absorption Fine Structure Technique. II. Experimental Practice and Selected Results.* Physical Review B, 1975. 11:12 p. 4825-4835

64. Stern, E.A., D.E. Sayers, and F.W. Lytle, *Extended X-Ray-Absorption Fine Structure Technique. III. Determination of Physical Parameters.* Physical Review B, 1975. 11:12 p. 4836-4846

65. Rehr, J.J., J. Mustre de Leon, S.I. Zabinsky, and R. C. Albers, *Theoretical X-ray Absorption Fine Structure Standards.* Journal of the American Chemical Society, 1991. 133(14): p. 5135-5140

66. Ravel, B. and M. Newville, *ATHENA, ARTEMIS, HEPHAESTUS: Data Analysis for X-ray Absorption Spectroscopy using IFEFFIT***.** Journal of synchrotron Radiation, 2005. 12: p. 537-541

67. Mansour, A.N., J.W. Cook, Jr., and D.E. Sayers, *Quantitative Technique for the Determination of the Number of Unoccupied d-Electron States in a Platinum Catalyst Using the $L_{2,3}$ X-ray Absorption Edge Spectra*. Journal of Physical Chemistry, 1984. 88: p. 2330-2334

# Chapter 2
# Synthesizing Carbide Supported Metal Catalysts

## 1. Introduction

The manipulation of catalyst synthesis methods is among the most direct ways to control the metal particle size and dispersion of heterogeneous, supported metal catalysts. As mentioned in chapter 1, the size and dispersion of metal catalyst particles can affect total, observed catalytic rates and selectivities by changing the chemistry of active sites, the total or relative number of active sites, or both. Therefore, it is very important to have a clear understanding of catalyst synthesis methods so that metal particle size and dispersion can be suitably controlled and their effects on catalytic properties easily studied.

One of the simplest methods used to deposit metals onto supports is dry impregnation, also known as incipient wetness. In this method, the pore volume of the oxide support is measured using BET analysis. Then, the desired amount of metal precursor salt is dissolved in the exact volume of water which is sufficient to uniformly fill the pores of the support. The sample is then dried (usually in a vacuum oven) and reduced in hydrogen or calcined in air. The main advantage of this very simple preparation method is that very high metal loadings can be obtained. However, there is very little control over the metal particle size and dispersion, which tends to be only a function of the amount of precursor loaded on the surface, the drying scheme, and the reducing/calcination scheme [1]. Consequently, catalysts synthesized using incipient wetness typically have metal particles which are relatively large when compared to particles resulting from other synthesis methods [1].

An alternative approach that is frequently used for metal loading is wet impregnation. The basis of this method lies in the fact that under favorable conditions, aqueous metal complexes will adsorb to the oxide supports. Thus, in this method, the oxide is added to an aqueous solution of the metal precursor (with a large excess of water compared to the amount used in dry impregnation). During the adsorption process, the pH of the solution is carefully controlled. There are several proposed mechanisms that are used to explain how metal complexes bind to oxide surfaces.

Brunelle [2] was among the first to study how the solution pH affected the adsorption capabilities of oxide surfaces. Brunelle proposed that the key characteristic of the oxide which determined its adsorption capabilities was its isoelectric point or point of zero charge (PZC). Essentially, when an oxide is immersed in water, the surface of the oxide equilibrates with the water by forming hydroxyls on its surface. As a result, the pH of the water is shifted. The final pH of the water is characteristic of the oxide, and is referred to as the PZC. If the pH is then forced below the PZC of the oxide through the addition of an acid, the hydroxylated surface is further protonated and therefore gains a positive charge. On the other hand, if the pH of the solution is forced above the PZC by the addition of a base, the surface is deprotonated and gains a negative charge. In

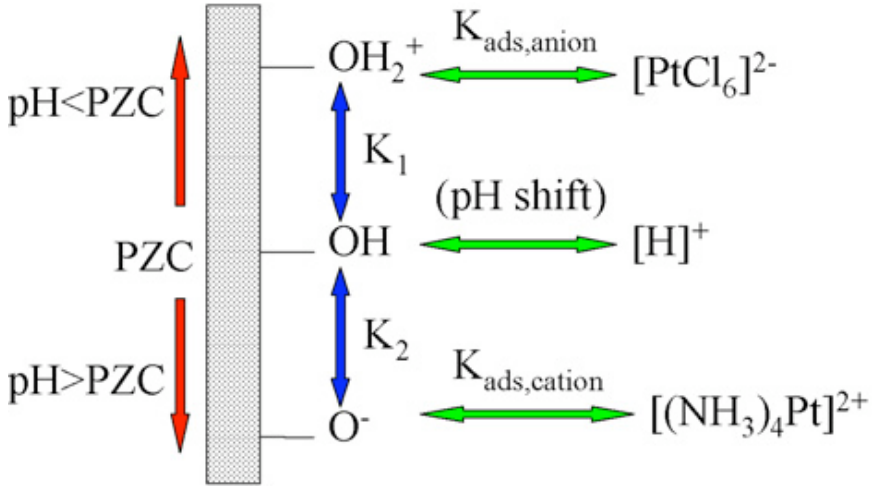


**Figure 2.1: Illustration of the "strong electrostatic adsorption" process. When the pH of a solution containing an oxide surface is forced below the PZC of the oxide, the surface is protonated and amenable to adsorbing anionic metal complexes. If the pH of the solution is raised above the PZC of the oxide, the surface is deprotonated and capable of adsorbing cationic metal complexes. Taken from Jiao et al. [1]**

either case, the charged surface is then able to adsorb ionic metal complexes of the opposite charge through electrostatic interactions [1-5]. This process has been termed either “ion exchange,” “strong electrostatic adsorption” (SEA), or the “double layer” mechanism and is illustrated in figure 2.1 [1,3-5] (the double layer refers to one layer which is the oxide surface and a second layer which is the layer of adsorbed precursor).

It has been reported that electrostatic binding does not always fully account for metal complex adsorption on oxides [5,6], so more complex theories have been developed. These include the triple layer theory [6] and specific site adsorption [6]. The distinction of these mechanisms is important in studying the detailed kinetics and thermodynamics of the metal adsorption process, however, for the purpose of this study, distinguishing between these mechanisms is not necessary. It is sufficient to emphasize that all of these processes involve the adsorption of the metal complex precursor directly to the oxide surface.

Since there is a direct, attractive interaction between the surface and the metal complexes in solution, the precursor is highly dispersed on the support. Furthermore, the binding is sufficiently strong enough to maintain this dispersion upon drying of the catalysts. As a result, when the precursor is reduced/calcined, the resulting particles are generally small and well dispersed [1,5-6]. Since there is no control of pH, this is not the case using dry impregnation. There is no interaction between the surface and the precursor [1], so the precursor tends to aggregate upon drying.

A major disadvantage of wet impregnation is that the metal loading is limited by the saturation point of the metal complex on the surface. The maximum loading for a given support is limited by the BET surface area (or site density, depending on the adsorption mechanism) of the support, the size of the metal complex, and repulsive forces between adsorbed metal complexes. In other words, the maximum loading is limited by the number of metal complex molecules which can adsorb directly on the surface and form a monolayer [1].

Since transition metal carbides behave more like metals than oxides (the band structure of carbides is metal-like, i.e. the d-band of the metal is situated around the fermi level and there is no band gap, see chapter 1, section 5), it may be important to consider additional support-precursor interactions which could affect the metal loading mechanism. For example, a common method for the synthesis of bimetallic metal particles is by a direct red-ox reaction [5]. In these synthesis, a colloidal mixture of the first metal is synthesized, then the precursor of the second metal is added. The particles of the first metal (zero valent metal) serves as a reducing agent for the second metal. This interaction is controlled by the Gibb's free energy of the reaction (and is analogous to the chemistry occurring in an electrochemical cell):

$$\Delta G^{\circ} = -nF(E_1^{\circ} - E_2^{\circ}) \qquad \text{Eq 2.1}$$

where *n* is the number of electrons transferred, *F* is faraday's constant, and $E_n$ is the reduction potential of the respective half cell reaction (n=1 is for the reduction of the second metal precursor while n=2 is for the oxidation of the zero-valent metal particles) [5]. Since the expression is negative, if the species which is to be reduced has a larger reduction potential than the species which is to be oxidized, the Gibb's free energy of the overall reaction will be negative and the reaction will be favorable. This phenomenon makes it easy to then reduce noble metal ions (such at Pt, Au, Ag, Pd, etc.) using base metals (i.e. Fe, Ni, Co, Cu, etc.) and has been shown to be effective in synthesizing many bimetallic systems and is often referred to as the "seed-germ" process [5,7]. Since carbides are metal like, it is possible that this phenomenon could occur in metal deposition on carbide surfaces as well.

A final consideration for wet impregnation metal loading is metal speciation [8,9]. Speciation refers to the chemical transformation which can occur to a metal salt when it is dissolved in water and subjected to various conditions (mainly

changes in pH or temperature) [8,9]. For example, the speciation series for $FeCl_2$ is presented below:

$$[FeCl_2]_{aq} \rightleftharpoons [FeCl]^+_{aq} \rightleftharpoons Fe^{2+}_{aq} \rightleftharpoons [FeOH]^+_{aq} \rightleftharpoons [FeOH_2]_{aq} \quad \text{Eq 2.2}$$

This chemistry is important for two reasons: 1) it affects the overall charge of the metal species. This will play a role in the binding of the metal precursor complex to the support by the SEA mechanism. 2) The ligand type and number can affect the reduction potential of the metal ion and, therefore, the metal loading thermodynamics through eq. 2.1.

In this chapter, we will determine the governing mechanism(s) by which aqueous metal precursors interact with $Mo_2C$, using a simple wet impregnation procedure. Figure 2.2 shows measured loadings of different metals on $Mo_2C$ using various precursors. The horizontal line in the graphs indicates the targeted

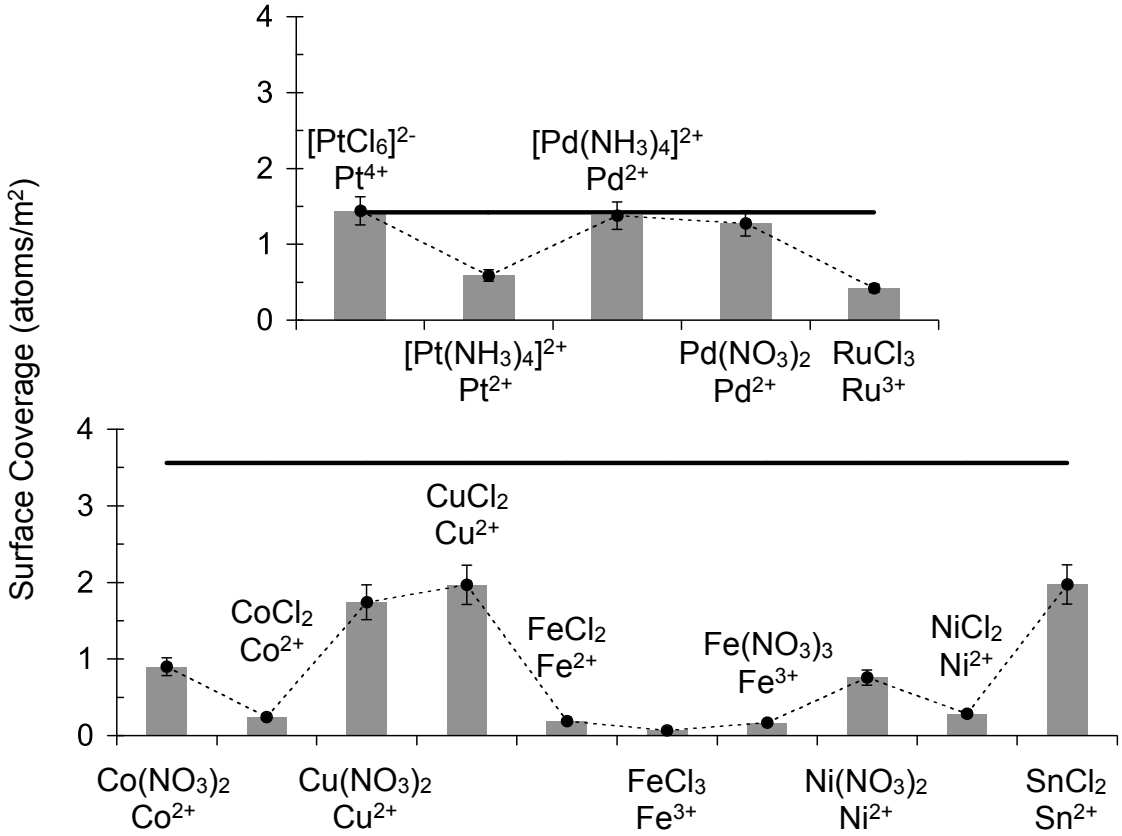


**Figure 2.2: Relative loadings for several different metals, using various precursors, on $Mo_2C$. Taken from the dissertation of Timothy King [9].**

metal loadings (i.e. the loadings which would be achieved if all the metal in solution were successfully deposited onto the support). It can be seen that the relative loading (defined as the actual loading divided by the targeted loading) of the metals is a strong function of not only the metal, but also the form of the precursor. We synthesized a number of carbide supported metal catalysts and used x-ray absorption spectroscopy (XAS) to study the state of the precursor metal adsorbed on the surface of $Mo_2C$. Using this information, we can hypothesize the dominant mechanism for metal loading. Further, we will show that there is a trend in the relative loading of the metal that relates mostly to the metal type and possibly the counter ion.

## 2. Experimental Setup

### *2.1. Catalyst Synthesis*

High surface area $Mo_2C$ was synthesized using a temperature programmed reaction procedure. The oxide precursor, (ammonium paramolybdate ($(NH_4)_6Mo_7O_{24}{\cdot}4H_2O$, 81-83% as $MoO_3$; Alpha Æsar) was crushed and sieved to particle sizes greater than 125 μm (120 mesh) and less than 250 μm (60 mesh). The powder was then supported in a tubular quartz reactor with quartz wool, and placed in a vertical furnace. The powder was heated in $H_2$ (400 mL/min; pre-purified; Cryogenic Gases) at 350 °C for 12 h, initially ramped at 5 °C/min. The gas was then changed to 15% $CH_4/H_2$ (375 mL/ min; Cryogenic Gases), and the temperature was increased at 2.67 °C/min to 590 °C and held for 2 h. The sample was then cooled to room temperature in 15% $CH_4/H_2$.

Metals were loaded onto the support via wet impregnation. The metal precursors selected for this synthesis can be viewed in table 1. The chosen metals represent a wide range of metal oxidation state, ligand, and metal reduction potential. First, an appropriate amount of metal precursor was dissolved in 70 mL of deionized water. The impregnation solution had a

concentration of 0.00227 mol metal/L (if 100% deposition is achieved, this corresponds to a 4% Pt/$Mo_2C$ catalyst). The solution was sparged with argon gas (Ultra-high purity; Cryogenic Gases) for 15 min to remove any dissolved oxygen. The initial pH of the salt solutions can be viewed in table 1. The freshly synthesized $Mo_2C$ powder was then transferred, in argon, to the solution as bubbling was maintained. The support powder was left in solution for 3 h and periodically stirred. Finally, the loaded support powder was transferred back into the quartz reactor tube, under argon flow.

Some of the samples for this study were dried in a pure He stream (20 mL/min; Cryogenic Gases) at room temperature over night. The samples were then stored in an Ar glove box in preparation for their transfer to Argonne National Lab (ANL) for XAS analysis. These samples are referred to as “Dried” samples. Another set of samples, prepared the same way, were initially dried at 110 °C for 2 h in $H_2$ and reduced in $H_2$ at 450 °C for 4 h increased at 5.67 °C/min. After reduction, these samples were also transfered into a glove box before being transfered to ANL. These samples are referred to as “Reduced.”

**Table 2.1:Metal precursors used in this study. The reported pH corresponds to 0.00227 M solution, the wet impregnation solution used in this study.**

| Metal Precursor | Description | pH of metal solution |
|---|---|---|
| $H_2PtCl_6$ | Sigma-Aldrich, ACS reagent | 2.5 |
| $Pd(NH_3)_4(NO_3)_2$ | Sigma-Aldrich, 99.99%, 10wt% solution in water | 7.3 |
| $Fe(NO_3)_3$ | Puratronic, 99.999% (metal basis) | 2.9 |
| $Co(NO_3)_2$ | Alfa Æsar, ACS 98.0-102.0% | 5.7 |
| $Ni(NO_3)_2$ | Fisher Scientific, Reagent grade | 5.7 |
| $Cu(NO_3)_2$ | Alfa Æsar, ACS 98.0-102.0% | 5.1 |
| $FeCl_2$ | Mallinckrodt, analytical reagent | 4.7 |
| $CoCl_2$ | Aldrich, 98% ACS Reagent | 6.2 |
| $NiCl_2$ | Alfa Æsar, ACS 99.95% | 5.9 |
| $CuCl_2$ | Alfa Æsar, ACS 99+% | 5.0 |

Metals were also deposited onto alumina supports using the same procedure as that for the $Mo_2C$ catalysts. Initially, the alumina powder (γ-phase, 99.97% (metal basis), 3 micron APS powder, S.A. 80-120 $m^2/g$) was pressed, crushed, sieved to a particle size greater than 125 μm (120 mesh) and less than 250 μm (60 mesh), then calcined for at least 12 h at 650 °C. The powder was then immersed in the appropriate metal precursor solution. An excess amount of the metal precursor was added to the solution to ensure a full monolayer of the precursor would adsorb to the alumina surface. It is important to note that the pH of the Pt precursor solution was sufficiently below the PZC of the alumina, and the pH of the Pd solution was sufficiently above the PZC of the alumina support. After the metal deposition, the catalyst was either dried in He, or reduced in $H_2$ at 450 °C using the same procedure used for the $Mo_2C$ catalyst. These catalysts were also refereed to as “Dried” and “Reduced”.

### *2.2. Elemental Analysis*

Inductively coupled plasma optical emission spectroscopy (ICP) was used to determine the amount of metal deposited on the $Mo_2C$ supports. The loading was determined using one of two procedures. The first was a direct method. Approximately 15 mg of powder catalysts was dissolved using 3 mL of aqua regia solution (75%vol HCl and 25%vol $HNO_3$). The solution was left overnight. Next, 1 mL of the aqua regia solution was diluted with 13 mL of deionized water. The dilution step was repeated once, resulting in two samples for ICP analysis from each original powder sample. The second method was an indirect method, and involved the analysis of the deposition solution used in the catalysts synthesis after synthesis was complete. For this method, 14 mL of the deposition solution was directly analyzed. The amount of metal deposited on the support was then calculated by subtracting the amount of metal remaining in the deposition solution from the initial amount loaded into the solution. All the solutions were analyzed using a Varian 710-ES ICP Optical Emission Spectrometer. Chemical standards for the analysis were obtained from Inorganic Ventures. For each analysis, quantification was performed by comparing the relative intensities of the

catalyst solutions to a linear calibration curve derived from the relative intensities of several standards of various concentrations.

### *2.3. Metal speciation calculations*

The relative concentration and equilibrium pH of the metal solutions of Cu, Ni, and Co were modeled using readily available thermodynamic data [11]. The required data is listed in table 2.2. The general speciation mechanism for all the species above is illustrated below:

$$MX_{2(aq)} \rightleftharpoons [MX]^+ + X^- \quad \text{Eq 2.3}$$

$$[MX]^+ \rightleftharpoons M^{2+} + X^- \quad \text{Eq 2.4}$$

$$M^{2+} + H_2O \rightleftharpoons [MOH]^+ + H^+ \quad \text{Eq 2.5}$$

$$[MOH]^+ + H_2O \rightleftharpoons M(OH)_2 + H^+ \quad \text{Eq 2.6}$$

where M is either Cu, Co, or Ni and X is either Cl or $NO_3$. The Gibb's free energy of each step is calculated using Eq. 2.7:

$$\Delta G^\circ_{rxn} = \Delta G^\circ_{products} - \Delta G^\circ_{reactants} \quad \text{Eq. 2.7}$$

Using eq. 2.8 and 2.9, the standard reduction for each of the species and the equilibrium constant for each step were calculated, respectively:

$$\Delta E^\circ_{red,[MX_n]^{(2-n)}} = -\left(\Delta G^\circ_{[MX_n]^{(2-n)} \rightleftharpoons M^0 + nX^-}\right)/nF \quad \text{Eq. 2.8}$$

$$\ln K_{eq} = \frac{-\Delta G^\circ_{rxn}}{RT} \quad \text{Eq. 2.9}$$

The concentrations of the respective species of each step can then be calculated using eq 2.10:

**Table 2.2: Required thermodynamic properties of the species used in the metal speciation calculations. The standard reduction potentials of the species are calculated using Eq 2.8 and the Gibb's free energy of the reduction reaction: $[MX_n]^{(2-n)+} + 2e^- \rightleftharpoons M^0 + nX^-$**

| Aqueous species | $\Delta G°_{formation}$ (kJ/mol) | E° (V) |
|---|---|---|
| $[CuCl_2]$ | -198.0 | 0.332 |
| $[CuCl]^+$ | -68.2 | 0.325 |
| $[Cu]^{2+}$ | 65.6 | 0.340 |
| $[Cu(NO_3)_2]$ | -157.3 | 0.339 |
| $[CuNO_3]^+$ | -45.0 | 0.344 |
| $[Cu(OH)_2]$ | -249.2 | 0.339 |
| $[CuOH]^+$ | -126.4 | 0.160 |
| $[NiCl_2]$ | -308.1 | -0.239 |
| $[NiCl]^+$ | -175.7 | -0.231 |
| $[Ni]^{2+}$ | -45.6 | -0.236 |
| $[Ni(NO_3)_2]$ | -268.8 | -0.239 |
| $[NiNO_3]^+$ | -157.4 | -0.239 |
| $[Ni(OH)_2]$ | -360.5 | -0.238 |
| $[NiOH]^+$ | -227.8 | -0.365 |
| $[CoCl_2]$ | -316.9 | -0.284 |
| $[CoCl]^+$ | -184.7 | -0.278 |
| $[Co]^{2+}$ | -54.4 | -0.282 |
| $[Co(NO_3)_2]$ | -277.2 | -0.283 |
| $[CoNO_3]^+$ | -164.9 | -0.278 |
| $[Co(OH)_2]$ | -369.3 | -0.283 |
| $[CoOH]^+$ | -236.6 | -0.411 |

$$\ln K_{eq} = \frac{[MX_n][X]}{[MX_{(n-1)}]} \qquad \text{Eq. 2.10}$$

Typically, in ionic solutions, interactions between ions can be significant, and the concentrations in eq. 2.10 need to be corrected using activity coefficients. However, in this analysis, the concentrations are very dilute (<<1M), and therefore it is assumed the activity coefficients are unity. Using the values in table 2.2 and the equations above, MATLAB was used to calculate relative concentrations (defined as the concentration of individual metal species divided by the total concentration of all the metal species) as a function of temperature (in this case T=25 °C for all calculations) and initial salt concentration. Using this model, the concentration of the speciation products of the metals salts under the conditions of the metal loading were calculated.

### *2.4. PZC Measurements*

The PZC of $Mo_2C$ was determined according to the procedure proposed by Park et al. [3] Figure 2.3 shows an example from literature for $SiO_2$ [1]. The PZC for $SiO_2$ was determined to be 4.2, the flat portion of the curve. In this analysis, $Mo_2C$ was synthesized according to the procedure previously described. Then, 18mL of deionized water was sparged with Ar. The pH of the water was adjusted to a specific value using either concentrated HCl or $NH_4OH$. After the pH stabilized, the pH was recorded, and the unpassivated $Mo_2C$ powder

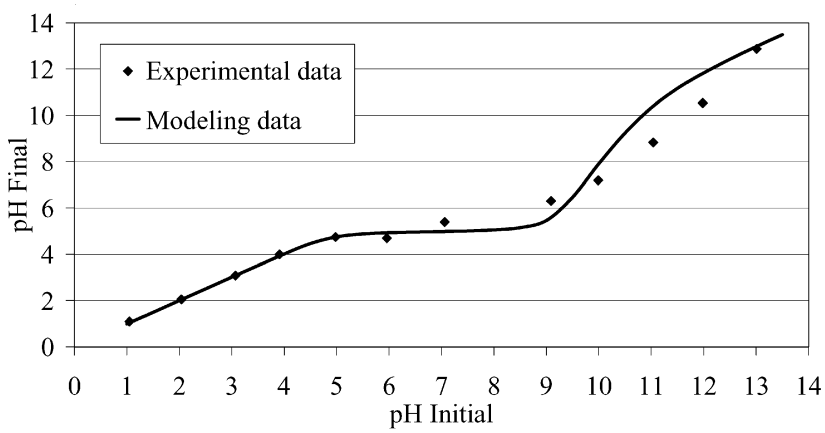


**Figure 2.3: PZC experiment and modeling for $SIO_2$. The PZC was determined to be 4.2. Taken from Jiao et al. [1]**

was transfered to the solution in Ar. The solution was continuously stirred, and the pH of the solution was recorded as a function of time. After the change in pH had stabilized, the final pH was recorded. Approximately 0.75 g of $Mo_2C$ was added. The surface area of this material was ~120 $m^2/g$. Using 18 mL of deionized water corresponds to a surface to volume ratio of 5000 $m^2/L$, similar to the value used in Park et al. [3]

### *2.5. X-ray Absorption Spectroscopy (XAS)*

X-ray absorption spectroscopy studies were performed at the Argonne National Laboratory Advanced Photo Source (APS) beamline MR-CAT 10-ID-B. Data was collected at the Fe K (7112 eV), the Ni K (8333 eV), the Cu K (8979 eV), the Pd K (24350 eV), and the Pt $L_3$ edges (11564 eV). Scans were collected in fluorescence mode using Ar ion chambers for detection. Samples were packed into wafers supported in a steel sample tube. The tube contained a hole in the side, and the pellet was packed at a 45° angle such that fluorescent radiation could be detected from the side of the holder as the x-ray beam passed through the tube. The steel sample holder was then placed in a glass in-situ reactor which had a Kapton window on the side for fluorescence detection. Upon arriving at APS, the samples were immediately transferred into a glove box from sealed, vacuumed desiccators. Sample preparations for the XAS experiments were performed in the glove box. The in-situ chamber was then transfered out of the glove box to the analysis chamber. The sample was isolated from air so that neither the metal nor the $Mo_2C$ support was oxidized by atmospheric oxygen.

XAS results were analyzed using free online software Athena and Artemis [12] using standard analysis procedures [13]. First, the background data of each curve was removed by fitting the pre-edge data to a linear function and subtracting out the result. The curves were then normalized by fitting the post-edge data to a third degree polynomial and dividing the data by the extrapolated value at $E_o$. Finally, the background of the post-edge data was removed using a cubic spline function. R-space data was plotted by first converting the post-edge

data into k-space with a $k^2$ weighting. Then, the k-space data ranging from about 2.5 $Å^{-1}$ to 13 $Å^{-1}$ was converted into R-space using a Fourier transform.

## 3. Results

### *3.1. Metal loadings*

The relative metal loadings on $Mo_2C$ for different metal precursors are presented in figure 2.4. The relative metal loading is defined as the measured loading divided by the targeted loading. The results show that the relative loading of the metal is a strong function of the metal type. For example, in general, noble metals (Pt, Pd, and Cu) have higher relative loadings than base metals (Fe, Ni, and Co). Additionally, the form of the metal precursor has an affect on the loading. Generally, the nitrates resulted in higher loadings then the chloride salts. The remainder of this chapter aims to understand why the nature of the metal as well as the nature of the precursor had an affect on the loading.

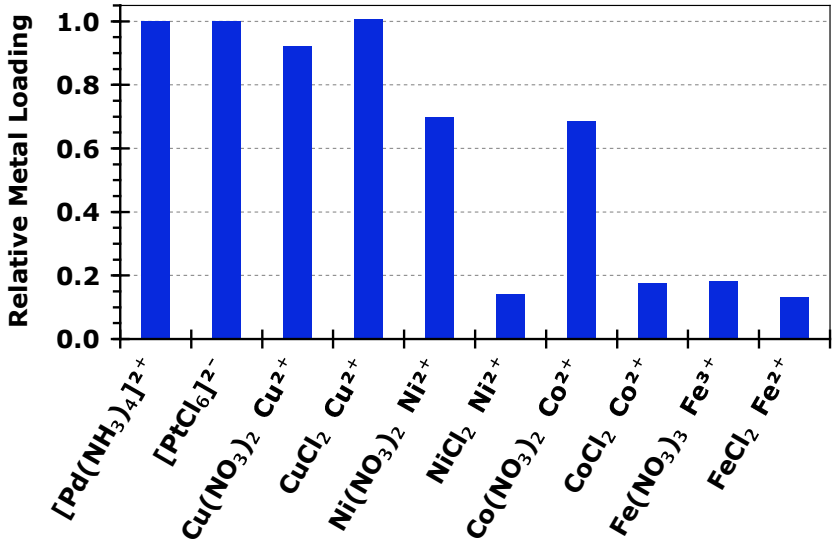


**Figure 2.4: The relative metal loading for several different metals and metal precursors on $Mo_2C$.**

### *3.2. Metal speciation in solution*

To understand how the precursor is interacting with the surface, it is important to understand the chemistry of the precursor in solution. It is possible,

depending on temperature and precursor concentration, that the nature of the precursor complex can change in solution. Of particular interest to this study is the difference between the speciation of the nitrate salts and the chloride salts, as there is a significant difference between the loading of these salts for the same metal, specifically the Ni and Co salts. The model described in section 2.3 was tested by comparing the calculated pH of the Cu, Ni, and Co precursor solutions to the measured pH of the same solution. Table 2.3 compares these results. The model fits the experimental data fairly well. The calculated pH values are within error of the experimental pH values.

**Table 2.3: The measured and predicted precursor solution pH values (T=25°C) using the model described in section 2.3.**

| Precursor | Solution pH | Predicted pH |
|---|---|---|
| $Cu(NO_3)_2$ | 5.1 ± 0.3 | 5.25 |
| $CuCl_2$ | 5.0 ± 0.3 | 5.25 |
| $Ni(NO_3)_2$ | 5.7 ± 0.3 | 5.92 |
| $NiCl_2$ | 5.9 ± 0.3 | 5.92 |
| $Co(NO_3)_2$ | 5.7 ± 0.3 | 5.91 |
| $CoCl_2$ | 6.2 ± 0.3 | 5.91 |

Figures 2.5 and 2.6 show the relative amounts of the Cu species formed from the speciation of $CuCl_2$ and $Cu(NO_3)_2$ as a function of initial precursor concentration. The conditions of the experiments performed above are marked by a vertical dotted line. Figure 2.5 illustrates that the mixture is dominated by the metal cation. If the initial concentration of the metal precursor is held below $10^{-3}$ mol/L, there is no significant amount of any metal chloride or metal hydroxide species. When the initial concentration is increased above $10^{-3}$ mol/L, the amount of the metal chloride complexes increases. As the concentration of precursor is increased and dissociates, the concentration of $[Cl]^-$ increases. As this occurs,

the equilibrium in equations 2.3 and 2.4 shift towards the reactants. Figure 2.6 shows the same trends for $Cu(NO_3)_2$.

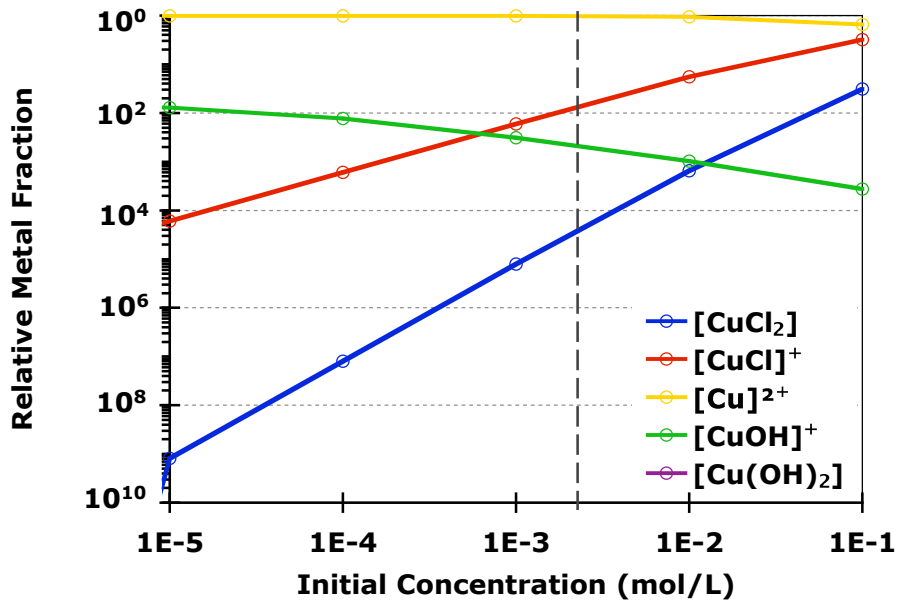


**Figure 2.5: Relative amounts of species produced from $CuCl_2$ solution as a function of initial metal concentration. The dotted line represents the conditions of the metal loading procedure.**

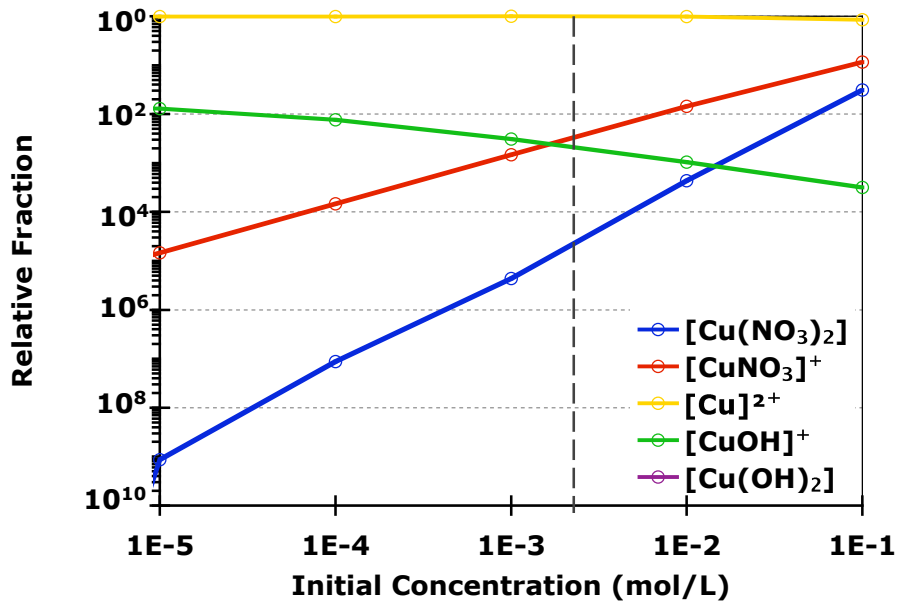


**Figure 2.6: Relative amounts of species produced from $Cu(NO_3)_2$ solution as a function of initial metal concentration. The dotted line represents the conditions of the metal loading procedure.**

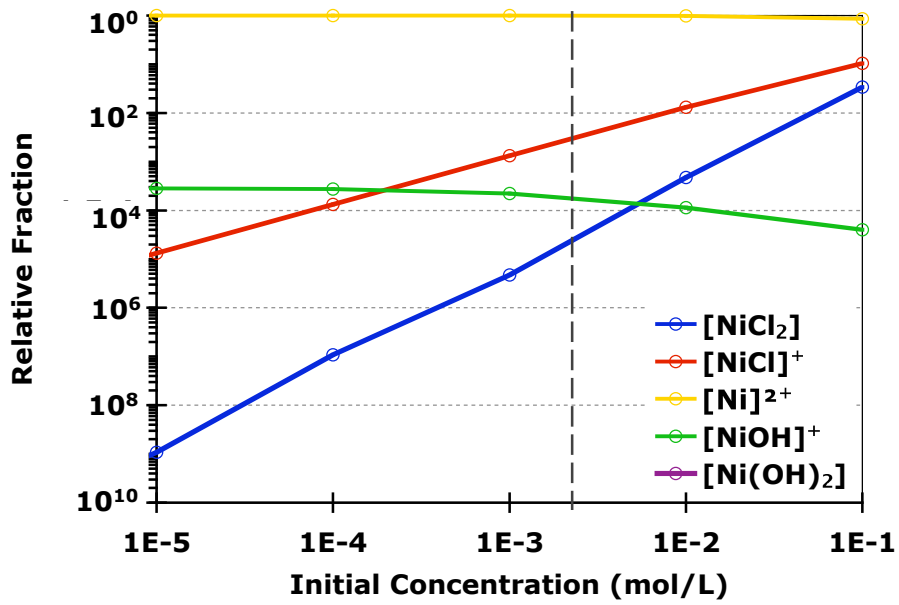


**Figure 2.7: Relative amounts of species produced from $NiCl_2$ solution as a function of initial metal concentration. The dotted line represents the conditions of the metal loading procedure.**

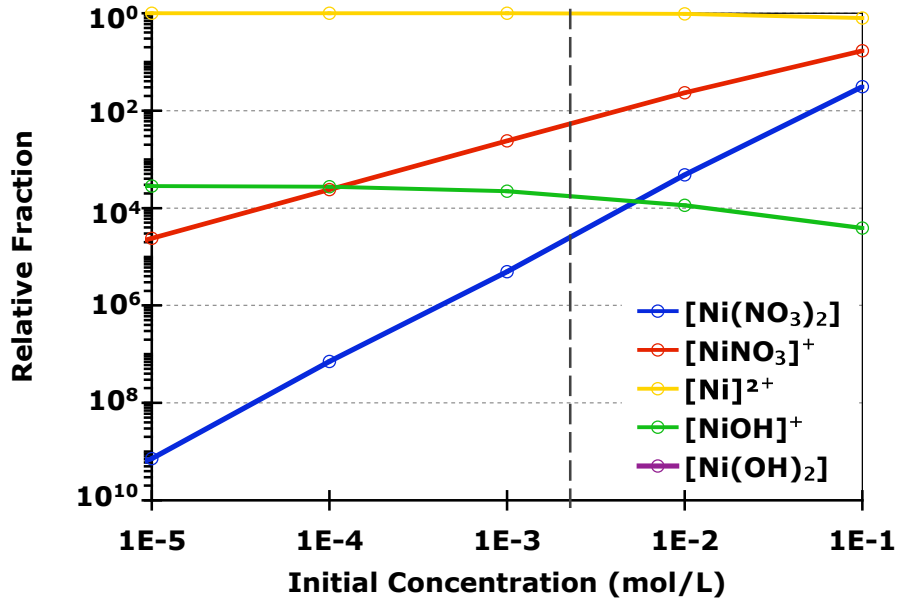


**Figure 2.8: Relative amounts of species produced from $Ni(NO_3)_2$ solution as a function of initial metal concentration. The dotted line represents the conditions of the metal loading procedure.**

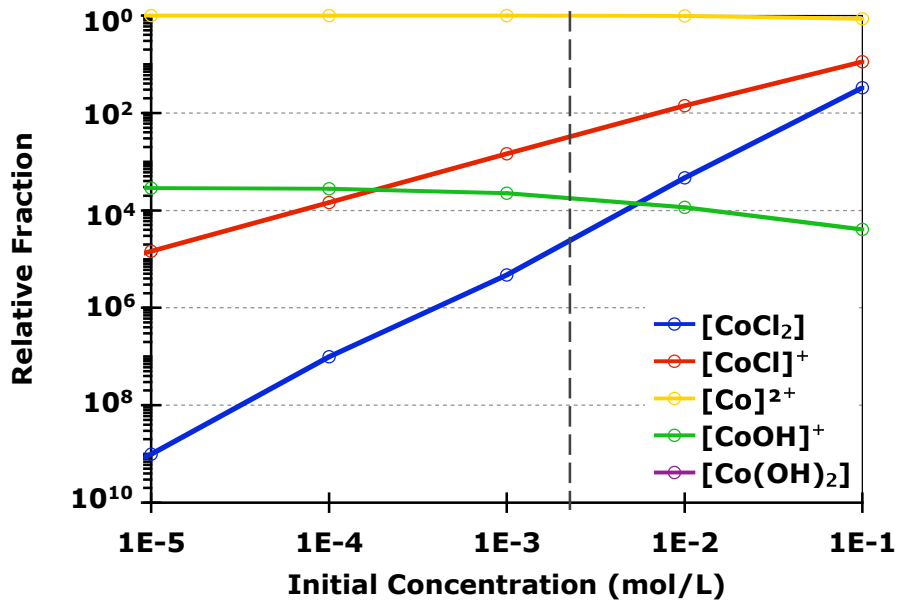


**Figure 2.9: Relative amounts of species produced from $CoCl_2$ solution as a function of initial metal concentration. The dotted line represents the conditions of the metal loading procedure.**

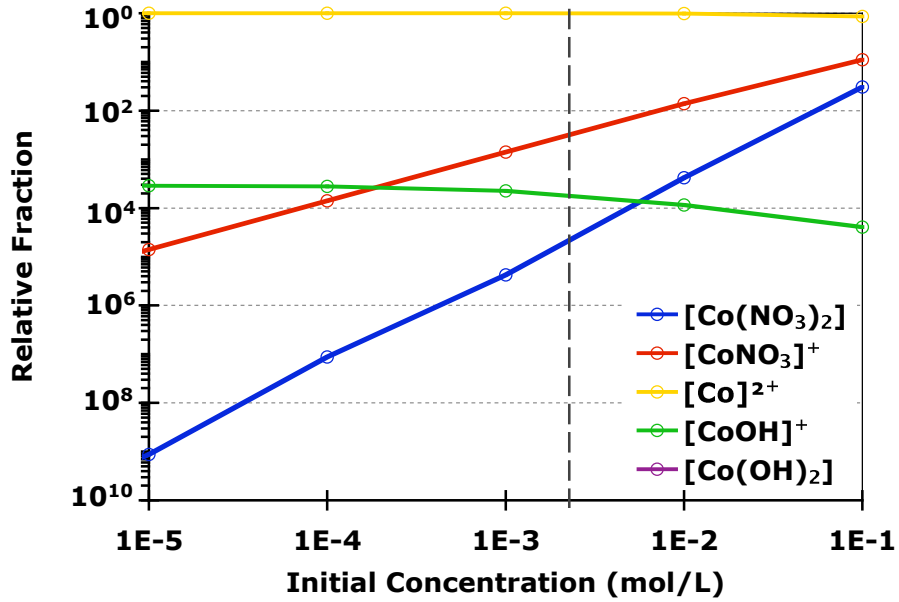


**Figure 2.10: Relative amounts of species produced from $Co(NO_3)_2$ solution as a function of initial metal concentration. The dotted line represents the conditions of the metal loading procedure.**

Figures 2.7 and 2.8 show the relative amounts of aqueous metal complexes as a function of initial $NiCl_2$ and $Ni(NO_3)_2$, and figures 2.9 and 2.10 and show that of $CoCl_2$ and $Co(NO_3)_2$, respectively. These graphs exhibit trends

similar to those for the Cu species. This analysis has demonstrated that, under the specific conditions of the reported metal loadings, the aqueous metal species can be treated primarily as cationic metal ions. This result will be important in assigning reduction potentials to the different precursors.

### *3.3. PZC measurements for $Mo_2C$*

Figure 2.11 displays the results of the PZC measurement for $Mo_2C$. The figure displays the final pH of $Mo_2C$ immersed in an aqueous solution as a function of initial pH. According to Park et al. [3], the PZC is represented by the flat portion of the curve. In the case of $Mo_2C$ shown below, this would correspond to ~5. Therefore, for the purpose of this study if electrostatic attraction contributed to the overall loading mechanism, then anions in solution below a pH of 4 and cations in a solution above a pH of 6 would likely benefit from the SEA mechanism.

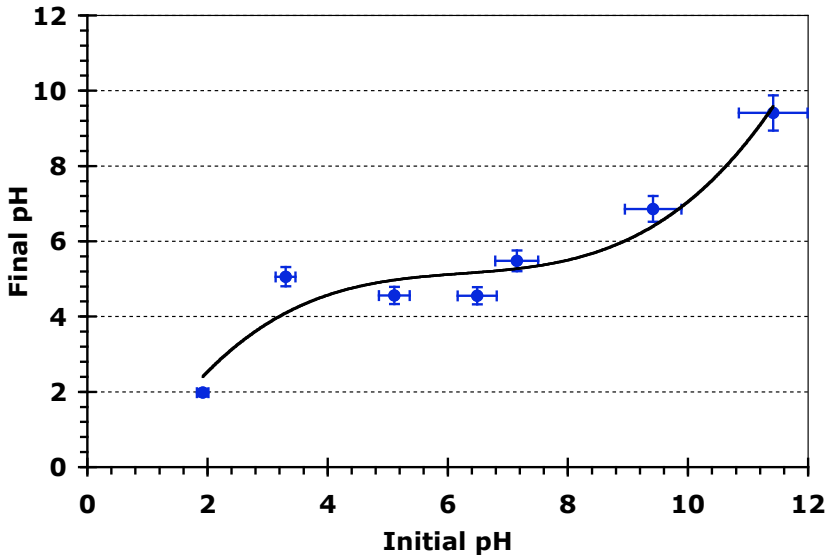


**Figure 2.11: PZC curve for $Mo_2C$. The PZC of $Mo_2C$ was determined to be ~5.**

### *3.4. XAS study of different metals loaded on $Mo_2C$*

The results of the x-ray absorption experiments for both “Dried” and “Reduced” $Pt/Mo_2C$ and $Pt/Al_2O_3$ samples are displayed in figures 2.12 and 2.13,

respectively. In each figure, the top graph displays the XANES results while the bottom graph compares the EXAFS results.

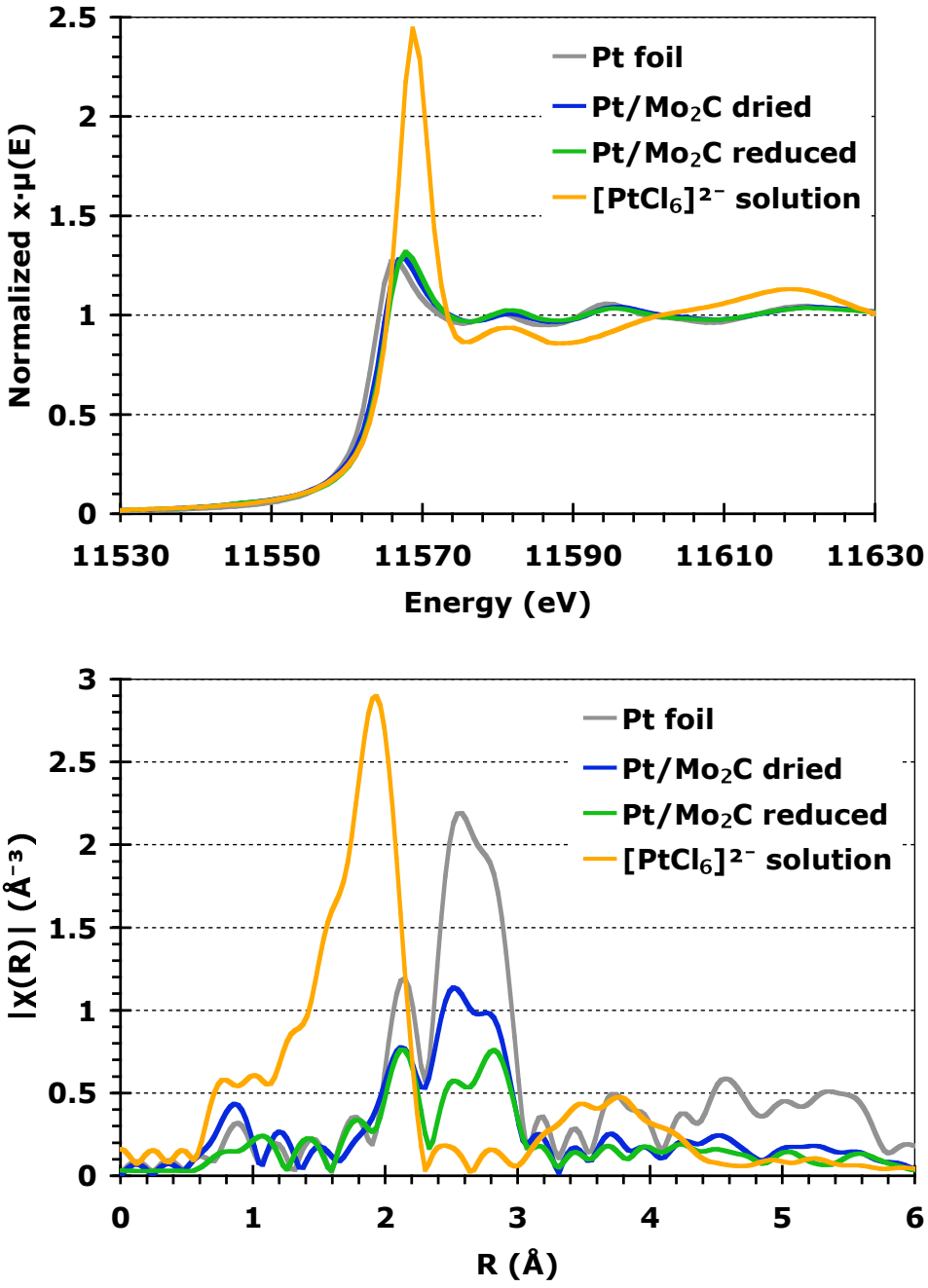


**Figure 2.12: XAS results comparing the XANES (top) and EXAFS (bottom) spectra for the "Dried" Pt/$Mo_2C$ (blue) and "Reduced" Pt/$Mo_2C$ (green) samples. Pt foil (grey) and the $[PtCl_6]^{2-}$ (orange) spectra are provided for reference.**

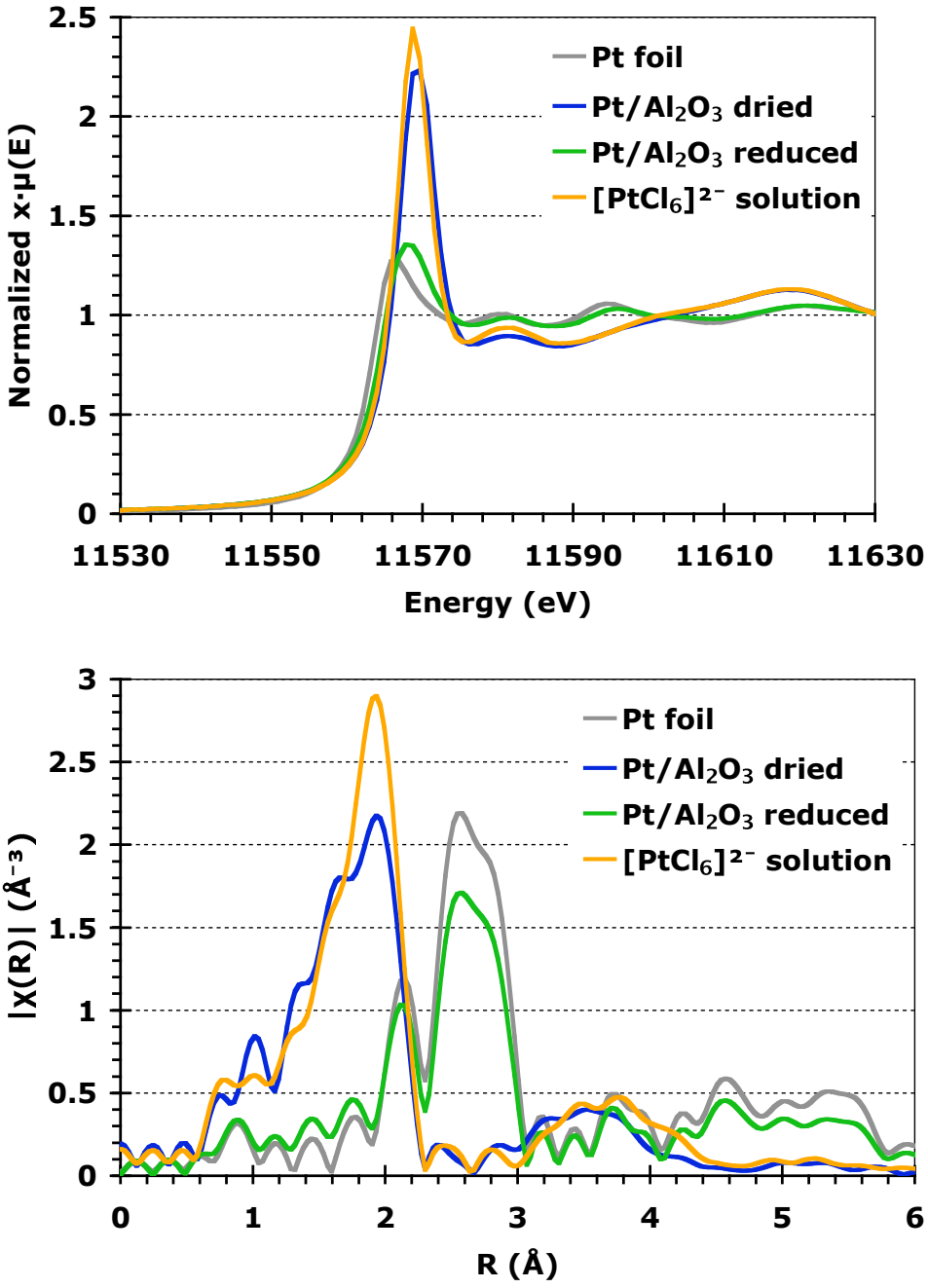


**Figure 2.13: XAS results comparing the XANES (top) and EXAFS (bottom) spectra for the "Dried" $Pt/Al_2O_3$ (blue) and "Reduced" $Pt/Al_2O_3$ (green) samples. Pt foil (grey) and the $[PtCl_6]^{2-}$ (orange) spectra are provided for reference.**

Figure 2.12 shows that in the case of Pt supported on $Mo_2C$, the Pt is reduced on both the "Dried" and "Reduced" samples. The initial peak of the XANES spectra of both samples in the top graph closely resemble the foil reference in both size and shape, and there is no peak corresponding to either

Pt-Cl or Pt-O coordination in the EXAFS spectra (R< 2 Å) in the bottom figure, such as in the $[PtCl_6]^{2-}$ spectra. The EXAFS spectra for both the "Dried" and "Reduced" samples closely resemble that of the Pt foil. However, there is a difference between the "Dried" and "Reduced" EXAFS spectra in that the size of the peak at ~2.5 Å decreases upon reduction relative to the peak at ~2.9 Å. This difference corresponds to a change in molybdenum coordination. The significance of this change will be discussed in detail in chapter 3.

The results for the $Pt/Al_2O_3$ catalyst (figure 2.13) are very different from the results for the $Pt/Mo_2C$ catalyst. The results for the "Reduced" $Pt/Al_2O_3$ closely resemble the Pt foil, but the results for the "Dried" sample resemble that of the $[PtCl_6]^{2-}$ solution. The XANES spectra shows a large white line while the EXAFS spectra indicates a significant Pt-Cl or Pt-O coordination. Since the same metal loading procedure was used for both the $Mo_2C$ and the $Al_2O_3$ catalysts, these results suggest that the $Mo_2C$ support reduces the $[PtCl_6]^{2-}$ precursor directly to zero-valent Pt metal.

Figures 2.14 - 2.17 show the XANES results for Pd, Cu, Ni, and Fe loaded samples, respectively. In figure 2.14, it can be seen that the "Dried" $Pd/Mo_2C$ spectra resembles that of the Pd foil, while the "Dried" $Pd/Al_2O_3$ resembles that of the oxidized Pd precursor solution. Likewise, in figure 2.15, both the "Dried" and the "Reduced" $Cu/Mo_2C$ samples resemble the Cu foil sample. Neither of the Cu samples were oxidized. On the other hand, in the case of the Ni and Fe catalysts shown in figures 2.16 and 2.17 respectively, the "Reduced" samples closely resemble the foil spectra while the "Dried" samples closely resemble the oxidized precursor solution spectra. In both cases, the "Dried" sample exhibits a large white line peak while the reduced samples do not have a peak. These results indicate that, like the Pt catalysts, $Mo_2C$ reduces both $[Pd(NH_3)_4]^{2+}$ and $Cu^{2+}$. However, $Mo_2C$ did not reduce either the $Ni^{2+}$ or $Fe^{2+}$ ions.

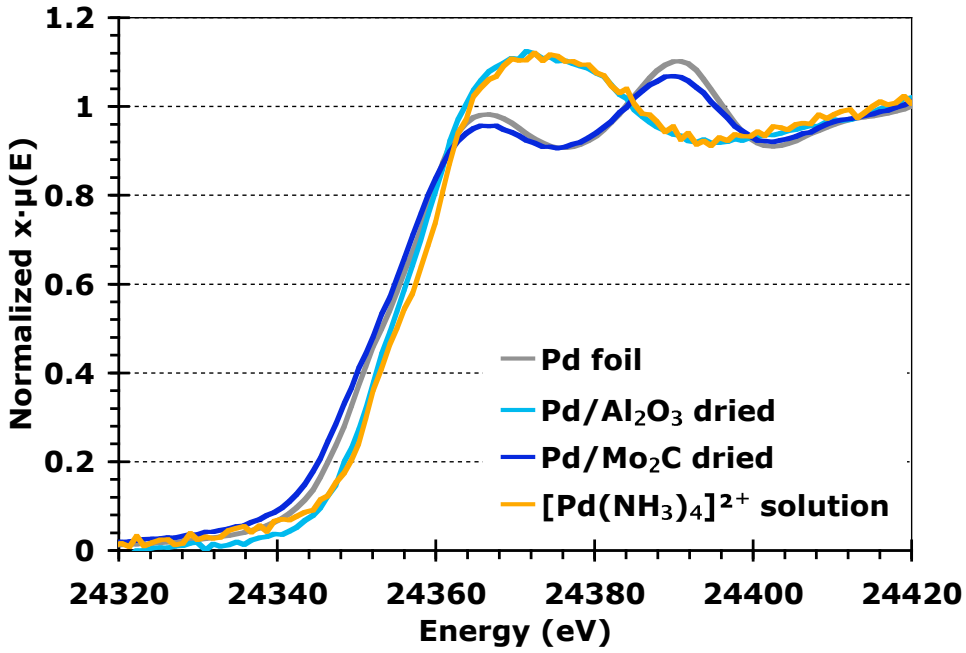


**Figure 2.14: XANES results comparing the spectra for the "Dried" $Pd/Al_2O_3$ (light blue) and "Dried" $Pd/Mo_2C$ (dark blue) samples. Pd foil (grey) and the $[Pd(NH_3)_4]^{2+}$ (orange) spectra are provided for reference.**

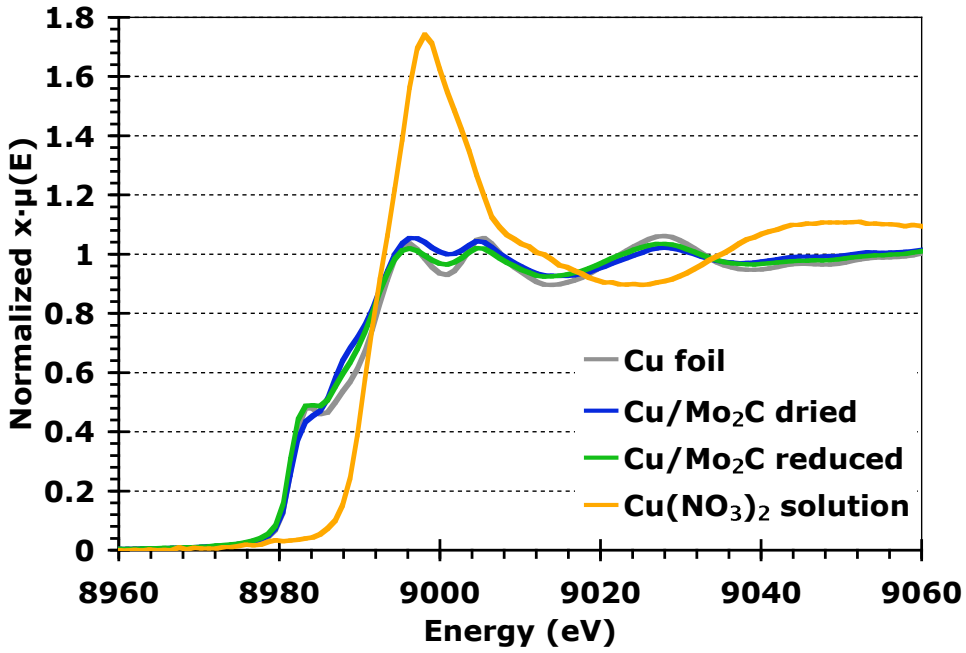


**Figure 2.15: XANES results comparing the spectra for the "Dried" $Cu/Mo_2C$ (blue) and "Reduced" $Cu/Mo_2C$ (green) samples. Cu foil (grey) and the $Cu(NO_3)_2$ (orange) spectra are provided for reference.**

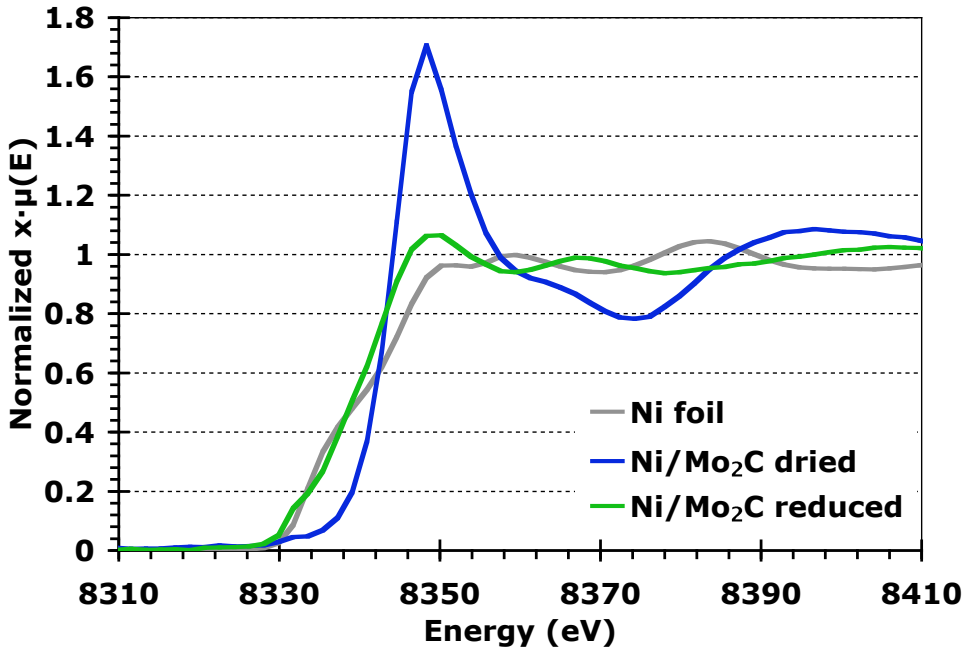


**Figure 2.16: XANES results comparing the spectra for the "Dried" Ni/$Mo_2C$ (blue) and "Reduced" Ni/$Mo_2C$ (green) samples. Ni foil (grey) is provided for reference.**

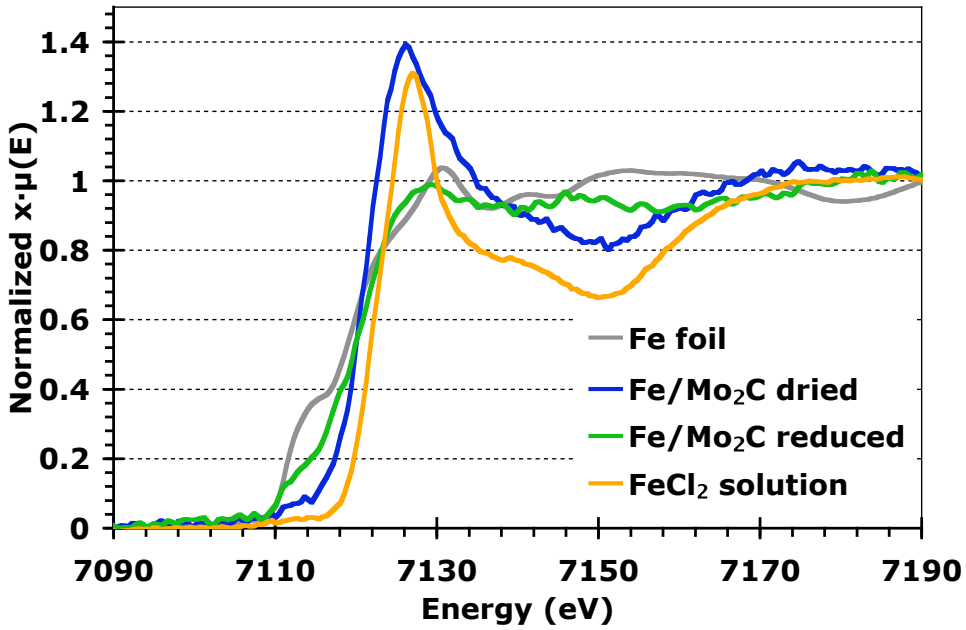


**Figure 2.17: XANES results comparing the spectra for the "Dried" Fe/$Mo_2C$ (blue) and "Reduced" Fe/$Mo_2C$ (green) samples. Fe foil (grey) and the $FeCl_2$ (orange) spectra are provided for reference.**

## 4. Discussion

If SEA plays a significant role in the loading of metals onto the $Mo_2C$ surface, then the relative loading of the metals should be a function of the impregnation solution pH. Our results show that the PZC for $Mo_2C$ is approximately at pH=5. Therefore, at pH>>5, the surface should be deprotonated with a negative charge, and electrostatically attract cations to the surface. For pH<<5, the surface should have a positive charge and attract anions. For the purpose of evaluating the applicability of the SEA mechanism for our catalysts, it is safe to assume that the pH of the loading solution should be outside the window of 4 < pH < 6. For this analysis, it is important to determine how adding $Mo_2C$ to the precursor deposition solution changes the pH of the solution (i.e. How will the pH of the solution containing $Mo_2C$ differ from the pH of the solutions reported in table 2.1?). Figure 2.11 shows that there is a window of 3 < pH < 7 in which adding $Mo_2C$ to the solution should return the initial solution pH to a final pH around the PZC. However, the width of this "window" depends on the powder surface area to liquid volume ratio [3]. In the PZC experiments, this ratio was ~5000 $m^2$/mL. In the actual loading experiments, this ratio was only ~1200 $m^2$/ mL. Since this value is smaller, the "window" should be smaller [3]. For the purpose of this study, it will be sufficient to assume the initial pH is approximately equal to the final pH of the solution.

Figure 2.18 shows the relative loading of different metals and precursors on the $Mo_2C$ surface as well as the pH of the impregnation solution. The "PZC window" of $Mo_2C$ is outlined by the red dotted lines. Any precursor species that lies outside of the window could be affected by SEA. In this study, the only species which could be affected are $H_2PtCl_6$, $Pd(NH_3)_4(NO_3)_2$, and $FeCl_3$. $H_2PtCl_6$ and $Pd(NH_3)_4(NO_3)_2$ would both benefit from the SEA process since the pH of the $H_2PtCl_6$ solution lies below the PZC of $Mo_2C$ and $H_2PtCl_6$ produce an anionic metal complex, and the pH of $Pd(NH_3)_4(NO_3)_2$ lies above the PZC of $Mo_2C$ and produces a cationic metal species. In both cases, electrostatics would attract the precursor to the surface. However, $FeCl_3$ would be hindered by SEA since its pH

is below the PZC of $Mo_2C$ but produces a metal cation (i.e. the surface would be positively charged and electrostatics would repel $Fe^{3+}$ adsorption). However, SEA is clearly not the major process involved in the metal loading mechanism since most of the precursors pH's lie within the PZC window of $Mo_2C$ but exhibit high relative loadings.

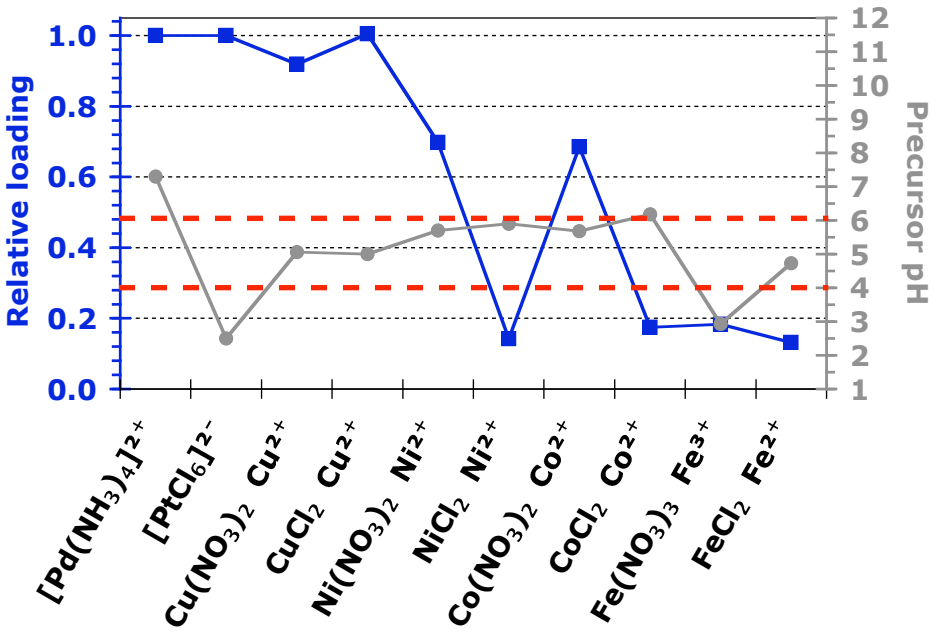


**Figure 2.18: Relative loading and impregnation pH as a function of metal precursor. Precursors with a pH outside of the PZC window (pH<4 or pH>6) may be affected by the SEA process.**

Figure 2.19 displays the relative loading of the metals on $Mo_2C$ as a function of the reduction potential of the metal complex ion. Generally, it can be seen that precursors which have high standard reduction potentials typically exhibit high relative loadings. For example, $[PtCl_6]^{2-}$, $[Pd(NH_3)_4]^{2+}$, and $Cu^{2+}$ all have standard reduction potentials greater than 0.3V, and all have very high relative loadings, close to 100%.

We hypothesize that the critical step in the loading mechanism is the reduction of the metal precursor complex by a surface species. It is unclear whether the oxidizing species is an Mo species, a C species, or some other unknown species. However, this hypothesis is supported by the XAS data. The

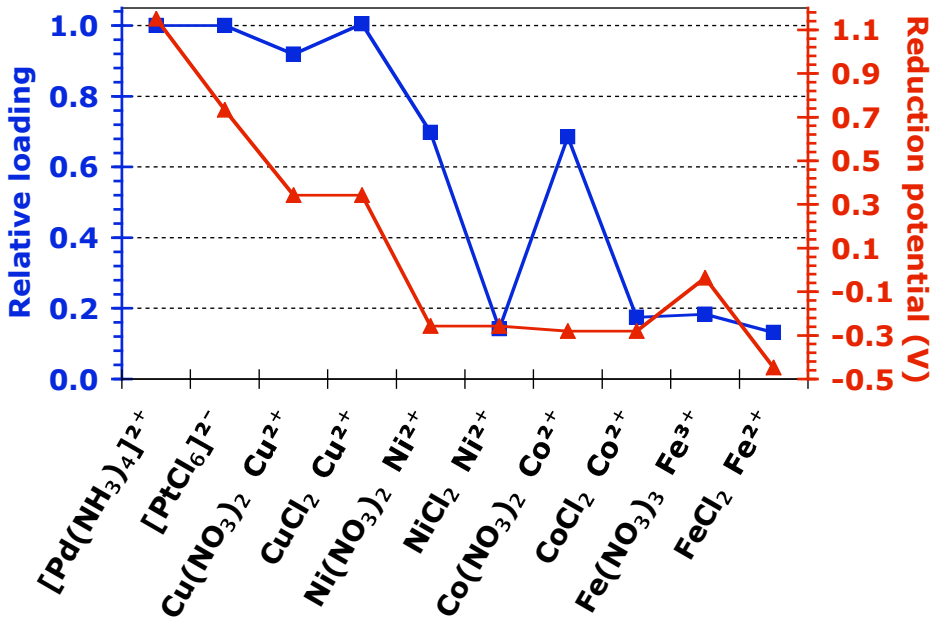


**Figure 2.19: Relative loading and ion reduction potential as a function of metal precursor.**

precursors of the "Dried" samples of the Pt, Pd, and Cu catalysts were shown to be zero valent while the "Dried" $Al_2O_3$ samples were shown to resemble the precursor solution. On the other hand, the "Dried" samples of the Ni and Fe catalysts were oxidized, also resembling the precursor solution. Therefore, if it is assumed that the reduction of the metal complexes is the important step, then based on the reduction potential of the Pt, Pd, and Cu precursors and e.q. 2.1, the reduction potential of the oxidizing species must be at least less than 0.3 V.

The nature of the counter ion also appears to play a role in the deposition mechanism. For example, in the case of the Ni and Co loading, the nitrate precursor obtained higher loadings than the chloride precursor. Since it was shown that the speciation of both the nitrate and chloride salts resulted in complete dissociation, then the loading of the metal should be independent of the counter ion. For this reason, we hypothesize that Cl anions poisoned the reduction sites on the $Mo_2C$ surface. Additionally, we hypothesize that the reduction potential of the oxidizing species is close to that of Ni and Co, ~-0.2 V. There are two consequence of this assumption. First, it is likely that the driving force for the reduction of the metals with high reduction potentials (i.e. Pt, Pd,

and Cu) is so great that it can overcome the blocking of reduction sites by Cl, whereas the metals with low reduction potential (i.e. Ni, Co, and Fe) cannot overcome this barrier. Second, if the reduction potential of the metal is very close to that of the oxidizing agent, then the overall driving force for the reaction is small, and thus the reaction will be kinetically hindered. If the driving force is large, the kinetic barrier will be very small. Thus, it is possible the relative loading of the Ni and Co nitrate salts could approach 100% if the time for these experiments was extended beyond 3 h.

Finally, we hypothesize that the SEA process is involved in the transport process of the metal ions from the solution to the surface. The proposed red-ox mechanism is then responsible for depositing the metal on the surface. If there is a favorable SEA effect under the conditions of the experiment, the two mechanisms work in series to deposit the metal on the surface. However, if the conditions of the experiment work against the SEA process, then it is again difficult to deposit metals on the surface. This point is evidenced from the Fe $(NO_3)_3$ data. The reduction potential of $Fe^{3+}$ is greater than that of $Ni^{2+}$ or $Co^{2+}$ and Cl anions are not present to poison the surface, thus one would expect the loading to be high. However, in this case, the pH of the solution is well below the PZC of $Mo_2C$. Thus, the $Mo_2C$ surface would have a positive charge. Therefore, it is proposed that diffusion of the $Fe^{3+}$ ions in solution to the surface would be hindered by the surface charge making the red-ox mechanism difficult.

## 5. Conclusions

We hypothesize that the mechanism for deposition of metals onto the carbide supports is dominated by the red-ox chemistry of the metal and the support. Further, the counter ion of the precursor metal salt affects the mechanism, as chlorine anions can poison the carbide surface. Generally, the ease of loading a metal onto a $Mo_2C$ support using the wet impregnation procedure described in this work can be predicted using three cooperative criteria.

First, metal precursor complexes with very high potentials (>0.3 V) yield loadings similar to the targeted loadings. The Pt, Pd, and Cu species in this study all exhibited high relative loadings. In this case, the strong interaction between the metal and the support was likely sufficient to overcome the poisoning of the surface by chloride ions. Second, if the reduction potential of the metal is low, higher loadings can be achieved using nitrate salts rather than chloride salts. This stems from the hypothesis that Cl anions poison the reducing sites on the surface. This hypothesis is supported by the results that nitrate salts of the Ni and Co precursor showed significantly higher loading than that of the chloride salts. Finally, SEA may only play a role in the transport process of the metal ion complexes to the metal surface. Satisfying SEA requirements is not necessary to obtain a high loading (as evidence in the Cu data), but unfavorable conditions may hinder the loading process. Evidence for this effect stems from the low loading of the $Fe(NO_3)_3$ precursor. This metal loading was less than the other nitrate salts even though the reduction potential is higher. The best explanation for this is that the solution pH is less than the PZC of $Mo_2C$, thus the $Mo_2C$ surface would have a positive charge and repel $Fe^{3+}$ ions.

The results of this study are far from exhaustive, and require much more work to verify the conclusions and hypothesis presented. In the short term, this work could include loading time studies, additional XAS work, and surface elemental analysis. Additional XAS experiments of the Ni and Co nitrate salts would confirm that the surface is capable of reducing these species as well. Additionally, time studies could be performed to verify if the loading of the Ni and Co nitrate precursors eventually does reach 100%. If these test are successful, then the likely conclusion would be that the reduction potential of the oxidizing species is very close to that of $Ni^{2+}$ and $Co^{2+}$. Thus the driving force for the reaction is small and the mechanism is kinetically hindered unlike the case in which the reduction potential is high, where the mechanism may not be kinetically hindered. The use of X-ray photoelectron spectroscopy would be a simple way to determine if chlorine ions poison the surface and prevent the

mechanism from proceeding for the metals with low reduction potentials. DFT calculations would also be performed to verify the energetic requirements associated with the blocking of sites by Cl for Ni reduction as opposed to Cu reduction.

An important detail from the analysis is the identity and reduction potential of the oxidizing species. As stated above, this species could be some complex Mo species, some C species, or some other unanticipated species that varies depending on the precursor in use or the solution pH. Identification of the species would require intricate chemical identification experiments. It could involve the use of ICP and UV-vis spectroscopy to identify the nature of species in the loading solution, as well as the use of Raman spectroscopy, Nuclear Magnetic Resonance (if the species is carbon based), and XAS to identify the coordination chemistry of the oxidizing species.

## 6. References


1. Jiao, L., and J.R. Regalbuto, *The Synthesis of Highly Dispersed Noble and Base Metals on Silica via Strong Electrostatic Adsorption: I. Amorphous Silica.* Journal of Catalysis, 2008. 260: p. 329–341
2. Brunelle, J.P., *Preparation of Catalysts by Metallic Complex Adsorption on Mineral Oxides.* Pure & Applied Chemistry, 1978. 50: p. 1211—1229.
3. Park, J. and J. Regalbuto, *A Simple, Accurate Determination of Oxide PZC and the Strong Buffering Effect of Oxide Surfaces at Incipient Wetness*. Journal of Colloid and Interface Science, 1995. 175: p. 239-252
4. Pinna, F., *Supported metal catalysts preparation.* Catalysis Today, 1998. 41: p. 129-137
5. Ertl, G., H. Knözinger, and J Weitkamp, *Preparation of Solid Catalysts*. Wiley-VCH, Inc. 1999
6. Lambert, J.F. and M. Che, *The Molecular Approach to Supported Catalysts Synthesis: State of the Art and Future Challenges.* Journal of Molecular Catalysis A: Chemical, 2000. 162: p. 5–18
7. Ferrando, R., J. Jellinek, and R.L. Johnston, *Nanoalloys: From Theory to Applications of Alloy Clusters and Nanoparticles.* Chemical Reviews, 2006. 108(3): p. 845- 910
8. Spieker, W.A., J. Liu, J.T. Miller, A.J. Kropf, J.R. Regalbuto, *An EXAFS Study of the Co-ordination Chemistry of Hydrogen Hexachloroplatinate(IV) 1. Speciation in Aqueous Solution*. Applied Catalysis A: General, 2002. 232: p. 219–235
9. Spieker, W.A., J. Liu, X. Hao, J.T. Miller, A.J. Kropf, J.R. Regalbuto, *An EXAFS Study of the Coordination Chemistry of Hydrogen Hexachloroplatinate(IV) 2. Speciation of Complexes Adsorbed onto Alumina*. Applied Catalysis A: General, 2003. 243: p. 53–66
10. King, T., *Carbide and Nitride Supported Water-Gas Shift Catalysts.* 2007, The University of Michigan
11. Wagman, D. D., *Selected Values of Chemical Thermodynamic Properties, vol. 3.* Institute for Materials Research, National Bureau of Standards; 1965
12. Ravel, B. and M. Newville, *ATHENA, ARTEMIS, HEPHAESTUS: Data Analysis for X-ray Absorption Spectroscopy using IFEFFIT***.** Journal of synchrotron Radiation, 2005. 12: p. 537-541

13. Newville, M., *Fundamentals of XAFS.* Consortium for Advanced Radiation Sources, University of Chicago, Chicago, IL. Revisions 2004.

## Chapter 3

## The effect of metal-support interactions on the size and shape of Pt particles supported on $Mo_2C$

### 1. Introduction

In chapter 2, the effects of loading conditions on the dispersion of supported metal catalysts using a wet impregnation procedure were discussed. It was mentioned that controlling these conditions is among the most direct ways to control the size and dispersion of the metal particles on a particular support. However, metal particles can be remarkably dynamic under the wide range of conditions catalysts are typically operated (high temperatures, highly reducing atmospheres, highly oxidizing atmospheres, etc.), and thus the physical characteristics of the particles can be significantly altered from those which were achieved through a particular synthesis method. For example, sintering (the agglomeration of metal particles, which results in a decrease of metal dispersion and increase in particle size) is a common phenomenon associated with industrial catalysts used over extended periods of time, and directly results in a change in the observed activities and selectivities of catalysts [1,2].

Metal-support interactions play a significant role not only on the dynamics of the metal under operating conditions (i.e. particle sintering), but also on the size and shape the metal particles. Figure 3.1 depicts three different configurations of a solid-solid-gas interface. In this figure, θ represents the contact angle between the two solid phases. This angle is related to the surface free energies of the interfaces by Young's equation [1]:

$$\gamma_{mg} \cdot \cos\theta = \gamma_{sg} - \gamma_{ms} \qquad \text{Eq. 3.1}$$

In Young's equation, γ is the surface free energy of the interface where *g* indicates the gas phase, *m* indicates the metal phase, and *s* indicates the support phase [1,3]. If $\gamma_{sg} > \gamma_{ms}$, then $\cos\theta > 0$ and $\theta < 90°$. This would result in the metal wetting the support surface or spreading into a thin film on the surface, as depicted in the middle and right frame in figure 3.1. However, if $\gamma_{sg} < \gamma_{ms}$, then $\cos\theta < 0$ and $\theta > 90°$. Therefore, the metal will form polyhedron particles with facets terminated in the appropriate surfaces which minimize the surface free energy of the particle (the Wulff construction of the particle [3]) [1,3].

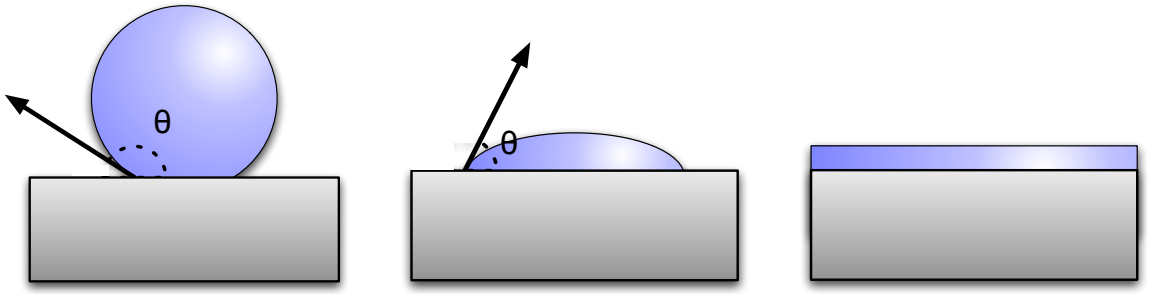


a) Non-wetting, θ > 90° b) Wetting, θ < 90° c) Spreading

**Figure 3.1: Depictions of metal particles on surface supports for different values of the metal-surface contact angle. Adapted from *Metal-Support Interactions in Catalysis, Sintering, and Redispersion* [1].**

A change in the particle shape results from an effort to minimize the free energy of the system. For example, if there is a strong interaction between the metal and the support (i.e. $\gamma_{ms}$ is very small), minimization of the free energy will drive the metal to wet the surface to maximize the metal-support contact or binding. On the other hand, if there is a weak or no interaction between the metal and the surface (i.e. $\gamma_{ms}$ is very large), the free energy of the system will be minimized by the formation of large particles where the metal-support interface is minimized. Young's equation nicely illustrates how a change in temperature (the free energies of the different interfaces are a function of temperature), nature of the gas phase (which will directly affect $\gamma_{sg}$), and the nature of the support (which will directly affect $\gamma_{ms}$) can influence the shape of metal particles. It is important to note that at low temperatures, particle transformation processes may not occur (or may take a long time) since there would be significant barriers to metal

diffusion on the support surface. However, when temperatures are sufficiently high, phenomenon such as wetting and sintering are possible.

In chapter 2, the results of the x-ray adsorption spectroscopy (XAS) experiments indicated that metal-support interactions may play a significant role in the structure of the Pt particles. Figure 3.2 shows the extended x-ray adsorption fine structure (EXAFS) results for the $Pt/Mo_2C$ catalysts discussed in chapter two. Briefly, two $Pt/Mo_2C$ samples were synthesized using a wet impregnation procedure. One of the samples was dried in 1% $O_2$/He after the loading procedure was completed while the other sample was dried at 110 °C for 2 h in $H_2$ and reduced at 450 °C for 4 h in $H_2$. These samples are referred to as "Dried" and "Reduced," respectively. The x-ray adsorption near edge structure (XANES) results (refer to chapter 2) indicated that both the catalysts were metallic. The arrows in figure 3.2 emphasize the difference between the EXAFS structure of the dried and reduced catalysts. As will be discussed further in this chapter, this difference is caused by an increase in Pt-Mo coordination and a decrease in Pt-Pt coordination. These results suggest a metal-support interaction may play a role in the final structure of the Pt particles.

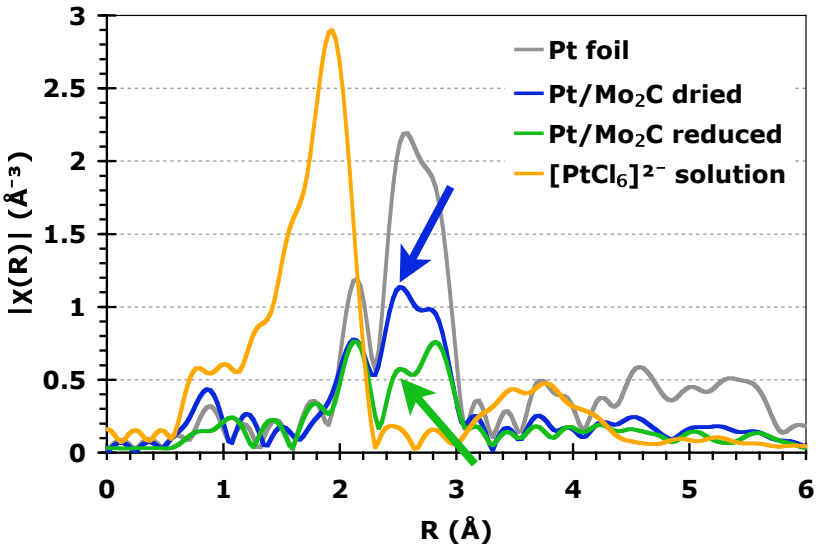


**Figure 3.2: EXAFS results for the "Dried" and "Reduced" $Pt/Mo_2C$ catalysts. The blue and green arrows indicate the change in the EXAFS structure that occurs with reduction.**

In this chapter, we will use several techniques to characterize the supported Pt particles: scanning electron microscopy (SEM), XAS, and density functional theory (DFT) calculations. This characterization will be performed for materials with a range of Pt loadings (from 0.5% to 12%), as establishing trends in the change of the characterization results will help us to understand the Pt growth mechanism and ultimately the Pt particles' shape and size. We will also observe trends in the water-gas shift (WGS) activity as a function of loading, as this will not only help us understand the shape and size of the particles, but also help us understand the location of the active site on the catalysts.

## 2. Experimental Procedures

### *2.1. Catalyst synthesis*

The catalysts in this section were synthesized using the same procedure described in chapter 2. Briefly, the $Mo_2C$ supports were synthesized by carburizing ammonia paramolybdate ($(NH_4)_6Mo_7O_{24}\cdot 4H_2O$; 81-83% as $MoO_3$; Alpha Æsar) using a 15% $CH_4/H_2$ mixture and a temperature programmed reduction method. The freshly synthesized material was transfered under Ar to a deaerated, aqueous solution containing the appropriate amount of $H_2PtCl_6$ salt to achieve the desired loading. For this study, 0.5%, 1,% 2%, 4%, 6%, 8%, and 12%wt $Pt/Mo_2C$ samples were synthesized. After the deposition was complete, the sample was dried at room temperature in $H_2$ and reduced in $H_2$ at 450 °C. Finally, the sample was passivated at room temperature using a 1% $O_2$/He gas mixture.

### *2.2. Elemental analysis and bulk characterization*

The procedures for ICP analysis of the catalysts compositions were described in Chapter 2. BET surface area analysis was performed using a single point procedure and a Micromeritics 2910 flow-through chemisorption instrument. The catalyst was first placed in a quartz u-tube reactor supported by quartz wool. The catalysts was then pretreated in 15% $CH_4/H_2$ at 590 °C for 4 h (this is the

same pretreatment used in the WGS reactor studies). Next, the gas flow was changed to UHP He, the temperature was maintained at 590 °C, and the sample was degassed for 15 min. After the sample had been degassed, the temperature was reduced to room temperature. The gas flow was changed to 30% $N_2$/He, and the sample was submerged in a liquid nitrogen bath. The amount of $N_2$ uptake was recorded using a TCD detector. Once uptake was complete, the liquid nitrogen bath was removed and replaced with a room temperature water bath. The amount of $N_2$ outgassing was measured with a TCD detector. This procedure was repeated twice. The total BET surface area was then calculated using the following formulas [5]:

$$V_{STP} = \frac{V_a}{m_{cat}} \left( \frac{273.15K}{273.15K + T_a} \right) \left( \frac{P_a}{760mmHg} \right) \quad \text{Eq. 3.2}$$

$$V_m = V_{STP} \left( 1 - \frac{P}{P_0} \right) \quad \text{Eq. 3.3}$$

$$SA = \frac{V_m N_{AVG} A_{N_2}}{L_{STP}} \quad \text{Eq. 3.4}$$

where $V$ is volume, $T$ is temperature, $P$ is pressure, $P_0$ is the saturation pressure of $N_2$, $m_{cat}$ is the mass of the catalysts analyzed, $N_{AVG}$ is Avogadro's number ($6.02 \times 10^{23}$ molecules/mol), $A_{N2}$ is the surface area of nitrogen molecule ($16.2 \times 10^{-2}$ m$^2$), $L_{STP}$ is the molar volume of an ideal gas at STP (22,414 mL/mol), and the subscripts 'a' and 'STP' refer to ambient conditions, and standard temperature and pressure conditions (0°C and 1 atm), respectively.

X-ray diffraction (XRD) analysis was performed using a Rigaku Miniflex DMAX-B rotating anode X-ray diffractometer with a Cu-Kα radiation source operated at 30 kV and 15 mA. Scans were conducted between 2θ of 20° and 80° at a rate of 2°/min and a resolution of 0.1°.

### *2.3. Scanning Electron Microscopy*

Initially, powder samples were secured to an SEM stub using copper tape. To minimize the amount of charging during SEM analysis, the samples were sputter coated with Au using an SPI sputter coater. The sample was degassed to below 10 mbar. The plasma current was adjusted to ~18 mA by adjusting the flow of Ar into the sputter chamber. The sample was sputtered using a Au target for 60-90 s. These conditions correspond to a Au thickness of 18.4-27.5 nm.

Scanning electron microscopy was performed using a Phillips XL30FEG SEM operated at between 15 keV and 25 keV and a spot size of 2-3. Elemental mapping was performed using X-ray Energy Dispersive Spectroscopy (XEDS) utilizing a UTW Si-Li Solid State X-ray Detector from EDAX. Mapping was conducted by detecting the Mo L and Pt M peaks. The resolution of the $Mo_2C$ maps were 10 nm/pixel.

### *2.4. X-ray Absorption Spectroscopy*

X-ray adsorption spectroscopy (XAS) studies were conducted at Argonne National Laboratory in fluorescence mode using the same procedures described in chapter 2. Briefly, the Pt L3 edge was recorded using fluorescence mode. Samples were packed into wafers supported in a steel sample tube. The tube contained a hole in the side, and the pellet was packed at a 45° angle such that fluorescent radiation could be detected from the side of the holder as the x-ray beam passed through the tube. The steel sample holder was then placed in a glass in-situ reactor which had a Kapton window on the side for fluorescence detection These samples were not stored in a glove box, and were handled in air. The samples were passivated (i.e. they were not pretreated) when they were analyzed. XAS results were analyzed using free online software Athena and Artemis [5] using standard analysis procedures [6].

## *2.5. Density Functional Theory Calculations*

Solid-state and molecular periodic DFT quantum mechanical calculations were performed using Dmol3 software with localized atomic basis sets. The ionic and electronic structures were described with semi-local pseudopotentials (DSPP) using the generalized gradient approximation with the Perdew-Wang non-local functional (GGA PW91) [7]. The calculations were performed using a cutoff of 4.4 Å. The β-Mo2C(100) surface was modeled as a 2x2 supercell with 8 atomic layers (4 layers of Mo and 4 layers of C, arranged in an alternating fashion) and 3x3x1 Monkhorst-Pack k-point sampling. The calculated lattice constants of the orthorhombic unit cell (a=4.73Å, b=6.17Å, c=5.34Å) are in good agreement with experimental values (a=4.72Å, b=6.00Å, c=5.19Å) [8].

Platinum (111) layers were added to the unit cell in a geometry that minimized the strain within the layers. The initial geometry of 1ML of Pt on $Mo_2C$ can be viewed in figure 3.3. The initial Pt-Pt bond distance of the Pt(111) layer was either 2.64Å, 2.86Å, or 2.95Å, as opposed to the bulk experimental value of 2.77Å or the predicted value of 2.83Å determined from DFT calculations.

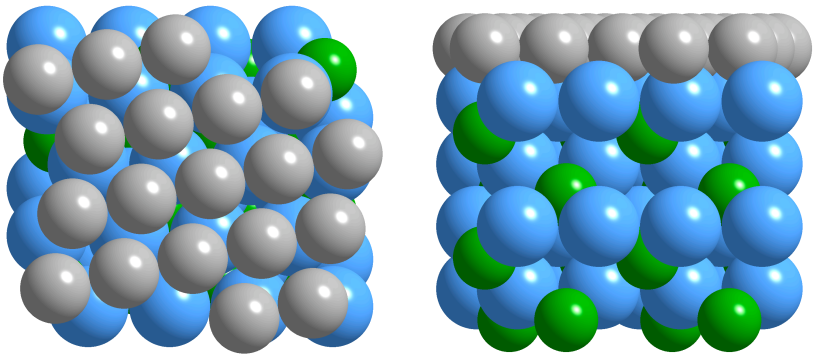

**Figure 3.3: A top view (left) and side view (right) of a unit cell of a 1 monolayer Pt(111)/ $Mo_2C$ structure. The geometry of the Pt(111) structure was set as to minimize the strain within the layer.**

In all calculations, the Pt atoms and the top four atomic layers of the $Mo_2C$ surface (2 layers of Mo and two layers of C) were allowed to relax and the atomic positions of the bottom two layers were fixed. The Pt binding energy for the entire

system of the Pt/$Mo_2C$ layer models were calculated according to the following formula:

$$E_{bind,Total} = (E_{Pt/Mo_2C} - E_{Mo_2C} - \frac{n}{12}E_{Pt_{bulk}})/n \qquad \text{Eq. 3.5}$$

where $E_i$ is the DFT energy of the respective model and $n$ is the number of Pt atoms in the Pt/$Mo_2C$ model. The Pt bulk calculation contained 12 atoms, hence in equation 3.5, the energy of the Pt bulk reference is multiplied by the ratio $^n/_{12}$ to account for the difference in the number of Pt atoms used in the calculations. The energy of individual layers were calculated using the following formula:

$$E_{bind,xPt} = (E_{xPt/Mo_2C} - E_{(x-1)Pt/Mo_2C} - \frac{n}{12}E_{Pt_{bulk}})/n \quad \text{Eq. 3.6}$$

In this equation, xPt/$Mo_2C$ represents the energy of the model with xML of Pt and (x-1)Pt/$Mo_2C$ represents the model with (x-1)ML of Pt. For these calculations, first the xML Pt/$Mo_2C$ structure was completely relaxed. Then, the xth layer of Pt was deleted from the model, and the energy of the unrelaxed, remaining structure was calculated. This was treated as the reference (x-1)ML Pt/$Mo_2C$ energy.

### *2.6. WGS Reaction Rates*

The steady state WGS activities for each catalyst were determined between 200 and 240 °C. Samples were loaded into a quartz u-tube reactor, supported with quartz wool. The mass of sample was adjusted among the different loadings to keep CO conversion below 10%. Typical sample amounts ranged from ~30 mg for $Mo_2C$ to as little as ~5 mg for the 12% Pt/$Mo_2C$ catalyst. The samples were diluted with low surface area $SiO_2$ such that the bed height (~0.25”) and volume were held approximately constant.

The catalysts were pretreated in flowing 15% $CH_4/H_2$ (100mL/min, Cryogenic Gases) at 590 °C for 4 h increased at 9.5 °C/min. Following the pretreatment, each sample was cooled to 240 °C and exposed to reformate

gases balanced in nitrogen (CO: 11%, $H_2O$: 21%, $H_2$: 43%, $CO_2$: 6%, $N_2$: 19%). Water was fed to the system using a high-performance liquid chromatography pump and mixed with the dry gas stream in a vaporizer maintained at 250 °C. The CO, $CO_2$, and $N_2$ concentrations of the effluent stream were analyzed using a SRI 8610C gas chromatograph with a single Carboxen 1000 column. Initial CO and $CO_2$ concentrations were measured directly by by-passing the reactor cell during catalyst pretreatment. Methanation is known to be a common side reaction associated with precious metal WGS catalysts [9], therefore CO conversions were calculated using both CO and $CO_2$ concentrations, as described in equations 3.7 and 3.8:

$$X_{CO} = \frac{A_{CO,in} - A_{CO,out}}{A_{CO,in}} \qquad \text{Eq. 3.7}$$

$$X_{CO} = \frac{A_{CO_2,in} - A_{CO_2,out}}{A_{CO,in}} \frac{C_{CO}}{C_{CO_2}} \qquad \text{Eq. 3.8}$$

where $A_i$ is the area under the peak in the chromatogram for the respective species and $C_i$ is the calibration constant for the respective species and has the units of $nmol^{-1}$. Using the calculated conversion, the forward reaction rate (normalized to the surface area of the catalysts) was calculated using the following equations:

$$r_+ = \frac{X_{CO} \cdot F_{o,CO}}{W_{cat} \cdot SA_{cat}} (1 - \beta) \qquad \text{Eq. 3.9}$$

$$\beta = \frac{[H_2][CO_2]}{[CO][H_2O]K_{eq}} \qquad \text{Eq. 3.10}$$

In these equations, $\beta$ is the extent of reaction and accounts for the approach to equilibrium in comparing the observed rates to the forward rates, $F_{o,CO}$ is the initial flow rate of CO, $W_{cat}$ is the weight of catalyst used, and $SA_{cat}$ is the measured BET surface area of the catalyst. In this analysis, since $[H_2]$ and $[H_2O]$

were not measured, they were calculated based on the measured CO conversion. All reported errors represent a 95% confidence limit.

## 3. Results

### *3.1. Bulk characterization results*

Figure 3.4 shows the ICP results plotting the nominal Pt loadings on $Mo_2C$ versus the measured loading. The data shows that the target loading is consistently met, even for loadings as high as 12%. Figure 3.5 shows the BET surface area of the catalysts as a function of Pt loading. All the catalysts exhibit a surface area in the range of 93-142$m^2$/g, however there is no apparent trend between Pt loading and measured BET surface area.

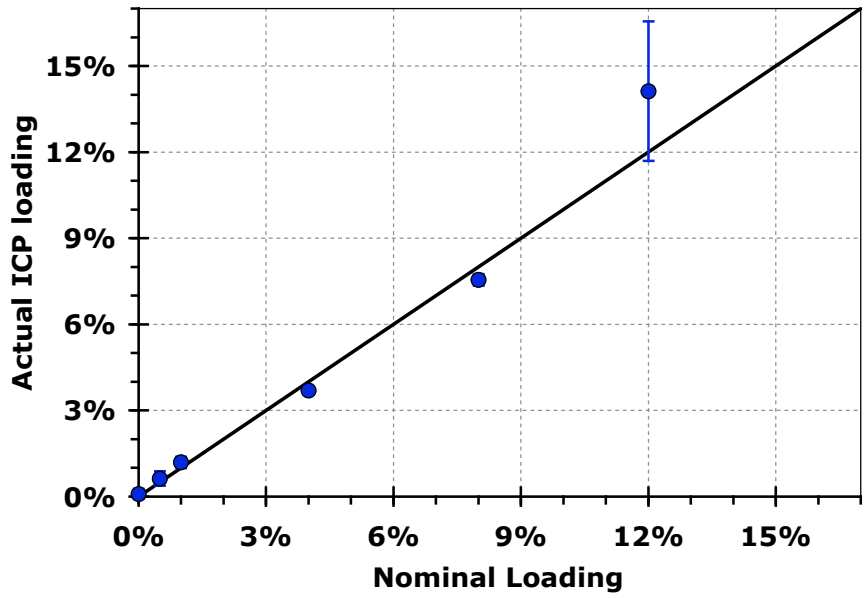


**Figure 3.4: Parity plot comparing the nominal loading and actual loading measured using ICP for several different Pt/$Mo_2C$ catalysts**

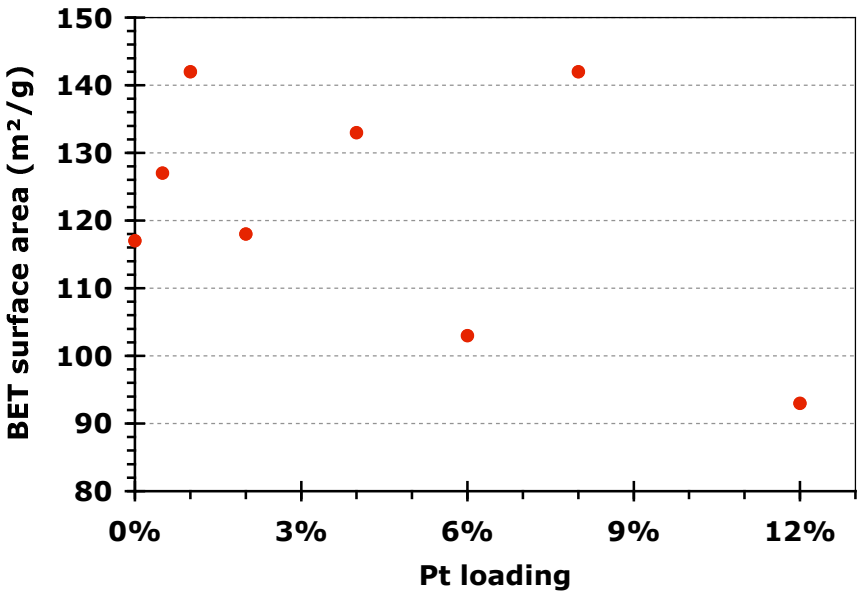


**Figure 3.5: BET surface area of the catalysts as a function of Pt loading.**

The x-ray diffraction patterns for several of the catalysts can be viewed in figure 3.6. The reference peaks for Pt metal are indicated by dashed grey lines. Diffraction patterns for catalysts with loadings below 8% Pt do not exhibit Pt peaks, however large Pt peaks are apparent for the 8% and 12% samples. For Pt particles to be below the detection limit of XRD, the Pt particles on $Mo_2C$ were likely small and well dispersed.

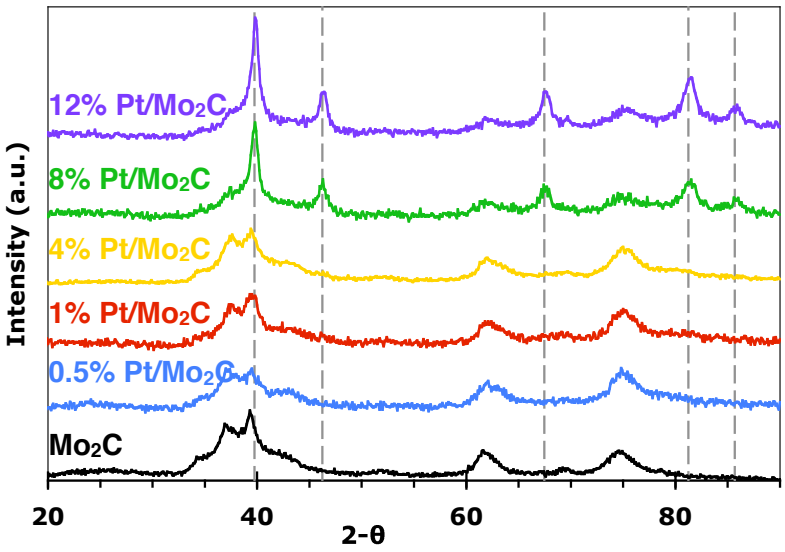


**Figure 3.6: XRD pattern of the $Mo_2C$ (black), 0.5% Pt/$Mo_2C$ (blue), 1% Pt/$Mo_2C$ (red), 4% Pt/$Mo_2C$ (yellow), 8% Pt/$Mo_2C$, and 12% Pt/$Mo_2C$ catalysts. The reference peaks for Pt are indicated by vertical, Grey, dashed lines.**

### *3.2. SEM/EDX*

Figures 3.7 through 3.9 display SEM micrographs of $Mo_2C$ and Pt/$Mo_2C$ catalysts. Figure 3.7 shows a $Mo_2C$ surface. These micrographs depict two features that are typically observed on the $Mo_2C$ particle surface: 1) Large crevasses dividing the surface into large strips. Presumably, these large cavities contribute to the high surface area of the support. 2) Relatively large, irregular, bright white particles. It is assumed that these are small, $Mo_2C$ fragments that result from the handling of the support. $Mo_2C$ is a very hard material, however the highly porous support particles are quite brittle and are easily crushed.

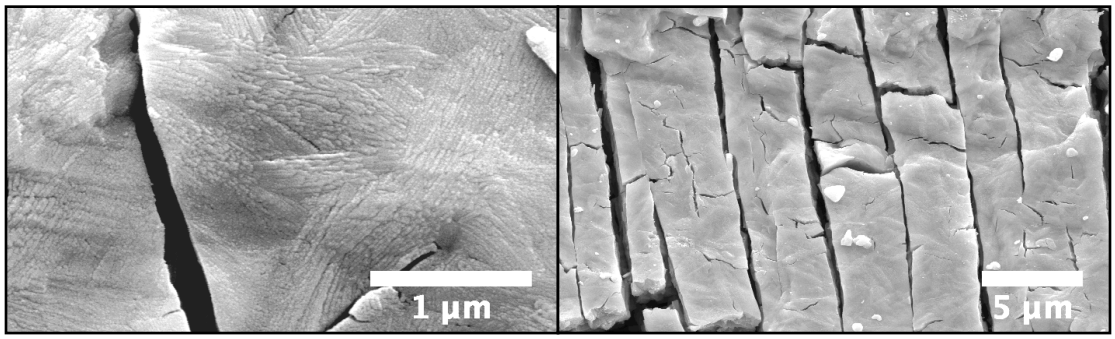


**Figure 3.7: SEM micrographs of a clean, $Mo_2C$ surface.**

Figure 3.8 shows micrographs of the surfaces of the 4% Pt/$Mo_2C$ and 8% Pt/$Mo_2C$ catalysts. In the left frame it is observed that small particles cover the entire surface of the 4% Pt/$Mo_2C$ catalyst. The particles are fairly uniform and well dispersed. The average size of the particles (determined by averaging over 100 different particles) is 27±0.2 nm. The right frame shows the surface of an 8% Pt/$Mo_2C$ catalyst. This surface looks similar to the 4% sample, however, the particles have agglomerated into patches with large cavities, in which the $Mo_2C$ surface can be observed, open between them. The pattern resembles tears in a stretched surface.

It should be noted that the Pt distribution on the $Mo_2C$ particles is not consistent from particle to particle. Particles tend to either have a large amount of highly dispersed Pt or no Pt at all. However, the distribution of Pt on a single particle is very uniform. The reason for this phenomenon is not known. One

explanation could be that the loading mechanism discussed in chapter 2 requires some sort of seeding or nucleation site that is not present on every particle.

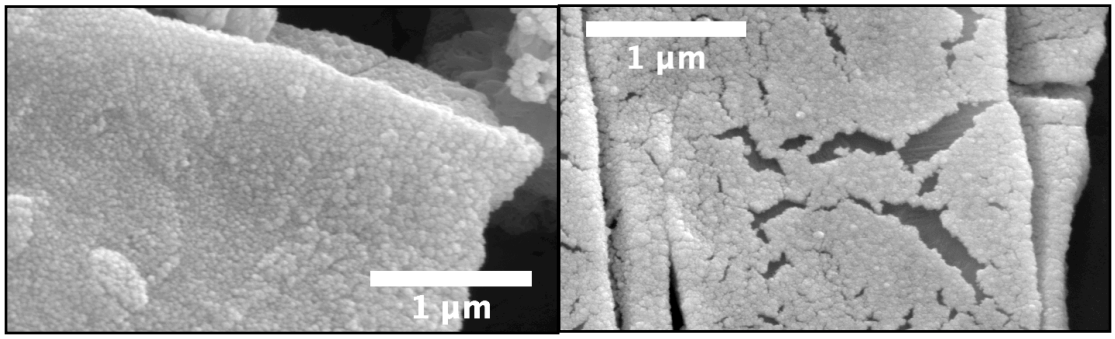


**Figure 3.8: SEM micrographs of a 4%Pt/$Mo_2C$ (left) and 8% Pt/$Mo_2C$ surface (right)**

Figure 3.9 displays an SEM micrograph and EDAX elemental map for the 8% Pt/$Mo_2C$ surface. The middle frame shows where Mo is present on the surface, and the right frame shows where Pt is present on the surface. Note that the gaps between patches of Pt particles are observed in the Pt map. The gaps are not apparent in the Mo map. These images confirm that Pt is dispersed across the entire surface and is not represented by the large, white particles that were also observed on the clean $Mo_2C$ surface. It also confirms that the large crevasses between the Pt patches are, to some extent, deficient of Pt.

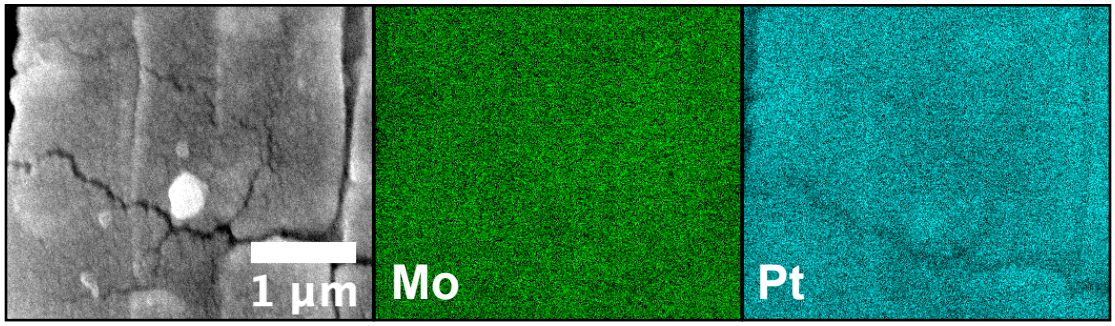


**Figure 3.9: SEM micrograph and EDAX elemental mapping of an 8% Pt/Mo2C surface. The middle frame displays Mo and the right frame displays Pt.**

### *3.3. X-ray absorption spectroscopy*

Figure 3.10 shows the XANES spectra for each of the Pt catalysts. All the spectra are identical and indicate that the Pt is metallic.

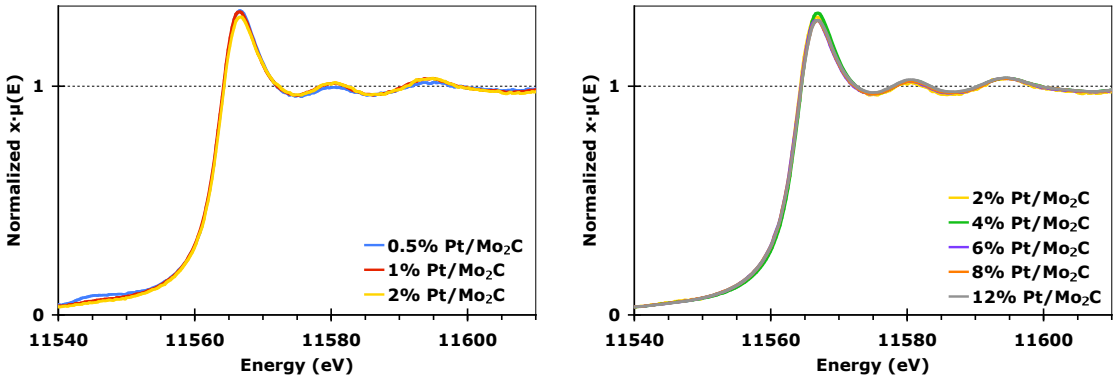


**Figure 3.10: Normalized XANES spectra of the 0.5% Pt/$Mo_2C$ (Blue), 1% Pt/$Mo_2C$ (Red), 2% Pt/$Mo_2C$ (Yellow), 4% Pt/$Mo_2C$ (Green), 6% Pt/$Mo_2C$ (Purple), 8% Pt/$Mo_2C$ (Orange), 12% Pt/$Mo_2C$ (Grey) catalysts**

Figures 3.11-3.17 shows the EXAFS spectra in k-space and R-space for each of the catalysts. The R-space data was calculated using the k-space data between ~2.5 $Å^{-1}$ and ~14 $Å^{-1}$. The EXAFS patterns of the catalysts with high loadings of Pt (≥ 2%) are all qualitatively very similar. They only differ in the magnitude of the R-space spectra. However, as the weight loading decreases below 2%, the EXAFS pattern begins to shift. The peak just below 3Å decreases in magnitude and the peak at about 2Å increases. This shift will be discussed in more detail below.

All the spectra were fit using theoretical, nearest neighbor Pt-Pt and Pt-Mo scattering amplitudes and phase shift functions calculated using FEFF [5], also presented in figures 3.11-3.17. The fits were generated using k, $k^2$, and $k^3$ weights and by setting the spectral shift ($E_o$) of each path to the same value. The fit parameters for all the catalysts are displayed in table 3.1. To demonstrate the robustness of the fits, they were also generated by allowing the spectral shift of the paths to differ. These results are displayed in table 3.2 and are very close to the results presented in figure 3.1. The fits replicate the peaks in R-space between 2 Å and 3 Å fairly well for all the catalysts, the region in which first metal nearest neighbor scattering is most significant.

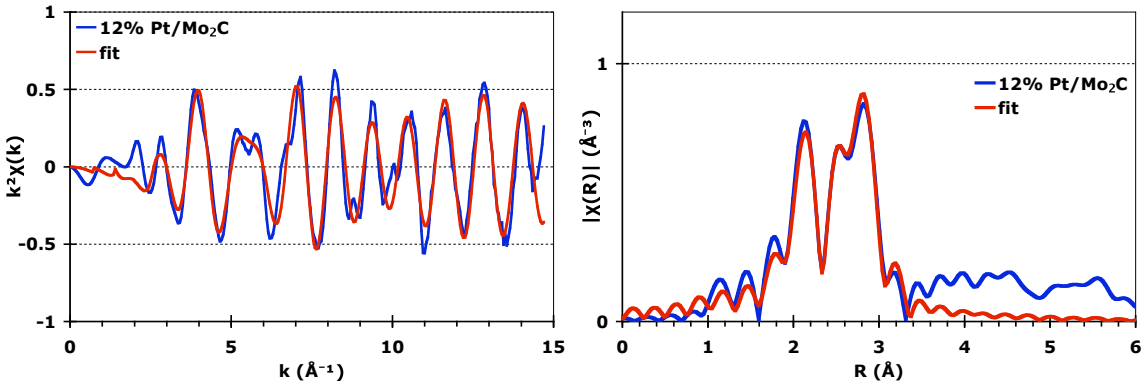


**Figure 3.11: EXAFS spectra (Blue) and the best fit (Red) for the 12% Pt/$Mo_2C$ catalyst presented in k-space (left) and R-space (right).**

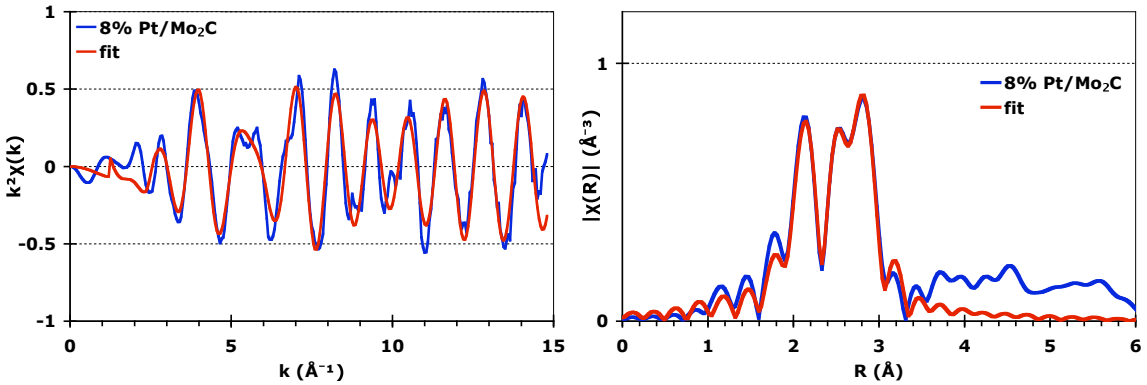


**Figure 3.12: EXAFS spectra (Blue) and the best fit (Red) for the 8% Pt/$Mo_2C$ catalyst presented in k-space (left) and R-space (right).**

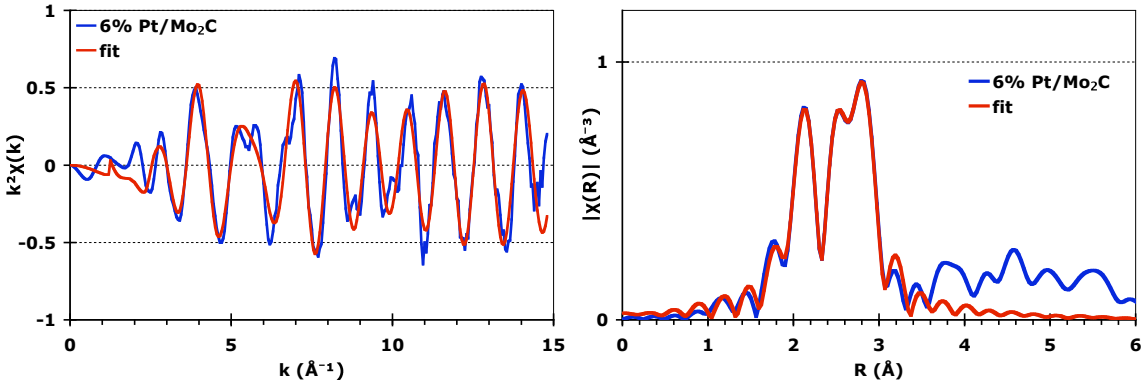


**Figure 3.13: EXAFS spectra (Blue) and the best fit (Red) for the 6% Pt/$Mo_2C$ catalyst presented in k-space (left) and R-space (right).**

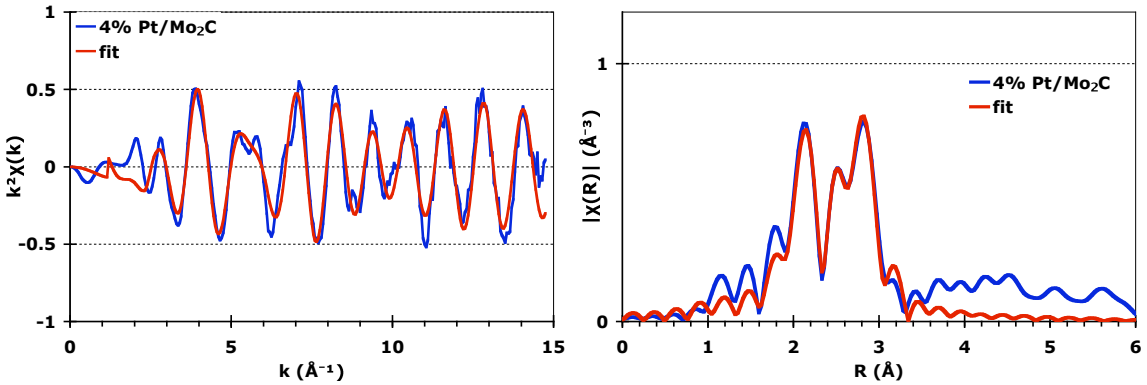


**Figure 3.14: EXAFS spectra (Blue) and the best fit (Red) for the 4% Pt/$Mo_2C$ catalyst presented in k-space (left) and R-space (right).**

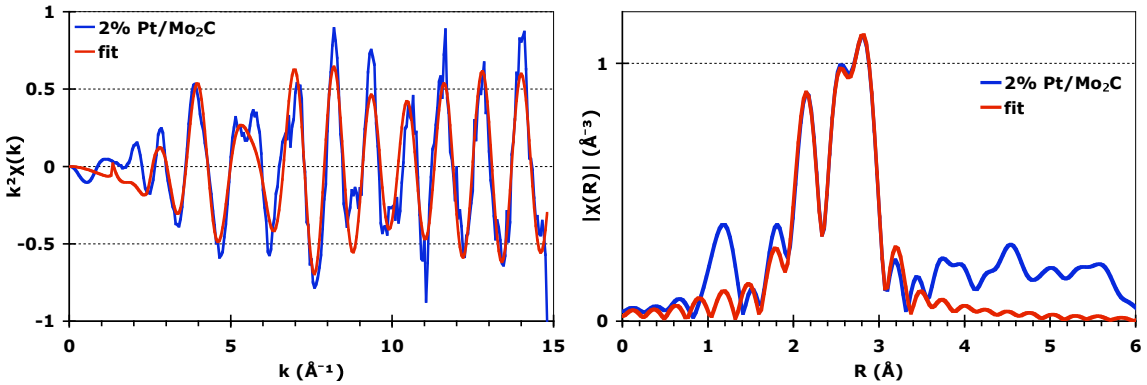


**Figure 3.15: EXAFS spectra (Blue) and the best fit (Red) for the 2% Pt/$Mo_2C$ catalyst presented in k-space (left) and R-space (right).**

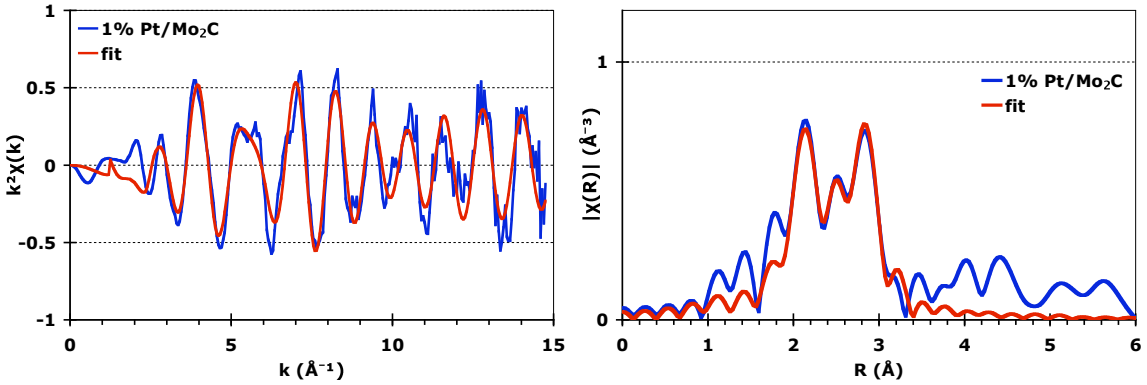


**Figure 3.16: EXAFS spectra (Blue) and the best fit (Red) for the 1% Pt/$Mo_2C$ catalyst presented in k-space (left) and R-space (right).**

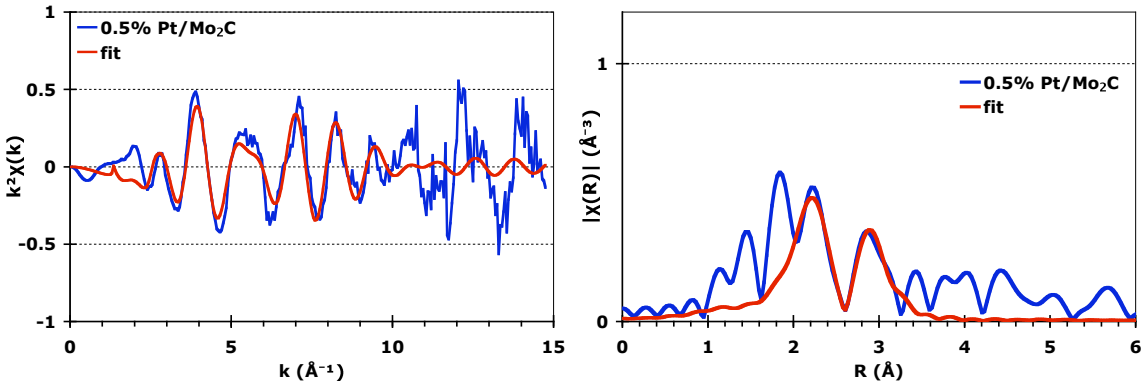


**Figure 3.17: EXAFS spectra (Blue) and the best fit (Red) for the 0.5% Pt/$Mo_2C$ catalyst presented in k-space (left) and R-space (right).**

**Table 3.1: EXAFS fit parameters. $S_o^2$ (the overall amplitude factor) was 0.75 for all fits. N is the average coordination of the scattering atom, R is the bond distance of the scattering path, and $\sigma^2$ is the Debye-Waller factor. $E_o$ (the energy shift) was set equal for both paths.**

| Catalyst | Path | N | R (Å) | $E_o$ (eV) | $\sigma^2$ |
|---|---|---|---|---|---|
| 12% Pt/$Mo_2C$ | Pt-Pt | 7.0 ± 1.1 | 2.76 ± 0.01 | 6.2 ± 1.1 | 0.005 ± 0.001 |
| | Pt-Mo | 1.7 ± 1.2 | 2.74 ± 0.03 | | 0.006 ± 0.005 |
| 8% Pt/$Mo_2C$ | Pt-Pt | 7.6 ± 0.7 | 2.75 ± 0.01 | 5.8 ± 0.7 | 0.006 ± 0.001 |
| | Pt-Mo | 1.2 ± 0.6 | 2.73 ± 0.02 | | 0.004 ± 0.003 |
| 6% Pt/$Mo_2C$ | Pt-Pt | 8.2 ± 0.4 | 2.76 ± 0.01 | 5.6 ± 0.4 | 0.006 ± 0.001 |
| | Pt-Mo | 1.1 ± 0.4 | 2.72 ± 0.01 | | 0.004 ± 0.002 |
| 4% Pt/$Mo_2C$ | Pt-Pt | 7.4 ± 0.9 | 2.75 ± 0.01 | 5.4 ± 0.8 | 0.006 ± 0.001 |
| | Pt-Mo | 1.6 ± 0.9 | 2.73 ± 0.02 | | 0.005 ± 0.003 |
| 2% Pt/$Mo_2C$ | Pt-Pt | 8.3 ± 0.7 | 2.77 ± 0.01 | 6.6 ± 0.6 | 0.005 ± 0.001 |
| | Pt-Mo | 1.3 ± 0.7 | 2.76 ± 0.02 | | 0.005 ± 0.004 |
| 1% Pt/$Mo_2C$ | Pt-Pt | 8.3 ± 1.1 | 2.76 ± 0.01 | 5.7 ± 1.0 | 0.007 ± 0.001 |
| | Pt-Mo | 1.3 ± 1.0 | 2.74 ± 0.03 | | 0.004 ± 0.004 |
| 0.5% Pt/$Mo_2C$ | Pt-Pt | 6.8 ± 2.0 | 2.78 ± 0.03 | 6.5 ± 2.1 | 0.010 ± 0.003 |
| | Pt-Mo | 1.5 ± 1.4 | 2.78 ± 0.04 | | 0.006 ± 0.005 |

**Table 3.2: EXAFS fit parameters. $S_o^2$ (the overall amplitude factor) was 0.75 for all fits. N is the average coordination of the scattering atom, R is the bond distance of the scattering path, $E_o$ is the energy shift, and $\sigma^2$ is the Debye-Waller factor.**

| Catalyst | Path | N | R (Å) | $E_o$ (eV) | $\sigma^2$ |
|---|---|---|---|---|---|
| 12% Pt/$Mo_2C$ | Pt-Pt | 7.6 ± 0.7 | 2.76 ± 0.01 | 7.0 ± 0.7 | 0.006 ± 0.001 |
| | Pt-Mo | 2.0 ± 0.6 | 2.72 ± 0.01 | 2.0 ± 2.3 | 0.007 ± 0.002 |
| 8% Pt/$Mo_2C$ | Pt-Pt | 8.0 ± 0.3 | 2.76 ± 0.01 | 6.4 ± 0.3 | 0.006 ± 0.001 |
| | Pt-Mo | 1.4 ± 0.3 | 2.74 ± 0.01 | 2.6 ± 1.5 | 0.005 ± 0.001 |
| 6% Pt/$Mo_2C$ | Pt-Pt | 8.2 ± 0.2 | 2.76 ± 0.01 | 6.1 ± 0.2 | 0.006 ± 0.001 |
| | Pt-Mo | 1.5 ± 0.2 | 2.72 ± 0.01 | 3.8 ± 1.2 | 0.006 ± 0.001 |
| 4% Pt/$Mo_2C$ | Pt-Pt | 8.1 ± 0.5 | 2.75 ± 0.01 | 5.8 ± 0.5 | 0.007 ± 0.001 |
| | Pt-Mo | 1.4 ± 0.4 | 2.71 ± 0.01 | 1.9 ± 2.0 | 0.005 ± 0.001 |
| 2% Pt/$Mo_2C$ | Pt-Pt | 8.7 ± 0.5 | 2.77 ± 0.01 | 6.8 ± 0.4 | 0.005 ± 0.001 |
| | Pt-Mo | 1.3 ± 0.4 | 2.75 ± 0.01 | 4.2 ± 2.0 | 0.006 ± 0.002 |
| 1% Pt/$Mo_2C$ | Pt-Pt | 8.4 ± 0.7 | 2.76 ± 0.01 | 6.3 ± 0.6 | 0.007 ± 0.001 |
| | Pt-Mo | 1.7 ± 0.5 | 2.74 ± 0.01 | 4.5 ± 2.1 | 0.006 ± 0.002 |
| 0.5% Pt/$Mo_2C$ | Pt-Pt | 6.8 ± 1.6 | 2.77 ± 0.01 | 3.3 ± 1.6 | 0.008 ± 0.002 |
| | Pt-Mo | 2.5 ± 1.0 | 2.82 ± 0.02 | 16.2 ± 2.8 | 0.006 ± 0.002 |

A remarkable result is that the Pt-Pt and Pt-Mo coordination numbers are similar for all the high loadings. This trend is depicted in figure 3.18 where the coordination numbers obtained from the fits in table 3.1 are displayed as a function of Pt loading. The Pt-Pt coordination is approximately 8, while the Pt-Mo coordination is approximately 1.4. As will be discussed in section 4, these results will lead to important conclusions about the structure of the Pt particles.

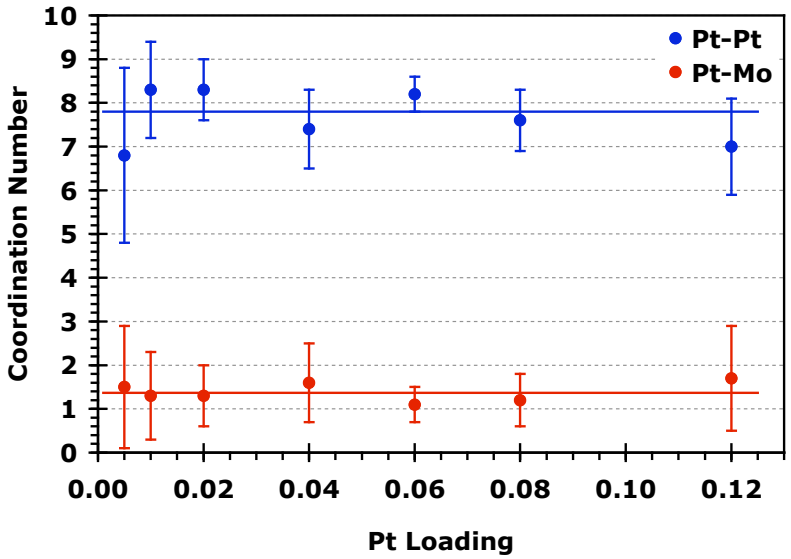


**Figure 3.18: Coordination number for the Pt-Pt and Pt-Mo scattering paths as a function of Pt loading. Coordination numbers were obtained from the EXAFS fit.**

It is important to discuss the structure of the low loading materials in more detail, as the observed differences mentioned above may affect the value of the coordination numbers for the low loading materials. As noted above, as the Pt loading decreases below 2%, the R-space peak at 3 Å begins to decrease and the peak below 2 Å begins to increase. This change could be due to the loss of metal coordination and the addition of p-block element coordination (such as oxygen), however, it is noted that this change coincides with an increase in the noise to signal ratio in the high k-pace spectra (which will directly affect the low R-space spectra) and that the fit parameters begin to deviate from the values of the high loading samples. Additionally, the error of these parameters increases. Regardless of the cause of this change in the spectra, the addition of this peak may affect the calculated coordination numbers reported in figure 3.18 and warrant further investigation.

Figure 3.19 shows the R-space data calculated from the k-space data in figure 3.11-3.17 after the data had been truncated at 12000 eV (k ~ 10.9 $Å^{-1}$). The bottom figure shows the high loading samples. Again, this data is qualitatively similar. The top figure shows the low loading data (0.5%, 1%, and 2% samples). This data also looks similar, however there is a slight broadening of the peak at

~2.25 $Å^{-1}$. The parameters of the best fits for these spectra are presented in table 3.3.

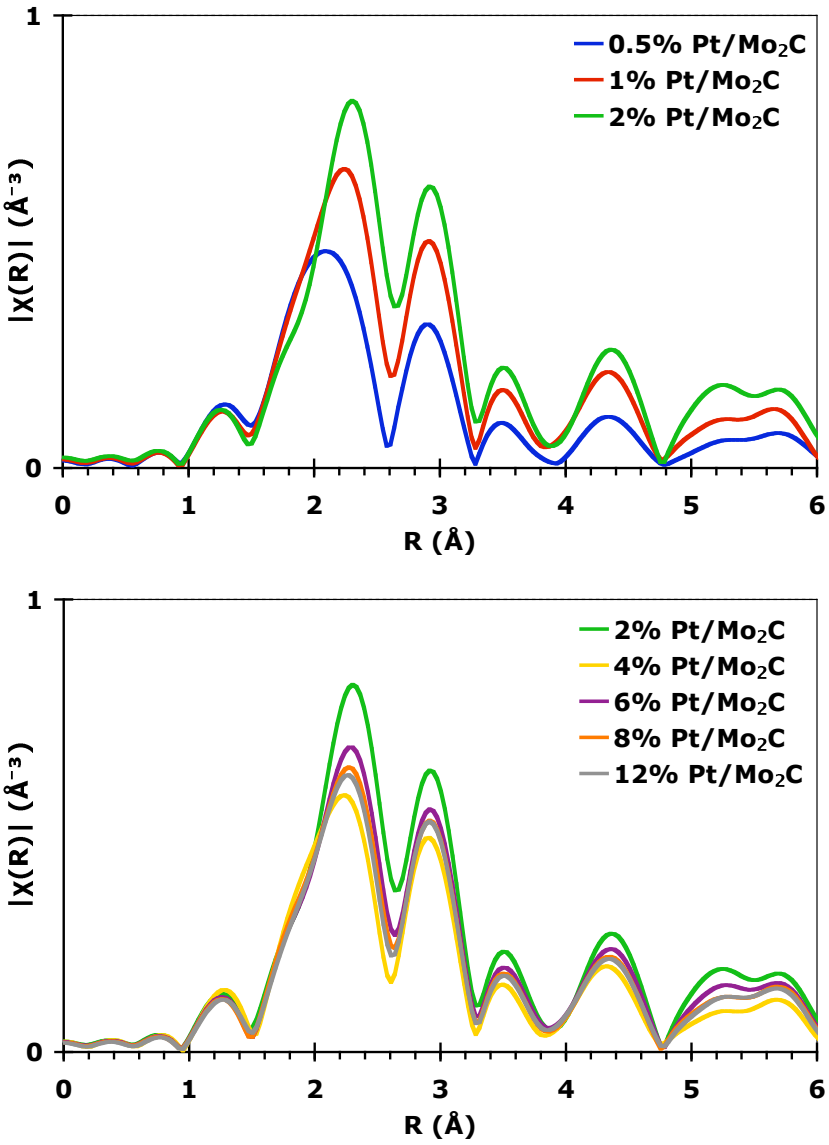


**Figure 3.19: R-space data for the catalysts after the energy data had been truncated at 12000 eV.**

**Table 3.3: EXAFS fit parameters for the data after truncated at 12000 eV. $S_o^2$ (the overall amplitude factor) was 0.75 for all fits. N is the average coordination of the scattering atom, R is the bond distance of the scattering path, $E_o$ is the energy shift, and $\sigma^2$ is the Debye-Waller factor.**

| Catalyst | Path | N | R (Å) | $E_o$ (eV) | $\sigma^2$ |
|---|---|---|---|---|---|
| 12% Pt/$Mo_2C$ | Pt-Pt | 7.5 ± 0.6 | 2.75 ± 0.01 | 5.2 ± 0.6 | 0.005 ± 0.001 |
| | Pt-Mo | 1.3 ± 0.4 | 2.71 ± 0.02 | | 0.004 ± 0.002 |
| 8% Pt/$Mo_2C$ | Pt-Pt | 7.9 ± 0.7 | 2.74 ± 0.01 | 4.9 ± 0.7 | 0.005 ± 0.001 |
| | Pt-Mo | 1.0 ± 0.4 | 2.70 ± 0.02 | | 0.002 ± 0.003 |
| 6% Pt/$Mo_2C$ | Pt-Pt | 8.2 ± 0.6 | 2.75 ± 0.01 | 5.2 ± 0.6 | 0.005 ± 0.001 |
| | Pt-Mo | 1.0 ± 0.4 | 2.71 ± 0.02 | | 0.003 ± 0.003 |
| 4% Pt/$Mo_2C$ | Pt-Pt | 7.8 ± 0.8 | 2.74 ± 0.01 | 4.4 ± 0.6 | 0.006 ± 0.001 |
| | Pt-Mo | 1.3 ± 0.4 | 2.70 ± 0.02 | | 0.003 ± 0.002 |
| 2% Pt/$Mo_2C$ | Pt-Pt | 9.2 ± 0.8 | 2.75 ± 0.01 | 5.4 ± 0.7 | 0.005 ± 0.001 |
| | Pt-Mo | 0.9 ± 0.5 | 2.72 ± 0.03 | | 0.003 ± 0.004 |
| 1% Pt/$Mo_2C$ | Pt-Pt | 9.4 ± 0.9 | 2.74 ± 0.01 | 3.9 ± 0.7 | 0.007 ± 0.001 |
| | Pt-Mo | 0.8 ± 0.4 | 2.69 ± 0.02 | | 0.001 ± 0.003 |
| 0.5% Pt/$Mo_2C$ | Pt-Pt | 8.6 ± 2.0 | 2.72 ± 0.02 | 2.2 ± 1.5 | 0.009 ± 0.003 |
| | Pt-Mo | 0.6 ± 0.7 | 2.67 ± 0.03 | | 0.001 ± 0.006 |

In general, the bond distances and spectral energy shifts reported in table 3.3 are consistently lower than the values in table 3.1. Additionally, these deviations increase significantly as the loading decreases below 2%. However, the coordination numbers for the 4%, 6%, 8%, and 12% samples are consistent with the values reported prior, again illustrating the robustness of the fits. On the other hand, the values of the 2%, and 1% samples are slightly higher while the values of the 0.5% sample are significantly different.

Truncating the energy data has a significant effect on the fit parameters for the low loading samples. Whether this is due to contributions of oxygen, or a higher noise to signal ratio in the high k-space data is unclear. Consequently, these results fosters a high level of uncertainty in the exact values of the coordination number, however, it can be concluded that these values are in the

same range as the coordination numbers of the high loading samples. Thus, the average Pt-Pt coordination number is ~8, and the average Pt-Mo coordination number is ~1.4.

### *3.4. DFT Calculations*

As stated in the introduction, the interaction between the metal and support plays a significant role in the morphology of the supported metal particles. DFT is a convenient, reliable tool which can be used to understand the magnitude of these interactions. Refer to chapter one for a detailed discussion of the β-$Mo_2C$ surface.

Figures 3.20 through 3.22 show the supported Pt models used in the DFT calculations for this study. There are two models which incorporate 1 monolayer of Pt. The first model consists of the $Mo_2C$ unit cell and a single Pt(111) sheet. The converged, relaxed structure can be viewed in figure 3.20 and is referred to as the "1ML Pt(111)" model. As can be seen in Table 3.4, the binding of Pt to the surface of the $Mo_2C$ is very favorable, ~ -0.8eV/Pt atom. However, as seen in figure 3.20, the structure of the Pt over-layer is distorted from the initial (111) layer seen in figure 3.3. The reason this occurs is that the Pt atoms prefer to bind in the hcp hollow sites of the surface. However, in this configuration, there are more Pt atoms (19) than hollow sites in the unit cell (16). Therefore, upon relaxing, atoms that are near hollow sites shift into the most favorable spot, which distorts the position and bond distances of the surrounding Pt atoms.

If the Pt monolayer is adjusted such that a single Pt atom is placed in each hollow site, the binding energy becomes slightly more favorable, -1.0 eV/Pt atom. This model is referred to as the "epitaxial 1ML Pt" model in table 3.4, and is illustrated in figure 3.20. Although this results in a regular pattern with long range order, this more favorable configuration is somewhat surprising because the Pt-Pt bond distance is stretched well beyond the typical, bulk Pt-Pt bond distance (2.83Å as calculated in DFT, refer to table 3.5). Apparently, the binding between

the Pt atoms and the $Mo_2C$ surface is strong enough to compensate for this large bond distance.

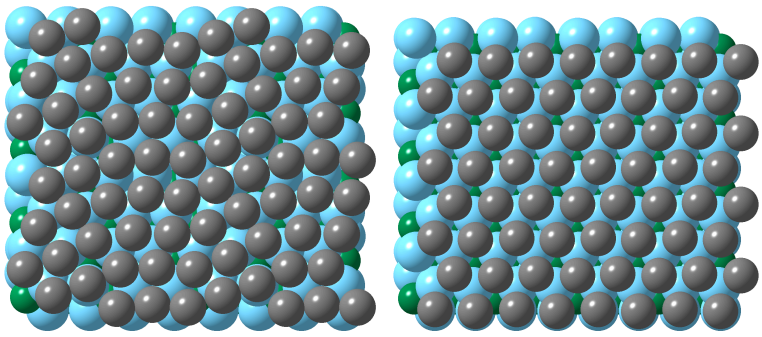

**Figure 3.20: Fully relaxed models of the $Mo_2C$ surface with one monolayer of Pt: left - the $Mo_2C$ surface with one Pt (111) sheet, right - the $Mo_2C$ surface with one Pt atom placed in every hcp site**

Figure 3.21 illustrates the fully relaxed structures of the two monolayer Pt/ $Mo_2C$ model. The picture on the left displays the $Mo_2C$ surface with both layers, while the picture on the right displays the same model with the top layer of Pt removed. The binding energy of the overall system is -0.2 eV. Table 3.4 shows the binding energy of each Pt layer separately. The binding energy of the first layer to the surface is essentially the same as the one monolayer model. On the other hand, the binding energy of the second layer to the first is unfavorable. Table 3.5 shows the average bond distance of the Pt atoms in the unit cell to their nearest neighbors. It can be seen that the distance between the first and second layer is large (2.92 Å) and the distance between the Pt atoms within the second layer are slightly contracted (2.79 Å).

As was observed for the one monolayer model, the Pt structure is distorted from the expected hexagonal (111) structure. The first layer is again distorted by Pt atoms shifting to hollow sites, but now there is even shifting of atoms away from the $Mo_2C$ surface. The red arrows in figure 3.15 indicated a Pt atom from the bottom layer which is shifted away from the surface and into the second layer. Presumably, by shifting Pt atoms away from the first layer and into the second layer, the model is able to accommodate more atoms in the hollow sites of the $Mo_2C$ surface.

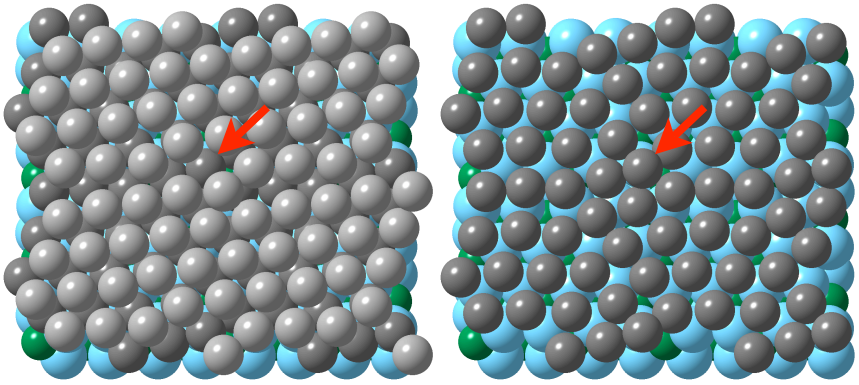

**Figure 3.21: Fully relaxed two monolayer Pt/$Mo_2C$ model: left - Both monolayers are displayed (top layer is light grey, bottom layer is dark grey), right - view of the model with the top layer stripped off. The red arrows indicate a Pt atom in the bottom layer which is being "pushed" into the top layer.**

Figure 3.16 illustrates the relaxed, three monolayer model. In this case, the layers are relatively close to the hexagonal structure. Like the previous two cases, the first monolayer strongly adsorbs to the $Mo_2C$ surface, but the other layers do not bind favorably. The average bond distances are very similar for all the Pt layers, and close to that of bulk Pt.

The results of these calculations can be explained in the context of the bond conservation theory. A single monolayer of Pt binds very strongly to the surface. These Pt atoms prefer Mo hollow sites. Since the Pt is strongly bound to the $Mo_2C$ surface, it cannot bind strongly to the second layer. This was evidenced by the unfavorable binding of the second layer in both the two and three monolayer models. In the case of the two monolayer model, the second layer is essentially under-coordinated, so the intralayer bond distances contract to account for the under-coordination. Additionally, pulling a Pt atom from the first layer to the second makes this contraction more favorable. In the three monolayer model, the second layer can bind to the third layer, and is therefore relaxed close to the bulk bond distances.

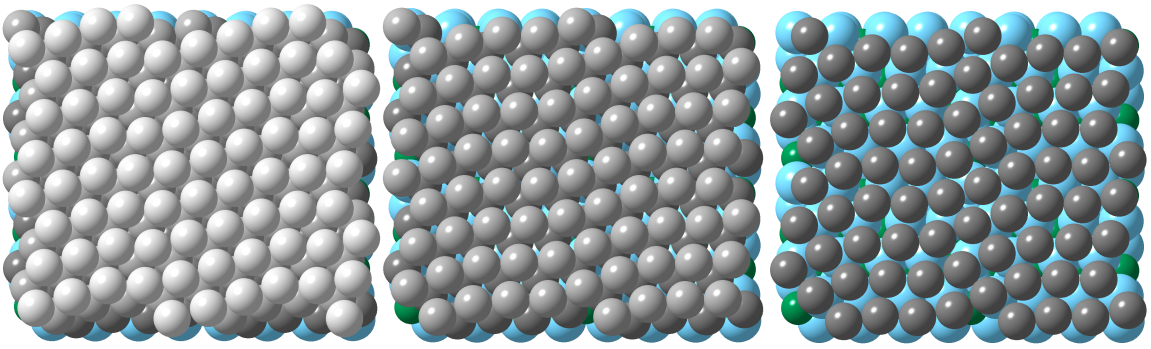

**Figure 3.22: Fully relaxed three monolayer Pt/$Mo_2C$ model: left - All three monolayers are displayed (top layer is light grey, middle layer is medium grey, bottom layer is dark grey), middle - view of the model with the top layer stripped off, right - view of the model with the top two layers stripped off**

We can draw the following conclusions about the real catalysts from these studies: 1) The most stable Pt structure is a single monolayer. On the real catalysts, the Pt atoms will not be confined by a unit cell, and are likely to spread on the surface to fill as many hollow sites as possible. The strong interaction between $Mo_2C$ and this first layer will make the Pt atoms more inert by altering their electronic structure compared to Pt atoms in a (111) surface, as will be discussed in more detail in chapter 4. 2) A two layer structure is highly unlikely. This stems from a combination of effects. First, since the first layer adsorbs strongly to the $Mo_2C$ surface, a bond conservation argument implies that the binding of the second layer must be less than the cohesive energy of Pt. Second, since the first layer adsorbs epitaxially to $Mo_2C$ and the Pt-Pt bonds are significantly stretched, a second layer would also have stretched Pt-Pt bonds. A second epitaxial layer would then be even more unfavorable (relative to the (111) layer used in these models) because not only is the layer not bound strongly to the first layer, but the intralayer bond distances would be stretched as well. 3) Additional layers would agglomerate into small particles since the energy of these layers are less favorable than bulk Pt.

It is worth emphasizing that the models studied in these calculations do not reflect the physical catalysts directly. For example, the standard deviations reported in table 3.5 for the bond distances of the Pt(111) models are quite large. On the real catalysts, these values would probably be more regular, as the atoms

in the real catalysts are not confined by unit cells and have freedom to relax to the most stable structure possible. These calculations are only intended to generate understanding of the chemical interactions between Pt and the $Mo_2C$ surface.

**Table 3.4: Binding energies of Pt layers from models illustrated in figures 3.20-3.22. The binding energies are calculates according to eq 3.5 and 3.6. All values have the units eV/Pt atom and are referenced to bulk Pt.**

| Model | Total system | 1st layer | 2nd layer | 3rd layer |
|---|---|---|---|---|
| 1ML Pt(111) | -0.8 | -0.8 | ----- | ----- |
| Epitaxial 1ML Pt | -1.0 | -1.0 | ----- | ----- |
| 2ML Pt(111) | -0.3 | -0.7 | 0.1 | ----- |
| 3ML Pt(111) | -0.1 | -0.8 | 0.2 | 0.1 |

**Table 3.5: Bond distances associated with the model systems presented in figures 3.20-3.22. The numbers represent an average of all the values within the unit cell. Standard deviations are provided in parenthesis. Subscripts represent the layer in which the Pt atom is located. All values have the units of angstroms. For reference, the Pt-Pt bond distance in bulk Pt is 2.83Å.**

| Model | Mo-$Pt_1$ | $Pt_1$-$Pt_1$ | $Pt_1$-$Pt_2$ | $Pt_2$-$Pt_2$ | $Pt_2$-$Pt_3$ | $Pt_3$-$Pt_3$ |
|---|---|---|---|---|---|---|
| 1ML Pt(111) | 2.86 (0.23) | 2.83 (0.22) | ----- | ----- | ----- | ----- |
| Epitaxial 1ML Pt | 2.73 (0.03) | 3.06 (0.07) | ----- | ----- | ----- | ----- |
| 2ML Pt(111) | 2.84 (0.20) | 2.80 (0.16) | 2.92 (0.18) | 2.79 (0.18) | ----- | ----- |
| 3ML Pt(111) | 2.87 (0.23) | 2.85 (0.24) | 2.88 (0.08) | 2.85 (0.20) | 2.86 (0.08) | 2.84 (0.19) |

### *3.5. Water-gas shift reaction rates*

The results of the WGS reaction rate studies can be viewed in figure 3.23. It can be generally observed that the rates increase as the Pt weight loading increases. The apparent activation barriers and pre-exponential factors are

displayed in table 3.6. The support alone had the highest activation energy and pre-exponential factors (90 kJ/mol and $5.0 \times 10^9$, respectively). The values of the apparent activation energies are within error and average to 67 kJ/mol.

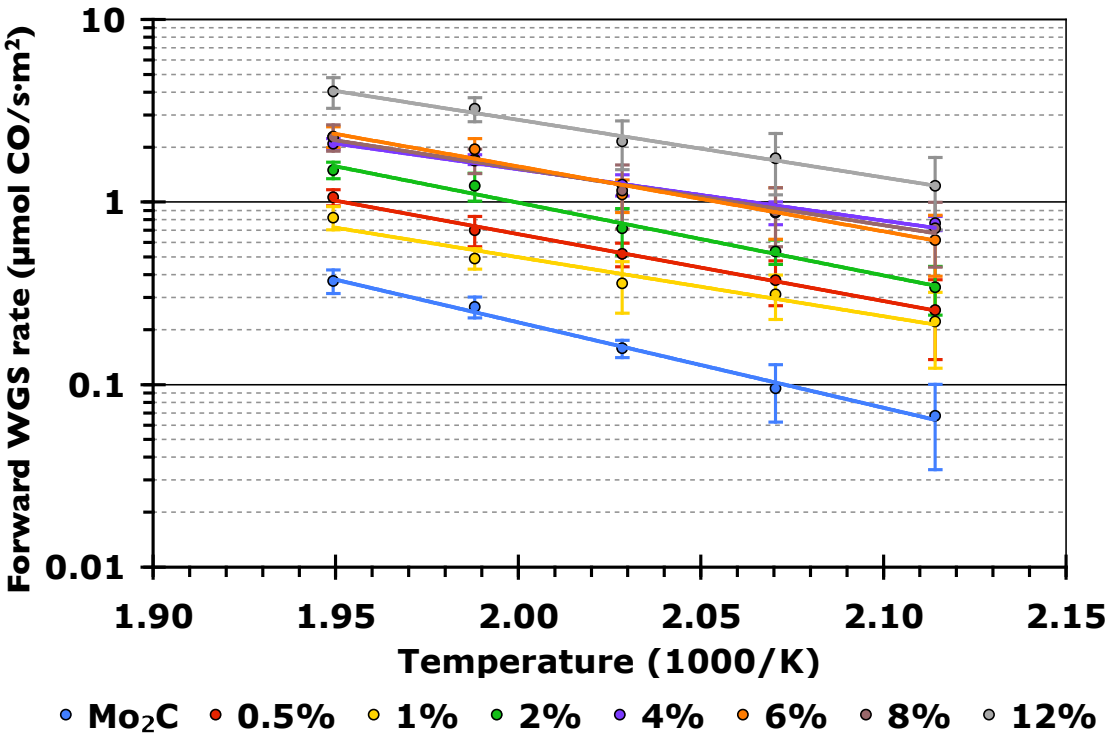


**Figure 3.23: WGS rates for various loading of Pt on $Mo_2C$ of various Pt loadings.**

**Table 3.6: Apparent activation barriers and pre-exponential factors as a function of metal loading for the Pt loaded $Mo_2C$ catalysts. The error of $A_{app}$ is orders of magnitude less than the absolute values and insignificant relative to the reported differences.**

| Catalyst | $E_{a,app}$ (kJ/mol) | $A_{app}$ |
|---|---|---|
| $Mo_2C$ | 90±4 | $5.0 \times 10^8$ |
| 0.5% Pt/$Mo_2C$ | 70±2 | $1.4 \times 10^7$ |
| 1% Pt/$Mo_2C$ | 66±13 | $3.9 \times 10^6$ |
| 2% Pt/$Mo_2C$ | 75±9 | $6.1 \times 10^7$ |
| 4% Pt/$Mo_2C$ | 60±4 | $2.9 \times 10^6$ |
| 6% Pt/$Mo_2C$ | 69±12 | $2.4 \times 10^7$ |
| 8% Pt/$Mo_2C$ | 66±3 | $1.3 \times 10^7$ |
| 12% Pt/$Mo_2C$ | 60±6 | $5.9 \times 10^6$ |

Figure 3.24 show the WGS rates for the different catalysts at 240°C as a function of Pt loading normalized the total mass of Pt. The WGS rate normalized to the total molar loading of Pt is almost inversely proportional to the Pt loading. This result implies that as the amount of Pt on the surface increases, the dispersion of the Pt is decreasing (i.e. the ratio of the total active sites to the number of Pt atoms on the surface is decreasing). The data fits a power equation with weight loading raised to -0.77.

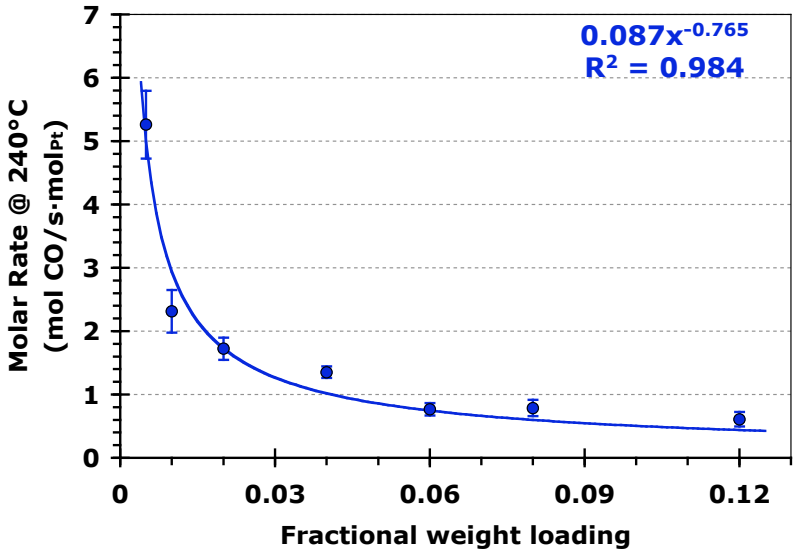


**Figure 3.24: WGS rates at 240°C of Pt/$Mo_2C$ as a function of Pt loading. Rates are normalized to total molar loading of Pt.**

## 4. Discussion

### *4.1. Particle Morphology*

The strength of the metal-support interaction plays a significant role in the shape of metal particles on a support. The DFT calculations presented in section 3.5 indicate that the Pt-$Mo_2C$ interface is more stable than bulk Pt.

The XAS results displayed in figure 3.18 indicated that as the average Pt-Pt and Pt-Mo coordination numbers remain essentially constant as a function of Pt loading. These are not the results one would expect if the Pt particles followed a typical growth mechanism exhibited by a metal that interacted weakly with the

support. For a typical growth mechanism, one would expect that as the weight loading increases, the size of the particles will increase as well. This would lead to an increase in the Pt-Pt coordination (approaching 12, the Pt-Pt coordination in bulk Pt) and a decrease in the Pt-Mo coordination (approaching zero as the number of Pt atoms bound to the surface becomes relatively small). This mechanism is illustrated in Figure 3.25a.

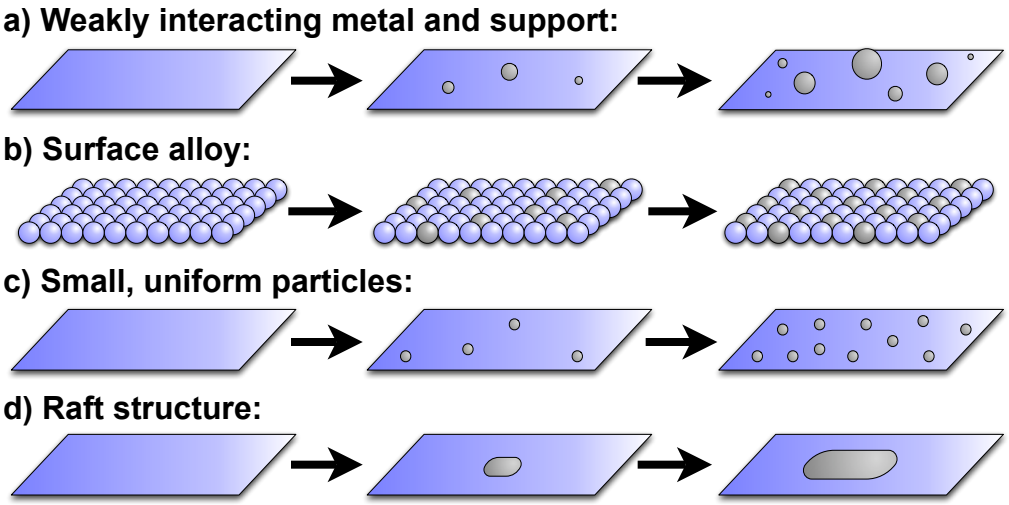


**Figure 3.25: Illustrations of proposed growth mechanisms for a) weakly interacting metal and support b) surface alloy c) small, uniform particles d) a raft structure**

Figures 3.25b-3.25d illustrate three possible growth mechanisms which would be consistent with the XAS results reported above. Figure 3.25b illustrates the formation of a surface alloy. In this case, the Pt atoms are incorporated into the $Mo_2C$ surface. As the Pt loading of the catalyst increases, the Pt-Pt and Pt-Mo coordination would remain constant; the PtMo alloy phase would penetrate deeper into the $Mo_2C$ bulk. Figure 3.25c illustrates a growth mechanism involving small, uniform particles. In this mechanism, as the Pt loading increases, the size of the particles on the surface remains the same, but the number of particles increases. If all the particles were approximately the same size, then the Pt-Pt coordination would remain constant. Further, if the particles were sufficiently small, Pt-Mo coordination would be observed and remain constant as well. Figure 3.25d shows the growth mechanism of a raft structure. Initially, Pt atoms wet as much of the surface as possible and form thin rafts. As the Pt loading

increases, the diameter of the raft increases, but the height of the raft stays relatively constant. For Pt-Mo to be observed in XAS, the raft must only be a few monolayers thick.

It is likely that the Pt phase does not form an alloy with the surface. If this were the case, the average Pt-Mo coordination number would be higher than 1.5. By comparing the WGS results described above to the remaining proposed growth mechanisms it is possible to deduce the likely mechanism. In figure 3.24, it was shown that as the weight loading of Pt increased, the WGS rates normalized to the mass of Pt decreased. This implies that as the weight loading of Pt increases, the dispersion of Pt decreases (the value of the exponential term holds significance about the location of the active site and will be discussed in more detail in section 4.2). However, if the growth mechanism involved small, uniform particles, the dispersion of Pt would remain constant. Only in the raft structure mechanism does the dispersion of Pt decrease with increasing weight loading. A model was derived to estimate the size of the raft-like particles using the average coordination numbers determined from the XAS experiments.

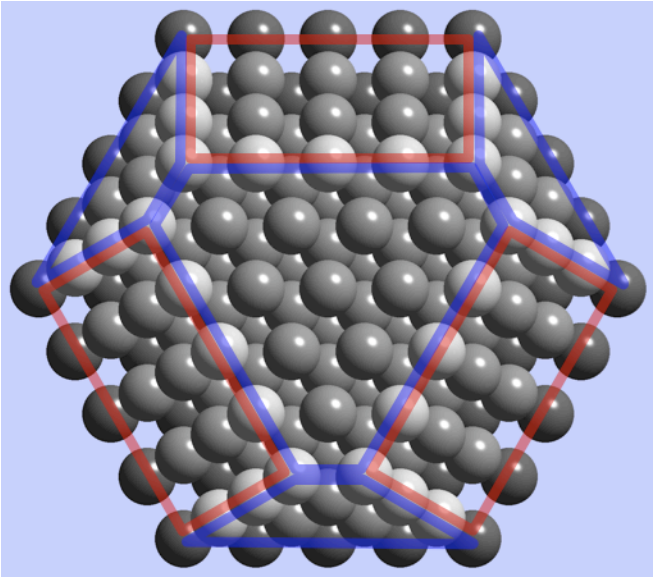

**Figure 3.26: Illustration of a model Pt raft structure. Terrace and bulk Pt atoms are grey, Pt atoms at the Pt-Mo interface are dark grey, and Pt atoms in the edge positions are light grey. (100) facets are outlined in red and (111) facets are outlined in blue.**

In this model, it was assumed that the base of the particle was a hexagon and that all the sides were of equal length. Using the illustration in figure 3.26, it is possible to determine the coordination number of each individual Pt atom in the structure and thereby determine the average coordination number of the structure. The coordination number for the different types of Pt atoms can be viewed in table 3.7.

**Table 3.7: Range of coordination number for individual Pt atoms presented in figure 3.21.**

| Atom type | Pt-Pt Coord No. | Pt-Mo Coord No. |
|---|---|---|
| Bulk | 12 | 0 |
| (111) terrace | 9 | 0 |
| (100) terrace | 8 | 0 |
| Edge | 6-7 | 0 |
| Interface | 3-9 | 3 |

As shown in table 3.7, the only atoms with Pt-Mo coordination are the atoms directly at the interface (for this model, it was assumed that the interface atoms preferred Mo hollow sites, which is consistent with the DFT calculations). This implies that the relative number of interface atoms must be high enough such that the Pt-Mo coordination is not “averaged out.” Figures 3.27-3.29 show how the Pt-Pt and Pt-Mo coordination numbers change as a function of particles diameter for a monolayer, 2 layer, and 3 layer Pt raft structures, respectively. Figure 3.27 shows that for a 1 monolayer Pt raft particle, the average Pt-Mo coordination is always 3, as all the Pt atoms are bound directly to the surface. On the other hand, the Pt-Pt coordination starts at ~4.25, and levels at ~6 as the particle size increases. A coordination number of 6 corresponds to the coordination of Pt atom in the middle of the raft, away from an edge. In figure 3.28, the Pt-Pt coordination of a two monolayer particles levels off at ~9 and the Pt-Mo coordination levels of at ~1.5. The Pt-Pt coordination number is 9 because any atom away from the edges of the particles would be coordinated to 6 Pt atoms within the same layer (as was seen in the case of the one monolayer

particle) and 3 Pt atoms in the other layer. The Pt-Mo coordination number of 1.5 is simply the consequence of the fact that the coordination of the bottom layer is three and the top layer is zero. In figure 3.29, the average Pt-Pt coordination of the 3 layer raft levels off at ~10 while the average Pt-Mo coordination levels off at ~1.

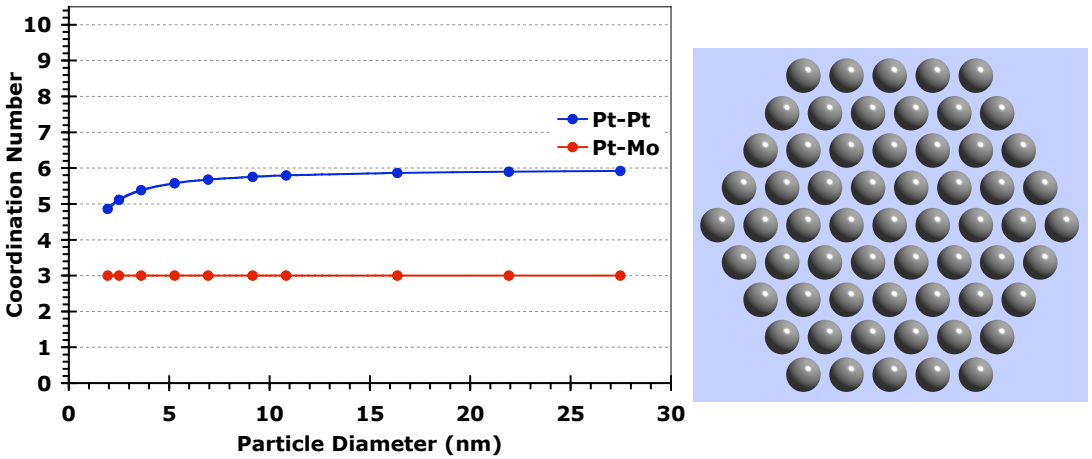


**Figure 3.27: Average Pt-Pt and Pt-Mo coordination number as a function of particle size calculated from the 1 monolayer, Pt raft model illustrated on the right**

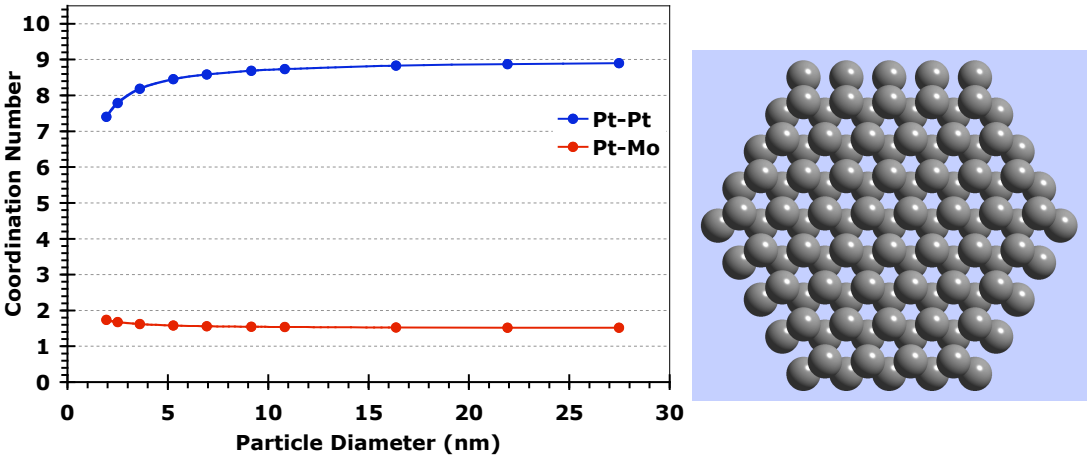


**Figure 3.28: Average Pt-Pt and Pt-Mo coordination number as a function of particle size calculated from the 2 monolayer, Pt raft model illustrated on the right**

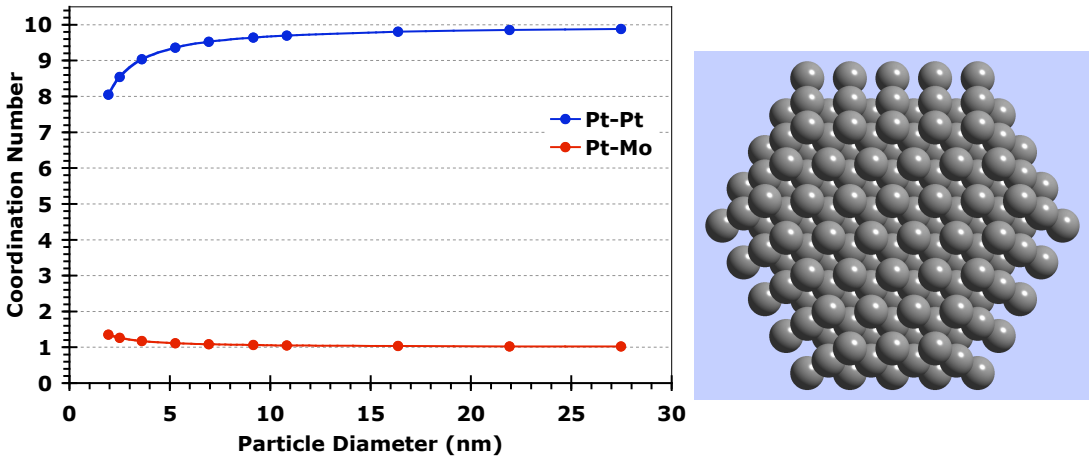


**Figure 3.29: Average Pt-Pt and Pt-Mo coordination number as a function of particle size calculated from the 3 monolayer, Pt raft model illustrated on the right**

From this model, it can be seen that for a sufficiently large particle (so the edge atoms can be ignored), the first monolayer will always have a Pt-Mo coordination of 3, and the remaining layers will have a Pt-Mo coordination of zero, so:

$$N_{Pt-Mo} \cong 3/ML \qquad \text{Eq 3.11}$$

where *ML* is the number of monolayers in the particle. Additionally, the top and bottom layers of a sufficiently large particle will have a Pt-Pt coordination of 9, while all the middle layers will have a Pt-Pt coordination of 12. Therefore, the average Pt-Pt coordination can be approximated by:

$$N_{Pt-Mo} \cong (9 + 12(ML - 2) + 9)/ML \qquad \text{Eq 3.12}$$

The EXAFS results in figure 3.13 indicate that the average Pt-Pt and Pt-Mo coordination numbers remain constant at approximately 8 and 1.4, respectively. According to the model discussed above, these results would indicate that the rafts should be between 1-2 monolayers thick. However, according to the DFT calculations in section 3.6, two monolayer rafts are unstable. Since the first monolayer binds very strongly to the $Mo_2C$ surface, it does not bind strongly to the second layer. In the two monolayer model, the

second layer stabilized itself by contracting the intralayer bond distances below the bulk value. When a third layer was added, the second layer relaxed again, presumably because it was stabilized by the additional layer.

The actual Pt structures are probably a mix of atomically dispersed Pt rafts and small, multilayer, raft-type particles. The DFT calculations suggest that single monolayers of Pt are the most favorable structure, but additional layers would form more stable particles. The XAS results indicate that a significant portion of the Pt is coordinated to the support since the Pt-Mo coordination remains at 1.4 even at high loadings. The remarkable conclusion is that the ratio of atomically dispersed Pt to Pt particles must be constant for all the catalysts. If this were not the case, the values of the Pt-Mo and Pt-Pt coordination number would not be constant. These conclusions are consistent with the XRD and SEM results. At low loadings, most of the Pt is probably atomically dispersed but accompanied by the small raft particles. The particles are small enough that they cannot be detected by XRD. In SEM, from a bird's eye view, they appear to be relatively large and cover the entire $Mo_2C$ surface. As the weight loading increases, a portion of the of the Pt must remain atomically dispersed, but the particle agglomerations are larger. These agglomerations are observed in SEM for the 8%wt catalyst, and become large enough to be detected by XRD.

### *4.2. Determining the location of the active site*

With knowledge about the shape of the Pt particles, the value of the exponential in figure 3.24 can be used to identify the location of the active site on the $Pt/Mo_2C$ catalyst. As a first approximation, assume that the particles can be described as hemispheres and that the rate of WGS at Pt sites is much faster than the rate at $Mo_2C$ sites far away from the Pt particles. The WGS rate normalized by weight of Pt ($\mu mol\ CO/s \cdot g_{Pt}$) can then be described by equation 3.13:

$$r = \frac{TOF \cdot N}{W_{Pt}} \qquad \text{Eq. 3.13}$$

where *TOF* is the turn-over frequency (μmol CO/s·Pt site), *N* is the number of sites (site/$g_{cat}$), and $W_{Pt}$ is the weight fraction of Pt ($g_{Pt}/g_{cat}$). The site density can be further described using equation 3.14:

$$N = n \cdot S \qquad \text{Eq. 3.14}$$

where *n* is the number of particles (particles/$g_{cat}$) and *S* is the number of sites per particle. The number of sites per particle will depend on the location of the active sites. For example, if it is assumed that the entire surface of the particle is active, then the number of active sites can be described by eq. 3.15:

$$S = q \cdot \left[2\pi R^2\right] \qquad \text{Eq. 3.15}$$

where *q* is the site density on Pt (site/$m^2$) and the term in brackets is simply the surface area of a hemisphere. If all the particles are assumed to be the same size, the radius of the particles can be calculated as a function of Pt weight loading in equation 3.16 by using the volume of a hemisphere and the density of Pt:

$$W_{Pt} = \rho_{Pt} \cdot n \cdot \left[{}^{2}/_{3}\pi R^3\right]$$

$$R = \left(\frac{3W_{Pt}}{2\rho n\pi}\right)^{1/3} \qquad \text{Eq. 3.16}$$

where $\rho_{Pt}$ is the density of Pt ($g/m^3$). Combining eq 3.13-3.16, one can derive an expression for the WGS rate normalized to the mass of Pt as a function of weight loading:

$$r = \frac{TOF}{W_{Pt}} \cdot [n \cdot (q \cdot 2\pi R^2)]$$

$$r = \frac{TOF}{W_{Pt}} \cdot nq \cdot 2\pi \left(\frac{3W_{Pt}}{2\rho n\pi}\right)^{2/3} \qquad \text{Eq. 3.17}$$

If *TOF*, *n*, *q*, and *ρ* are assumed to be constant as a function of Pt loading, then eq. 3.17 can be simplified to:

$$r \propto W_{Pt}^{-1/3} \qquad \text{Eq. 3.18}$$

This exponential value is far from the experimental value of -0.77 derived in figure 3.24. However, this value can change drastically if the active sites are assumed to be at the perimeter of the particle, or if the particle is modeled as a small cylinder rather than a hemisphere. Table 3.8 summarizes these results. For the cylinder models, *h* is the height of the particles, and is assumed to also be constant as a function of weight loading.

**Table 3.8: Parameters describing the relationship of WGS rates (normalized to mass of Pt) to the shape of the Pt particles and the location of the active sites.**

| | | | |
|---|---|---|---|
| Hemispheres: | $V = {}^2/_3\pi R^3$ | $R = \left(\frac{3W_{Pt}}{2\rho n\pi}\right)^{1/3}$ | |
| Active site: | Surface: | $S = q \cdot \left[2\pi R^2\right]$ | $r \propto W_{Pt}^{-1/3}$ |
| | Perimeter: | $S = q \cdot [2\pi R]$ | $r \propto W_{Pt}^{-2/3}$ |
| Cylinders: | $V = h\pi R^2$ | $R = \left(\frac{W_{Pt}}{\rho n h\pi}\right)^{1/2}$ | |
| Active site: | Surface: | $S = q \cdot \left(h(2\pi R) + \pi R^2\right)$ | $r \propto W_{Pt}^{-1/2}$ |
| | Perimeter: | $S = q \cdot [2\pi R]$ | $r \propto W_{Pt}^{-1/2}$ |

To a first approximation, modeling the particles as hemispheres and placing the active sites at the perimeter provides a value of the exponential very close to that of the experimental value. However, this value can change if one adds the contribution of $Mo_2C$ sites to the overall rate, as in eq. 3.19:

$$r_T = r_{Mo} + r_{Pt} \qquad \text{Eq. 3.19}$$

where $r_T$ is the total, observed rate, $r_{Mo}$ is the rate attributed to the $Mo_2C$ sites, and $r_{Pt}$ is the rate attributed to the Pt sites (and are the same values derived above). The rate attributed to the Mo sites can be described using an expression similar to eq. 3.13:

$$r_{Mo} = \frac{TOF_{Mo} \cdot M}{W_{Pt}} \qquad \text{Eq. 3.20}$$

where $TOF_{Mo}$ is the turnover frequency of the Mo sites and $M$ is the number of sites per gram of catalyst. $M$ can be described by eq. 3.21:

$$M = \mu \cdot B - \mu \cdot n \cdot CA_{Pt} \qquad \text{Eq. 3.21}$$

In the first term, $\mu$ represents the site density of the $Mo_2C$ surface (sites/$m^2$), and $B$ is the BET surface area of the $Mo_2C$ support. This term represents the total number of sites on the $Mo_2C$ surface. In the second term, $n$ is the number of Pt particles per gram of catalysts and $CA_{Pt}$ is the cross-sectional area of a Pt particle ($\pi R^2$). This term represents the number of Mo sites that are covered up by the Pt particles. Combining eq. 3.20 and 3.21 with the expression for $R$ derived for hemisphere particles, $r_{Mo}$ can be derived. Eq. 3.23 shows the results for $r_{Pt}$ derived above for hemispherical particles with the active site at the interface.

$$r_{Mo} = TOF_{Mo} \cdot \mu \cdot \left[ B \cdot W_{Pt}^{-1} - n\pi \left( \frac{3}{2\rho n\pi} \right)^{2/3} W_{Pt}^{-1/3} \right] \quad \text{Eq. 3.22}$$

$$r_{Pt} = TOF_{Pt} \cdot nq \cdot 2\pi \left( \frac{3}{2\rho n\pi} \right)^{1/3} W_{Pt}^{-2/3} \quad \text{Eq. 3.23}$$

As mentioned above, $r_T$ would be the sum of eq. 3.22 and eq. 3.23, which is a complicated function of $W_{Pt}$. It is possible to derive a simplified expression as a function of a single $W_{Pt}$ term, however the exponential value will depend heavily on the relative values of the coefficients of the three terms. For example, if $TOF_{Pt} >> TOF_{Mo}$, then $r_{Pt} >> r_{Mo}$ and $r \propto W_{Pt}^{-2/3}$, as was derived above. On the other hand, if $TOF_{Mo} >> TOF_{Pt}$, then the exponential term will rely on the relative magnitudes of $B$ and $n$. Additionally, this process becomes more complex if one incorporates the atomically dispersed phase into the model. However, all the parameters presented are physical quantities that could be measured through experiment (these will be described in more detail in chapter 4).

To a first approximation, one can conclude that the most active sites reside at the interface, as this model using hemispherical particles best fits the experimental data. However, evaluation of the quantities in eq. 3.22 and 3.23 would enable further understanding of the location of the active site.

## 5. Conclusions

We used a number of techniques to characterize the Pt/$Mo_2C$ catalysts. The structures can be characterized by a number of different findings. First, the structures were likely a mixture of atomically dispersed Pt coupled with small, raft like structures that are several monolayers thick. DFT calculations showed the a single monolayer of Pt is very stable on the $Mo_2C$ surface. However, because of the strong bonding between $Mo_2C$ and this single layer, additional layers do not bind to the first layer, suggesting that multiple monolayer structures would be unstable. XAS experiments showed that as the metal loading increased, the Pt-

Pt and Pt-Mo coordination numbers remained relatively constant around 8 and 1.4, respectively. According to the model in section 4, the Pt-Mo coordination would be well below 1.5 if the particles were more than 2ML thick. There must be atomically dispersed Pt to compensate for this small coordination number.

Additionally, the WGS results showed that as the weight loading of Pt increased, the dispersion decreased. Additionally, the apparent activation energy for all the different weight loadings were similar. This implies that the nature of the active site and the reaction mechanism is not affected by the Pt loading. To a first approximation, we hypothesize that the active site is at the metal-support interface, and will discuss this more in chapter 4.

## 6. References


1. Stevenson, S.A., J.A. Dumesic, R.T.K. Baker, and E. Ruckenstein, *Metal-Support Interactions in Catalysis, Sintering, and Redispersion.* Van Nostrand Reinhold Co. 1987
2. Bartholomew, C.H. and R.J. Farrauto, *Fundamentals of Industrial Catalytic Processes, Second Edition*. John Wiley and Sons, Inc. 2006
3. Henry, C.R., *Morphology of Supported Nanoparticles,* Progress in Surface Science, 2005. 80: p. 92–116
4. AutoChem 2910: *Automated Catalyst Characterization System, Operator's Manual.* Micromeritics Instrument Corp., v. 4, 1999
5. Ravel, B. and M. Newville, *ATHENA, ARTEMIS, HEPHAESTUS: Data Analysis for X-ray Absorption Spectroscopy using IFEFFIT***.** Journal of synchrotron Radiation, 2005. 12: p. 537-541
6. Newville, M., *Fundamentals of XAFS.* Consortium for Advanced Radiation Sources, University of Chicago, Chicago, IL. Revisions 2004.
7. J.P. Perdew, J.A. Chevary, S.H. Vosko, K.A. Jackson, M.R. Pederson, D.J. Singh, C. Fiolhais, *Atoms, Molecules, Solids, and Surfaces - Applications of the Generalized Gradient Approximation for Exchange and Correlation*. Physical Review B, 1992. 46: p. 6671-6687
8. Parthé, E. and V. Sadagopan, *The Structure of Dimolybdenum Carbide by Neutron Diffraction Technique.* Acta Crystallographica, 1963. 16: p. 202-205
9. Ladebeck, J.R. and J.P. Wagner, *Catalyst Development for Water-Gas Shift*. Handbook of Fuel Cells - Fundamentals, Technology, and Applications. John Wiley and Sons, Inc. 2003. Vol 3, part 2, p. 190-201

# Chapter 4
# Understanding the WGS mechanism on Pt/$Mo_2C$ and the role of the metal and the support

## 1. Introduction

As discussed in chapter one, literature has shown that $Mo_2C$ is a very active water-gas shift catalyst. Moon et al. showed that, depending on the synthesis conditions, $Mo_2C$ performed comparably to Cu/Zn/$Al_2O_3$ for low temperature WGS [1]. In the dissertation of Timothy King [2], it was reported that the WGS activity of $Mo_2C$ could be enhanced with the addition of Pt. It was suggested from kinetic studies that WGS on $Mo_2C$ occurred through a red-ox mechanism (refer to chapter 1 for a detailed discussion), while the mechanism on Pt/$Mo_2C$ was a dual site, Langmuir-Hinshelwood mechanism (where CO adsorption and H2O activation occurred on different sites).

There have been few, detailed analyses of the WGS mechanism on $Mo_2C$. Tominaga et al. [3], one of the first groups to study WGS on $Mo_2C$, studied the red-ox mechanism on a Mo-terminated $Mo_2C$ surface. They suggested that the red-ox mechanism was most likely. They argued that it is most favorable for an adsorbed OH on the surface to further dissociate than it is to diffuse across the surface, approach an adsorbed CO, and form an intermediate. Additionally, they propose the rate limiting step to be CO oxidation by the surface oxygen. However, their calculated activation barrier is very large, 550 kJ/mol, likely due to that fact that they only considered a Mo-terminated surface.

Lui and Rodriguez also investigated the WGS mechanism on $Mo_2C$ using DFT calculations [4]. However, Lui et al. recognized that, under WGS conditions, the surface may have oxygen on it. Therefore, they investigated the mechanism

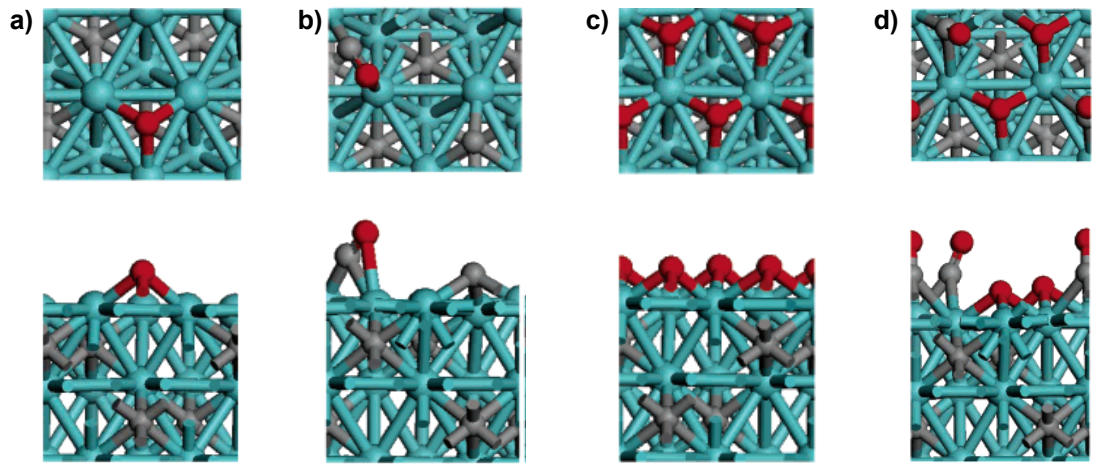


**Figure 4.1: Top and side views of the surfaces studied by Lui et al [4]. a) Mo-terminated with a single oxygen atom adsorbed, b) C-terminated with a single oxygen atom adsorbed, c) Mo-terminated with one monolayer of oxygen, d) C-terminated with one monolayer of oxygen.**

over Mo-terminated, C-terminated, O-terminated, and oxy-carbide terminated surfaces. The surfaces used in their calculations are shown in figure 4.1. It should be noted that in this study, the surface atoms displayed in the oxygen monolayer (as opposed to the singly adsorbed oxygen atom) were not permitted to participate in the WGS mechanism. Figure 4.2 shows the calculated reaction step energies for the red-ox mechanism on the different surfaces. Additionally, Lui et al. derived a microkinetic model, and plotted the theoretical rates for each surface (based on their DFT energies) relative to the rate for a copper surface. They concluded that the most active surface was the oxy-carbide surface.

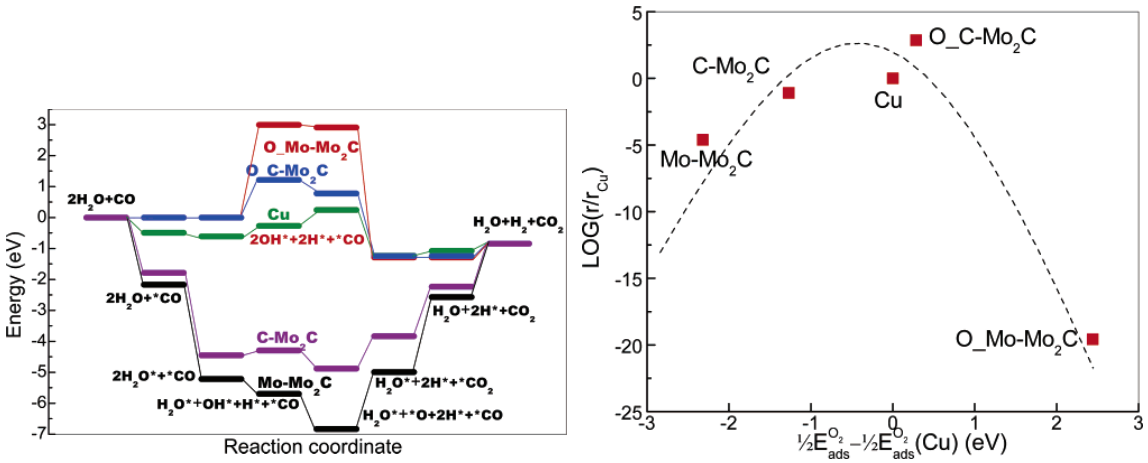


**Figure 4.2: Results from Lui et al. [4] LEFT - Red-ox reaction mechanism over various $Mo_2C$ surfaces with different terminations. RIGHT - Results from microkinetic modeling of the DFT calculated energies. Rates and oxygen binding energies are referenced to values for Cu.**

However, they note that this surface is much less stable than an O-terminated surface, which was essentially inert.

In this chapter, we will try to further understand the roles of $Mo_2C$ and Pt in the WGS mechanism. We will present experimental results that support the prominence of the red-ox mechanism, as well as surface characterization results which suggest that the carbide surface is O-terminated. However, we will propose a variation of the red-ox mechanism from that which was proposed by Lui et al. [4] In this model, surface oxygen atoms within the top layer will be active in the reaction mechanism. We will present DFT calculations that are consistent with our experimental findings. Additionally, we will use the epitaxial Pt monolayer model derived in chapter three to evaluate the possible roles played by Pt in the WGS mechanism.

## 2. Experimental Procedure

### *2.1. Catalyst synthesis*

The catalysts in this section were synthesized the same procedure described in chapter 2. In short, the $Mo_2C$ supports were synthesized by carburizing ammonia paramolybdate ($(NH_4)_6Mo_7O_{24}\cdot 4H_2O$; 81-83% as $MoO_3$; Alpha Æsar) using a 15% $CH_4/H_2$ mixture and a temperature programmed reduction scheme. The freshly synthesized material was transfered under Ar to a deaerated, aqueous solution containing an appropriate amount of $H_2PtCl_6$ salt to achieve the desired loading, four weight percent. After the loading was complete, the sample was dried at room temperature in $H_2$ and reduced in $H_2$ at 450 °C. Finally, the sample was passivated at room temperature using a 1% $O_2$/He gas mixture.

### *2.2. Elemental analysis*

BET surface area analysis were recorded using a Micromeritics 2910 flow through chemisorption unit. The samples were pretreated as described above.

Then, 30% $N_2/H_2$ was flown over the sample, and the temperature was reduced to 77 K. BET surface areas were calculated from single point $N_2$ desorption peaks. The surface area was then calculated using the equations presented in chapter 3.

Inductively coupled plasma optical emission spectroscopy (ICP) was used to determine the actual weight loading of Pt on the 4% $Pt/Mo_2C$ sample. The sample was first dissolved in 3 mL of aqua regia (75%vol HCl and 25%vol $HNO_3$). One milliliter of the acid solution was diluted with 13 mL of deionized water. The resulting solution was analyzed using a Varian 710-ES ICP Optical Emission Spectrometer. Signal intensities were calibrated using chemical standards obtained from Inorganic Ventures.

### *2.3. WGS reaction rates*

Water-gas shift experiments were performed using the same procedure reported in chapter 3. The catalysts were initially pretreated in 15% $CH_4/H_2$ flown at 100 mL/min at 590 °C for 4 h. The $Cu/Zn/Al_2O_3$ sample was pretreated according to vendor recommendations (4% $H_2/N_2$ flown at 100 mL/min at 200 °C for 4 h heated at 2.9 °C/min). The catalysts were then exposed to a reformate gas mix (11% CO, 21% $H_2O$, 43% $H_2$, 6% $CO_2$, 19% $N_2$), and steady state CO and $CO_2$ product concentrations were recorded using a GC. Refer to chapter 3 for a discussion of how the conversion and forward rates were calculated.

### *2.4. In-situ XPS experiments*

X-ray photoelectron spectroscopy studies were performed using a Kratos Axis Ultra XPS and a monochromatic Al source with an in-situ reaction chamber. The chamber is capable of heating samples to 600 °C in various gas flows at ambient pressure without exposing the sample to air. The $Mo_2C$ and $Pt/Mo_2C$ powders were pressed into pellets and secured, side by side, onto a sample stub. The as synthesized, passivated materials were degassed at ambient temperature under vacuum ($<10^{-6}$ torr) overnight then characterized. The

samples were then pretreated using the typical pretreatment protocol, degassed under vacuum overnight, and characterized. The samples were finally exposed to the same gas mixture used during the WGS rate measurements at 240 °C, degassed under vacuum overnight, and characterized. For each catalyst, high resolution scans at the Mo 3d, C 1s, O 1s, and Pt 4f regions were recorded. The resulting data was deconvoluted using the software CasaXPS. The Mo 3d and Pt 4f peaks (the peaks which exhibit doublets) were deconvoluted under the constraints that the ratio of the peaks were 3:2 (or 4:3 for Pt) and the spacing of the peaks was ~3.1eV (or ~3.3eV for Pt). Relative surface concentrations were calculated using Kratos sensitivity factors.

### *2.5. Pulse chemisorption experiments*

Pulse chemisorption experiments were conducted using a Micromeritics 2910 chemisorption instrument. Before the analysis, the catalysts were pretreated according to the typical protocol. The temperature of the catalysts was then reduced to 240 °C and the carrier gas was switched to pure Ar. In a separate loop (~5 mL) line, pure Ar was bubbled through a DI water saturator (T=46 °C, which corresponds to a $H_2O$ vapor pressure of 75.7 mmHg, or 10% mol) and pulsed through the sample 10 times. Next, 10% CO/Ar was flown through the loop line and pulsed through the sample 10 times. This procedure was repeated once. The composition of the effluent gas was analyzed using a Pfeiffer Vacuum ThermoStar GSD 300 Mass Spectrometer. The signals for CO (m/z=28,16), $CO_2$ (m/z=44,28), $H_2O$ (m/z=18,17), $H_2$ (m/z=2), $CH_4$ (m/z=16,15), and $O_2$ (m/z=32,16) were monitored throughout the duration of the experiment.

### *2.6. DFT calculations*

#### *2.6.1. General DFT calculations*

DFT calculations were performed using DACAPO software with the GGA-PW91 [5] exchange-correlation function. The ion cores were described by ultrasoft pseudo-potentials and calculations were performed using plane-wave

basis sets and a cutoff density of 350eV. The $Mo_2C$(100) surface was modeled as a 1x1 supercell (described previously in chapters 1 and 3) with 5 atomic layers separated in the z-direction by 12Å of vacuum (3 layer of Mo and 2 layers of C, arranged in an alternating fashion) and 3x3x1 Monkhorst-Pack k-point sampling. The calculated lattice constants of the orthorhombic unit cell (a=4.73Å, b=6.17Å, c=5.34Å) are in good agreement with experimental values (a=4.72Å, b=6.00Å, c=5.19Å) [6]. In all calculations, the upper two atomic layers, along with the adsorbates, were allowed to fully relax until the maximum forces were below 0.1eV/Å.

Unless otherwise stated in the text, oxygen adsorption energies were referenced to water vapor and hydrogen gas, using equation 4.1:

$$E_{ads,O} = E_{slab,O} + E_{H_2} - E_{slab} - E_{H_2O} \qquad \text{Eq. 4.1}$$

When constructing free energy reaction diagrams, it was assumed that entropic effects were negligible for surface intermediates (surface intermediates have no translational or rotational contributions to entropy, and enthalpy contributions are much larger than entropic contributions from vibrational modes). Therefore, entropic effects were not considered for surface reactions. However, entropic effects are significant for steps involving gas phase species, mainly adsorption and desorption steps. In these cases, entropic effects were calculated using tabulated data from NIST chemistry webbook [7].

Metal d-band centers ($\varepsilon_f$) and fillings ($f$) were calculated according to equations 4.2 and 4.3:

$$\epsilon_d = \frac{\int_{-\infty}^{\infty} E\rho(E)dE}{\int_{-\infty}^{\infty} \rho(E)dE} \qquad \text{Eq. 4.2}$$

$$f = \frac{\int_{-\infty}^{E_f} E\rho(E)dE}{\int_{-\infty}^{\infty} \rho(E)dE} \qquad \text{Eq. 4.3}$$

where $E$ is energy, $\rho(E)$ is the density of states, and $E_f$ is the fermi level.

### 2.6.2. Surface free energy calculations

To understand the competition between oxygen and CO for sites on the $Mo_2C$ surface, a surface free energy diagram was constructed (using a procedure similar to that presented in ref [8,9]). DFT energies for several different surface structures consisting of various coverages of CO and O were calculated. The surface free energy of any combination of CO and O surface coverage was calculated using eq. 4.4:

$$\Delta G = (G_{ads/slab} - G_{slab} - \Delta\mu_{CO}N_{CO} - \Delta\mu_{O}N_{O})/A_{slab} \quad \text{Eq. 4.4}$$

where $\Delta\mu_{CO}$ and $\Delta\mu_{O}$ are the chemical potential of CO and O respectively (referenced to the chemical potential at 0 K and 0 atm), $N_{CO}$ and $N_{O}$ are the number of CO and O molecules adsorbed on the unit cell surface, and $A_{slab}$ is the surface area of the slab. By ignoring entropic contributions to $G_{ads/slab}$ and $G_{slab}$, equation 4.4 can be simplified to eq. 4.5 where the total adsorption energy of the system ($E_{ads}$) is given by eq. 4.6:

$$\Delta G = E_{ads} + \sum_{n} \tilde{\mu}_n(T, p^\circ) + \frac{1}{2}kT \ln\left(\frac{p_n}{p^\circ}\right) \quad \text{Eq. 4.5}$$

$$E_{ads} = E_{ads/slab} + N_{H_2O}E_{H_2} - E_{slab} - N_{CO}E_{CO} - N_{H_2O}E_{H_2O} \quad \text{Eq. 4.6}$$

The species chemical potentials are calculated as a function of temperature and pressure according to eq. 4.7 and 4.8, where $n$ is either CO, $H_2$, or $H_2O$:

$$\mu_O = \mu_{H_2O} - \mu_{H2} \quad \text{Eq. 4.7}$$

$$\mu_n = E_n + \tilde{\mu}_n(T, p^\circ) + \frac{1}{2}kT \ln\left(\frac{p_n}{p^\circ}\right) \quad \text{Eq. 4.8}$$

## 3. Results

### *3.1. Catalyst characterization*

BET and ICP Pt loading results for the catalysts used in this analysis can be viewed in table 4.1.

**Table 4.1: BET surface area and ICP Pt loading of the catalysts used in this study**

| Catalyst | BET surface area ($m^2/g$) | ICP Pt weight loading |
|---|---|---|
| $Mo_2C$ | 117 | ----- |
| $Pt/Mo_2C$ | 133 | 3.80% |
| $Cu/Zn/Al_2O_3$ | 60 | ----- |

### *3.2. WGS reaction rates*

Figure 4.3 shows the WGS reaction rates. The $Pt/Mo_2C$ catalyst exhibited the highest rates, about an order of magnitude higher than the $Mo_2C$ catalysts. The $Pt/Mo_2C$ catalyst was also more active than the $Cu/Zn/Al_2O_3$ catalyst. Table

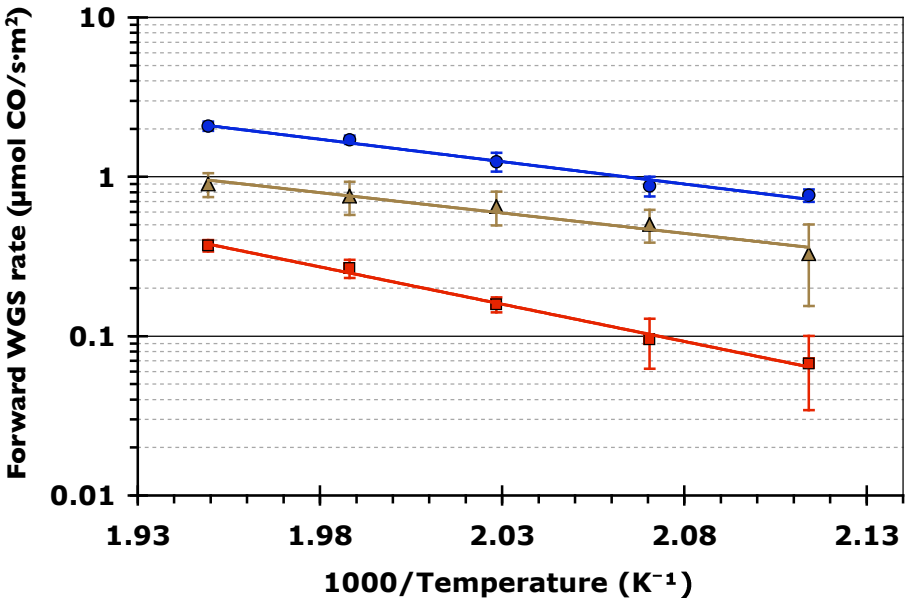


**Figure 4.3: Forward WGS rate for $Pt/Mo_2C$ (●), $Mo_2C$ (■), and $Cu/Zn/Al_2O_3$ (▲)**

4.2 shows the apparent activation energies and pre-exponential factors derived from the rate data in figure 4.3. The addition of Pt to the $Mo_2C$ support caused a reduction in the apparent activation energy and the apparent pre-exponential factor.

**Table 4.2: Apparent activation energy and pre-exponential factor for the various catalysts. The error of $A_{app}$ is orders of magnitude less than the absolute values and insignificant relative to the reported differences.**

| Catalyst | Apparent activation energy (kJ/mol) | Apparent pre-exponential factor |
|---|---|---|
| $Mo_2C$ | 90±4 | $5.0x10^8$ |
| $Pt/Mo_2C$ | 60±4 | $2.9x10^6$ |
| $Cu/Zn/Al_2O_3$ | 51±6 | $1.4x10^5$ |

*3.3. In-situ XPS results*

Figure 4.4 shows the 3d Mo spectra for the $Mo_2C$ catalyst and the $Pt/Mo_2C$ catalyst after synthesis, after pretreatment, and after exposure to WGS conditions. The data was deconvoluted into peaks for $Mo^{5+}$ ($Mo_4O_{11}$), $Mo^{4+}$ ($MoO_2$), $Mo^{3+}$ ($Mo^{\delta+}$, an oxy-carbide phase [10]), and $Mo^{2+}$ ($Mo_2C$). Initially, both samples exhibit large amounts of $Mo^{5+}$. However, during pretreatment, the contributions of the $Mo^{5+}$ species are completely removed while the $Mo^{4+}$ and $Mo^{3+}$ species remain. Remarkably, the results of the catalysts after pretreatment and after exposure to WGS conditions look identical for both catalysts. There does not seem to be a significant change in the Mo chemistry during WGS. It is noted that there is a shift and broadening of the $Mo^{4+}$ peaks in the pretreated and WGS samples. This is likely an artifact due to the selected background. However, this does not affect the main conclusion that the chemistry of the Mo is relatively unchanged after exposure to WGS conditions.

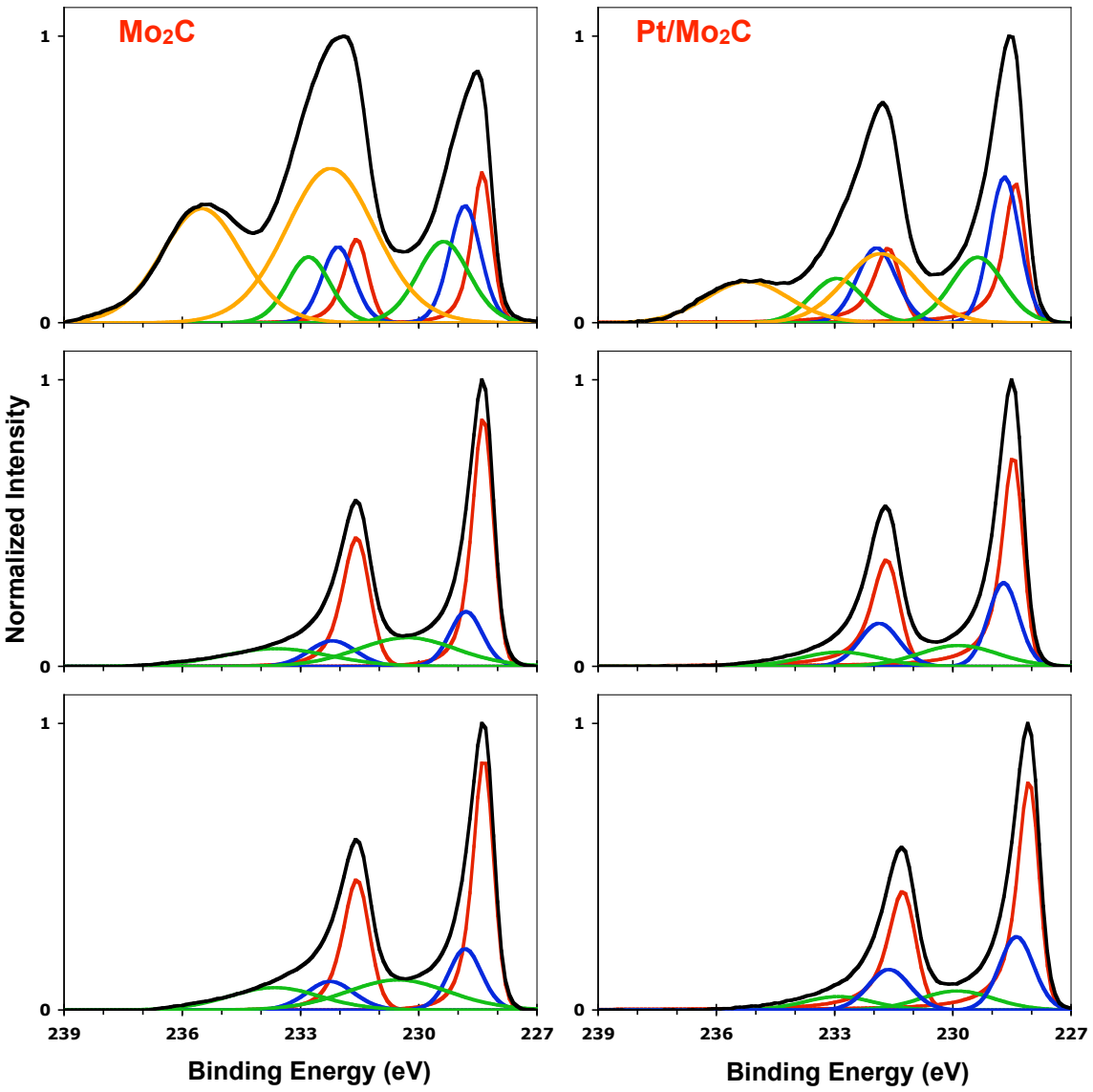


**Figure 4.4: Mo 3d XPS spectra for the $Mo_2C$ (left column) and Pt/$Mo_2C$ (right column) catalysts. The catalysts were analyzed *in-situ* as received (top row), after pretreatment (middle row), and after exposure to WGS conditions (bottom row). The real data (black curve) has been deconvolued into $Mo^{5+}$ ($Mo_4O_{11}$, yellow), $Mo^{4+}$ ($MoO_2$, green), $Mo^{3+}$ ($Mo^{\delta+}$, an oxy-carbide phase, blue), and $Mo^{2+}$ ($Mo_2C$, red) components.**

Figure 4.5 provides quantitative information relating the amount of a specific Mo species relative to the $Mo^{2+}$ species as a function of process conditions. As observed in figure 4.5, both catalysts exhibit a significant decrease in the amounts of $Mo^{3+}$, $Mo^{4+}$, and $Mo^{5+}$ present near the surface after pretreatment, but the relative amounts of each remained essentially unchanged after exposure to WGS conditions.

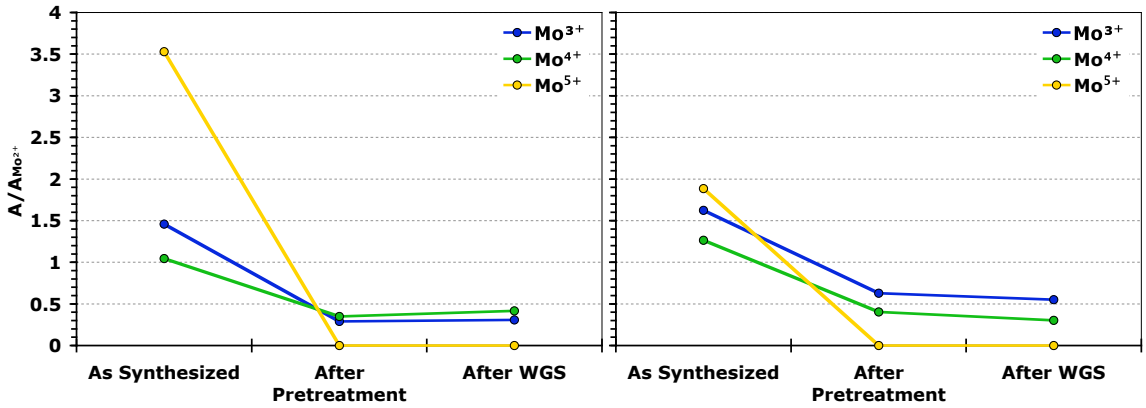


**Figure 4.5: Quantitative analysis of the Mo 3d spectra presented in figure 4.4 for the Mo2C (left) and Pt/Mo2C (right) catalysts as synthesized, after pretreatment, and after exposure to WGS. The data is presented as the ratio of the area of $Mo^{n+}$ to $Mo^{2+}$ (where n=3, 4, or 5).**

Figure 4.6 shows the ratio of carbon and oxygen to the total amount of metal detected by XPS for the different catalysts. The relative amount of oxygen and carbon detected on the $Mo_2C$ surface is much larger than the relative amount of the same elements on the Pt/$Mo_2C$ surface. However, some amount of the oxygen and carbon detected on the $Mo_2C$ surface probably resides just below the surface (since XPS can detect elements several angstroms into the surface). The amount of subsurface oxygen and carbon on the Pt/$Mo_2C$ surface is expected to be less since the addition of Pt on the surface would limit the detection of these species residing within the top few Mo layers. Therefore, the absolute ratios reported in figure 4.6 are less significant than the change in the values. For both catalysts, the amount of carbon and oxygen is reduced on the surface after pretreatment. However, after exposure to WGS conditions, the

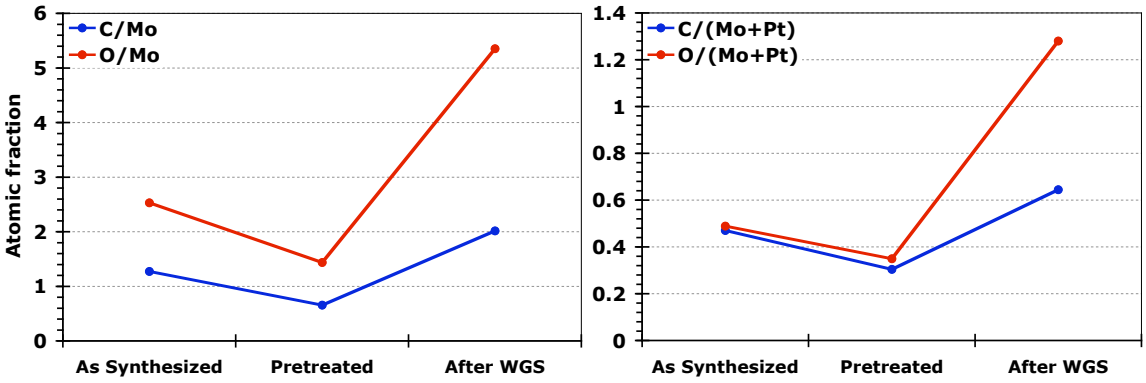


**Figure 4.6: The relative amounts of carbon and oxygen (compared to the total amount of metal detected) on the $Mo_2C$ (left) and Pt/$Mo_2C$ (right) catalyst as synthesized, after pretreatment, and after exposure to WGS conditions.**

amount of both carbon and oxygen increases significantly. These studies demonstrate that the $Mo_2C$ surface is capable of sustaining a high coverage of oxygen. However, the oxygen must not be able to penetrate far into the surface since the chemical nature of Mo does not change after WGS. Oxygen is restricted to the surface.

### *3.4. Pulse Chemisorption experiments*

Pulse chemisorption experiments were performed to gain insight into the dominant WGS mechanism on the $Pt/Mo_2C$ catalyst. In this experiment, the catalyst was initially pretreated in 15% $CH_4/H_2$ for 4 h at 590 °C, then dosed sequentially with pulses of $H_2O$ and CO. The effluent was analyzed using mass spectrometry. The results of this experiment are illustrated in figure 4.7.

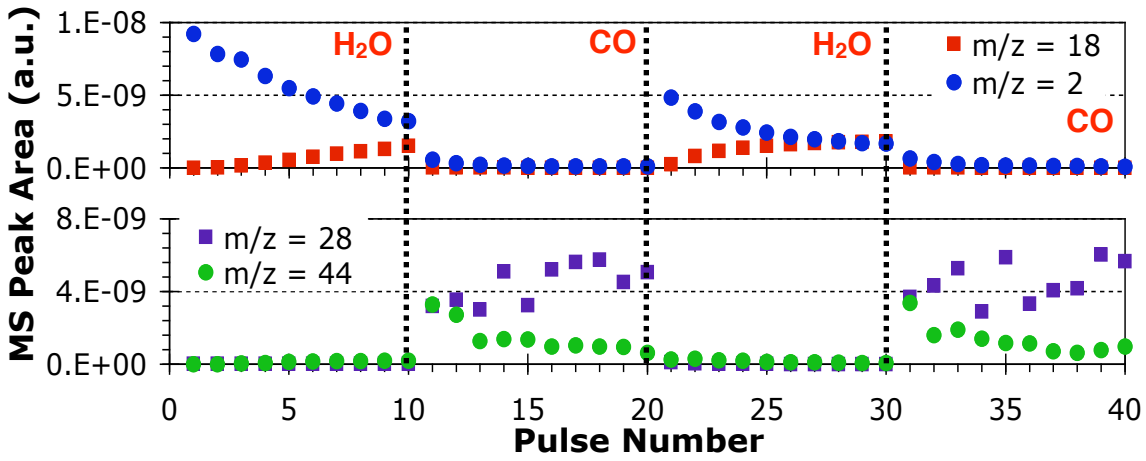


**Figure 4.7: Pulse chemisorption experiments performed over $Pt/Mo_2C$. The peak areas indicative of the amount of species in the product stream. The red text indicates the species which is being pulsed. The products are: TOP: $H_2$ (●), $H_2O$ (■); BOTTOM: $CO_2$ (●), CO (■).**

During the $H_2O$ pulse, only $H_2$ desorbed as a product. As the amount of $H_2O$ in the product stream increased, the amount of $H_2$ produced decreased suggesting that surface was being saturated with oxygen. During the CO pulses, significant amounts of $CO_2$ were produced. As the amount of $CO_2$ decreased, the amount of unreacted CO in the product stream increased, suggesting the surface was being depleted of oxygen. Only negligible amounts of $H_2O$ and $H_2$ were

observed during CO pulsing. Similar results were observed when the process was repeated.

### *3.5. DFT calculations*

A detailed discussion of the (100) $Mo_2C$ surface used as the basis of this study presented in this chapter was presented in chapter 1. In this study, we are interested in understanding the structure of the surface under reaction conditions and the energetics associated with the WGS mechanism on the $Mo_2C$ and Pt/ $Mo_2C$ catalysts. For review, figure 4.8 displays a Mo-terminated (100) $Mo_2C$ surface. The surface exhibits three unique threefold hollow sites of decreasing reactivity: 1) fcc - sites which have fourth layer carbons underneath, 2) hcp - sites which have third layer molybdenum atoms directly underneath, 3) carbon - sites which have second layer carbons directly below.

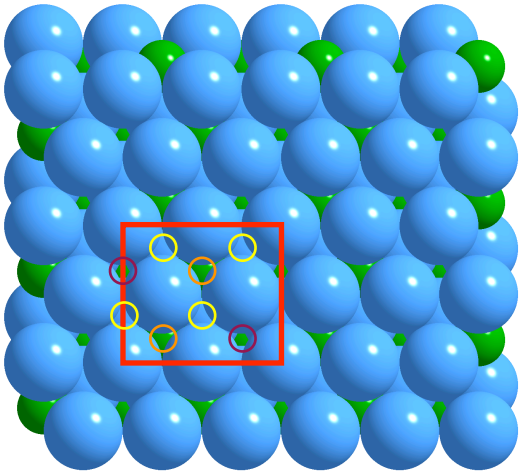

**Figure 4.8: Mo-terminated (100) surface. A unit cell is outlined in red, and fcc, hcp, and carbon sites are indicated by purple, yellow, and orange circles, respectively.**

Figure 4.9 illustrates two distinct mechanisms by which oxygen can populate the $Mo_2C$ surface. Initially in both mechanisms, oxygen accumulates on the surface forming a full monolayer, binding to the hcp sites. In mechanism “A”, oxygen continues to populate the surface, increasing the oxygen coverage beyond one monolayer to 1.25ML. In mechanism “B”, oxygen populates a subsurface site (i.e. a sites below the top Mo layer in the fcc site). Figure 4.10 shows the DFT binding energy of oxygen as a function of oxygen coverage for

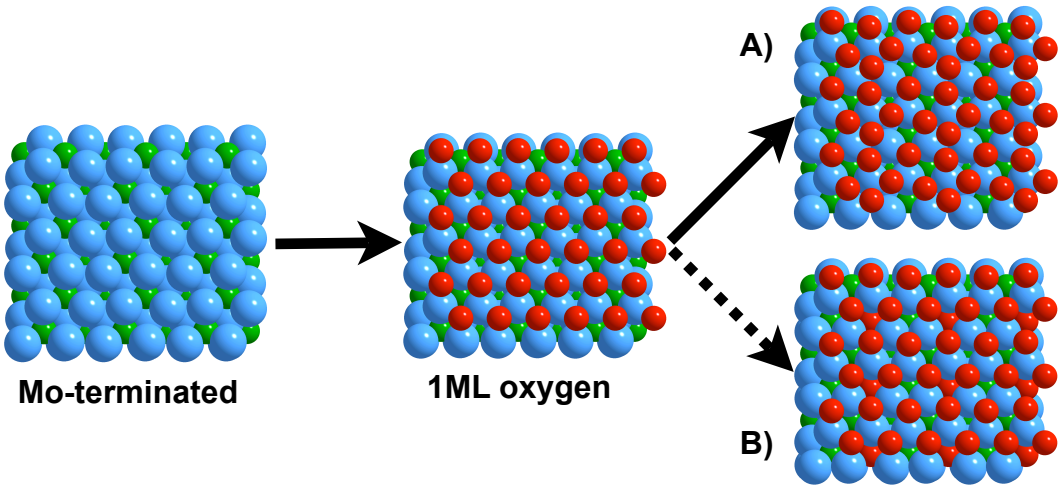


**Figure 4.9: Illustration of two different mechanisms by which oxygen can populate the $Mo_2C$ surface**

both mechanisms. In this analysis, the oxygen binding energy was evaluated two ways by referencing the energy to both molecular oxygen as well as water and hydrogen. For coverages less than one monolayer, oxygen adsorption is always favorable regardless of the reference state. However, oxygen adsorption referenced to molecular oxygen is always more favorable than that referenced to water by -2.2eV/O atom. When the oxygen coverage exceeds one monolayer, mechanism "A" is highly endothermic for both cases. However, mechanism "B" is

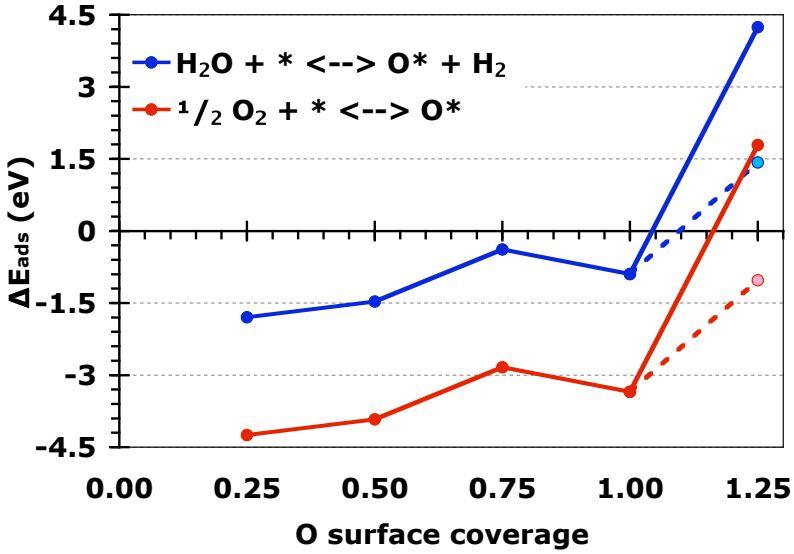


**Figure 4.10: Oxygen binding energy on (100) $Mo_2C$ as a function of oxygen surface coverage. When the coverage exceeds 1ML, the solid line represents data for mechanism "A" in figure 4.7 and the dashed line represents mechanism "B" in figure 4.9.**

only favorable if the oxygen adsorption energy is referenced to molecular oxygen.

The surface is very active towards oxygen binding. Although it is favorable to bind oxygen to the surface up to a full monolayer, water is not a strong enough oxidant to drive the surface oxygen into the subsurface site, consistent with the XPS results discussed above.

Under WGS conditions, it is plausible that CO and oxygen could compete for sites on the $Mo_2C$ surface. This must be necessary for the $Mo_2C$ catalyst, but may not be necessarily true for the $Pt/Mo_2C$ catalyst. Table 4.3 shows the adsorption energies for several different coverages of oxygen and CO on a Mo-terminated $Mo_2C$ surface (the coverages add up to a monolayer). The energies are calculated according to eq. 4.5. As the number of CO molecules increases, the adsorption energy of the configurations increase, which suggests in general that the surface binds CO stronger than it binds oxygen.

**Table 4.3: Adsorption energies for several different configurations of monolayer coverage of oxygen and CO coverage on $Mo_2C$**

| Adsorption Configuration | Adsorption Energy (eV) |
|---|---|
| 4O atoms | -4.5 |
| 3O atoms, 1 CO molecule | -4.6 |
| 2O atoms, 2 CO molecules | -5.8 |
| 1O atoms, 3 CO molecules | -6.3 |
| 4 CO molecules | -7.1 |

To determine which configurations dominate in the surface under various conditions, the surface free energy (calculated using eq. 4.4) was plotted as a function of oxygen and CO chemical potential (calculated using eq. 4.6 and 4.7). These results are presented in figure 4.11. In this figure, the most favorable configuration for a range of oxygen and CO chemical potentials is represented by areas shaded with different colors (all the coverages studied are favorable is

some range of conditions, but in the narrow range displayed in figure 4.11, only the oxygen and CO-terminated surfaces are favorable). The chemical potentials for oxygen and CO from 100°C to 250°C using the partial pressure of the experimental gas concentration are traced out by the grey line. This entire temperature range falls in the O-terminated regime.

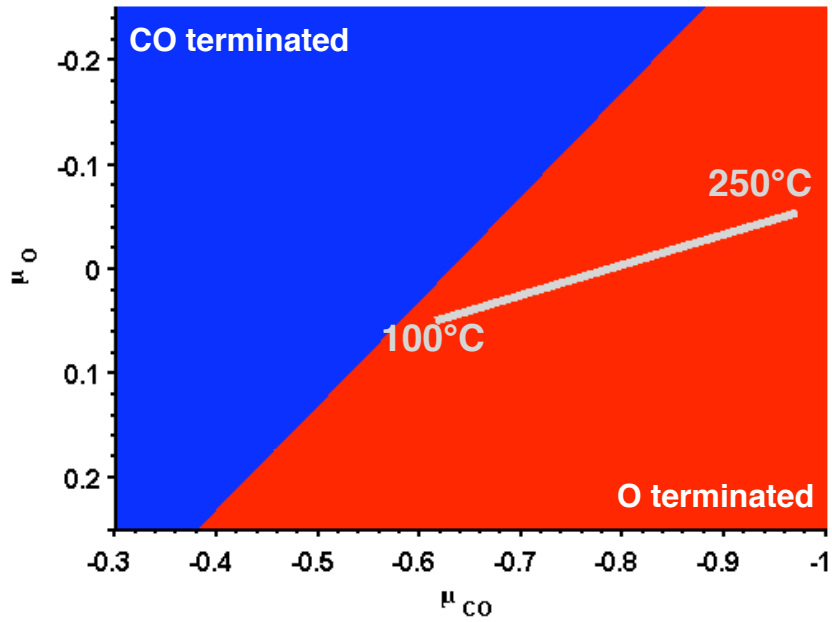


**Figure 4.11: A plot of the surface terminations with the lowest free energies as a function of oxygen and CO chemical potential. The blue region represent a CO-terminated surface, and the red region represents the O-terminated surface. The grey line represents a trace of the chemical potentials in the range of 100°C to 250°C and partial pressures of the experiments described in this section.**

## 4. Discussion

### *4.1. WGS mechanism on $Mo_2C$*

The in-situ XPS experiments indicated that $Mo_2C$ sustained high oxygen surface coverages. After exposure to the WGS conditions, the amount of oxygen on the surface increased. However, the chemistry of the molybdenum did not significantly change. This implies that the surface oxygen is unable to penetrate into the bulk. The results of the DFT calculations presented in figure 4.10 are consistent with this interpretation. Water is not a strong enough oxidant to drive oxygen into the subsurface (unlike molecular oxygen which can drive oxygen

subsurface, which is why a low concentration of oxygen is used to passivate the surface). Similar results were reported by Lui et al. [4].

The results from the pulse chemisorption experiments imply that the red-ox mechanism is the dominant mechanism in WGS on $Mo_2C$. As water is pulsed over the catalysts, hydrogen is evolved, increasing the amount of oxygen on the surface. When CO is subsequently pulsed, the catalyst produced $CO_2$. When water was pulsed again, the amount of hydrogen evolved from the surface was greater than the amount of the last pulse of the first cycle. This implies that CO removed some of the oxygen built up on the surface by water. If a mechanism involving a reactive intermediate dominated this reaction, one would expect to see very little hydrogen production during water uptake, as intermediates form through the reaction of hydroxyls on the surface with CO [11]. Consequently, one would expect to see large amounts of $H_2$ and $CO_2$ produced with subsequent CO pulsing from the decomposition of the intermediate. These results have been observed for other catalysts using a similar method [11].

Lui et al. [4] proposed that the most active surface would be a C-terminated surface with one monolayer of oxygen. This surface (as seen in figure 4.1) is essentially the same as a surface with half a monolayer of oxygen and half a monolayer of CO, presented in section 3.5. However, according to the surface free energy results, this surface would not be stable under WGS conditions, rather the O-terminated surface would be stable. Lui et al. reported that this surface was the least active, because adsorbates adsorbed unfavorably. However, in their model, the surface oxygen atoms were not allowed to participate in the reaction.

Table 4.4 shows the DFT calculated reaction energies for the red-ox mechanism allowing the surface oxygen to participate directly in the reaction, as illustrated in figure 4.12.

**Table 4.4: Reaction step energies associated with the red-ox mechanism on an oxygen terminated $Mo_2C$ surface. A * represents an adsorption site on top of the oxygen layer while a $^v$ represents an oxygen vacancy site in the oxygen layer.**

| Reaction step | Reaction energy (eV) |
|---|---|
| $CO + ^* \rightleftharpoons CO^*$ | 0.0 |
| $CO^* + O^v \rightleftharpoons CO_2^v$ | -0.2 |
| $CO_2^v \rightleftharpoons CO_2 + ^v$ | 0.2 |
| $H_2O + ^v \rightleftharpoons H_2O^v$ | -0.9 |
| $H_2O^v + O^v \rightleftharpoons 2OH^v$ | -0.9 |
| $2OH^v \rightleftharpoons H_2 + 2O^v$ | 0.8 |

The energies in table 4.4 represent the enthalpy of the reactions. The adsorption of CO is thermo-neutral, but the oxidation of the adsorbed CO is slightly exothermic. Desorption of $CO_2$ from an oxygen vacancy is mildly endothermic, so the CO oxidation process is essentially thermo-neutral. However, once the vacancy is formed, the surface aggressively binds water and readily dissociates it into hydroxyls. Figure 4.13 shows the potential energy diagram (which includes entropic effects) for the reaction mechanism calculated at 240 °C.

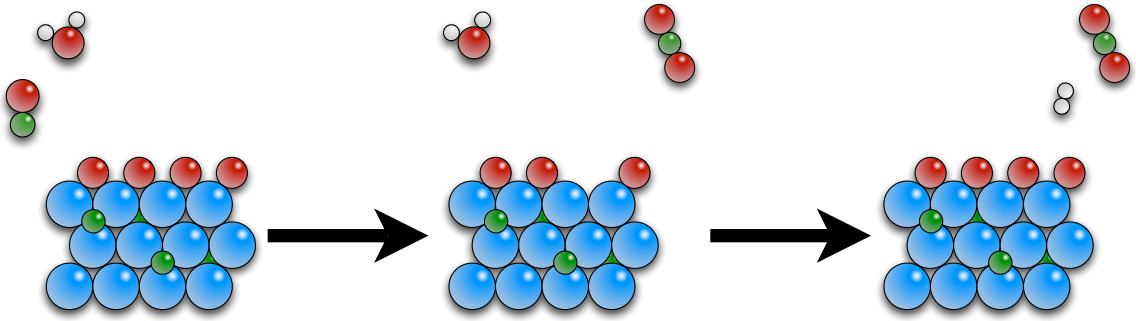

**Figure 4.12: Illustration of the red-ox mechanism involving a surface oxygen on $Mo_2C$**

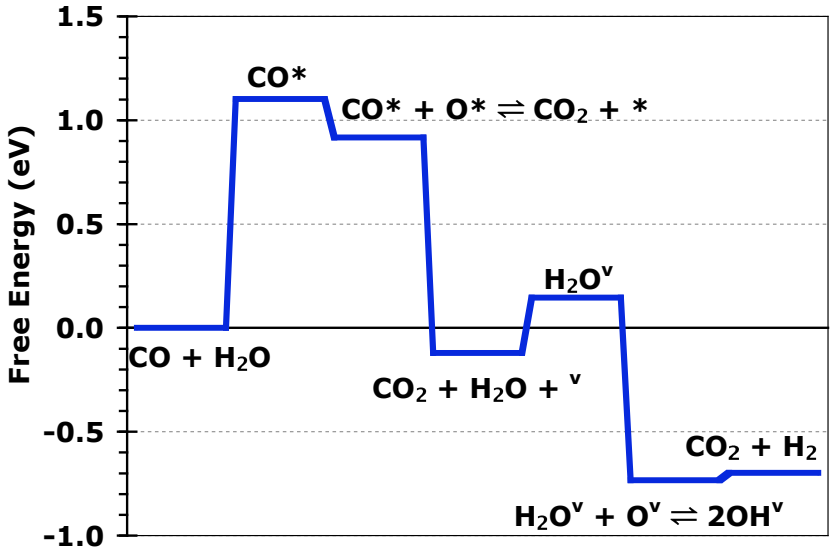


**Figure 4.13: Free energy diagram for the WGS red-ox mechanism on an O-terminated $Mo_2C$ surface calculated at 240°C.**

Entropic contributions affect $CO_2$ and $H_2$ desorption such that $CO_2$ desorption is very favorable and $H_2$ desorption is slightly unfavorable. Additionally, the effects hinder CO adsorption such that it is very unfavorable. The low coverage of CO on the surface probably contributes to the high apparent activation barrier for $Mo_2C$ observed in table 3.2. This point will be discussed in detail below.

### *4.2. The role of Pt in the WGS mechanism*

In literature, it is generally accepted that Pt WGS catalysts are bifunctional [11]. Either the support or the metal-support interface provide water dissociation sites while Pt simply provides CO adsorption sites. It was discussed above that an oxygenated $Mo_2C$ surface easily dissociates water. However it does not bind CO strongly. It is therefore reasonable to hypothesize that $Pt/Mo_2C$ catalysts are bifunctional as well.

Table 4.5 provides reaction energies for various reactions relevant to the WGS mechanism on a Pt(111) surface and a $Pt/Mo_2C$ surface. In chapter three, it was concluded that the supported Pt was a mixture of atomically dispersed Pt atoms and small Pt particles. The Pt in the particles can be modeled as Pt(111)

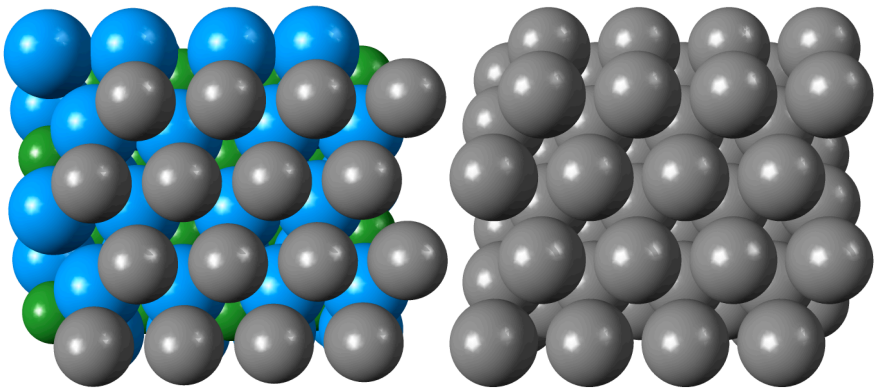

**Figure 4.14: Pt/$Mo_2C$ and Pt(111) surfaces used in the calculations reported in table 4.5**

surfaces and the atomically dispersed Pt can be modeled as an epitaxial monolayer of Pt on an $Mo_2C$ surface, as illustrated in figure 4.14.

Generally, the epitaxial monolayer of dispersed Pt on $Mo_2C$ was less active than the Pt(111) surface: CO and H adsorb weaker while OH adsorbs stronger (This behavior will be discussed in detail in section 4.3). In terms of molecular adsorption, $H_2$ dissociation and water dissociation are both less favorable on Pt/$Mo_2C$. Consequently, in the WGS mechanism, Pt probably only serves as a binding site for CO (including entropic effects to the results of table 4.5 would make the dissociation processes even more unfavorable). Figure 4.15 shows the free energy diagram for the WGS mechanism on $Mo_2C$ in which the monolayer of Pt serves as a binding site.

**Table 4.5: DFT calculated reaction energies for various steps relevant to the red-ox mechanism on Pt(111) as well as a monolayer of Pt on $Mo_2C$.**

| Reaction step | Pt(111) | Pt/$Mo_2C$ |
|---|---|---|
| $H_2 + 2^* \rightleftharpoons 2H^*$ | -1.1 | -0.1 |
| $H_2O + 2^* \rightleftharpoons OH^* + H^*$ | 0.2 | 0.6 |
| **Gas Phase adsorption** | **Pt(111)** | **Pt/$Mo_2C$** |
| $CO + ^* \rightleftharpoons CO^*$ | -1.8 | -1.3 |
| $H + ^* \rightleftharpoons H^*$ | -2.9 | -2.4 |
| $OH + ^* \rightleftharpoons OH^*$ | -2.3 | -3.1 |

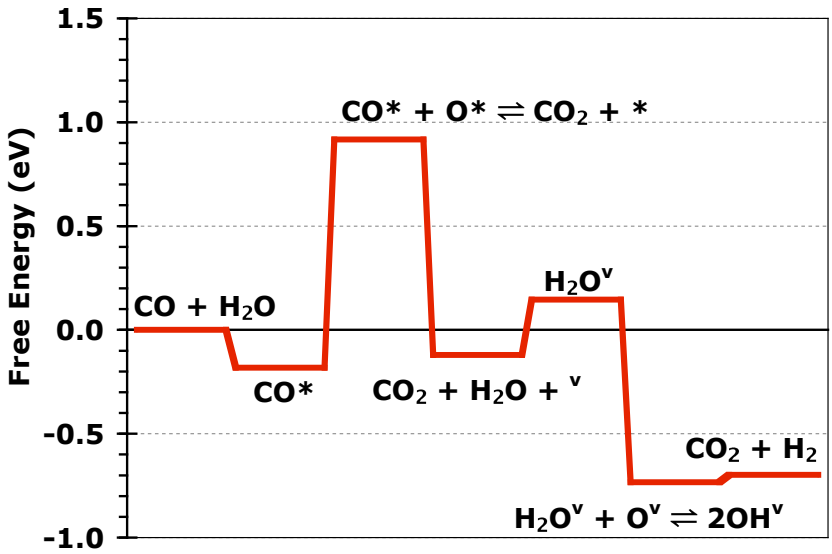


**Figure 4.15: Free energy diagram for the WGS red-ox mechanism on an O-terminated $Mo_2C$ surface in which an atomically dispersed Pt layer serves as the CO binding site.**

Even with the addition of Pt, the CO oxidation step appeared to be the rate limiting step. However, the addition of Pt could significantly affect the overall rate by increasing the amount of CO available to the oxygen on the $Mo_2C$ surface since CO adsorption is very difficult on the O-terminated $Mo_2C$ surface. This effect may manifest itself through the reduction of the apparent pre-exponential factor and apparent activation barrier observed in table 4.2. This hypothesis can be tested through the derivation of a simple microkinetic model, which will be discussed in more detail in Chapter 6.

### *4.3. Electronic effect of $Mo_2C$ on Pt*

In chapter 3, it was reported that there is a very strong interaction between Pt and the $Mo_2C$ surface. Additionally, it was shown above that the chemistry of the epitaxial Pt/$Mo_2C$ is altered from that of Pt(111). These two points suggest that $Mo_2C$ may be altering the electronic structure of Pt. Figure 4.16 presents the d-bands of Pt(111) and Pt of the Pt/$Mo_2C$ structure. The calculated d-band centers are presented in the figure as $\varepsilon_d$.

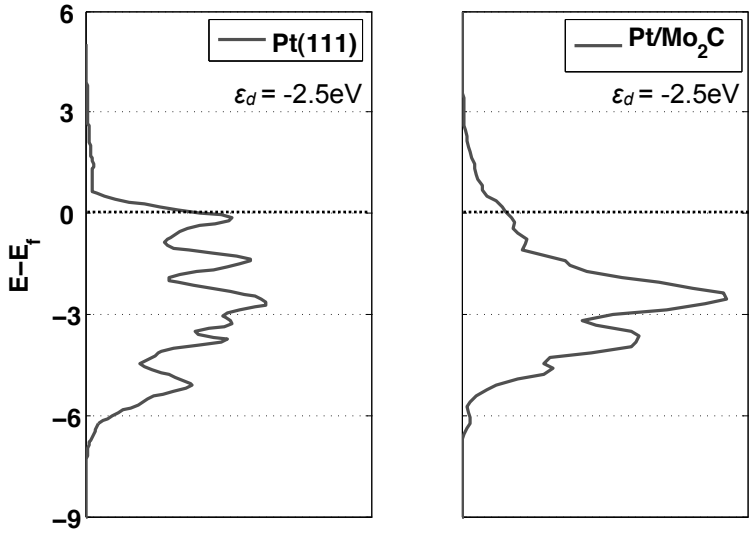


**Figure 4.16: d-band structure for Pt(111) (left) and Pt on Pt/$Mo_2C$ (right). The calculated d-band centers are presented as $\varepsilon_d$.**

According to the d-band model presented in chapter 1, if the d-band center of the site is closer to the fermi level, the site should have a higher chemical activity than a site with a low d-band center relative to the fermi level. The Pt/$Mo_2C$ system does not follow this model. Even though the d-band center of Pt/$Mo_2C$ is the same as Pt(111), the chemistry is clearly different, as illustrated in table 4.5. Additionally, the change in chemistry shows different trends, CO and H adsorb weaker on Pt/$Mo_2C$ but OH adsorbs stronger.

According to Xin et al. [12] some skin-alloys and adsorbates can deviate from the d-band model. This deviation can be understood by breaking down the adsorption energy into contributions from the s- and p-bands and the d-band, as in equation 4.8:

$$\Delta E_{ads} = \Delta E_{sp} + \Delta E_d \qquad \text{Eq. 4.8}$$

where $\Delta E_{ads}$ is the adsorption energy, $\Delta E_{sp}$ is the contribution of the sp-band, and $\Delta E_d$ is the contribution of the d-band.

Consider the case of CO adsorption on Pt(111) and Pt/$Mo_2C$. According to the Blyholder CO adsorption model [13,14], CO adsorption on metals is governed

by the interaction of the filled 5σ and unfilled 2π* of CO with the d-states of the model. Using a tight-binding framework, Hammer et al. [14] developed equation 4.9 to describe the d-band hybridization contributions to CO binding on metals:

$$E_{d-hyb} \simeq -4\left[f\frac{V_\pi^2}{\epsilon_{2\pi}-\epsilon_d}+fS_\pi V_\pi\right]-2\left[(1-f)\frac{V_\sigma^2}{\epsilon_d-\epsilon_{5\sigma}}+(1+f)S_\sigma V_\sigma\right] \quad \text{Eq. 4.9}$$

In equation 4.9, the first term represents contributions from the 2π* orbital and the second term represents contributions from the 5σ CO orbital. The coefficients of these terms originate from the degeneracy of the states. Within each orbital interaction term, the first term represents favorable interactions due to the hybridization of the orbitals and the second term represents energy costs due to the orthogonalization of the orbitals (Pauli repulsion). In these expressions, *f* is the filling factor of the d-band (the number of electrons divided by 10, ~0.9 for Pt), $\varepsilon_i$ is the energy of the respective orbital ($\varepsilon_d$ is the d-band center and the energy states of the CO orbitals after hybridization with the sp-band, which are considered constants), $V_i$ is the coupling matrix of the respective orbital and the d-states, and $S_i$ is the orbital overlap integral. Equation 4.9 can be simplified using the following approximations [14]:

$$S_i \approx -\alpha V_i \quad \text{Eq. 4.10}$$

$$S_\sigma / S_\pi \approx 1.3 \quad \text{Eq. 4.10}$$

After combining equation 4.9-4.11, the d-band contribution of the adsorption energy is a function of only *f*, $\varepsilon_d$, and $V_{2\pi}$. $V_{2\pi}$ can be calculated according to equation 4.12 [15]:

$$V_\pi = \eta_{pd\pi}\frac{\hbar^2 r_d^{3/2}}{m d^{7/2}} \quad \text{Eq. 4.12}$$

In equation 4.12, $\eta_{pd\pi}$ is a constant that is independent of the metal, $\hbar^2/m$ = 7.62 eV·Å$^2$, $r_d$ is the extent of the d-orbitals (1.04 for Pt), and *d* is the metal-CO bond

**Table 4.6: Parameters for evaluation of the d-band contribution (eq 4.9) to the CO binding energy on Pt(111) and Pt/$Mo_2C$**

| | $f$ | $\varepsilon_d$ (eV) | $d$ (Å) | $V_{2\pi}$ (eV) |
|---|---|---|---|---|
| Pt(111) | 0.92 | -2.5 | 1.86 | 1.25 |
| Pt/$Mo_2C$ | 0.93 | -2.5 | 1.93 | 1.11 |

distance. Table 4.6 lists these parameters for CO adsorbed on the Pt(111) and Pt/$Mo_2C$ surfaces.

Essentially, the contributions of the sp-band to adsorbate binding are always assumed to be constant, so the change in the adsorption energy stems from the change in the interaction with the d-band. This change is a function of $f$, $\varepsilon_d$, and $V_{2\pi}$. Table 4.6 shows that the only parameter that is changes between the Pt(111) and Pt/$Mo_2C$ surface is $V_{2\pi}$ and further inspection shows that this difference originates from the difference in the CO-metal bond distance. On Pt (111), CO is much closer to the surface than on Pt/$Mo_2C$.

The difference in bond distance is a result of a change in the electron density of Pt. Analysis of the d-band filling reveals that there is no charge transfer into the d-state of Pt from the surface Mo of $Mo_2C$. However, bader charge analysis indicates that there is a total charge transfer from Mo to Pt of ~0.5 electrons. This transfer must occur to the sp-band of Pt. As a result of the increased charge transfer, the CO bond distance is slightly elongated. This effect has a detrimental effect to the binding of CO and H but a beneficial effect on the binding of OH [12].

## 5. Conclusions

We propose that the WGS mechanism on Pt/$Mo_2C$ catalyst follows a red-ox mechanism which involves surface oxygen, and the catalyst is bifunctional. In this scenario, the $Mo_2C$ provides dissociation sites for water, and the Pt phase provides binding sites for CO. This is supported by XPS and DFT calculations. XPS analysis showed large amounts of oxygen on the $Mo_2C$ surface under WGS

conditions, though the molybdenum oxidation state was primarily $Mo^{2+}$ (that of $Mo_2C$). These results were consistent with DFT calculations which showed that water is not a strong enough oxidant to drive oxygen subsurface. Additionally, CO adsorbs weakly to the O-terminated $Mo_2C$ surface.

On the other hand, Pt were unable to dissociate water, but binds CO strongly. The atomically dispersed Pt on $Mo_2C$ (discussed in detail in chapter 3) is chemically less active than Pt(111). This fact stems from a change in the electronic structure of Pt induced by Mo. Although the d-band center of Pt does not change (when compared to Pt(111)), the structure is altered by the stretching and strong binding induced by the $Mo_2C$ surface. Additionally, charge transfer from Mo to the sp-states of Pt increases the charge density of Pt and results in elongated adsorbate-metal bonds, which affects the binding energy of Pt.

Ultimately, the addition of Pt to $Mo_2C$ may not directly affect the rate determining step (which is hypothesized to be CO oxidation), however it does greatly enhance the amount of CO adsorbed on the surface. This may manifest itself through a reduction of the apparent activation energy and the apparent pre-exponential factor. However, more work is required to confirm or refute this hypothesis. Microkinetic modeling combined with DFT transition state calculations can help to elucidate there hypotheses.

## 6. References


1. Moon, D.J. and J.W. Ryu, *Molybdenum Carbide Water–Gas Shift Catalyst for Fuel Cell-Powered Vehicles Applications.* Catalysis Letters, 2004. 92(1–2): p. 17-24
2. King, T., *Carbide and Nitride Supported Water-Gas Shift Catalysts.* 2007, The University of Michigan
3. Tominaga H. and M. Nagai, *Density Functional Theory of Water-Gas Shift Reaction* on Molybdenum Carbide. Journal of Physical Chemistry B, 2005. 109: p. 20415-20423
4. Liu, P. and J.A. Rodriguez, *Water-Gas Shift Reaction on Molybdenum Carbide Surfaces: Essential Role of the Oxycarbide.* Journal of Physical Chemistry B, 2006. 110: p. 19418-19425
5. J.P. Perdew, J.A. Chevary, S.H. Vosko, K.A. Jackson, M.R. Pederson, D.J. Singh, C. Fiolhais, *Atoms, Molecules, Solids, and Surfaces - Applications of the Generalized Gradient Approximation for Exchange and Correlation*. Physical Review B, 1992. 46: p. 6671-6687
6. Parthé, E. and V. Sadagopan, *The Structure of Dimolybdenum Carbide by Neutron Diffraction Technique.* Acta Crystallographica, 1963. 16: p. 202-205
7. NIST Chemistry WebBook: NIST Standard Reference Database Number 69. http://webbook.nist.gov/chemistry/
8. Reuter, K. and M. Scheffler, *Composition, Structure, and Stability of $RuO_2$ (110) as a Function of Oxygen Pressure*. Physical Review B, 2002. 65: 035406
9. Reuter K. and M. Scheffler, *Composition and Structure of the $RuO_2$(110) Surface in an $O_2$ and CO Environment: Implications for the Catalytic Formation of $CO_2$.* Physical Review B, 2003. 68: 045407
10. Perez-Romo, P., C. Potvin, J.-M. Manoli, M.M. Chehimi, and G. Djéga-Mariadassou, Phosphorus-Doped *Molybdenum Oxynitrides and Oxygen-ModifiedMolybdenum Carbides: Synthesis, Characterization, and Determination of Turnover Rates for Proplyene Hydrogenation.* Journal of Catalysis, 2002. 208: p. 187–196
11. K.G. Azzam, I.V. Babich, K. Seshan, L. Lefferts, *Bifunctional Catalyst for the Single-Stage Water–Gas Shift Reaction in Fuel Cell Applications. Part 1. Effect of the Support on the Reaction Sequence.* Journal of Catalysis, 2007. 251: p. 153–162

12. Xin, H. and S. Linic, *Exceptions to the d-band Model of Chemisorption on Metal Surfaces: The Dominant Role of Repulsion Between Adsorbate States and Metal d-States.* Journal of Chemical Physics, 2010. 132: 221101

13. Blyholder, G., *Molecular Orbital View of Chemisorbed Carbon Monoxide*. The Journal of Physical Chemistry, 1964. 68(10): p. 2772-2777

14. Hammer, B., Y. Morikawa, and J.K. Nørskov. *CO Chemisorption at Metal Surfaces and Overlayers.* Physical Review Letters, 1996. 76: p. 2141-2144

15. Harrison, W.A., *Electronic Structure and the Properties of Solids: the Physics of the Chemical Bond.* Freeman, 1980

# Chapter 5

# Comparing $Pt/Mo_2C$ catalysts to oxide supported catalysts

## 1. Introduction

Panagiotopoulou et al. [1] explicitly showed that the nature of the support caused a measurable change on the activity of oxide supported Pt WGS catalysts. Generally, catalysts supported on “irreducible” supports (such as $Al_2O_3$) performed worse than catalysts supported on “reducible” supports (e.g. $TiO_2$ and $CeO_2$). This demonstrates that there is a clear support effect associated with these catalysts.

Boisen et al. [2] also showed that the nature of the support plays a role in the activity of WGS catalysts, but further demonstrated that the nature of the support affected the role of the metal in the mechanism. On an inert support ($MgAl_2O_4$), the WGS activity of a wide range of metals (Fe, Co, Ni, Cu, Ru, Rh, Pd, Ag, Re, Ir, Pt, and Au) exhibited a strong correlation with the oxygen binding energy of the metal, however exhibited no correlation to the CO binding energy of the metal. The oxygen binding energy correlation followed a familiar “volcano curve,” with Cu performing the best. On the other hand, when the same metals were supported on a very active support ($Ce_{0.75}$ $Zr_{0.25}O_2$) there was no longer a correlation between oxygen binding energy and the WGS rates. However, the activity did correlate with CO binding energy, and Pt performing the best. These results suggest that when metals are supported on irreducible supports, water dissociation occurs on the metal and competes for sites with CO. However, when the metal is supported on an active, reducible support, the support (or metal-support interface) provides sites for water dissociation while the metal provides sites for CO adsorption.

These conclusions agree with results from literature that show that metals supported on active, reducible supports are bifunctional in nature. However, the nature of the reducible support directly affects the WGS mechanism. *Azzam et al.* [3,4] performed experiments using $Pt/TiO_2$, $Pt/CeO_2$, and $Pt/ZrO_2$ catalysts that suggest the three catalysts all support different WGS mechanisms. $Pt/TiO_2$ supports a red-ox mechanism while $Pt/CeO_2$ and $Pt/ZrO_2$ support formate mechanisms. These results are consistent with results from other groups for $CeO_2$ [4] and $TiO_2$ [5].

In chapter 4, it was shown that $Mo_2C$, like the oxide supports discussed above, played a central role in the WGS red-ox mechanism. In this chapter, we will compare the activity of $Pt/Mo_2C$ to traditional oxide supported Pt WGS catalysts ($Pt/TiO_2$, $Pt/CeO_2$, and $Pt/Al_2O_3$) with the aim of understanding how the role played by $Mo_2C$ compares to the role played by these oxides. In chapter 4, it was determined that the $Pt/Mo_2C$ catalysts supported a red-ox type mechanism, the same mechanism proposed in literature for the $TiO_2$ catalyst. Additionally, it was suggested that the $Mo_2C$ surface stores oxygen for this mechanism. Considering that an O-terminated $Mo_2C$ surface is active for WGS, it is conceivable that a molybdenum oxide catalyst should be active too. Therefore, we will also compare $Pt/Mo_2C$ to a $Pt/MoO_2$ catalyst. We will closely examine the role of $Mo_2C$, $TiO_2$, and $MoO_2$ in the WGS reaction to determine what special characteristics of $Mo_2C$ make $Pt/Mo_2C$ such an active catalyst.

## 2. Experimental Setup

### *2.1. Catalyst synthesis*

The molybdenum carbide supported catalyst in this section was synthesized using the same procedure described in chapter 2. In short, the $Mo_2C$ support was synthesized by carburizing ammonia paramolybdate ($(NH_4)_6Mo_7O_{24}\cdot 4H_2O$; 81-83% as $MoO_3$; Alpha *Æ*sar) using a 15% $CH_4/H_2$ mixture and a temperature programmed reduction scheme. The freshly synthesized material

was transfered under Ar to a deaerated, aqueous solution containing an appropriate amount of $H_2PtCl_6$ salt to achieve the desired loading. For this study, a 4%wt Pt/$Mo_2C$ samples was synthesized. After the loading was complete, the sample was dried at room temperature in $H_2$ and reduced in $H_2$ at 450 °C. Finally, the sample was passivated at room temperature using a 1% $O_2$/He gas mixture.

The molybdenum dioxide ($MoO_2$) sample was synthesized using a similar temperature programmed reaction process as described for the carbide synthesis. Ammonia paramolybdate was supported in a tubular reactor with quartz wool, and placed inside a vertical furnace. The powder was heated in hydrogen to 350 °C for 12 h initially increased at 5 °C/min. Next, the gas flow was changed to 1% $O_2$/He (20 mL/min) and the temperature was raised to 425 °C for 2 h, increased at 0.83 mL/min. Finally, the temperature was reduced back to room temperature. The procedure for metal loading followed that of the carbide catalyst exactly.

For the synthesis of the oxide catalysts, titanium dioxide ($TiO_2$, Aerosil Aeroxide P25, 99.5% $TiO_2$), cerium oxide ($CeO_2$, description) and aluminum oxide ($Al_2O_3$, Alpha Æsar) were calcined at 500 °C for 10 h. Platinum was loaded onto these supports using a dry impregnation method. Appropriate amounts of the platinum precursor salt ($H_2PtCl_6$) were added to just enough water to fill the volume of micropores in the supports (as measured by BET). The solution was added drop wise to the support and shook vigorously to ensure even coverage. The supports were then dried at 110 °C under vacuum overnight, and calcined at 450 °C for 4 h.

Since the final surface area for each of the catalyst supports were different, the Pt loading on each surface was adjusted such that the nominal Pt surface coverage was similar at $3.6\times10^{-4}$ g Pt/$m^2$, the surface coverage of the 4% wt Pt/$Mo_2C$ catalyst.

A $Cu/Zn/Al_2O_3$ sample was obtained from Süd Chemie to bench mark the performance of all the catalysts. It was pretreated according to the supplier's recommendations, and tested under the same conditions as the other catalysts.

### *2.2. Catalysts Characterization*

X-ray diffraction (XRD) measurements were performed on a Rigaku Miniflex DMAX-B rotating anode X-ray diffractometer with a Cu-Kα radiation source operated at 30 kV and 15 mA. Scans were conducted between 2θ of 20° and 80° at a rate of 2°/min and a resolution of 0.1°. Pt crystallite sizes were calculated according to the Scherrer equation:

$$\tau = \frac{K\lambda}{\beta \cos\theta} \qquad \text{Eq 5.1}$$

where $\tau$ is the crystallite domain size, $K$ is the shape factor (typically taken to be 0.9), $\lambda$ is the x-ray wavelength (1.54 nm for Cu-Kα) $\beta$ is the full width at half maximum of the peak (in radians), and $\theta$ is the Bragg angle of the peak (in radians).

Scanning electron microscopy was performed using a Phillips XL30FEG SEM operated at 25 keV. XEDS was performed using a UTW Si-Li Solid State X-ray Detector from EDAX. Mapping was conducted by detecting the Mo L and Pt M peaks. The resolution of the $Mo_2C$ maps were 62 nm/pixel. The resolution of the $MoO_2$ maps were 6 nm/pixel.

BET surface area analysis were recorded using a Micromeritics 2910 flow through chemisorption unit. The samples were pretreated as described above. Then, 30% $N_2/H_2$ was flown over the sample, and the temperature was reduced to 77 K. BET surface areas were calculated from single point $N_2$ desorption peaks. CO uptake experiments were also conducted in a Micromeritics 2910. After the samples were pretreated, the temperatures were increased in helium to ensure complete desorption of hydrogen. The temperature of the carbide catalyst

was raised to 600 °C while the temperature of the oxide catalysts were raised to 400 °C. After the temperature was lowered to ambient, the samples were pulsed with 5% CO/He. Uptake values were recorded with a TCD.

Inductively coupled plasma optical emission spectroscopy (ICP) was used to determine the weight loading of Pt on the molybdenum samples. The molybdenum samples were first dissolved in 3 mL of aqua regia (75%vol HCl and 25%vol $HNO_3$). One milliliter of each acid solution was diluted with 13 mL of deionized water. The resulting solution was analyzed using a Varian 710-ES ICP Optical Emission Spectrometer. Chemical standards for the analysis were obtained from Inorganic Ventures.

### *2.3. WGS reaction rates*

Water gas shift experiments were performed using the same procedure reported in chapter 3. In short, the catalysts were initially pretreated. The carbide catalyst was pretreated in 15% $CH_4/H_2$ flown at 100 mL/min at 590 °C for 4 h. The $MoO_2$ catalyst was pretreated in 4% $H_2/N_2$ flown at 100 mL/min at 300 °C for 4 h. The $TiO_2$, $CeO_2$, and $Al_2O_3$ catalysts were pretreated in 10% $H_2/N_2$ at 300 °C for 1 h. The $Cu/Zn/Al_2O_3$ sample was pretreated according to vendor recommendations (4% $H_2/N_2$ flown at 100 mL/min at 200 °C for 4 h heated at 2.9 °C/min). The catalysts were then exposed to a reformate gas mix (11% CO, 21% $H_2O$, 43% $H_2$, 6% $CO_2$, 19% $N_2$), and steady state CO and $CO_2$ product concentrations were recorded using a GC. Refer to chapter 3 for a discussion of how the conversion and forward rates were calculated.

The conversion of each of the catalysts were held in the differential regime (<10%). To accomplish this, the temperature range in which the tests were performed was adjusted. Rates for the least active catalysts ($Pt/MoO_2$ and $Pt/Al_2O_3$) were recorded from 400 °C to 440 °C. Rates for the other oxide catalysts ($Pt/TiO_2$ and $Pt/CeO_2$) were recorded from 260 °C to 300 °C.

### *2.4. DFT calculations*

DFT calculations were performed using DACAPO software. The $Mo_2C$ (100) surface was modeled as a 1x1 supercell with 5 atomic layers (3 layer of Mo and 2 layers of C, arranged in an alternating fashion) and 3x3x1 Monkhorst-Pack k-point sampling. The calculated lattice constants of the orthorhombic unit cell (a=4.73 Å, b=6.17 Å, c=5.34 Å) are in good agreement with experimental values (a=4.72 Å, b=6.00 Å, c=5.19 Å) [6]. As discussed in chapter 4, an oxygen terminated surface best describes the $Mo_2C$ surface under reaction conditions. In all calculations, the upper two atomic layers, in addition to the adsorbates, were allowed to relax.

The $MoO_2$ bulk structure is very close to that of rutile, except that there is a slight distortion in Mo-O bond lengths, which arise due to a Peierls instability [7]. The $MoO_2$ geometry was optimized according to the monoclinic crystal structure. The calculated lattice constants (a=5.75 Å, b=4.97 Å, c=5.87 Å, β=120.3°) are comparable to the experimental values (a=5.61 Å, b=4.86 Å, c=5.63 Å, β=120.9°) [7]. Ab-initio thermodynamic calculations indicated that a surface with all the bridged oxygen sites filled was the most energetically stable under the relevant conditions discussed in this contribution. Therefore, this surface was used in the calculations.

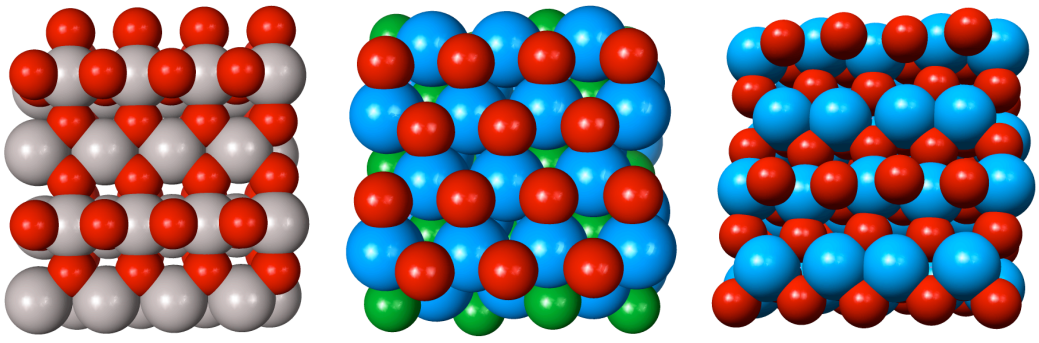

**Figure 5.1: Illustrations of the $TiO_2$ (left), O-terminated $Mo_2C$ (center), and $MoO_2$ (right) surfaces used in this study. Each illustration represents a 2x2 representative of the unit cells.**

The $TiO_2$ surface used in this study is the rutile (110) surface. This is the most stable crystal structure, and additionally, produces the most reducible $TiO_2$ surface. Illustrations for all the surfaces can be viewed in figure 5.1.

## 3. Results

### *3.1. Catalyst Characterization*

XRD results of the catalysts can be viewed in figures 5.2-5.6. The dashed, grey, vertical lines indicate the position of Pt peaks. The $TiO_2$ (2θ ~40.2°), $CeO_2$ (2θ ~40.2°), and $MoO_2$ (2θ ~40.6°) catalysts exhibit small peaks that are close to the highest intensity Pt peak (2θ ~39.8°) that are not observed in the support scans. Unfortunately, the $Mo_2C$ and $Al_2O_3$ support patterns have peaks that overlap this Pt peak. Table 5.1 displays Pt particle sizes calculated using the Scherrer equation (Eq. 5.1) for the $TiO_2$, $CeO_2$, and $MoO_2$ catalysts.

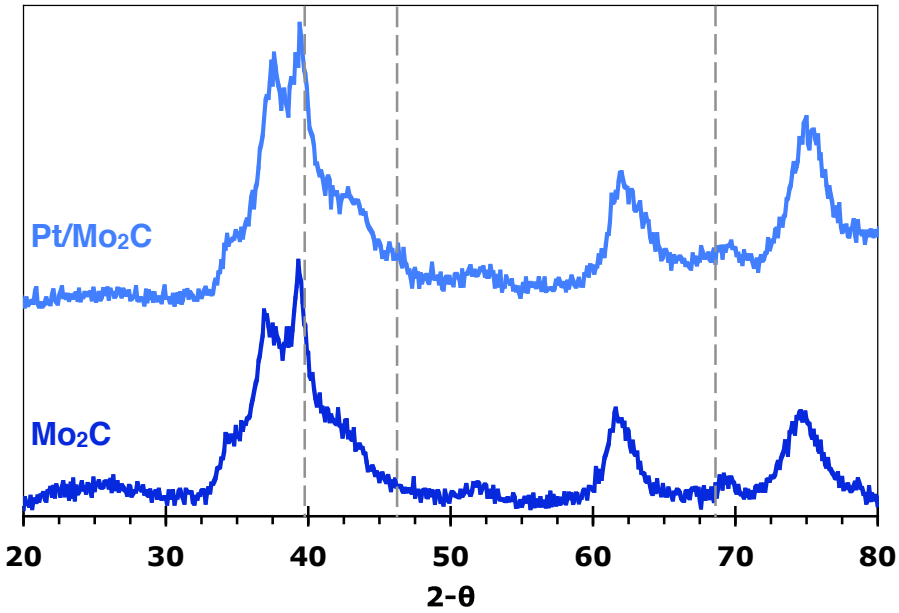


**Figure 5.2: XRD pattern for $Pt/Mo_2C$ (top) and $Mo_2C$ (bottom). The location of Pt peaks are indicated by grey dashed lines.**

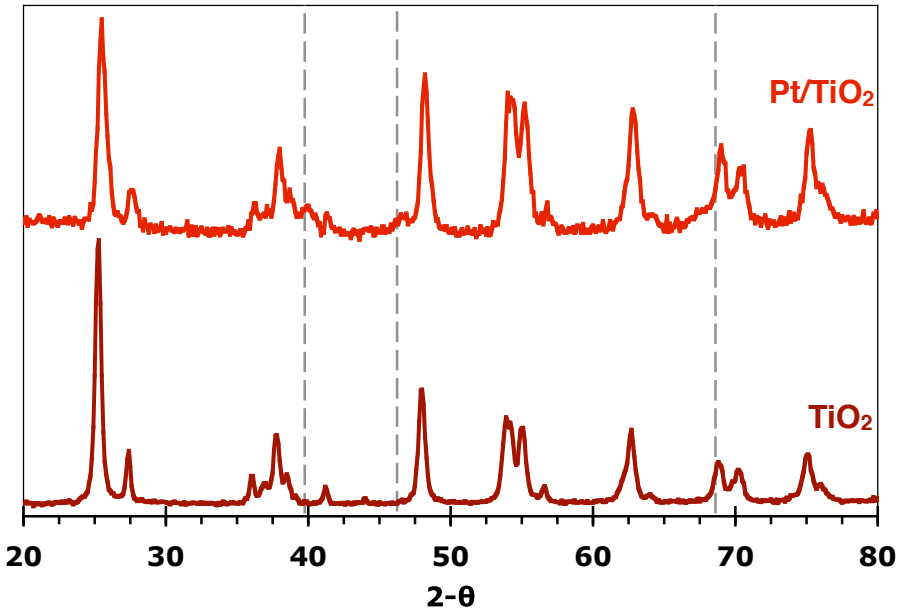


**Figure 5.3: XRD pattern for $Pt/TiO_2$ (top) and $TiO_2$ (bottom). The location of Pt peaks are indicated by grey dashed lines.**

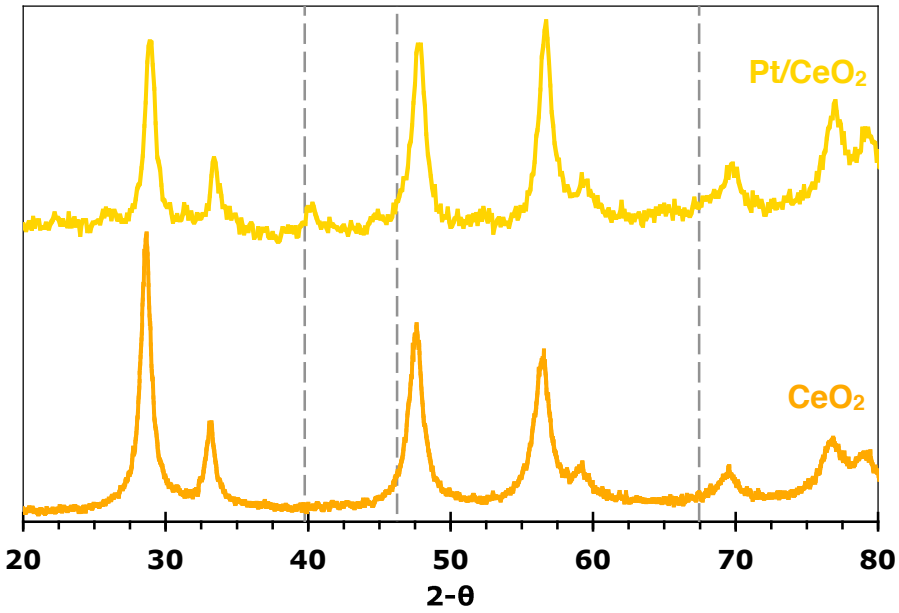


**Figure 5.4: XRD pattern for $Pt/CeO_2$ (top) and $CeO_2$ (bottom). The location of Pt peaks are indicated by grey dashed lines.**

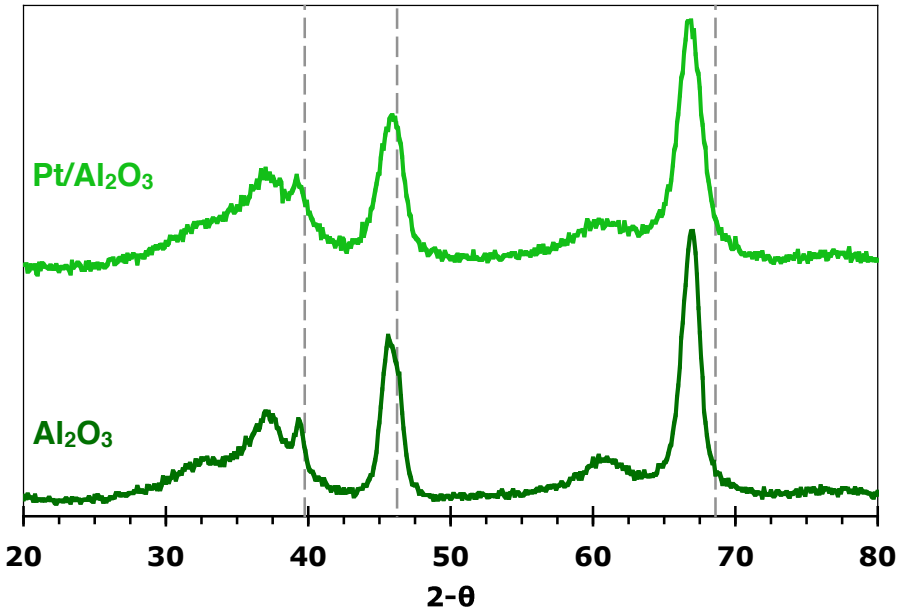


**Figure 5.5: XRD pattern for $Pt/Al_2O_3$ (top) and $Al_2O_3$ (bottom). The location of Pt peaks are indicated by grey dashed lines.**

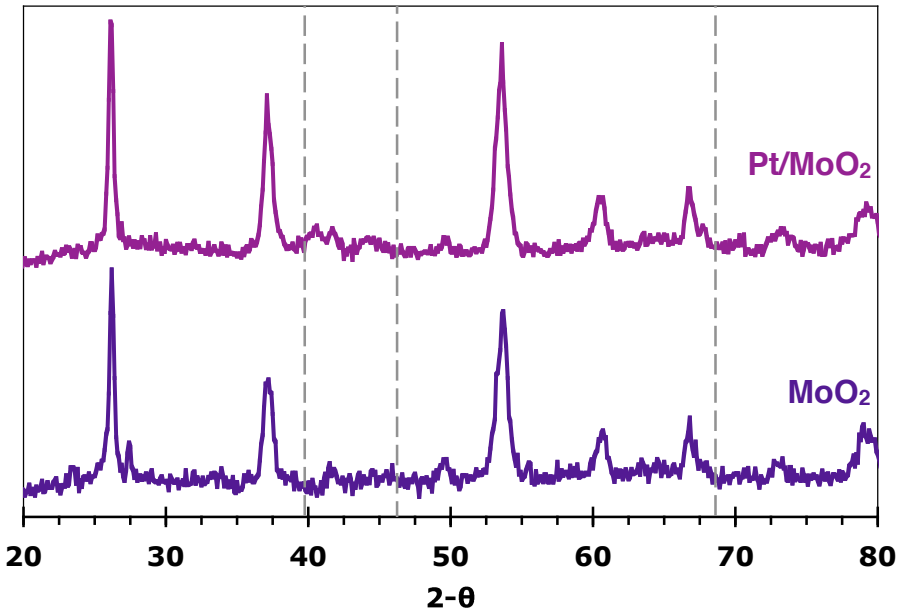


**Figure 5.6: XRD pattern for $Pt/MoO_2$ (top) and $MoO_2$ (bottom). The location of Pt peaks are indicated by grey dashed lines.**

Figures 5.7 and 5.8 show the SEM/EDX mapping micrographs of the Pt/ $Mo_2C$ and Pt/ $MoO_2$ surfaces. Figure 5.7 and the analysis of the Pt structures on $Mo_2C$ were discussed in detail in chapter 3. Figure 5.8 shows the SEM/EDX mapping of the $Pt/MoO_2$ catalysts. The Pt particles are identified as the large

spherical structures. Statistical averaging indicates that the average Pt particle size about 1 μm.

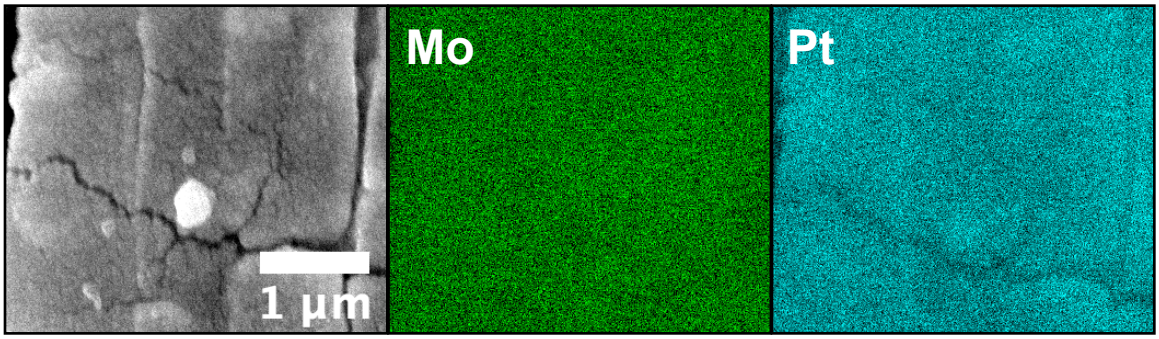


**Figure 5.7: SEM micrograph and EDAX elemental mapping of an 8% Pt/$Mo_2C$ surface. The middle frame displays Mo and the right frame displays Pt. Refer to chapter 3 for a detailed discussion.**

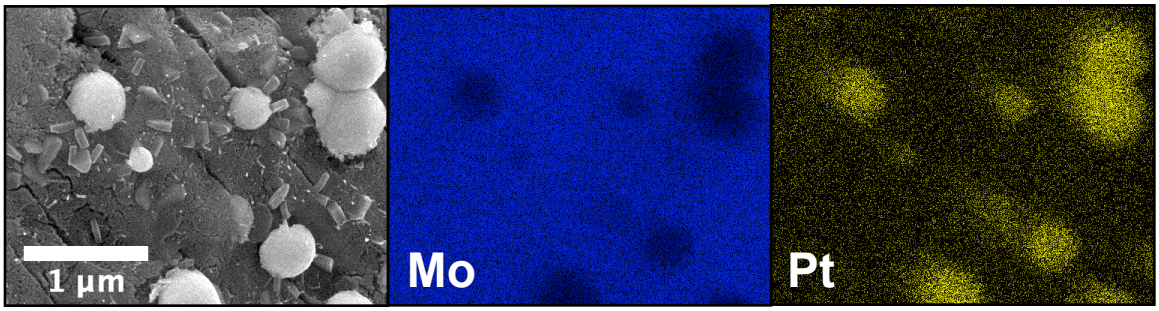


**Figure 5.8: SEM micrograph and EDAX elemental mapping of the Pt/$MoO_2$ surface. The middle frame displays Mo and the right frame displays Pt.**

Table 5.1 shows the complete results of the catalyst characterization. In addition to the characterization described above, this table includes BET surface areas, metal dispersions (calculated from CO uptake values), and Pt particle sizes calculated from a variety of the techniques used. Platinum loading data is also included. For the molybdenum catalysts (which used a wet impregnation procedure) these were measured using ICP. The oxide loadings (which were achieved using a dry impregnation procedure) were assumed to achieve 100% loading and calculated using the actual metal contents in the loading experiments.

It is observed that the Pt particle size on $MoO_2$ is significantly larger than $Mo_2C$. Additionally, the Pt uptake during the loading procedure was about half the

nominal loading. These results indicate that the interaction between Pt and $MoO_2$ is significantly less than that of Pt and $Mo_2C$ discussed in chapters 2 and 3.

**Table 5.1: Characterization results of the Pt catalysts**

| Catalyst | BET surface area ($m^2/g$) | Pt loading | | Metal Dispersion (%) | Pt Particles Diameter (nm) |
|---|---|---|---|---|---|
| | | Nominal | Actual | | |
| $Pt/Mo_2C$ | 133 | 4.0% | 3.8% | > 200[b] | 27 ± 2[c] |
| $Pt/TiO_2$ | 57 | 1.7% | 2.0%[a] | 31 | 14[d]<br>8[e] |
| $Pt/CeO_2$ | 151 | 4.5% | 5.0%[a] | 88 ± 6 | 3 ± 1[d]<br>10[e] |
| $Pt/Al_2O_3$ | 78 | 2.3% | 2.7%[a] | 51 ± 18 | 10 ± 4[d] |
| $Pt/MoO_2$ | 21 | 1.6% | 0.9% | > 200[b] | 970 ± 110[c]<br>12[e] |
| $Cu/Zn/Al_2O_3$ | 60 | ----- | ----- | ----- | ----- |

[a] *Values were determined based on concentration of precursor solutions.*
[b] *CO binds to the support, so values could not be accurately determined from adsorption experiments*
[c] *Determined from SEM imaging*
[d] *Determined from Chemisorption dispersion calculations*
[e] *Determined from the Scherrer Equation*

### *3.2. WGS reaction rates*

Figure 5.9 shows the WGS reaction rate results normalized to total BET surface area; figure 5.10 shows the WGS rate data normalized to total mol of Pt loaded on the support. Qualitatively, both graphs look similar. This is not surprising since all the catalysts were synthesized with similar molar Pt loadings. As in chapter 4, the $Pt/Mo_2C$ catalyst is slightly more active than the $Cu/Zn/Al_2O_3$ catalyst. Of the oxide catalysts, the $Pt/CeO_2$ catalysts showed the highest activity; the $Pt/TiO_2$ catalysts showed the second highest activity. Both of these oxides were much more active than the $Pt/Al_2O_3$ catalyst or the $Pt/MoO_2$ catalyst, which was essentially inactive even at the high temperatures used in this study. Table 5.2 shows the apparent activation energies and pre-exponential factors of the catalysts.

**Table 5.2: Results from the kinetic analysis of the WGS data. The error of $A_{app}$ is orders of magnitude less than the absolute values and insignificant relative to the reported differences**

| Catalyst | WGS Temp Range (°C) | $E_{a,app}$ (kJ/mol) | $A_{app}$ | Literature values (kJ/mol) |
|---|---|---|---|---|
| $Pt/Mo_2C$ | 240-200 | 60±4 | $2.9x10^6$ | ------ |
| $Pt/TiO_2$ | 300-260 | 51±6 | $3.8x10^4$ | 59 [8], 66 [10], |
| $Pt/CeO_2$ | 300-260 | 80±1 | $4.5x10^7$ | 91 [8], 75 [9], 90 [10] |
| $Pt/Al_2O_3$ | 440-400 | 86±8 | $3.2x10^6$ | 84 [9], 80 [10], |
| $Pt/MoO_2$ | 440-400 | 47±9 | $1.3x10^3$ | ------ |
| $Cu/Zn/Al_2O_3$ | 240-200 | 51±6 | $1.4x10^5$ | ------ |

The $Mo_2C$, $TiO_2$, and $MoO_2$ all have similar apparent activation barriers. In chapter 4, it was shown that the $Pt/Mo_2C$ catalyst supported a red-ox type mechanism. As discussed in the introduction, the $TiO_2$ catalyst also exhibits a red-ox type mechanism. This suggests that the $MoO_2$ catalyst may also follow a red-ox type mechanism. The $Al_2O_3$ and $CeO_2$ catalysts have a very different apparent activation energies. It has been shown in literature that these catalysts do not exhibit a red-ox type mechanism [3,4].

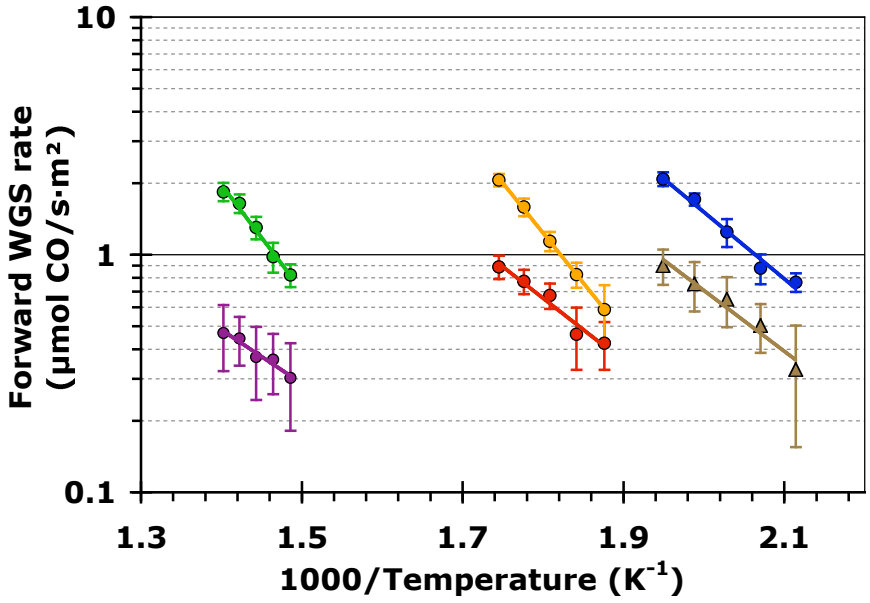


**Figure 5.9: WGS rates normalized to the total BET surface area of the catalyst: $Pt/Mo_2C$ - Blue, $Pt/CeO_2$ - Yellow, $Pt/TiO_2$ - Red, $Pt/Al_2O_3$ - Green, $Pt/MoO_2$ - Purple, $Cu/Zn/Al_2O_3$ - Brown**

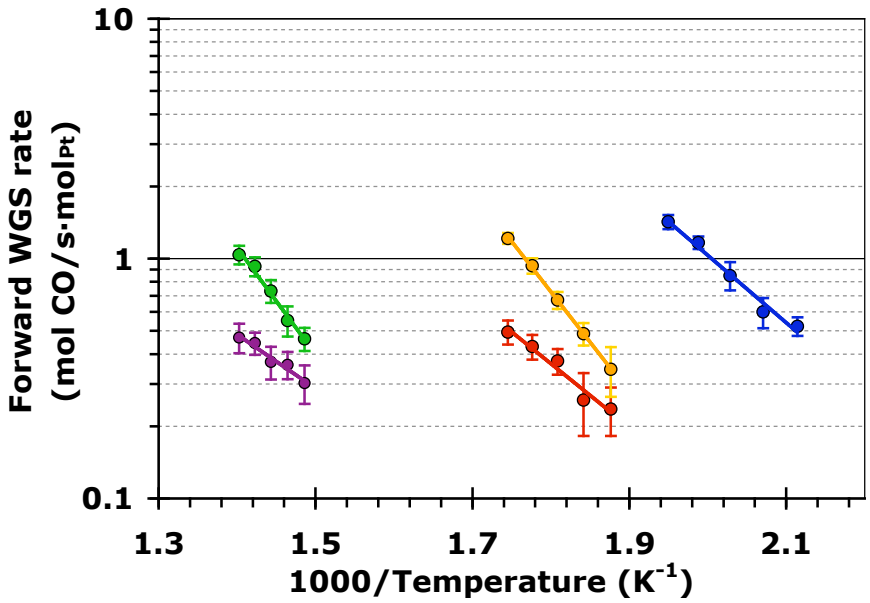


**Figure 5.10: WGS rates normalized to the total moles of Pt on the catalyst: Pt/$Mo_2C$ - Blue, Pt/$CeO_2$ - Yellow, Pt/$TiO_2$ - Red, Pt/$Al_2O_3$ - Green, Pt/$MoO_2$ - Purple**

### *3.3. DFT calculations*

Figure 5.11 shows the free energy diagram of the WGS red-ox mechanism on the $MoO_2$, O-terminated $Mo_2C$ surface, and the $TiO_2$ surface. The steps of the mechanism are indicated below, and indexed on the graph by the numbers:

⓪ $$CO + H_2O + {}^{v} + O^{v}$$ Eq. 5.2

① $$H_2O + {}^{v} + O^{v} \rightleftharpoons 2OH^{v}$$ Eq. 5.3

② $$2OH^{v} \rightleftharpoons H_2 + 2O^{v}$$ Eq. 5.4

③ $$CO + {}^{*} \rightleftharpoons CO^{*}$$ Eq. 5.5

④ $$CO^{*} + O^{v} \rightleftharpoons CO_2 + {}^{*} + {}^{v}$$ Eq. 5.6

The first step of the mechanism is water adsorption and dissociation to form two hydroxyls adsorbed to the surface. This step is favorable on every surface. It is the most favorable on the $MoO_2$ surface and least favorable on the $Mo_2C$ surface (although still favorable overall by ~ 0.6 eV). The second step, decomposition of the hydroxyl groups to form hydrogen, differentiates the surfaces. The hydroxyl groups are very stable on the $MoO_2$ surface. Thus, this

step is very endothermic, ~ 1.4 eV. On the other hand, the hydroxyl groups are very unstable on the $TiO_2$ surface, so this step is very exothermic, ~ -1.5 eV. As was discussed in chapter 4, hydroxyl stability on the $Mo_2C$ surface is in an optimal range such that this step is essentially thermo-neutral. The next step in the mechanism is CO adsorption. This step is only favorable by the $MoO_2$ surface. Therefore, as discussed in chapter 4, Pt serves as a binding site for CO on the $Mo_2C$ and, apparently, the $TiO_2$ surface. In figure 5.11, the grey data represents the adsorption of CO on a $Mo_2C$ surface with one "epitaxial" monolayer of Pt (see chapter 3 and 4 for a detailed discussion of this model). Again, adding Pt to the $Mo_2C$ surface makes the third step essentially thermo-neutral. The final step also differentiates the surfaces. The mechanism has been mainly downhill for the $TiO_2$ surface to this point, but oxidation of CO by a surface oxygen to form $CO_2$ is endothermic, ~ 0.7 eV. On the $MoO_2$ surface, this step is exothermic, ~ -0.5 eV. On the $Mo_2C$ surface (using a Pt binding site) this step is again almost thermo-neutral.

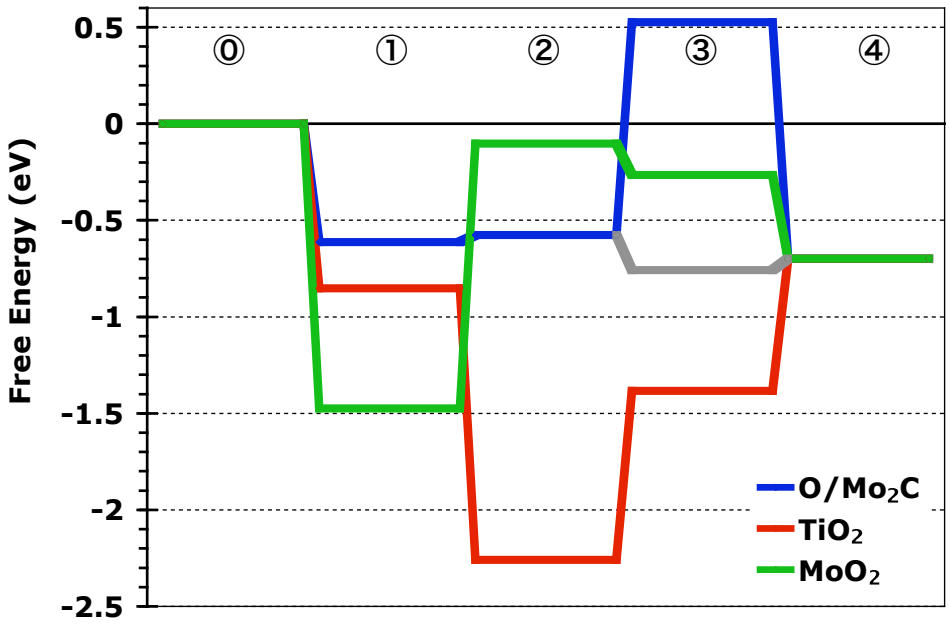


**Figure 5.11: Free energy diagram of the WGS red-ox mechanism on $O/Mo_2C$ (Blue), $TiO_2$ (Red), and $MoO_2$ (Green).**

## 4. Discussion

The water-gas shift results indicate that, on a surface area basis, the $Mo_2C$ catalyst exhibited the highest rate. Additionally, the $Mo_2C$, $TiO_2$, and $MoO_2$ catalyst exhibited similar apparent activation barriers. The $Al_2O_3$ and $CeO_2$ catalyst exhibited similar apparent activation barriers to each other, but different from the previous three. In chapter 4, it was concluded that the $Mo_2C$ surface exhibited a red-ox type mechanism. Literature has shown that $TiO_2$ catalysts also exhibit a red-ox mechanism [3,5]. For this reason, it is assumed that the $MoO_2$ surface also exhibits a red-ox type mechanism.

Evaluation of the potential energy diagram in figure 5.11 offers some clarity for the energetics involved in the red-ox mechanism on the three different catalyst surfaces, and the resulting difference in catalytic activity. For the $MoO_2$ surface, water dissociation and CO oxidation are favorable, but decomposition of the hydroxyls is very endothermic and probably rate limiting. On the other hand, water decomposition and hydroxyl decomposition are very facile on the $TiO_2$ surface, but CO oxidation is very endothermic and probably rate limiting. With the addition Pt on the $Mo_2C$ surface, the overall mechanism is slightly downhill, but most of the steps are thermo-neutral. Both the hydroxyl decomposition and CO oxidation may be rate limiting on this surface.

The discussion above implies that there may be two different (but related) critical parameters to benchmark the activity of the support. They are hydroxyl stability and oxygen binding energy. These values are given in table 5.3 for the surfaces discussed above. The trends displayed in table 5.3 correlate well with the trends of the different catalysts in figure 5.11. The rate limiting step for the $TiO_2$ surface was CO oxidation. This is manifest through the strong binding energy of oxygen to the $TiO_2$ surface. Analogously, the rate limiting step for the $MoO_2$ surface was hydrogen formation. Table 5.3 shows that hydroxyls are the

most stable on this surface. The red-ox mechanism exhibits a thermo-neutral path on the $Mo_2C$ surface because this surface exhibits intermediate values for both binding energies.

**Table 5.3: Oxygen vacancy formation and hydroxyl stability of the surfaces (all values are in eV)**

| | $O^v \rightleftharpoons 0.5O_2 + {}^v$ | $OH^* \rightleftharpoons 0.5H_2 + O^*$ |
|---|---|---|
| $TiO_2$ | 5.0 | -0.3 |
| $O/Mo_2C$ | 3.3 | 0.4 |
| $MoO_2$ | 2.9 | 1.1 |

Fernandez et al. [11] showed that there is a linear relationship between oxygen binding energy and OH binding energy (thus, also hydroxyl stability) on a surface. Considering these results and the results of Boisen et al. [2], discussed in the introduction, for various catalysts with the same metal using different supports, we should be able to use oxygen binding energy as a descriptor for the activity of a support for WGS. However, it should be emphasized that one needs to consider the nature of the active site. For example, the active site for CO oxidation on the $TiO_2$ catalyst is likely a metal-support interface. In this case, the relative binding energy of oxygen at this site compared to the oxygen binding energy of the O-terminated $Mo_2C$ surface should indicate the relative activities of the two catalysts.

An interesting side note that arises from this interpretation relates to the perception of pyrophoricity, that is the tendency of a material to oxide very rapidly in oxygen atmospheres creating copious amounts of heat. This is obviously an undesirable characteristic of a material, as it makes handling of the material much more difficult. Further, the highly oxidized material may have vastly different characteristics than are desired for a suitable catalyst. The current low temperature WGS industrial catalyst, $Cu/Zn/Al_2O_3$, suffers from this shortcoming, as does the catalyst which has been the focus of this work, $Pt/Mo_2C$. However, as discussed above, the binding energy of oxygen to the $Mo_2C$ surface is ideal

for the WGS red-ox mechanism. We concluded that it was strong enough to dissociate water, but weak enough to easily oxidize CO. However, according to the results in table 5.3, a suitable oxygen binding energy is -6.6eV/oxygen molecule (i.e. very exothermic). Therefore, one could say that if a surface is active enough to dissociate water, it must aggressively bind oxygen. Considering these conclusions, it seems that pyrophoricity may be a necessary characteristic of a highly active WGS catalysts rather than an undesired one.

## 5. Conclusions

Pt/$Mo_2C$ exhibited the highest rates of all the catalysts tested. When comparing the $Mo_2C$ support to the other oxide catalysts (with similar mechanisms), it is observed that $Mo_2C$ serves as an effective support because the oxygen binding energy of the surface falls in a range which is well suited for WGS. Titania, which binds oxygen stronger than $Mo_2C$, has difficulty oxidizing CO but easily dissociates water and produces hydrogen. On the other hand, molybdenum dioxide, which binds oxygen weaker than $Mo_2C$, easily oxidizes CO but has difficulty producing hydrogen because hydroxyls are very stable on the surface. The oxygen binding energy is quite high (~6.6 eV/$O_2$ molecule), which manifests itself in the pyrophoric nature of the support. This leads us to speculate that pyrophoricity is a necessary characteristic of a highly active WGS catalysts.

## 6. References


1. Panagiotopoulou P. and D.I. Kondarides, *Effect of the Nature of the Support on the Catalytic Performance of Noble Metal Catalysts for the Water–Gas Shift Reaction.* Catalysis Today, 2006. 112: p. 49–52
2. Boisen, A., T.V.W. Janssens, N. Schumacher, I. Chorkendorff, and S. Dahl, *Support effects and catalytic trends for water gas shift activity of transition metals.* Journal of Molecular Catalysis A: Chemical, 2010. 315: p. 163–170
3. K.G. Azzam, I.V. Babich, K. Seshan, L. Lefferts, *Bifunctional Catalyst for the Single-Stage Water–Gas Shift Reaction in Fuel Cell Applications. Part 1. Effect of the Support on the Reaction Sequence.* Journal of Catalysis, 2007. 251: p. 153–162
4. Jacobs, G., A.C. Crawford, and B.H. Davis, *Water-gas Shift: Steady State Isotope Switching Study of the Water-Gas Shift Reaction Over Pt/ceria Using in-situ DRIFTS.* Catalysis Letters, 2005. 100(3–4): p. 147-152
5. Kalamaras, C.M., P. Panagiotopoulou, D.I. Kondarides, and A.M. Efstathiou, *Kinetic and Mechanistic Studies of the Water–Gas Shift Reaction on Pt/$TiO_2$ Catalyst.* Journal of Catalysis, 2009. 264(2): p. 117-129
6. Parthé, E. and V. Sadagopan, *The Structure of Dimolybdenum Carbide by Neutron Diffraction Technique.* Acta Crystallographica, 1963. 16: p. 202-205
7. Eyert, V., R. Horny, K.-H. Höck, and S. Horn, *Embedded Peierls Instability and the Electronic Structure of $MoO_2$.* Journal of Physics: Condensed Matter, 2000. 12: p. 4923–4946
8. Thinon, O., K. Rachedi, F. Diehl, P. Avenier, and Y. Schuurman, *Kinetics and Mechanism of the Water–Gas Shift Reaction Over Platinum Supported Catalysts* Topics in Catalysis, 2009. 52: p. 1940–1945
9. Phatak, A.A., N. Koryabkina, S. Rai, J.L. Ratts, W. Ruettinger, R.J. Farrauto, G.E. Blau, W.N. Delgass, and F.H. Ribeiro, *Kinetics of the Water–Gas Shift Reaction on Pt Catalysts Supported on Alumina and Ceria.* Catalysis Today, 2007. 123: p. 224–234
10. Panagiotopoulou P. and D.I. Kondarides, *A Comparative Study of the Water-Gas Shift Activity of Pt Catalysts Supported on Single ($MO_x$) and Composite ($MO_x/Al_2O_3$, $MO_x/TiO_2$) Metal Oxide Carriers.* Catalysis Today, 2007. 127: p. 319–329
11. Fern, E.M, F. Abild-Pedersen, J. Kleis, B. Hinnemann, J. Rossmeisl, T. Bligaard, and J.K. Nørskov, *Scaling Relationships for Adsorption Energies on Transition Metal Oxide, Sulfide, and Nitride Surfaces,* Angewandte Chemie International Edition, 2008. 47: p. 4683 –4686

# Chapter 6
# General conclusions and future work

## 1. General Conclusions

The major goals of this work were to understand the underlying mechanism governing metal loading on carbide supports, to characterize the supported metal structures, to gain a general understanding of Pt/$Mo_2C$ catalysts under operating WGS conditions, and to understand the principal characteristics of the catalyst at the root of its high activity. Most of the observed phenomenon stem from a strong metal-support interaction.

It is hypothesized that the red-ox chemistry of the precursor salt and the support surface dominate the loading mechanism. Generally, metal precursors with high reduction potentials (such as Pt, Pd, and Cu) exhibited high loadings compared to metals with low reduction potentials (Fe, Ni, and Co). Additionally, the nature of the precursor salt may play a role in the mechanism. Chloride ions may poison the surface and inhibit the loading mechanism. The direct interaction between the support and the precursor metal helps to form a highly dispersed metal phase.

We used a combination of x-ray absorption spectroscopy and density functional theory calculations to deduce that the Pt phase of the Pt/$Mo_2C$ catalyst is a mixture of atomically dispersed metal and small metal particles. The Pt-Pt and Pt-Mo coordination numbers stayed relatively constant as a function of Pt metal loading. Additionally, DFT calculations showed that there is a very strong interaction between the first layer of Pt and the $Mo_2C$ surface, however additional layers are thermodynamically unfavorable. This suggest that Pt would prefer to

wet the entire surface, but will form particles in areas where the $Mo_2C$ surface cannot be accessed.

Figure 6.1 illustrates our understanding of the catalyst under WGS operating conditions:

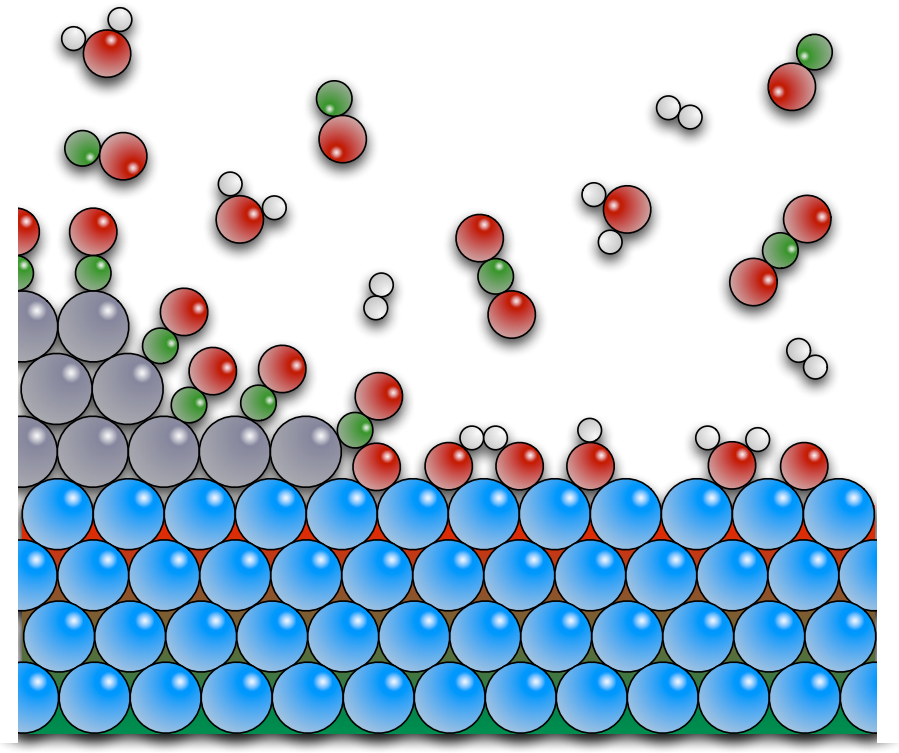

**Figure 6.1: Illustration of the Pt/$Mo_2C$ surface under WGS operating conditions.**

Under WGS operating conditions, the bulk phase of the catalyst remains a carbide. However, the surface is saturated with oxygen groups (i.e. adsorbed water, hydroxyl groups, and surface oxygen). The Pt phase provides binding sites for CO adsorption and oxidation, which occurs at the metal/support interface. The chemistry of the particles mimics that of Pt(111), but the chemistry of the atomically dispersed phase is altered from that of Pt(111). A charge transfer from Mo to the sp-states of Pt causes the adsorbate bonds to be elongated. For most adsorbates, this decreases the binding energy, however for OH it increases it [1]. Oxygen is removed from the surface during CO oxidation at the Pt-$Mo_2C$ interface, and replenished through $H_2O$ dissociation. The hydroxyls

also present on the surface decompose to form hydrogen. This mechanism is consistent with the red-ox mechanism, also observed on $Pt/TiO_2$ catalysts. [2,3]

## 2. Immediate future projects

In chapter 4, it was proposed that the addition of Pt to the $Mo_2C$ increased the overall rate by enhancing the coverage of CO on the surface. This hypothesis could be tested, and the measured, experimental data could be directly related to the theoretical, DFT calculations through a microkinetic model. Consider the following, simplified red-ox mechanism steps:

$$\text{①} \quad H_2O + {}^v + O^v \rightleftharpoons 2OH^v \qquad \text{Eq. 6.1}$$

$$\text{②} \quad 2OH^v \rightleftharpoons H_2 + 2O^v \qquad \text{Eq. 6.2}$$

$$\text{③} \quad CO + {}^* \rightleftharpoons CO^* \qquad \text{Eq. 6.3}$$

$$\text{④} \quad CO^* + O^v \rightleftharpoons CO_2 + {}^* + {}^v \qquad \text{Eq. 6.4}$$

where $^v$ represents an oxygen vacancy site which can be occupied by either an oxygen atom or a hydroxyl molecule, and * represents a CO binding site. For the $Mo_2C$ catalyst, the CO binding site is assumed to be on top of an O-terminated surface, while the binding site is atop a Pt atom on the $Pt/Mo_2C$ catalyst. If we assume that eq. 6.3 is the rate limiting step, then by using the quasi-equilibrium approximation we can derive the following equations:

$$K_1 = \frac{V_{OH}^2}{P_{H_2O} V_* V_O} \qquad \text{Eq. 6.5}$$

$$K_2 = \frac{V_O^2 P_{H_2}}{V_{OH}^2} \qquad \text{Eq. 6.6}$$

$$K_3 = \frac{\theta_{CO}}{P_{CO} \theta_*} \qquad \text{Eq. 6.7}$$

$$r_4 = k_4 \left( \theta_{CO} V_O - P_{CO_2} V_* \theta_* / K_4 \right) \qquad \text{Eq. 6.8}$$

$$\theta_* = 1 - \theta_{CO} \qquad \text{Eq. 6.9}$$

$$V_* = 1 - V_O - V_{OH} \quad \text{Eq. 6.10}$$

$K_n$ is the equilibrium constant for the n$^{th}$ elementary step, $r_4$ is the total rate of the 4$^{th}$ elementary step ($r_4^+$ will be referred to as the forward rate), and eq. 6.9 and 6.10 represent a site balance for the CO adsorption sites and oxygen vacancy sites, respectively. The equilibrium constant of each step can be calculated using the familiar thermodynamic equations:

$$\ln K_n = -\Delta G_n / RT \quad \text{Eq. 6.11}$$

$$\Delta G_n = \Delta H_n - T\Delta S_n \quad \text{Eq. 6.12}$$

In eq. 6.12, the change in enthalpy of each step can be calculated using DFT calculations. If it is assumed that the entropy of surface intermediates are negligible to that of gas phase molecules, the change in entropy can be calculated from values of the gas phase species taken from the NIST chemistry webbook [4]. Using equations 6.5 - 6.10, all the variables in the model can be solved for:

$$\theta_{CO} = K_3 P_{CO} \theta_* \quad \text{Eq. 6.13}$$

$$\theta_* = 1/\left(1 + K_3 P_{CO}\right) \quad \text{Eq. 6.14}$$

$$V_O = K_1 K_2 P_{H_2O} V_* / P_{H_2} \quad \text{Eq. 6.15}$$

$$V_O = K_1 P_{H_2O} V_* \left(K_2 / P_{H_2}\right)^{1/2} \quad \text{Eq. 6.16}$$

$$V_* = 1 \Big/ \left(1 + K_1 K_2 P_{H_2O} / P_{H_2} + K_1 P_{H_2O} \left(K_2 / P_{H_2}\right)^{1/2}\right) \quad \text{Eq. 6.17}$$

$$r_{obs} = r_4 = k_4(\theta_{CO} V_O - P_{CO_2} V_* \theta_* / K_4) \quad \text{Eq. 6.18}$$

By using a similar analysis as presented by Lynggaard et al. [5], the observable, apparent activation barrier can be calculated from the model presented above using the flowing equations derived from a simple Arrhenius analysis of the observed rates:

$$E_{app}^{\ddagger} = RT^2 \frac{d(\ln r_{obs}^{+})}{dT} \qquad \text{Eq. 6.19}$$

Combining eq. 6.18 and 6.19, an analytical solution of the apparent activation barrier for this case is derived:

$$E_{app}^{\ddagger} = [E_4^{\ddagger}] + [H_1 + H_2 + H_3] - [\theta_{CO} H_3 + V_O(H_1 + H_2) + V_{OH}(H_1 + 0.5H_2)] \qquad \text{Eq. 6.20}$$

where $E_4^{\ddagger}$ is the activation barrier for step 4 and $H_n$ (where n=1, 2, or 3) is the enthalpy change associated with the $n^{th}$ step. As discussed by *Lynggaard et al*. [5], this is a typical expression for the apparent activation energy with three different terms (divided by square brackets in eq. 6.20). The first term is the activation barrier of the rate limiting step (which can be approximated using DFT). The second term relates to the change in enthalpy of the formation of the reactant species in the rate limiting step. The final term relates to the enthalpy required to free open sites for the reaction (i.e. the energy associated with removing intermediates from the surface) and is a function of surface coverage of the intermediates.

If the model derived above reproduces experimental values, the equations can be used to understand how the rate limiting activation energy, surface coverages, and heats of reactions all contribute to the overall kinetics. If the model does not represent the experimental data, it can be simply modified by assuming additional or different rate limiting steps or by adding additional steps for species adsorption/desorption. This information will provide more thorough knowledge of the reaction mechanism and the effect of Pt on the overall rate kinetics (i.e. does the increase in CO coverage of the provided by Pt increase the rate? Does the presence of CO change the rate limiting step?)

## 3. Alternative projects

Transition metal carbides exhibit interesting chemical properties that differ greatly from the equivalent parent metal or oxide. In an effort towards developing rational catalyst design methodologies, it would be fruitful to understand how this chemistry can be controlled. For example, when the $Mo_2C$ surface is exposed to water, the surface is terminated in oxygen groups. In the presence of CO, this is beneficial for WGS. On the other hand, if the surface is exposed to a highly reducing atmosphere, the surface would presumably be Mo-terminated and exhibit a different chemistry. Under these conditions, CO would dissociate on the surface, enabling Fisher-Trospch chemistry. Lui et al. [6] showed that the chemical activity of different molybdenum materials changed depending on the p-block element incorporated into the Mo lattice. The activities for CO and S adsorption were as follows: Mo > MoP > γ-MoC ≅ δ-MoN. Therefore, one should be able to “fine tune” the activity of a surface by using different formulations of p-block elements and through sufficient control of operating conditions. A systematic study of such materials and conditions could lead to a predictive methodology for obtaining ideal chemistries for various reactions.

Another class of materials that show promise for catalysis are core-shell nano-alloys. These show particular interest in electrochemical reactions and fuel cell applications. Due to the strong interaction exhibited between carbides and metals/metal precursors, it should be possible to easily synthesize core-shell carbide nano-particles. Nørskov et al. [7] showed that the activity of catalysts for the oxygen reduction reaction is a strong function of oxygen and hydroxyl binding energies. Platinum metal exhibits the highest rates. As shown in this study, carbide metal interactions drastically change the chemistry of the supported metal. One could tune the properties of the metal by testing different metal-carbide support combinations to obtain a catalyst that optimizes these activities.

## 4. References


1. Xin, H. and S. Linic, *Exceptions to the d-band Model of Chemisorption on Metal Surfaces: The Dominant Role of Repulsion Between Adsorbate States and Metal d-States.* Journal of Chemical Physics, 2010. 132: 221101
2. K.G. Azzam, I.V. Babich, K. Seshan, L. Lefferts, *Bifunctional Catalyst for the Single-Stage Water–Gas Shift Reaction in Fuel Cell Applications. Part 1. Effect of the Support om the Reaction Sequence.* Journal of Catalysis, 2007. 251: p. 153–162
3. Kalamaras, C.M., P. Panagiotopoulou, D.I. Kondarides, and A.M. Efstathiou, *Kinetic and Mechanistic Studies of the Water–Gas Shift Reaction on Pt/$TiO_2$ Catalyst.* Journal of Catalysis, 2009. 264(2): p. 117-129
4. NIST Chemistry WebBook: NIST Standard Reference Database Number 69. http://webbook.nist.gov/chemistry/
5. Lynggaard, H., A. Andreasen, C. Stegelmann, and P. Stoltze, *Analysis of Simple Kinetic Models in Heterogeneous Catalysis.* Progress in Surface Science, 2004. 77: p. 71–137
6. Lui, P. and J.A. Rodriguez, *Catalytic Properties of Molybdenum Carbide, Nitride and Phosphide: a Theoretical Study*. Catalysis Letters, 2003. 91 (3–4): p. 247-252
7. Nørskov, J.K., J. Rossmeisl, A. Logadottir, L. Lindqvist, J.R. Kitchin, T. Bligaard, and H. Jónsson, *Origin of the Overpotential for Oxygen Reduction at a Fuel-Cell Cathode.* Journal of Physical Chemistry B, 2004. 108: p. 17886-17892